Stojan S. Djokić
Editor

Modern Aspects of Electrochemistry

48

Electrodeposition
Theory and Practice

Springer

MODERN ASPECTS OF ELECTROCHEMISTRY, No. 48:

ELECTRODEPOSITION

THEORY AND PRACTICE

For other titles published in this series, go to
www.springer.com/series/6251

Modern Aspects of Electrochemistry

Series Editors:
Ralph E. White
Department of Chemical Engineering
University of South Carolina
Columbia, SC 29208

Constantinos G. Vayenas
Department of Chemical Engineering
University of Patras
Patras 265 00
Greece

Managing Editor:
Maria E. Gamboa-Aldeco
1107 Raymer Lane
Superior, CO 80027

MODERN ASPECTS OF ELECTROCHEMISTRY, No. 48:

ELECTRODEPOSITION

THEORY AND PRACTICE

Edited by

Stojan S. Djokić
Elchem Consulting Ltd., Canada

Springer

Editor
Dr. Stojan S. Djokić
Elchem Consulting Ltd.
15511-103 Street NW.
Edmonton AB T5X 6B3
Canada
sdjokic@telus.net

ISBN 978-1-4419-5588-3 e-ISBN 978-1-4419-5589-0
DOI 10.1007/978-1-4419-5589-0
Springer New York Dordrecht Heidelberg London

Library of Congress Control Number: 2010925320

Preface

In the past few decades, research in the electrochemical and chemical deposition of metals, alloys, and compounds has brought about significant achievements that are important for the practical applications. The research in this area was related and/or supported with the developments in electronics, aerospace, automotive, energy conversion, and biomedical industries.

The aim of this issue of Modern Aspects of Electrochemistry is to review the latest developments in the science of electrochemical and chemical deposition of various metals, alloys, and/or compounds.

Competent scientists/researchers in their respective fields from all around the world were invited to write this volume and I am very thankful to them to make this volume a reality.

Nikolić and Popov in Chapter 1 discuss the effects of codeposition of hydrogen on the structure of electrodeposited copper. The simultaneous hydrogen evolution and codeposition is more extensively studied in the cases of electrodeposition of chromium or iron group of metals and/or alloys. An increased hydrogen evolution during the electrodeposition of metals leads to noticeable changes in mass and heat transfer, limiting current density, and Ohmic resistance. Consequently, the simultaneous hydrogen evolution significantly influences the surface morphology of the deposited copper, thus leading to the formation of open porous structure with extremely high surface area. The honeycomb-like or other different features of the surface morphology as well as various shapes of electrochemically prepared powders are correlated to the amount of simultaneously evolved hydrogen during the electrodeposition process. From a practical point of view, due to extremely high surface area, materials prepared in this way can be technologically very useful for the applications as electrodes in fuel cells, batteries, or sensors.

Chapter 2, by Štrbac and Wieckowski, gives an impressive overview of a new class of electrode materials that deserve an advanced focus in the future. This chapter is related to the electrochemical or spontaneous deposition of Ru and Os on Au(111) and Pt(111) single crystal surfaces. The contribution of this chapter is particularly important for the understanding of the principles of reactivity

at single crystal electrodes modified by metal nanoislands in the heterogeneous catalysis research. On the applied side, the authors correlate the surface structure and its catalytic activity with the reactions relevant for the fuel cells.

In Chapter 3, by Shaigan, electrodeposition for electrochemical conversion and storage devices is presented. This chapter discusses the latest developments on metal, metal oxide, and conductive polymer electrodeposition processes developed and studied for the applications in the fields of fuel cells, batteries, and capacitors. The importance of electrodeposited materials, which are used or may have the future potential applications in the energy conversion or storage, is clearly shown.

In Chapter 4 by Popov et al., the aspects of the newest developments of the effect of surface morphology of activated electrodes on their electrochemical properties are discussed. These electrodes, consisting of conducting, inert support which is coated with a thin layer of electrocatalyst, have applications in numerous electrochemical processes such as fuel cells, industrial electrolysis, etc. The inert electrodes are activated with electrodeposited metals of different surface morphologies, for example, dendritic, spongy-like, honeycomb-like, pyramid-like, cauliflower-like, etc. Importantly, the authors correlate further the quantity of a catalyst and its electrochemical behavior with the size and density of hemispherical active grain.

Brevnov and Mardilovich present in Chapter 5 the electrochemical micromachining and surface microstructuring based on porous-type anodization of patterned films. Anodic dissolution of aluminum in unprotected areas results in the formation of the porous Al_2O_3 features, whose trapezoidal shape is dictated by the ratio of the vertical and lateral dissolution rates. On the other hand, in the areas protected by the anodization mask, the Al phase is preserved. As a result, the obtained microstructure represents a combination of regions of Al and Al_2O_3. Micro- and nanostructured Al and Al_2O_3 substrates can be used as templates in soft lithography. This aspect of surface treatment is very important for applications in the microelectronics and solar cell industries as well in the fabrication of passive electrical components. The review further focuses on the technological merits of these microfabrication methods and their application for fabrication of 3D metallic and ceramic microstructures.

Djokić and Cavallotti in Chapter 6 discuss the latest developments in the field of electroless deposition. This review is

complementary to Djokić's chapter published in Modern Aspects of Electrochemistry, vol. 35. The electroless deposition itself is quite suitable for the production of different structures and materials discussed in the previous chapters of this volume. If properly carried out, this simple process produces very uniform and continuous coatings on complex shapes, which are difficult to obtain by other competitive technologies. The electroless deposition is used in many areas of production of modern materials and devices. Recent advances in electronics, energy conversion, biomedical fields, etc. are presented. For the successful operation of electroless deposition on the industrial scale, the basic mechanistic aspects should further be investigated.

This new volume of Modern Aspects of Electrochemistry brings to the scientists, engineers, and students new concepts and summarized results in the field of science of electrochemical and chemical deposition, which may have significant influence for future practical applications.

Stojan S. Djokić
Edmonton, AB

Contents

Chapter 2

NOBLE METAL NANOISLANDS DECORATION OF AU(111) AND PT(111) SINGLE CRYSTAL SURFACES

Svetlana Strbac and Andrzej Wieckowski

Chapter 3

ELECTRODEPOSITION FOR ELECTROCHEMICAL ENERGY CONVERSION AND STORAGE DEVICES

Nima Shaigan

Chapter 4

THE EFFECT OF MORPHOLOGY OF ACTIVATED ELECTRODES ON THEIR ELECTROCHEMICAL ACTIVITY

Chapter 5

ELECTROCHEMICAL MICROMACHINING AND MICROSTRUCTURING OF ALUMINUM AND ANODIC ALUMINA

Dmitri A. Brevnov and Peter Mardilovich

Chapter 6

ELECTROLESS DEPOSITION: THEORY AND APPLICATIONS

Stojan S. Djokić and Pietro L. Cavallotti

List of Contributors, MAE 48

Dmitri A. Brevnov
Applied Materials Inc., 3330 Scott Blvd., Santa Clara, CA 95054, USA, dmitri_brevnov@amat.com

Pietro L. Cavallotti
CMIC "G.Natta" Department, Politecnico, Via Mancinelli, 7, Milano, Italy, pietro.cavallotti@polimi.it

Stojan S. Djokić
Elchem Consulting Ltd., Edmonton, AB, Canada T5X 6B3, sdjokic@telus.net

Peter Mardilovich
Hewlett-Packard Company, 1000 NE Circle Blvd, Corvallis, OR 97330, USA, peter.mardilovich@hp.com

Nebojša D. Nikolić
ICTM – Institute of Electrochemistry, University of Belgrade, Njegoseva 12, POB 473, 11001 Belgrade, Serbia, nnikolic@tmf.bg.ac.rs

Konstantin I. Popov
Faculty of Technology and Metallurgy, University of Belgrade, Karnegijeva 4, POB 3503, 11001 Belgrade, Serbia, kosta@tmf.bg.ac.yu

Nima Shaigan
NRC Institute for Fuel Cell Innovation, 4250 East Mall, Vancouver, BC, Canada V6T 1W5, nima.shaigan@nrc-cnrc.gc.ca

Svetlana Štrbac
ICTM – Institute of Electrochemistry, University of Belgrade, Njegoseva 12, POB 473, 11001 Belgrade, Serbia, sstrbac@elab.tmf.bg.ac.rs

Andrzej Wieckowski
Department of Chemistry, University of Illinois, Urbana, IL, USA, andrzej@scs.uiuc.edu

Predrag M. Živković
Faculty of Technology and Metallurgy, University of Belgrade, Karnegijeva 4, POB 3503, 11001 Belgrade, Serbia, peca@tmf.bg.ac.rs

Modern Aspects of Electrochemistry

Topics in Number 45 include:

- The cathodic reduction of nitrate and electrochemical membrane technology
- Non-haloaluminate ionic liquids
- The properties of nanowires composed of metals and semiconductors.
- Ammonium electrolysis as a renewable source of fuel
- The usefulness of synchrotron x-ray scattering to a wide range of electrode phenomena

Topics in Number 46 include:

- Comprehensive review of the structural aspects and anti-corrosion properties of passive films on metals and alloys
- Research on nano- and micro-fabrications based on anodizing treatments combined with chemical/mechanical processes such as laser irradiation, atomic force micro-probe processing and thin film deposition techniques
- Passivity of aluminum-based amorphous alloys and stainless steels and the catalytic activity of copper-based amorphous alloys
- Theoretical analysis of the admittance behavior of passive film/electrolyte junction based on the theory of amorphous semiconductor Schottky barriers

1

Hydrogen Co-deposition Effects on the Structure of Electrodeposited Copper

Nebojša D. Nikolić[1] and Konstantin I. Popov[1,2]

[1] *ICTM-Institute of Electrochemistry, University of Belgrade, Njegoševa 12, Belgrade, Serbia*
[2] *Faculty of Technology and Metallurgy, University of Belgrade, Karnegijeva 4, Belgrade, Serbia*

I. INTRODUCTION

The creation of open porous structures with an extremely high surface area is of great technological significance because such structures are ideally suited for electrodes in many electrochemical devices, such as fuel cells, batteries, and chemical sensors.[1] The open porous structure enables the fast transport of gases and liquids, while the extremely high surface area is desirable for the evaluation of electrochemical reactions. The electrodeposition technique is very suitable for the preparation of such structures because it is possible to control the number, distribution, and pore size in these structures by the choice of appropriate electrolysis parameters.

These metal structures can be formed in both potentiostatic and galvanostatic regimes of electrolysis and their formation are always accompanied by strong hydrogen co-deposition. Hydrogen evolution is the second reaction which occurs at the cathode during electrodeposition processes from aqueous solutions; in some cases it can be

S.S. Djokić (ed.), *Electrodeposition: Theory and Practice*,
Modern Aspects of Electrochemistry 48, DOI 10.1007/978-1-4419-5589-0_1,

ignored while in other cases it cannot.[2] Co-deposition of hydrogen during chromium electroplating is the best documented system,[3,4] because the cathode current efficiency for chromium electrodeposition is 10–25%. Generally, the effect of hydrogen co-deposition during metal electrodeposition processes can be manifested through:[2]

1. Hydrogen absorption which occurs in the substrate metal as H atoms, not H_2 molecules, but may gather as molecule bubbles in voids or vacancies, thus leading to hydrogen embrittlement.
2. Hydrogen bubbles which cling to the surface in an adsorbed state; this leads to the growth of pores as the deposition continues around the bubbles before they are released.
3. Hydrogen bubble evolution can provide a stirring effect and lead to a substantial bubble raft at the free surface of the solution.

The most often employed electrolytes for the electrodeposition of copper are those based on aqueous solutions of sulfuric acid (H_2SO_4) and cupric sulfate ($CuSO_4$).[5] The main species present in aqueous sulfuric acid solutions containing Cu(II) are: bisulfate ions (HSO_4^-), cupric ions (Cu^{2+}), aqueous cupric sulfate ($CuSO_{4(aq)}$), hydrogen ions (H^+), and sulfate ions (SO_4^{2-}).[6–8] In an aqueous solution of sulfuric acid and cupric sulfate, two weak electrolytes, HSO_4^- and $CuSO_{4(aq)}$, are formed according to the following reactions:

$$H^+ + SO_4^{2-} \rightleftarrows HSO_4^- \quad (1)$$

$$Cu^{2+} + SO_4^{2-} \rightleftarrows CuSO_{4(aq)} \quad (2)$$

Pitzer's model[9] was used to calculate the ionic equilibrium in the $CuSO_4$–H_2SO_4–H_2O system over a wide range of concentrations and temperatures.[8] Using Pitzer's model, the relative concentrations of hydrogen ions (H^+) as a function of the total copper concentration and solution acidity were calculated, and this dependence is presented in Fig. 1. From Fig. 1 it can be clearly seen that increasing the copper concentration produces a sharp decrease in the hydrogen ion concentration, while increasing the concentration of sulfuric acid produces an increase in the hydrogen ion concentration.

According to (1) and (2), the addition of sulfuric acid to the solution decreases the concentration of free sulfate ions due to the

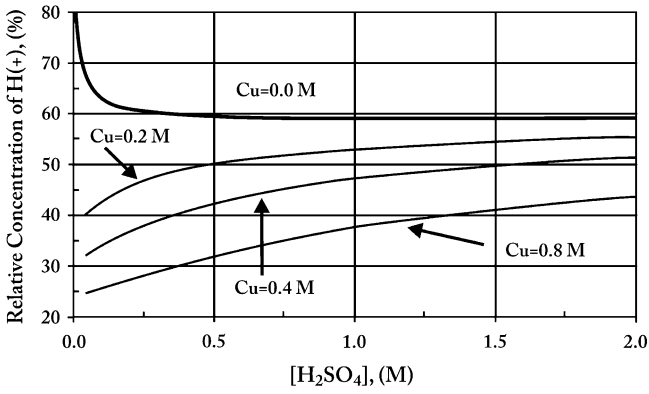

Figure 1. Relative concentration of hydrogen ions as function of sulfuric acid and total copper concentrations, at 25°C ($C_{RH+} = [H^+]/[H_T]$). (Reprinted from Ref. [8] with permission from Elsevier).

formation of bisulfate ions. The addition of cupric sulfate to the solution increases the concentration of bisulfate ions and decreases the concentration of hydrogen ions.

In the case of copper electrodeposition,[10] as opposed to other metals such as nickel and cobalt,[11,12] there are well-defined ranges of current densities and overpotentials without and with hydrogen co-deposition. The beginning of the hydrogen evolution reaction, as the second reaction, corresponds to some overpotential belonging to the plateau of the limiting diffusion current density, being higher than the critical overpotential for the initiation of dendritic growth and lower than that for instantaneous dendritic growth.[13] Increasing the overpotential intensifies the hydrogen evolution reaction and at some overpotential outside the plateau of the limiting diffusion current density, hydrogen evolution becomes vigorous enough to change the hydrodynamic conditions in the near-electrode layer. This offers the possibility of detailed investigations and comparison of the morphologies of copper, and consequently, of any other metals, obtained without and with hydrogen co-deposition.

In the case of copper, electrodeposition at low overpotentials produces large grains with relatively well-defined crystal shapes. Further increasing the overpotential leads to the formation of cauliflower-like and carrot-like protrusions, and finally, dendritic deposits are formed in the absence of strong hydrogen co-deposition.[13]

Strong hydrogen co-deposition leads to a mixing of the solution and changes the mass transfer limitations at an electrode surface. At the same time, the evolved hydrogen bubbles exert substantial effects on mass and heat transfer, limiting current density and ohmic resistance,[14–16] as well as on the morphology of the deposit, leading to the formation of open porous structures with an extremely high surface area.[1,10,17–19]

Electrodeposition of copper under conditions of a vigorous hydrogen co-deposition is of high technological significance, because open porous structures of copper with an extremely high surface area are suitable for the construction of nanocomposite anodes (consisting of Cu and CeO_2) for solid oxide fuel cells.[1] Also, copper shows a high activity for nitrate ion reduction,[20] as well as for a reaction in which nitrate is reduced to ammonia in high yield in aqueous acidic perchlorate and sulfate media.[21]

Bearing in mind the great practical significance of copper deposits obtained under the conditions of hydrogen co-deposition, as well as the fact that detailed investigations at high current densities and overpotentials have been performed only from the point of view of the formation of metal powders,[13,22–25] a better understanding of the effect of hydrogen evolution on the electrodeposition of copper at high overpotentials is necessary.

The morphology of electrodeposited copper in the presence of vigorous hydrogen evolution was described recently,[1] and the mechanism of the formation of this type of morphology was established by Nikolić et al.[10]

The aim of this chapter was to give comprehensive treatment of the morphology of copper electrode posited at high overpotentials, especially in the presence of hydrogen co-deposition, obtained in the potentiostatic conditions from different electrolytes and at different temperatures.

II. THE CONCEPT OF "THE EFFECTIVE OVERPOTENTIAL"

1. The Definition of the Concept and Mathematical Model

The polarization curve for copper electrodeposition from 0.15 M $CuSO_4$ in 0.50 M H_2SO_4 is shown in Fig. 2. The average current efficiencies for hydrogen evolution reaction, $\eta_{av}(H_2)$, in potentiostatic

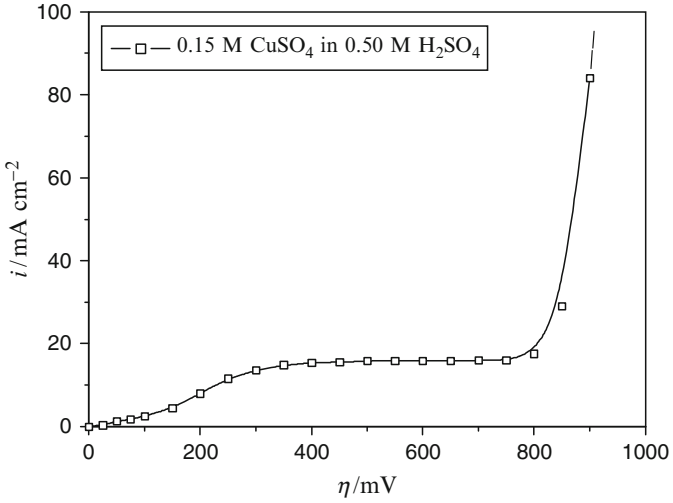

Figure 2. Polarization curve for the cathodic process of copper deposition from 0.15 M $CuSO_4$ in 0.50 M H_2SO_4. Temperature: 18.0 ± 1.0°C. (Reprinted from Ref. [10] with permission from Elsevier).

deposition are derived from the dependences of the current of copper electrodeposition on time and the dependences of the volume of the evolved hydrogen on time[10] using procedure described in Ref. [26]

The average current efficiency for hydrogen evolution reaction at an overpotential of 700 mV was very small (near 2.0%),[10] and at lower overpotentials it even cannot be observed. The average current efficiency for the hydrogen evolution at an overpotential of 800 mV was 10.8%, while at an overpotential of 1,000 mV was 30.0%.[10] The critical overpotential for the beginning of the hydrogen evolution can be estimated to be about 680 mV.[10]

The morphologies of copper electrodeposits obtained potentiostatically, onto vertical stationary copper wire electrodes previously covered by copper thin films[10] from a copper solution containing 0.15 M $CuSO_4$ in 0.50 M H_2SO_4, at a temperature of 18.0 ± 1.0°C in different hydrogen co-deposition conditions are shown in Figs. 3–10.

The deposits obtained at an overpotential of 550 mV with different quantities of electricity are shown in Figs. 3–6. At this overpotential, there is no hydrogen co-deposition at all. The deposit obtained with a quantity of electricity of 2.5 mA h cm^{-2} is shown

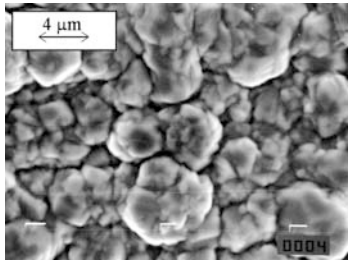

Figure 3. Copper deposit obtained at an overpotential of 550 mV. Quantity of electricity: 2.5 mA h cm^{-2}. (Reprinted from Ref.[10] with permission from Elsevier).

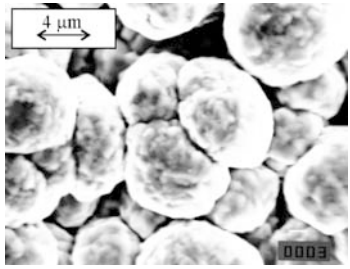

Figure 4. Copper deposit obtained at an overpotential of 550 mV. Quantity of electricity: 5.0 mA h cm^{-2}. (Reprinted from Ref.[10] with permission from Elsevier).

in Fig. 3. The surface film is completed, the grains grown by electrodeposition on the initially formed nuclei practically touch each other and there is no new nucleation on already existing grains. The difference in size between grains can also be observed. This is due to the fact that the nucleation does not occur simultaneously over the whole cathode surface, but it is a process extended in time, so that crystals generated earlier may be considerably larger in the size than ones generated later. These differences increase with an increased quantity of electrodeposited metal, what can be seen from Fig. 4 presenting the copper deposit obtained with a quantity of

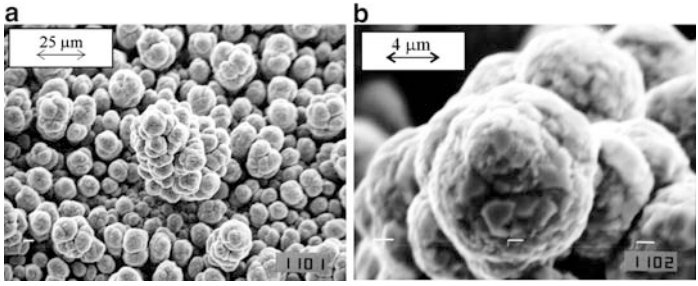

Figure 5. Copper deposit obtained at an overpotential of 550 mV: (**a**) cauliflower-like structure, and (**b**) the detail from Fig. 5a. Quantity of electricity: 10 mA h cm^{-2}. (Reprinted from Ref. [10] with permission from Elsevier).

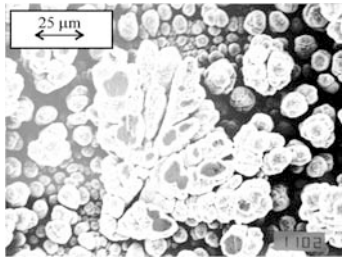

Figure 6. Copper deposit obtained at an overpotential of 550 mV. Quantity of electricity: 20 mA h cm^{-2}. (Reprinted from Ref. [17] with permission from Elsevier).

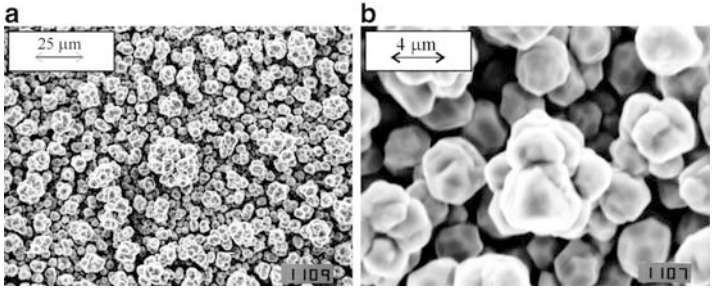

Figure 7. Copper deposit obtained at an overpotential of 700 mV: (**a**) cauliflower-like structure, and (**b**) the detail from Fig. 7a. Quantity of electricity: 2.5 mA h cm^{-2}. (Reprinted from Ref. [10] with permission from Elsevier).

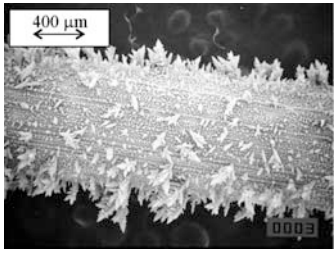

Figure 8. Copper deposit obtained at an overpotential of 700 mV. Quantity of electricity: 5.0 mA h cm^{-2}. (Reprinted from Ref. [10] with permission from Elsevier).

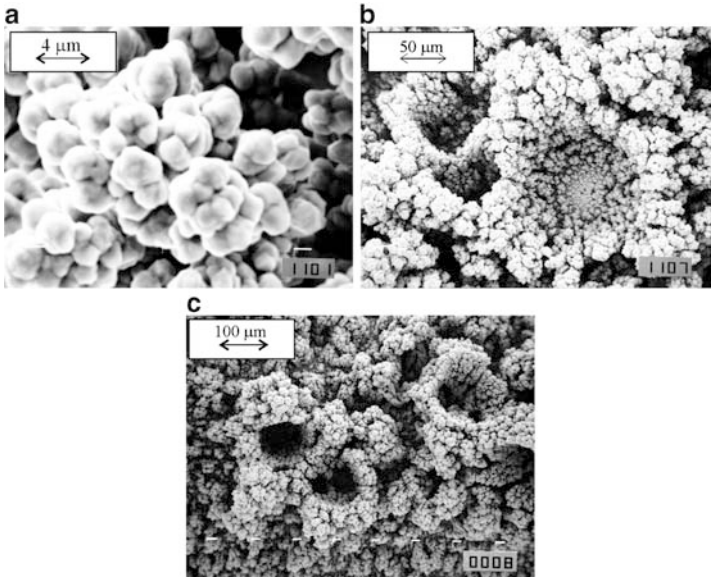

Figure 9. Copper deposit obtained at an overpotential of 800 mV. (**a**, **b**) quantity of electricity: 5.0 mA h cm^{-2} and (**c**) quantity of electricity: 10 mA h cm^{-2}. (Reprinted from Ref. [10] with permission from Elsevier).

electricity of 5.0 mA h cm^{-2}. These enlarged differences are also the consequence of the fact that some smaller grains are consumed by the larger ones,[27] as can be deduced from Figs. 3 and 4. This is also illustrated by Fig. 5a. The increase of the quantity of the

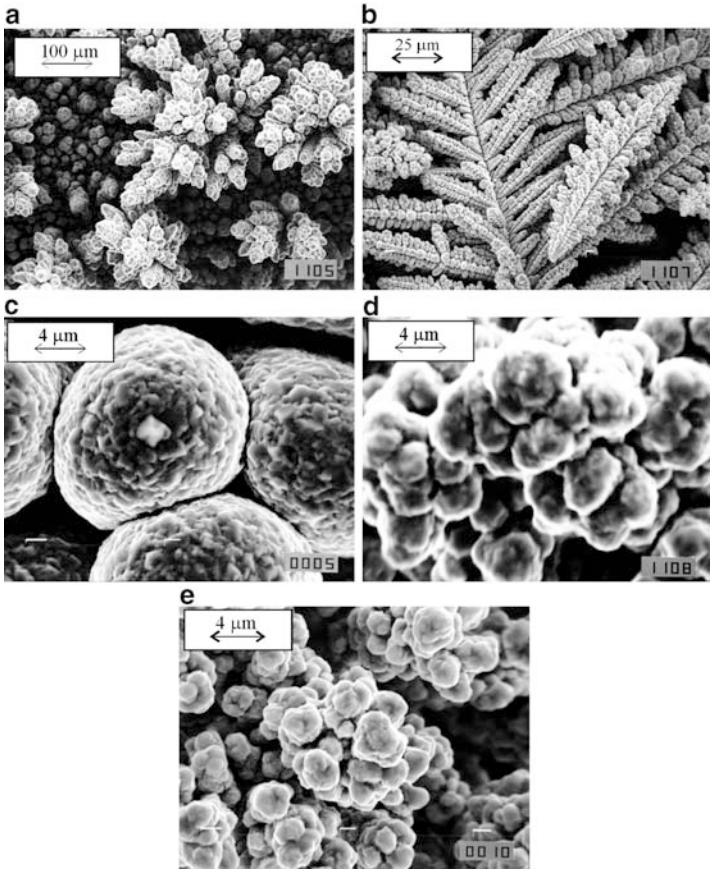

Figure 10. Copper deposits obtained with a quantity of the electricity of 20 mA h cm^{-2} and at overpotentials of: (**a**) 550 mV, (**b**) 700 mV, (**c**) 450 mV, (**d**) 800 mV, and (**e**) 1,000 mV. (Reprinted from Ref. [10] with permission from Elsevier).

electrodeposited metal led to the formation of a cauliflower-like structure (Fig. 5a, b). Furthermore, from Fig. 5a it can be seen that the spherical diffusion layers inside linear diffusion layer of the macroelectrode are formed around these cauliflower-like particles. Finally, further increase of the quantity of the electrodeposited metal produces dendritic deposit (Fig. 6).

On the other hand, it is well known that the induction time of dendrite growth initiation strongly decreases with increasing overpotential of electrodeposition.[28] The situation on the electrode surface after deposition with 2.5 mA h cm^{-2} at 700 mV (Fig. 7) is very similar to the situation after 10 mA h cm^{-2} at 550 mV (Fig. 5). The most important difference is in the shape and size of growing grains, being less globular and smaller in electrodeposition at 700 mV. Besides, the interparticle distances are relatively equal which indicate that these distances are not due to appearance of hydrogen co-deposition, which is still very small at 700 mV. Dendrites appear at 700 mV after deposition with 5.0 mA h cm^{-2} (Fig. 8).[10]

The electrodeposition at 800 mV with the quantity of the electricity of 5.0 mA h cm^{-2} (Fig. 9) did not lead to the formation of copper dendrites as at previously analyzed overpotential of 700 mV. The agglomerates of small copper grains become dominant form of the copper morphology electrodeposited at this overpotential (Fig. 9a) being similar to that from Fig. 7b. Also, there are large holes or craters between the agglomerates of these grains, which is probably due to the hydrogen co-deposition (Fig. 9b). This copper deposit is denoted as a honeycomb-like structure with craters as main characteristic,[10] as was shown earlier for copper and tin deposits in Ref. [1] The honeycomb-like structure is formed at 800 mV and with twice the quantity of electricity (Fig. 9c), as well as at an overpotential of 1,000 mV.[10] (see also Sect. III).

It is known that the hydrogen evolution effects onto the hydrodynamic conditions inside electrochemical cell.[29–31] The increase in hydrogen evolution rate leads to the decrease of the diffusion layer thickness and, hence, to the increase of limiting diffusion current density of electrode processes. It was shown[29] that if the rate of gas evolution at the electrode is larger than 100 cm^3/cm^2 min (>5 A/cm^2), the diffusion layer becomes only a few micrometers thick. It is also shown[29] that a coverage of an electrode surface with gas bubbles can be about 30%. If the thickness of the diffusion layer in conditions of natural convection is $\sim 5 \times 10^{-2}$ cm and in strongly stirred electrolyte $\sim 5 \times 10^{-3}$ cm,[32] it is clear that gas evolution is the most effective way to decrease mass transport limitations for electrochemical processes in mixed activation – diffusion control.

The overpotential η and the current density i are related by

$$\eta = \frac{b_c}{2.3} \ln \frac{i}{i_o} + \frac{b_c}{2.3} \ln \frac{1}{1 - (i/i_L)}, \tag{3}$$

where i_o, i_L, and b_c are the exchange current density, the limiting diffusion current density and cathodic Tafel slope for electrochemical process in mixed activation – diffusion control.[13] The first term in (3) corresponds to the activation part of deposition overpotential and the second one is due to the mass transfer limitations. If one and the same process takes place under two different hydrodynamic conditions, characterized by two different values of the limiting diffusion current densities $i_{L,1}$ and $i_{L,2}$, (3) can be rewritten in the forms:

$$\eta_1 = \frac{b_c}{2.3} \ln \frac{i_1}{i_o} + \frac{b_c}{2.3} \ln \frac{1}{1 - (i_1/i_{L,1})} \tag{4}$$

and

$$\eta_2 = \frac{b_c}{2.3} \ln \frac{i_2}{i_o} + \frac{b_c}{2.3} \ln \frac{1}{1 - (i_2/i_{L,2})}, \tag{5}$$

where η_1 and η_2 and i_1 and i_2 are the corresponding values of overpotentials and current densities. The same degree of diffusion control is obtained if

$$\frac{i_1}{i_{L,1}} = \frac{i_2}{i_{L,2}} \tag{6}$$

or,

$$i_2 = i_1 \frac{i_{L,2}}{i_{L,1}} \tag{7}$$

and substitution of i_2 from (7) in (5) and further rearranging gives

$$\eta_2 = \frac{b_c}{2.3} \ln \frac{i_1}{i_o} + \frac{b_c}{2.3} \ln \frac{1}{1 - (i_1/i_{L,1})} + \frac{b_c}{2.3} \ln \frac{i_{L,2}}{i_{L,1}} \tag{8}$$

and
if (4) is taken into account:

$$\eta_2 = \eta_1 + \frac{b_c}{2.3} \ln \frac{i_{L,2}}{i_{L,1}}. \tag{9}$$

Hence, if

$$i_{L,2} > i_{L,1} \tag{10}$$

in order to obtain the same degree of diffusion control in two hydrodynamic conditions, (9) must be satisfied, meaning that

$$\eta_2 > \eta_1. \tag{11}$$

The results presented here can be then explained as follows. In the absence of strong hydrogen evolution, the diffusion layer is due to the natural convection and does not depend on the overpotential of electrodeposition. As excepted, for deposition times lower than the induction time for dendritic growth initiation, the same type of deposit at larger overpotential (Fig. 7) is obtained as at lower overpotential (Fig. 5), being somewhat different in grain sizes and particle shapes.

The vigorous hydrogen evolution changes the hydrodynamic conditions and decreases the degree of diffusion control. Hence, (9) should be rewritten in the form:

$$\eta_1 = \eta_2 - \frac{b_c}{2.3} \ln \frac{i_{L,2}}{i_{L,1}}, \tag{12}$$

where η_1 becomes the effective overpotential, $\eta_1 = \eta_{eff}$, related to conditions of natural convection at which there is the same degree of diffusion control as at overpotential η_2 with the hydrogen co-deposition. Hence, the dendritic growth can be delayed or completely avoided, as can be seen from Fig. 9c, meaning that there is a really lower degree of diffusion control at an overpotential of 800 mV with the hydrogen co-deposition than at an overpotential of 700 mV where the hydrogen co-deposition is very small.

Hence, on the basis of presented results, we can propose a concept of "effective overpotential" for a metal electrodeposition. This concept is proposed – thanks to morphologies of copper deposits obtained at high deposition overpotentials (800 mV and more)[10] where the hydrogen evolution occurs. These copper deposits are probably the consequence of the stirring of electrolyte in the near-electrode layer by evolving hydrogen. This process leads to a decrease of the thickness of diffusion layer, and consequently, up to an increase of the limiting current density. According to (12), the increase of the limiting current density leads to a metal deposition at an overpotential, which is effectively lower than the specified one. Then, the obtained morphologies of copper deposits become similar to the ones obtained at some lower overpotential at which the hydrogen co-deposition does not exist.

The better understanding of the concept "effective overpotential" can be realized by taking into account the fact that the time of dendritic growth initiation depends on used deposition overpotentials. Increasing deposition overpotentials lead to decreasing times for

the beginning of dendritic growth.[28] Observing deposits obtained at overpotentials belonging to the limiting diffusion current density plateau (550 and 700 mV), one can notice that cauliflower-like forms are obtained at an overpotential of 550 mV (Fig. 5a), and dendritic forms at an overpotential of 700 mV (Fig. 8). Meanwhile, the electrodeposition with a quantity of the electricity of 20 mA h cm^{-2} leads to the formation of degenerate dendritic structure at 550 mV (Figs. 6 and 10a). Copper dendrites remain a main characteristic of the electrodeposition at 700 mV (Fig. 10b). On the other hand, it can be shown that copper dendrites are not formed by the electrodeposition at lower overpotential (for example, at 450 mV where the hydrogen evolution was also zero) with a quantity of the electricity of 20 mA h cm^{-2} (Fig. 10c). The main forms of the copper deposit obtained at this overpotential are copper globules. Also, dendritic forms are not formed with a quantity of the electricity of 20 mA h cm^{-2} and during electrodepositions at overpotentials of 800 and 1,000 mV (Fig. 10d, e). The agglomerates of copper particles remain the main characteristics of the structure of deposits obtained at these overpotentials. The macromorphology of these deposits will be discussed later.

Anyway, the structure of copper deposits obtained at overpotentials of 800 and 1,000 mV with a quantity of the electricity of 20 mA h cm^{-2} was similar to those obtained at lower overpotentials before the beginning of dendritic growth. The absence of copper dendrites at overpotentials of 800 and 1,000 mV after the electrodeposition with 20 mA h cm^{-2}, as well as the similarity of the obtained morphologies of copper deposits with those obtained at lower overpotentials before dendritic growth initiation clearly indicates that there is really lower degree of diffusion control at these overpotentials than at overpotentials of 550 and 700 mV, respectively.

The concept of "effective overpotential" can be probably applied in other cases where there is a change of hydrodynamic conditions in the near-electrode layer. The change of hydrodynamic conditions, and consequently, of metal morphologies can be caused by stirring of plating solutions in ultrasonic field,[33] in an imposed magnetic field (magnetohydrodynamic effect – MHD effect),[34–39] as well as by stirring of solution by RDE (rotating disk electrode).[40]

2. The Concept of "Effective Overpotential" Applied for Metal Electrodeposition Under an Imposed Magnetic Field

Nickel deposits obtained at a cathodic potential of −1,300 mV/SCE without and with a parallel orientation of magnetic field of 500 Oe, are shown in Fig. 11a, b, respectively. Figure 11a shows that the nickel deposit obtained without an imposed magnetic field consisted of bunch of nickel grains, while it can be seen from Fig. 11b that the nickel deposit obtained under a magnetic field with a parallel orientation to the electrode surface was a porous structure and without bunch of nickel grains.

Figure 12 shows copper deposits obtained at a cathodic potential of −500 mV/SCE without and with a magnetic field of 500 Oe applied to be parallel to the electrode surface. It can be seen from

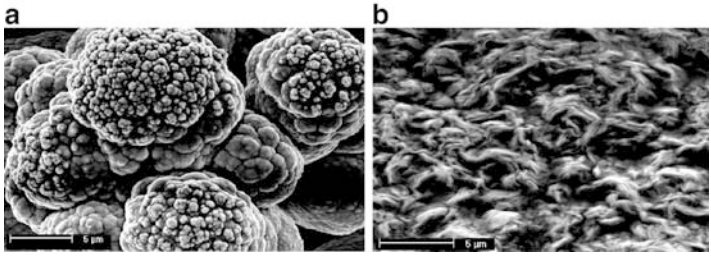

Figure 11. Nickel deposits obtained at a cathodic potential of −1,300 mV/SCE: (**a**) without and (**b**) with a magnetic field of parallel orientation of 500 Oe. (Reprinted from Ref. [39] with permission from the Serbian Chemical Society).

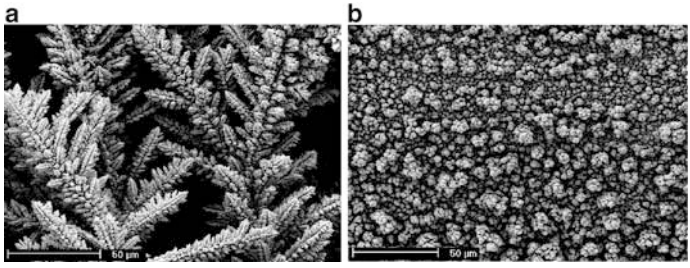

Figure 12. Copper deposits obtained at a cathodic potential of −500 mV/SCE: (**a**) without and (**b**) with a magnetic field of parallel orientation of 500 Oe. (Reprinted from Ref. [39] with permission from the Serbian Chemical Society).

this figure that the copper deposit obtained without the parallel field (Fig. 12a) had dendritic structure, while the copper deposit obtained with the parallel field (Fig. 12b) had cauliflower-like structure.

The application of the concept of "effective overpotential" for the case of the change of hydrodynamic conditions caused by magnetic field effects means that morphologies of nickel and copper deposits obtained under parallel fields (the largest magnetohydrodynamic (MHD) effect) should be, at macro level, similar to those obtained at some lower overpotentials or potentials without imposed magnetic fields. This assumption can be confirmed by the following consideration:

Figure 13a shows the nickel deposit obtained at a cathodic potential of −1,200 mV/SCE without an applied magnetic field. It can be noticed that there is similarity at a macro level between the morphology of this nickel deposit and the morphology of nickel deposit obtained at a potential of −1,300 mV/SCE under the parallel field (Fig. 11b). The both nickel deposits are without dendritic

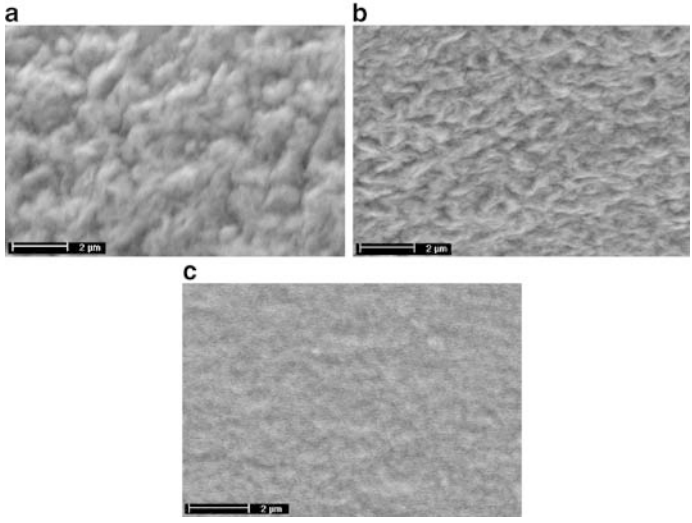

Figure 13. Nickel deposits obtained at a cathodic potential of −1,200 mV/SCE: (**a**) without, (**b**) with a magnetic field of parallel orientation of 500 Oe, and (**c**) the nickel deposit obtained at a cathodic potential of −1,000 mV/SCE without an applied magnetic field. (Reprinted from Ref. [39] with permission from the Serbian Chemical Society).

and globular parts and with clearly visible nickel grains. The only difference is in compactness of deposits, which is a consequence of larger nucleation rate and more intensive hydrogen evolution at a potential of −1,300 mV/SCE than at a potential of −1,200 mV/SCE.

Also, the concept of "effective overpotential" can be illustrated and by the comparison of the nickel deposit obtained at a cathodic potential of −1,200 mV/SCE under the parallel field with the nickel deposit obtained at −1,000 mV/SCE without an imposed magnetic field. Morphologies of these nickel deposits are shown in Fig. 13b, c. Figure 13b shows the morphology of the nickel deposit obtained at a potential of −1,200 mV/SCE under a parallel field of 500 Oe, while Fig. 13c shows the morphology of the nickel deposit obtained at −1,000 mV/SCE without an applied magnetic field. From Fig. 13b, c it can be observed that there is similarity at a macro level between these nickel deposits. The boundaries between adjacent nickel grains cannot be observed. Anyway, the nickel deposit obtained at −1,200 mV/SCE under the parallel field (Fig. 13b) was more similar to that obtained at −1,000 mV/SCE without an applied magnetic field than to that obtained at −1,200 mV/SCE without an imposed magnetic field (Fig. 13a).

This concept can be also applied for the case of the electrodeposition of copper. As mentioned earlier, the morphology of the copper deposit obtained at cathodic potential of −500 mV/SCE under the parallel field was of cauliflower-like structure (Fig. 12b), while the morphology of the copper deposit obtained without the applied magnetic field had very dendritic structure (Fig. 12a). It is known that dendritic structures are main characteristic of electrodeposition in conditions of full diffusion control, while cauliflower-like structures are a characteristic of a dominant diffusion in mixed control of electrodeposition process.[13]

Anyway, it can be seen that the application of a parallel field of 500 Oe led to shifting of the formation of characteristic morphological forms toward lower cathodic potentials for about 100–200 mV.

Of course, the influence of magnetic field appears to be restricted to the diffusion-limited regions. During electrolysis under parallel fields, the Lorentz force induces convective flow of the electrolyte close to electrode surface. A magnetically stimulated convection leads to a decrease of the diffusion layer thickness thus increasing the diffusion-limited current density.[39] As a rule, it was adopted that the limiting diffusion current density depends on magnetic field, as $i_L \propto B^{1/3}$.[41] Anyway, the increase of the

limiting current density caused by the effect of applied magnetic fields with a parallel orientation leads to a decrease of the degree of diffusion control of the deposition process, and then, the electrodeposition process occurs at some overpotential which is effectively lower. This overpotential at which a metal electrodeposition occurs when the change of hydrodynamic conditions is caused by the effect of imposed magnetic fields (i.e., by the magnetohydrodynamic effect) also represents "effective overpotential" of electrodeposition process.

Similar effects can be observed during electrodeposition in an ultrasonic field.[33] Copper deposits obtained in an ultrasonic field were compact and more ordered structure than copper deposits obtained without an effect of ultrasonic fields.

It is very clear from previous consideration that the proposed concept can be applied and for the case of electrodeposition of nickel. This concept is usable for all cases where there is the change of the hydrodynamic conditions in the near-electrode layer, which can be induced by the agitation of electrolyte by evolving hydrogen, ultrasonic and magnetic fields, or simply by vigorous stirring of an electrolyte.

III. PHENOMENOLOGY OF A FORMATION OF A HONEYCOMB-LIKE STRUCTURE DURING COPPER ELECTRODEPOSITION

The initial stage of the electrodeposition at an overpotential of 1,000 mV corresponding to the electrodeposition time of 10 s is given in Fig. 14a–d. These and other experiments whose results are presented in this section (Figs. 14–19) were performed potentiostatically from 0.15 M $CuSO_4$ in 0.50 M H_2SO_4 at a temperature of $18.0 \pm 1.0°C$, onto vertical stationary copper wire electrodes which were not previously covered by copper thin films. The parallelism between the process of the copper electrodeposition and the hydrogen evolution can be easily seen in Fig. 14a. From this figure, both the sites of the formation of hydrogen bubbles (i.e., sites at which the hydrogen evolution starts) and the agglomerates of copper grains between them can be noticed.

It can be seen from Fig. 14b that the hydrogen evolution reaction, as well as the copper electrodeposition are initiated at irregularities at an electrode surface. The irregularities at an electrode surface represent the most convenient sites (active centres)

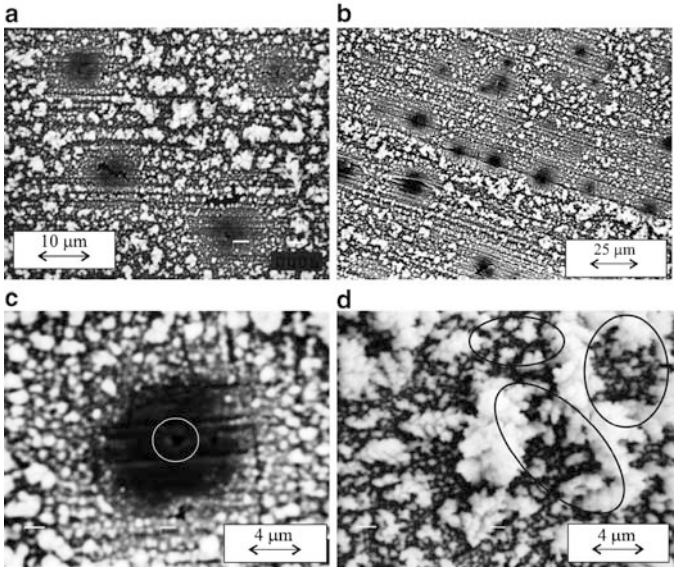

Figure 14. (**a**) Copper deposit obtained at an overpotential of 1,000 mV. Time of electrolysis: 10 s, (**b**) the positions of formation of hydrogen bubbles and agglomerates of copper grains, and (**c**, **d**) the details from Fig. 14a and b. (Reprinted from Ref. [18] with permission from Springer).

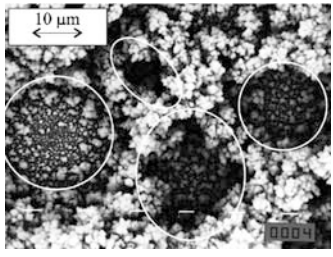

Figure 15. Copper deposit obtained at an overpotential of 1,000 mV. Time of electrolysis: 30 s. (Reprinted from Ref. [18] with permission from Springer).

for the beginning of hydrogen evolution, i.e., for the formation of hydrogen bubbles. The true position of the formation of a hydrogen bubble can be seen from Fig. 14c showing a bare part of the copper electrode (part in circle in Fig. 14c).

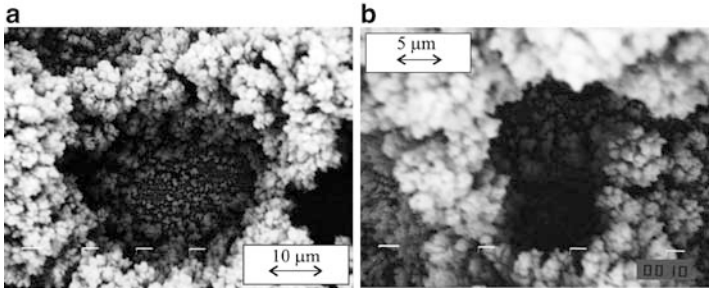

Figure 16. Copper deposit obtained at an overpotential of 1,000 mV: (**a**) "regular hole", and (**b**) "irregular hole". Time of electrolysis: 60 s. (Reprinted from Ref. [18] with permission from Springer).

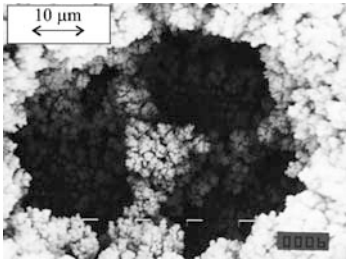

Figure 17. Copper deposit obtained at an overpotential of 1,000 mV. Time of electrolysis: 120 s. (Reprinted from Ref. [18] with permission from Springer).

The mechanism of formation of bubbles at an electrode surface has been described for a long time.[29–31,42] The gas formed at the electrode dissolves in the electrolyte, which becomes supersaturated. At the nucleation sites on the electrode, small bubbles are formed, grow to a certain size and are then detached. The higher the current density, the more the solution becomes saturated; more and more nucleation sites become active, and also the rate of growth of the bubbles increases.[31] Jenssen and Hoogland[31] also pointed out that at lower current densities, only the irregularities at the edges (formed by the cutting of the foil) are active, and the amount of bubbles formed at the lower edge is sufficient to take up all the hydrogen formed. This is no longer the case at higher current density, and then bubbles are also formed at the less deformed surface.

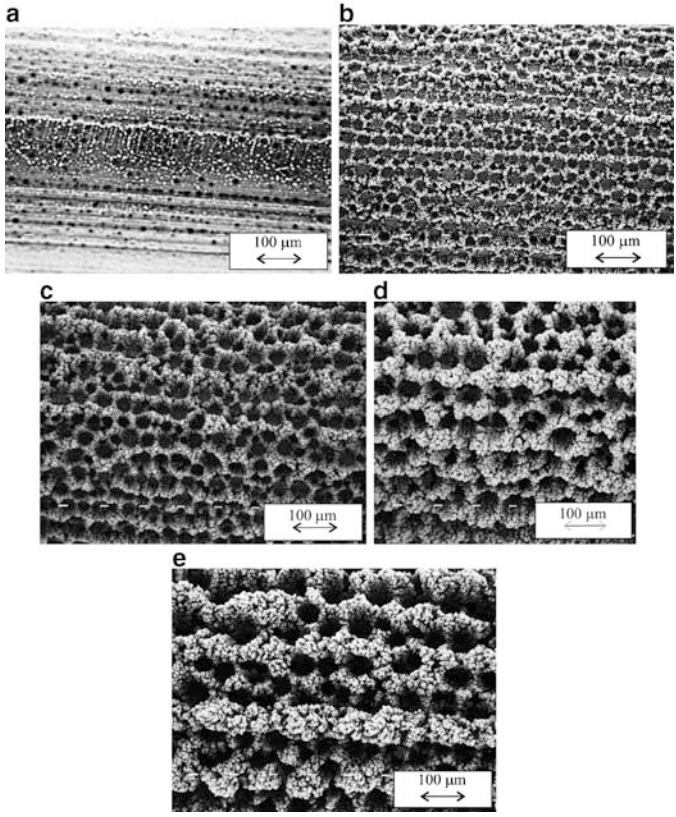

Figure 18. Copper deposits obtained at an overpotential of 1,000 mV. Time of electrolysis: (**a**) 10, (**b**) 30, (**c**) 60, (**d**) 120, and (**e**) 150 s. (Reprinted from Ref. [18] with permission from Springer).

Figure 14d shows typical agglomerates consisted of relatively small copper grains and situated between the bubbles (parts in ellipses in this figure). The different size and periodicity of agglomerates of copper grains can be explained as follows: It was assumed[43] that the active centres have different activity or different critical overpotential with respect to the formation of nuclei. The nuclei can be formed on those centres whose critical overpotential is lower or equal to the overpotential externally applied to the cell. The higher the applied overpotential, the greater the number of

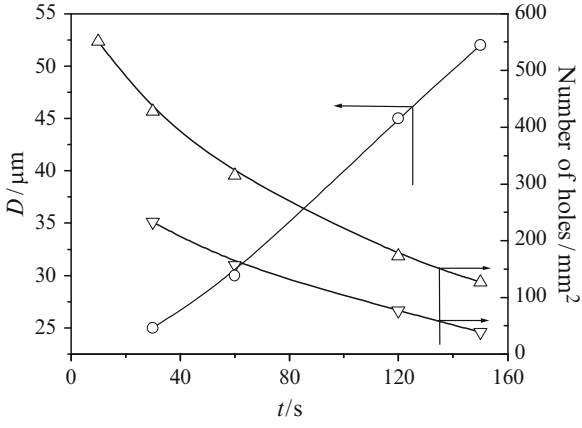

Figure 19. The dependence of average diameters of the surface holes, *D* (*open circles*), number of "regular holes" per square millimeter surface area of copper electrodes (*open triangles*) and number of "irregular holes" per square millimeter surface area of copper electrodes (*inverted traingles*) on electrolysis times. (Reprinted from Ref. [18] with permission from Springer).

active sites take part in nucleation process. The active sites are mainly placed on the irregularities at an electrode surface,[44] as can be seen in Fig. 14b. On the other hand, nucleation does not occur simultaneously over the entire cathode surface, but it is a process extended in time so that crystals generated earlier may be considerably larger in size than the ones generated later. Besides, in the case of fast electrodeposition processes, the nucleation exclusion zones around already existing nuclei are formed,[45,46] and in the case of the slower ones, there is an effect on the nucleation rate distribution around growing grains.[47,48] This causes the periodicity in the surface structure of polycrystalline electrolytic deposits.[49–51]

The copper deposit obtained with the electrodeposition time of 30 s is given in Fig. 15, from which can be seen two characteristic groups of holes or craters. The origin of one group of holes is due to the attachment of hydrogen bubbles at surface area of an electrode. These holes have regular circular shapes and, in Fig. 15 they are given in circles. The second group of holes have irregular shapes, and these holes are given in ellipses in Fig. 15. The formation of

these irregular craters is not associated with the process of hydrogen evolution, and it can be assumed that the origin of these holes is of the agglomerates of relatively small copper grains shown in Fig. 14d.

The formation of craters or holes as a consequence of the hydrogen evolution can be explained by the analysis of Figs. 14a, c and 15 in the following way: In the initial stage of the electrodeposition, hydrogen bubbles are formed at active sites at an electrode surface (Fig. 14a, b), and copper growth is blocked at these sites. These hydrogen bubbles grow with a time of electrodeposition, and in one moment, they get detached from an electrode surface realizing a fresh electrode surface for a new copper nucleation. This can be seen from Figs. 14c and 15, showing a bare copper electrode at a position where the formation of a hydrogen bubble begins (Fig. 14c) and a position of already formed hole covered with a thin copper film (parts in circles in Fig. 15). Anyway, the processes of the formation of hydrogen bubbles at active sites, their detachment from an electrode surface when critical size is reached as well as their repeated formation at growing electrode represent successive steps that led to the formation of this type of holes. The typical crater or hole formed due to the attachment of hydrogen bubbles ("regular hole"), which is obtained with the electrodeposition time of 60 s, is shown in Fig. 16a.

The explanation for the formation of the second group of craters can be given as follows: as already pointed out, at an overpotential of 1,000 mV, the process of hydrogen evolution is competitive with the process of copper electrodeposition. As a consequence of a parallel evaluation of these processes, both the sites of a formation of hydrogen bubbles and the agglomerates of copper grains between them were obtained (Fig. 14). The agglomerates of these copper grains exactly represent nucleation centres for the formation of craters or holes belonging to the other group (parts in ellipses in Fig. 14d). The further electrolysis process leads to copper nucleation and growth primarily at these agglomerates owing to the concentration of current lines at them, which will lead to a joining closely formed agglomerates and a formation of hole in one moment. This effect of current distribution at growing surface will be enhanced by the additional physical blocking of copper growth by the hydrogen bubbles preventing nucleation processes at lateral sides of the agglomerates and enhancing the nucleation processes at the top of the agglomerates. In addition, these agglomerates initiate walls, which will limit the growth of hydrogen bubbles. Hence, as a result of all these parallel

processes, holes of "irregular" shapes are formed. These holes are situated among those formed due to the attachment of hydrogen bubbles, and these craters are deeper than those obtained due to the attachment of hydrogen bubbles. The typical "irregular hole" is given in Fig. 16b, presenting a hole obtained with the electrodeposition time of 60 s.

Mechanisms describing the formation of holes of this type are based on the amplification of electrode surface coarseness[52,53] in diffusion-controlled electrodeposition and to the tip[54] and edge[55] effects of current density distribution at electrode surface. More about these mechanisms can be found in Ref. [13]

With the evaluating electrodeposition process, a coalescence of closely formed hydrogen bubbles was observed. The typical coalesced hydrogen bubble obtained at an overpotential of 1,000 mV with electrolysis time of 120 s is shown in Fig. 17. The number of holes formed of coalesced hydrogen bubbles increases with time of electrolysis. In Fig. 17, it can be seen that a structure of hole formed of coalesced hydrogen bubbles consisted of smaller holes which were mutually separated by a "bridge" of copper agglomerates. Agglomerates of copper grains that separate smaller holes inside a large hole are at a lower level than the agglomerates of copper grains around a large hole.

The decrease in a number of formed holes can be easily observed in Fig. 18, showing morphologies of copper deposits obtained with times of electrolysis of 10, 30, 60, 120, and 150 s. This decrease can be primarily ascribed to a coalescence of a closely formed hydrogen bubbles. On the other hand, the number of craters formed of an initially formed copper agglomerates also decreases with electrolysis times, and it can be expected that these craters will completely disappear with a longer time of electrolysis. This is due to the current distribution at a copper growing surface; that is, the fact that a new copper nucleation and growth primarily takes place at the edges of these holes, which will lead to totally closing and losing of holes from this group with longer electrolysis times. In this way, only the holes formed due to the hydrogen evolution will remain at a surface area of electrode.

Figure 19 shows the dependence of average diameters of craters or holes, D, formed due to the attachment of hydrogen bubbles on electrolysis time, from which the increase in average diameters of holes with the electrolysis time can be clearly seen. The dependences of the number of craters or holes formed due to the attachment

of hydrogen bubbles per square millimeter surface area ("regular holes") and those formed due to the effect of current distribution ("irregular holes") on the electrolysis time are also shown in Fig. 19. The decrease in the number of both groups of craters or holes can be observed in this figure.

The logarithm of the number of "regular holes" per square millimeter surface area of copper electrode as a function of electrolysis time gives the straight line, which points out that the decrease in number of holes with electrolysis time follows the first-order reaction low.[18] This can be very useful in the determination of the mechanism of the formation and growth of holes during metal electrodeposition in the presence of hydrogen evolution, as well as in the investigation of the different parameters that affects the honeycomb-like copper structure formation.

IV. THE EFFECT OF DEPOSITION CONDITIONS ON COPPER DEPOSITS MORPHOLOGY

1. The Surface Preparation

The initial stage of electrodeposition of copper from 0.15 M $CuSO_4$ in 0.50 M H_2SO_4 at an overpotential of 1,000 mV, onto stationary vertical copper wire electrodes previously covered by thin copper films is shown in Fig. 20. The detailed description of the formation of this type of cylindrical copper electrodes is described in Refs. [56,57] In this case, for the difference of that observed in Fig. 14b, irregularites or active centres at an electrode surface were "killed" by the electrodeposition of uniform thin copper film at an overpotential of 300 mV during 2 min.[17] Then, a higher energy was needed for the formation of hydrogen bubbles. From Fig. 20, it can be seen that a number of formed bubbles was considerably smaller than number of bubbles formed onto the electrode with active centres (Fig. 14b). Simultaneously, the diameter of the formed holes was larger, and they were random oriented at electrode surface.

Figure 21 shows copper deposits obtained at an overpotential of 1,000 mV with different quantities of the electricity, onto stationary vertical copper wire electrodes previously covered by thin copper films. The dependences of average diameters of craters or holes, D formed due to the attachment of hydrogen bubbles and number of craters or holes formed due to the attachment of hydrogen bubbles

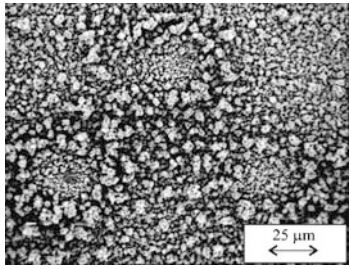

Figure 20. Copper deposit obtained at an overpotential of 1,000 mV. Time of electrolysis: 10 s. Solution: 0.15 M $CuSO_4$ in 0.50 M H_2SO_4; temperature: $18.0 \pm 1.0°C$; working electrode: copper electrode previously covered by copper thin film. (Reprinted from Ref. [18] with permission from Springer).

per square millimeter surface area ("regular holes") on electrolysis time, formed on this type of cylindrical copper electrodes are shown in Fig. 22.

Analyzing the data in Figs. 19 and 22, we can notice that average diameters of holes formed at stationary vertical copper wire electrodes which were not previously covered by copper thin films were about two times smaller than those obtained by electrodeposition onto copper electrodes previously covered with a thin copper film. On the other hand, the number of the formed holes per square millimeter surface area ("regular holes") was approximately five to ten times larger than the number of holes per square millimeter surface area obtained by electrodeposition onto copper electrodes with uniform thin copper films.

The obtained differences clearly point out the significance of preparing a working electrode for electrodeposition processes at high overpotentials, at which there is a parallelism between the process of the copper electrodeposition and the hydrogen evolution. The observed differences in average diameters of the formed holes or craters as well as in the number of the formed craters or holes can be explained as follows: the surface area of copper electrodes which were not previously covered by copper thin films consisted of a large number of irregularities, which presented active sites (centres), that is, energetic the most convenient sites for the formation

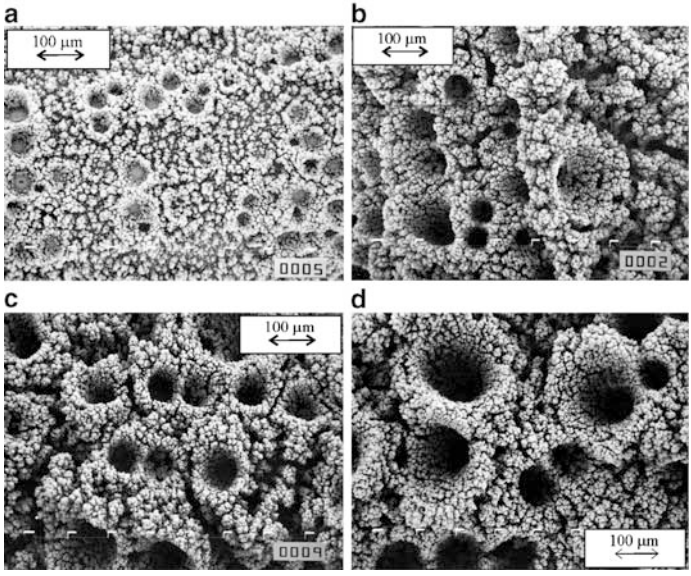

Figure 21. Copper deposits obtained potentiostatically at an overpotential of 1,000 mV. Quantities of electricity: (**a**) 2.5 mA h cm^{-2}, (**b**) 10 mA h cm^{-2}, (**c**) 15 mA h cm^{-2}, (**d**) 20 mA h cm^{-2}. Solution: 0.15 M $CuSO_4$ in 0.50 M H_2SO_4; temperature: 18.0 ± 1.0°C; working electrode: stationary vertical copper wire electrode previously covered by copper thin film. (Reprinted from Ref. [17] with permission from Elsevier).

of hydrogen bubbles. In the initial stage of electrodeposition process, the number formed hydrogen bubbles at such electrode was considerably larger than the number of bubbles formed at the electrode with "killed" active centres. Then, in the growth process, the same quantity of evolved hydrogen is distributed over larger number of hydrogen bubbles, resulting in the formation of honeycomb-like structure with larger number of holes with smaller diameters.

2. The Effect of Concentration of Cu(II) Ions

Figure 23 shows the polarization curves for the copper electrodeposition from 0.075 M $CuSO_4$ in 0.50 M H_2SO_4 (*solution (I)*), 0.30 M $CuSO_4$ in 0.50 M H_2SO_4 (*solution (II)*) and 0.60 M $CuSO_4$ in 0.50 M H_2SO_4 (*solution (III)*). All experiments whose results are presented in Figs. 23–30 and Table 1 were performed

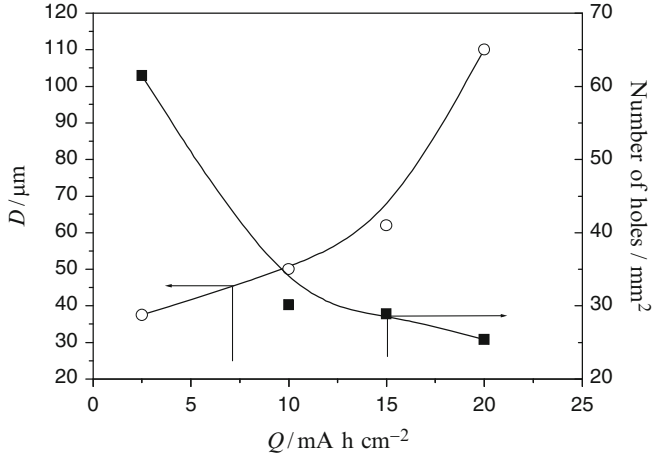

Figure 22. The dependence of average diameters of the surface holes, *D*, (*open circles*) and number of "regular holes" per square millimeter surface area of copper electrodes (*closed squares*) on the quantity of the electricity. (Reprinted from Ref. [17] with permission from Elsevier).

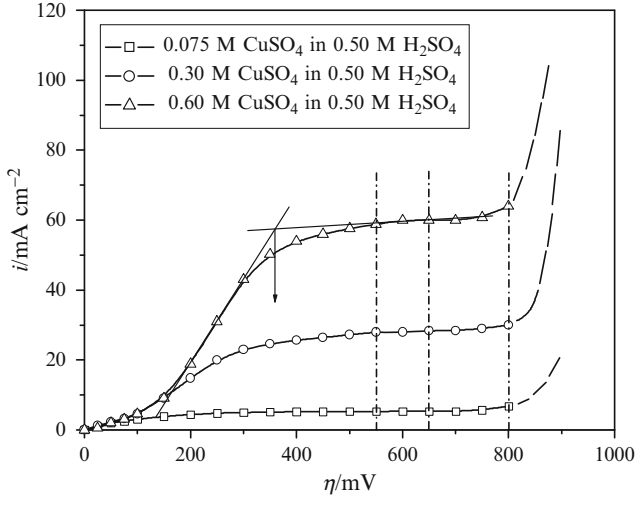

Figure 23. Polarization curves for the cathodic process of copper deposition from: 0.075 M $CuSO_4$ in 0.50 M H_2SO_4 (*solution (I)*), 0.30 M $CuSO_4$ in 0.50 M H_2SO_4 (*solution (II)*), and 0.60 M $CuSO_4$ in 0.50 M H_2SO_4 (*solution (III)*). (Reprinted from Ref. [19] with permission from MDPI).

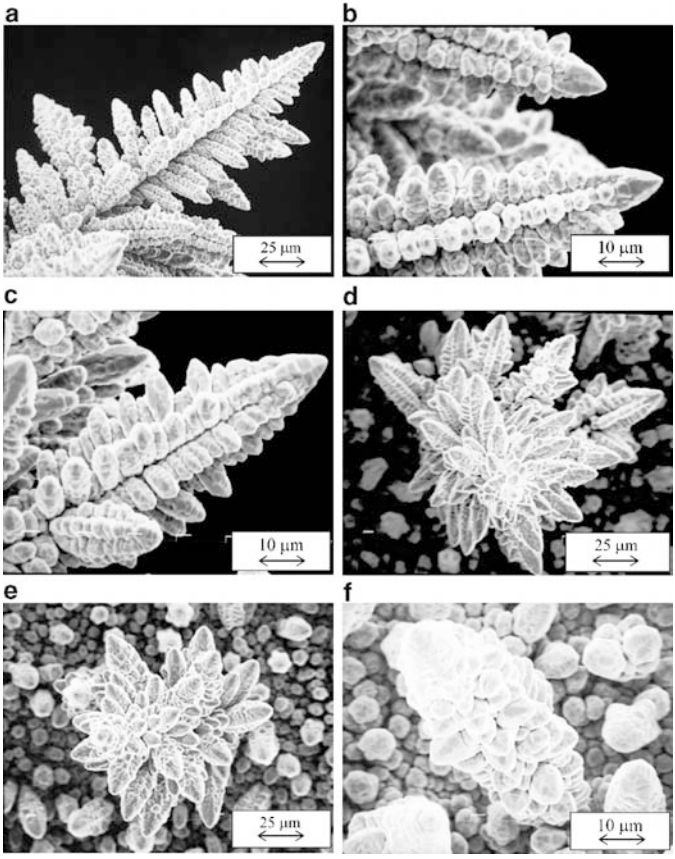

Figure 24. Copper deposits obtained at an overpotential of 650 mV. Quantity of electricity: 10 mA h cm^{-2}. (**a**, **b**): *solution (I)*; (**c**, **d**): *solution (II)*; (**e**, **f**): *solution (III)*. (Reprinted from Ref. [19] with permission from MDPI).

potentiostatically at a temperature of 18.0 ± 1.0°C. The beginning of the plateau of the limiting diffusion current density is determined as the intersect of straight lines joining currents in mixed activation – diffusion and diffusion control of electrodeposition, as shown in the Fig. 23. The end of this plateau is determined as the overpotential at which current starts to grow with the increasing overpotential. The increase in the concentration of Cu(II) ions leads

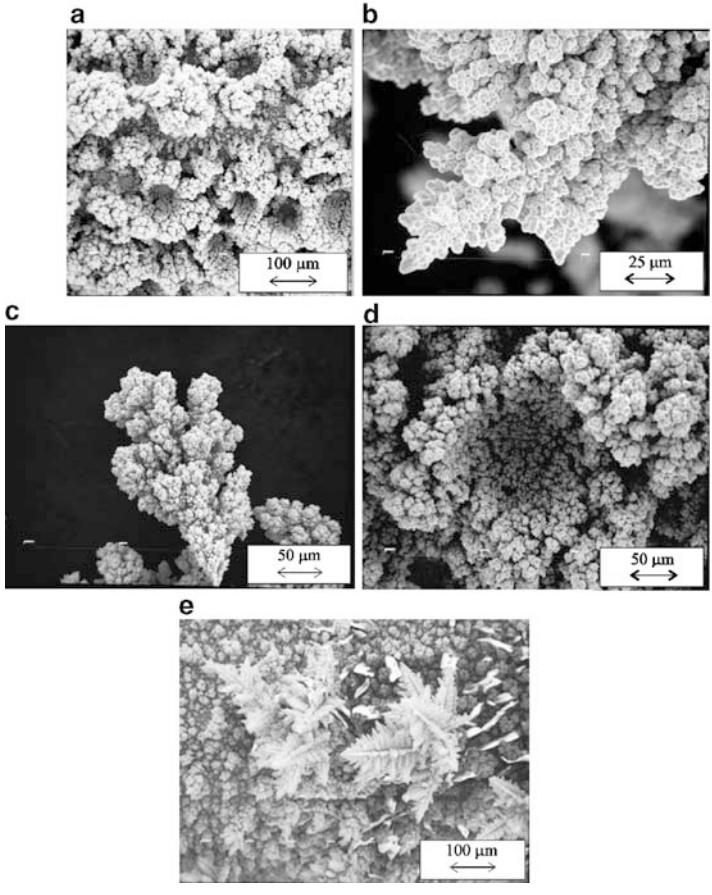

Figure 25. Copper deposits obtained at an overpotential of 800 mV. Quantity of electricity: 10 mA h cm^{-2}. (**a**) *solution (I)*; (**b**–**d**) *solution (II)*; (**e**) *solution (III)*. (Reprinted from Refs. [15, 60] with permissions from MDPI and Elsevier).

to a shift of overpotentials at which the limiting diffusion current density plateaus initiate toward the larger overpotentials, while the end of these plateaus remains practically constant (Fig. 23).

The effect of hydrogen evolution on copper electrodeposition was examined at overpotentials of 550, 650, 800, and 1,000 mV. For all examined solutions, overpotentials of 550 and 650 mV corresponded to the plateau of the limiting diffusion current density,

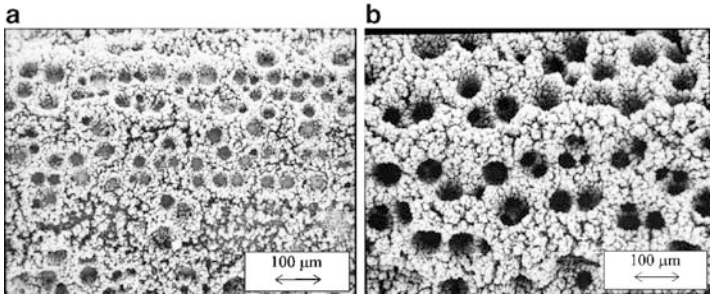

Figure 26. Copper deposits obtained at an overpotential of 1,000 mV from 0.075 M $CuSO_4$ in 0.50 M H_2SO_4. Quantity of electricity: (**a**) 2.5 mA h cm^{-2}, (**b**) 20 mA h cm^{-2}. (Reprinted from Ref. [58] with permission from Elsevier).

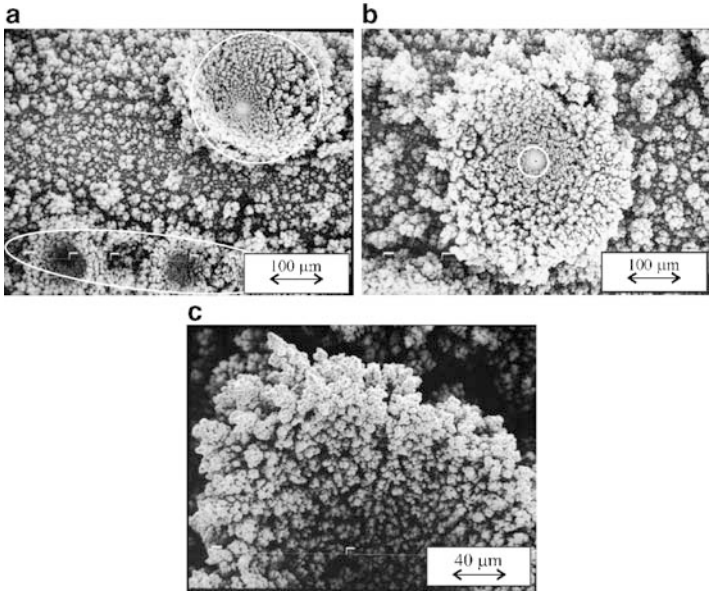

Figure 27. Copper deposits obtained at an overpotential of 1,000 mV from 0.30 M $CuSO_4$ in 0.50 M H_2SO_4. (**a**) Quantity of the electricity: 2.5 mA h cm^{-2}, (**b**, **c**) quantity of the electricity: 5.0 mA h cm^{-2}. (Reprinted from Ref. [58] with permission from Elsevier).

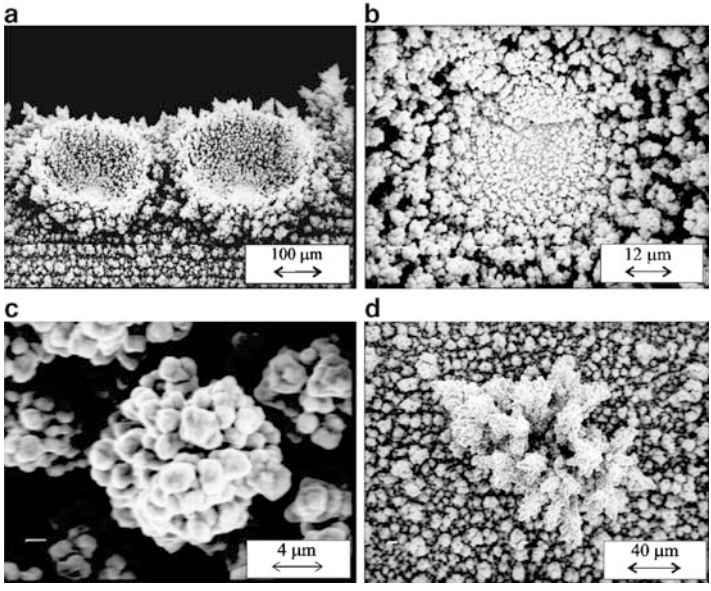

Figure 28. Copper deposits obtained at an overpotential of 1,000 mV from 0.60 M $CuSO_4$ in 0.50 M H_2SO_4: (**a**) dish-like holes, (**b**) the bottom, and (**c**) the wall of the dish-like hole, and (**d**) dendrite formed between holes. Quantity of the electricity: 2.5 mA h cm^{-2}. (Reprinted from Ref. [58] with permission from Elsevier).

while overpotentials of 800 and 1,000 mV were about 50 and 250 mV outside the plateau of the limiting diffusion current density, respectively (Fig. 23).

The summary of the obtained values of the average current efficiencies of hydrogen evolution in the dependence of concentration of Cu(II) ions and overpotential of electrodeposition[19,58] are given in Table 1.

It can be seen from Table 1 that the average current efficiencies of hydrogen evolution, $\eta_{av}(H_2)$ decreased with the increasing $CuSO_4$ concentration at all overpotentials. At the first sight, this was unexpected because the concentration of H_2SO_4 was same for all solutions. The explanation for it can be obtained by the analysis of ionic equilibrium of the species in the $CuSO_4$–H_2SO_4–H_2O system (Fig. 1). According to this equilibrium, it is the result of decreasing the hydrogen ion concentration with the increasing copper concentration.[59]

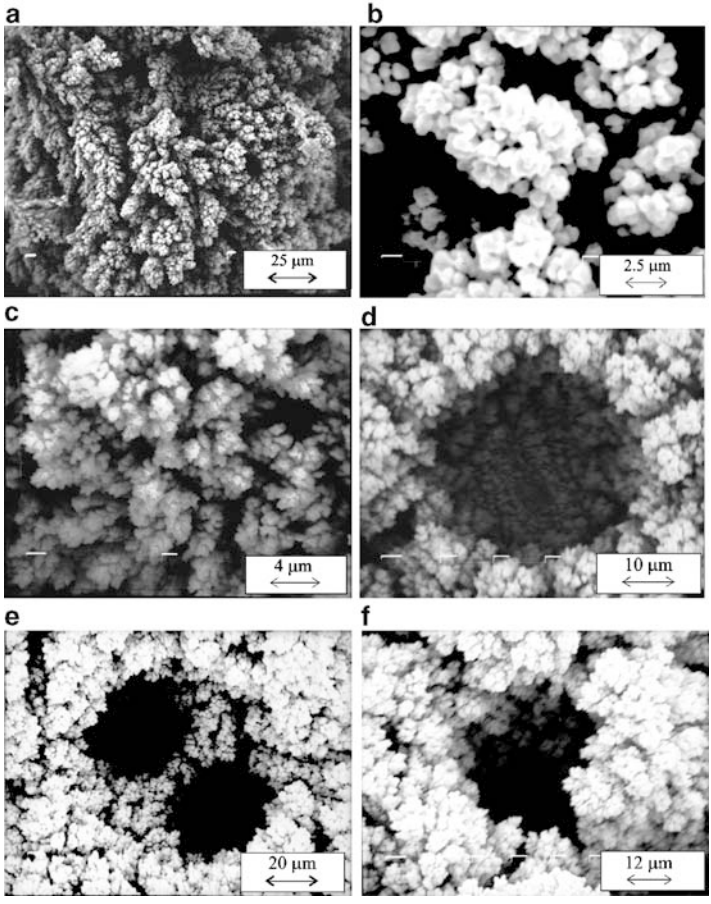

Figure 29. Copper deposits obtained at an overpotential of 1,000 mV from 0.075 M $CuSO_4$ in 0.50 M H_2SO_4: (**a, b, e, f**) quantity of the electricity: 20 mA h cm^{-2}, (**c, d**) quantity of the electricity: 5.0 mA h cm^{-2}. (Reprinted from Ref. [58] with permission from Elsevier).

(i) Morphologies of Copper Deposits Obtained at Overpotentials up to 800 mV

The copper deposit electrodeposited from 0.075 M $CuSO_4$ in 0.50 M H_2SO_4 at an overpotential of 550 mV with a quantity of the electricity of 10 mA h cm^{-2} was cauliflower-like structure. Copper

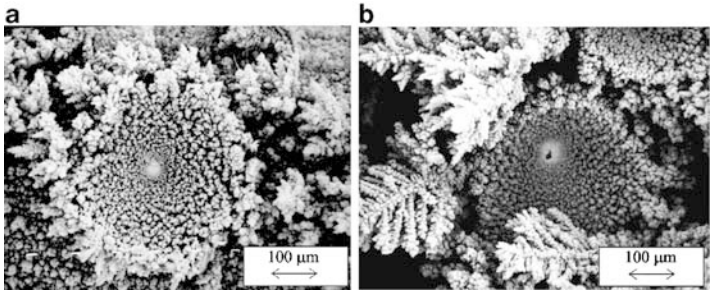

Figure 30. Copper deposits obtained at an overpotential of 1,000 mV from 0.60 M $CuSO_4$ in 0.50 M H_2SO_4: (**a**) quantity of the electricity: 5.0 mA h cm^{-2}, (**b**) quantity of the electricity: 20 mA h cm^{-2}. (Reprinted from Ref. [58] with permission from Elsevier).

Table 1.
The average current efficiencies of hydrogen evolution in the function of concentration of Cu(II) ions. (Reprinted from Refs. [19,58] with permissions from MDPI and Elsevier).

	The average current efficiencies of hydrogen evolution, $\eta_{av}(H_2)$ (in %), at overpotentials of:		
Solution for copper Electrodeposition	650 mV	800 mV	1,000 mV
0.075 M $CuSO_4$ in 0.50 M H_2SO_4	7.5	42.2	68.7
0.30 M $CuSO_4$ in 0.50 M H_2SO_4	0.83	3.5	16.0
0.60 M $CuSO_4$ in 0.50 M H_2SO_4	0	0.66	4.6

deposits electrodeposited from 0.30 M and 0.60 M $CuSO_4$ in 0.50 M H_2SO_4 at the same overpotential and with the same quantity of the electricity were globular structures.[19] Electrodepositions of copper with two times larger than the quantity of electricity led to the change of morphology of copper deposits. Copper dendrites were formed during electrodeposition of copper from *solution (I)*, while the mixture of cauliflower-like and globular forms was obtained by electrodeposition from *solution (II)* and *solution (III)*. At this overpotential, there was hydrogen evolution only from *solution (I)* (the average current efficiency of hydrogen evolution, $\eta_{av}(H_2)$, was 1.7%).[19]

Morphologies of copper deposits obtained at an overpotential of 650 mV from 0.075 M, 0.30 M, and 0.60 M $CuSO_4$ in 0.50 M H_2SO_4

are shown in Fig. 24. It can be seen from Fig. 24 that copper dendrites were formed during copper electrodeposition from all three solutions. Meanwhile, it is very clear from Fig. 24 that the shape of copper dendrites depended strongly on the concentration of Cu(II) ions. Very branchy copper dendrites consisting of corncob-like elements were formed from *solution (I)* (Fig. 24a, b). Copper dendrites formed from *solution (II)* presented a mixture of very branchy dendritic forms (Fig. 24c) and those shaped like flowers (Fig. 24d). Finally, the copper deposits obtained from *solution (III)* presented a mixture of flower-like (Fig. 24e) and corncob-like forms (Fig. 24f).

Figure 25 shows the morphologies of copper deposits obtained at an overpotential of 800 mV, from which the strong effect of concentration of Cu(II) ions on copper electrodeposition can be seen.

The honeycomb-like structure was formed from *solution (I)* (Fig. 25a).

A mixture of dendritic forms (Fig. 25b), degenerate dendrites (Fig. 25c), and holes formed due to the attached hydrogen bubbles (Fig. 25d) was obtained by electrodeposition from *solution (II)*.

Finally, only dendritic copper forms are obtained from *solution (III)* (Fig. 25e). These dendritic forms were more branchy structures than those formed from the same solution by the electrodeposition at an overpotential of 650 mV and with the same quantity of the electricity (cf. Fig. 24e, f).

The careful analysis of the morphologies of copper deposits shown in Figs. 24 and 25 indicated that an increase in the concentration of Cu(II) ions led to a shift of the formation of characteristic morphological shapes of copper deposits toward higher electrodeposition overpotentials by about 100–150 mV. This is because of the increase of a critical overpotential of dendritic growth initiation with the increase of concentration of Cu(II) ions.[19] For example, copper dendrites formed at 800 mV from *solution (III)* (Fig. 25e) were very similar to those obtained at 650 mV from *solutions (I)* and *(II)* (Fig. 24a–c). The globular forms obtained from *solutions (II)* and *(III)* at an overpotential of 550 mV were very similar to ones obtained from 0.15 M $CuSO_4$ in 0.50 M H_2SO_4 at an overpotential of 450 mV.[10] The different shapes of copper dendrites formed at an overpotential of 650 mV from solutions with different concentrations of Cu(II) ions (Fig. 24) also pointed out the strong effect of concentration of Cu(II) ions on electrodeposition of copper at an overpotential of 650 mV.

(ii) Morphologies of Copper Deposits Obtained at an Overpotential of 1,000 mV

The copper deposits obtained from 0.075 M $CuSO_4$ in 0.50 M H_2SO_4 at an overpotential of 1,000 mV with the quantities of electricity of 2.5 and 20 mA h cm^{-2} are shown in Fig. 26, from which it can be seen that honeycomb-like structures were formed by electrodepositions from this solution.

The copper deposits obtained at an overpotential of 1,000 mV from 0.30 M $CuSO_4$ in 0.50 M H_2SO_4 with quantities of electricity of 2.5 and 5.0 mA h cm^{-2} are shown in Fig. 27, from which it can be clearly seen that the structures of the deposits obtained from 0.30 M $CuSO_4$ in 0.50 M H_2SO_4 were completely different from those obtained from 0.075 M $CuSO_4$ in 0.50 M H_2SO_4 (Fig. 26).

Two types of craters or holes formed due to the attachment of hydrogen bubbles can be observed by analysis of the copper deposit shown in Fig. 27a. One type of holes is presented in the ellipse in Fig. 27a. These holes are similar to those forming the honeycomb-like structure during copper electrodeposition from 0.075 M $CuSO_4$ in 0.50 M H_2SO_4. These holes are grouped and mutually separated by agglomerates of relatively small copper grains.

The other type of holes is shown in the circle in the same figure. From Fig. 27a, it can be seen that the shape of this hole is dish or shell-like. The diameter of dish-like holes is larger than the diameter of the holes forming the honeycomb-like structure, while their number is smaller than the number of holes forming the honeycomb-like structure. A typical dish-like hole electrodeposited with the quantity of the electricity of 5.0 mA h cm^{-2} is shown in Fig. 27b. The bottom of the dish-like hole is covered by almost compact copper deposit (the part in the circle in Fig. 27b), while the wall of this hole consists of small, very disperse agglomerates of copper grains (Fig. 27c). From Fig. 27c, it can also be seen that copper dendrites were formed at the shoulders of the dish-like holes electrodeposited with this quantity of electricity. Also, cauliflower-like forms were formed between the holes or craters belonging to these different types (Fig. 27a).

The electrodeposition processes at an overpotential of 1,000 mV from 0.60 M $CuSO_4$ in 0.50 M H_2SO_4 led to the formation of dish-like holes only. The typical dish-like holes formed with the quantity of the electricity of 2.5 mA h cm^{-2} are shown in Fig. 28a, from which it can be seen that copper dendrites were formed at their

shoulders. The bottom of the dish-like holes was almost compact (Fig. 28b), while the interior of the hole was constructed of disperse agglomerates of copper grains (Fig. 28c). Very branched copper dendrites and small cauliflower-like forms were formed among the dish-like holes during the electrodeposition of copper from this solution (Fig. 28d).

On the basis of the presented analysis of the electrodeposition processes at an overpotential of 1,000 mV (Figs. 26–28), it is obvious that increasing the concentration of Cu(II) ions leads to a change in the shape of the holes from those forming a honeycomb-like structure to dish-like holes.

It should be noted that the honeycomb-like structure was formed from 0.075 M $CuSO_4$ in 0.50 M H_2SO_4 at an overpotential of 1,000 mV, with a considerably larger quantity of co-deposited hydrogen ($\eta_{av}(H_2) = 68.7\%$) than that formed by electrodeposition at 800 mV from the same solution ($\eta_{av}(H_2) = 42.2\%$),[19]) or from 0.15 M $CuSO_4$ in 0.50 M H_2SO_4 at 800 mV ($\eta_{av}(H_2) = 10.8\%$) and 1,000 mV ($\eta_{av}(H_2) = 30.0\%$).[10] It was found[19,58] that the maximum $CuSO_4$ concentration (in 0.50 M H_2SO_4) which enabled the formation of the honeycomb-like structure was 0.15 M. The critical quantity of evolved hydrogen leading to the change of the hydrodynamic conditions in the near-electrode layer for this solution group was estimated to correspond to $\eta_{av}(H_2)$ of 10.0%.[19]

The more vigorous hydrogen evolution at this overpotential from 0.075 M $CuSO_4$ in 0.50 M H_2SO_4 makes a more visible channel structure formed through the interior of the deposit. A typical channel structure is shown in Fig. 29a, which was obtained by manipulation of the copper deposit in order that the cross section view could be seen. The top view of a part of the copper deposit shown in Fig. 29a is shown in Fig. 29b, from which it can be seen that irregular channels are distributed over the surface area of the deposit among disperse agglomerates of copper grains. These channels were generated in situ by the simultaneous processes of copper growth and vigorous hydrogen evolution. It is also known[61] that a channel or a stream copper structure can be formed ex situ by the use of an acoustically excited Ar gas bubble.

Naturally, both the formation holes and channels through the interior of the deposit occur simultaneously, and these processes can not be observed separately. As already stated, in the initial stage of the electrodeposition process, both nuclei of copper and "nuclei"

of hydrogen bubbles are formed at the active sites of the electrode surface.[18] The hydrogen bubbles isolate the substrate and then the current lines are concentrated around these hydrogen bubbles making rings consisted of agglomerates of copper grains around them. The current lines are also concentrated at the nuclei of copper formed in the initial stage between the hydrogen bubbles. Anyway, the bubbles cause an increase of the local current density around them, resulting in a faster growth of the copper deposit around the growing bubbles, as well as in increasing rate of hydrogen evolution.

As a result of the current distribution at the growing copper surface, new copper nucleation and hydrogen evolution will occur primarily at the top of these agglomerates. Some of the new, small, freshly formed hydrogen bubbles which are formed at agglomerates around previously formed large hydrogen bubbles will coalesce with them, leading to their growth with electrolysis time as already shown.[18] This is confirmed by the very porous structure of the interior of walls of the holes (Fig. 29c), which consist of disperse agglomerates of copper grains among which numerous irregular channels are present. A typical hole formed of growing hydrogen bubbles is shown in Fig. 29d. In the growth process, the coalescence of closely formed large hydrogen bubbles can also be observed (Fig. 29e).

Meanwhile, some of the freshly formed hydrogen bubbles will not find a way to coalesce with the large hydrogen bubbles because they are situated among copper nuclei which initiate a barrier for their development into large hydrogen bubbles. This effect, with already discussed current density distribution will lead to the formation of a porous channel structure through the interior of the copper deposit (Fig. 29a).

Simultaneously, holes of irregular shapes (Fig. 29f) were formed from nuclei of copper formed in the initial stage of the electrodeposition between the hydrogen bubbles.[18] The current distribution at the growing copper surface was responsible for the formation of this type of hole.

Anyway, there are two effects of hydrogen evolution on copper electrodeposition leading to the formation of the honeycomb-like structures. The first effect is a stirring of the solution in the near-electrode layer caused by a vigorous hydrogen evolution leading to the decrease of the diffusion layer thickness and the increase of the limiting diffusion current density.[10] The second effect concerns

the morphology of the copper deposits due to the effect of hydrogen bubbles on the current density distribution on the growing electrode surface. The uniform distribution of morphological forms on the electrode surface means the same hydrodynamic conditions exist over the whole electrode surface and the honeycomb-like structure indicates to the local effect of hydrogen bubbles.

Dish-like holes were formed from the more concentrated solution (0.60 M $CuSO_4$ in 0.50 M H_2SO_4), accompanied by a considerably lower quantity of evolved hydrogen ($\eta_{av}(H_2) = 4.6\%$) than was the case with the holes forming a honeycomb-like structure (0.075 M and 0.15 M $CuSO_4$ in 0.50 M H_2SO_4).

On the basis of the obtained value of the average current efficiency of hydrogen evolution of 4.6% and morphologies of copper deposits shown in Fig. 28 (very branchy copper dendrites developed between dish-like craters or holes), it is clear that the hydrogen evolution was insufficient to produce effective stirring of the solution in the near-electrode layer, which would lead to a decrease of the diffusion layer thickness, and consequently, no change in the hydrodynamic conditions and no inhibition of dendritic growth. The electrodeposition process was primarily controlled by the diffusion of ions to the electrode surface, rather than the kinetics of the electrodeposition.[13,23]

The initial stage of the formation of dish-like holes was the same as the initial stage of the formation of the honeycomb-like structure. The nuclei of copper and the "nuclei" of hydrogen bubbles were formed at active sites on the electrode surface and the formed hydrogen bubbles isolate the substrate causing a concentration of the current lines around them. Meanwhile, because of the low hydrogen co-deposition current density, the number of the formed "nuclei" of hydrogen bubbles was smaller than the number which led to the formation of the honeycomb-like structure. In the growth process, they have enough space to develop into large bubbles, making holes with a dish-like shape at the surface area of electrode. Dendrites formed at their shoulders (Fig. 28a) as well as very developed dendrites between them (Fig. 28d) clearly indicate the insufficiency of the evolved hydrogen to disturb the diffusion layer of the macroelectrode. Further copper nucleation and hydrogen evolution primarily occur at the shoulders of the growing holes and the copper dendrites between them. Most of the freshly formed hydrogen bubbles at the shoulder of the dish-like holes coalesce with

previously formed large hydrogen bubbles, leading to their growth with the electrolysis time (Fig. 30a) and making the interior of holes very porous and constructed of cauliflower- or raspberry-like forms. At the same time, the almost compact deposit at the bottom of the dish-like holes represents the position of the formation of the initial bubble (Fig. 28b), and it can be supposed that its origin is the thin copper film previously electrodeposited at 400 mV. It is of interest to note that regardless of the quantity of electricity passed, or the deposition time, the dendrites grew only at the edges of the dish-like holes. This is due to the fact that the electrodeposition of copper occurs on the dendrite branches in the same way as on any other part of the electrode surface, except on the tip of the dendrite protrusions themselves, where the process is under activation control, resulting in regular dendritic forms (Fig. 30b).[62–64] At larger deposition times, the growth of dendrites become dominant and the dish-like protrusion cease to grow. Also, it can be seen from Figs. 28a and 30a that in the "shadow" of the dish-like holes there is a lower density of grains on the initial substrate relative to the overshadowed parts of electrode, which is the consequence of the concentration of current lines at them.

In dependence on the quantity of electricity, the average diameter of the dish-like holes was in the range of 200–360 μm. The number of dish-like holes was estimated to be 2.5 holes/mm^2 surface area of the copper electrode, and it did not change with the quantity of the electricity, which can be explained by the absence of coalescence of the formed hydrogen bubbles. The comparative dependences of the average diameters, D, and the number of holes per square millimeter surface area of copper electrodes on the quantity of the electricity for both, dish-like holes and holes making the honeycomb-like structure during the electrodeposition at 1,000 mV from 0.075 M $CuSO_4$ in 0.50 M H_2SO_4 are shown in Fig. 31, from which it can be seen that the number of formed dish-like holes per square millimeter surface area of the copper electrode was considerably smaller than the number of holes forming the honeycomb-like structure and that the average diameter of the dish-like holes was about five times larger than the average diameter of the holes forming the honeycomb-like structure. This illustrates successfully the fact that a smaller number of "nuclei" of hydrogen bubbles is formed in the initial stage of electrodeposition of dish-like holes in relation to the number of formed "nuclei" of hydrogen bubbles leading to the formation of the honeycomb-like structure.

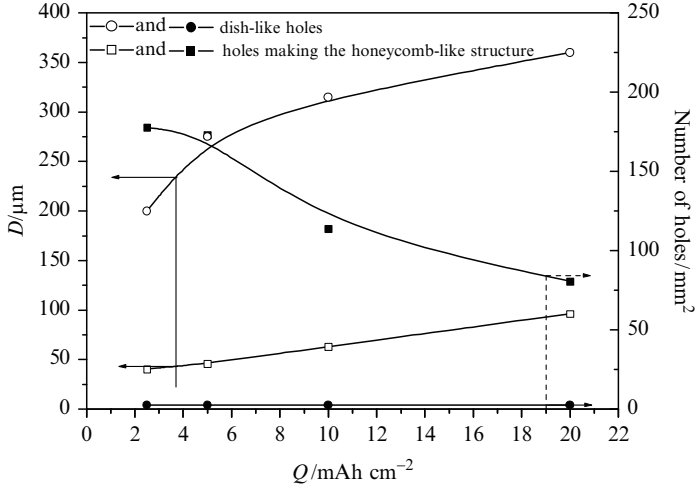

Figure 31. The dependence of average diameters of the surface holes, *D*, (*open style*) and number of holes per square millimeter surface area of copper electrodes (*solid style*) on quantities of electricity, for electrodepositions of copper from 0.075 M $CuSO_4$ in 0.50 M H_2SO_4 and 0.60 M $CuSO_4$ in 0.50 M H_2SO_4. (Reprinted from Ref. [58] with permission from Elsevier).

Furthermore, the morphology of the copper deposit obtained from 0.60 M $CuSO_4$ in 0.50 M H_2SO_4 at an overpotential of 1,000 mV consisted of all the morphological forms characteristic for copper electrodeposition at high overpotentials: holes formed due to hydrogen evolution (Fig. 28a), dendritic forms (Fig. 28d), and small cauliflower-like forms (Fig. 28d). The formation of these different morphological forms which leads to nonuniformity of the electrode surface can be explained by different local electrodeposition conditions inside the diffusion layer of the macroelectrode. It is known[65] that electrochemical processes on microelectrodes in bulk solution can be under activation control at overpotentials which correspond to the plateau of the limiting diffusion current density of the macroelectrode. Bockris et al.[63,64] and Popov et al.[62] showed that electrodeposition to the tip of a dendrite, consequently to a microelectrode, inside the diffusion layer of the macroelectrode is under activation control, while the same process is simultaneously under full diffusion control on the macroelectrode. In the absence of dendrite precursors, some cauliflower-like forms can be formed

on the surface of the macroelectrode when the electrodeposition process is under full linear diffusion control. Then, local spherical diffusion layers inside the diffusion layer of the macroelectrode are formed around them.[10] Hence, for defined electrodeposition conditions, control of the electrodeposition process at some specified points of the macroelectrode can be different from the process control at the macroelectrode in general. This explains and the nonuniformity of the electrode surface obtained from 0.60 M $CuSO_4$ in 0.50 M H_2SO_4.

The polarization characteristic of a macroelectrode is easy to determine, as well as the kind of mass transfer control on it. It is very difficult, or even impossible, to do the same for some specified points on it. On the other hand,[13,66] the morphology of metal deposits indicates the conditions under which they were formed. Hence, from the local morphology of a deposit, the type of process control on selected points of the macroelectrode can be derived.

The morphology of the copper deposit obtained at an overpotential of 1,000 mV from 0.30 M $CuSO_4$ in 0.50 M H_2SO_4 presented a mixture of morphological forms characteristic for copper deposits obtained from solutions with lower (0.075 M) and higher (0.60 M) concentrations of Cu(II) ions. Thus, a mixture of both types of holes was obtained by the electrodeposition at this overpotential from 0.30 M $CuSO_4$ in 0.50 M H_2SO_4. It was estimated that the percent of holes forming the honeycomb-like structure was about 80% of the total number of formed holes. On the basis of this fact, it can be concluded that for a concentration of supporting electrolyte of 0.50 M H_2SO_4, the concentration of 0.30 M $CuSO_4$ presents the transitional concentration between lower and higher concentrations of Cu(II) ions. This could be explained by different hydrodynamic conditions at different points of the electrode surface.

3. The Effect of Concentration of H_2SO_4

The polarization curves for the electrodeposition of copper from 0.15 M $CuSO_4$ with the addition of 0.125, 0.25, and 1.0 M H_2SO_4 are shown in Fig. 32. All experiments whose results are presented in Figs. 32–37 and Table 2 were performed potentiostatically at a temperature of 18.0 $\pm$ 1.0°C. It can be seen from Fig. 32 that the beginning of the plateau of the limiting diffusion current density was slightly shifted to higher electrodeposition overpotentials with the decreasing concentration of H_2SO_4. The ends of the plateau of

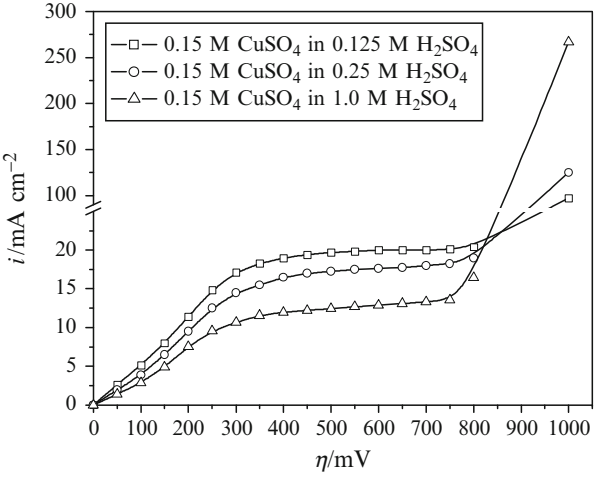

Figure 32. Polarization curves for the cathodic process of copper deposition from: 0.15 M $CuSO_4$ in 0.125 M H_2SO_4, 0.15 M $CuSO_4$ in 0.25 M H_2SO_4, and 0.15 M $CuSO_4$ in 1.0 M H_2SO_4. (Reprinted from Ref. [67] with permission from Elsevier).

the limiting diffusion current density practically do not depend on the concentration of H_2SO_4 and they correspond to an overpotential of about 750 mV. The negligible shifting of the end of the plateau of the limiting diffusion current density to lower electrodeposition overpotentials can be only observed at a polarization curve obtained from 0.15 M $CuSO_4$ in 1.0 M H_2SO_4. At overpotentials higher than 750 mV, the fastest growth of current with increasing overpotential is obtained from 0.15 M $CuSO_4$ in 1.0 M H_2SO_4 and it decreases with the decrease of the H_2SO_4 concentration. The limiting diffusion current density value decreased with the increasing concentration of H_2SO_4. The decrease in the values of the limiting diffusion current density with increasing H_2SO_4 concentration is a consequence of the decrease of the Cu(II) ion activity with increasing acidity of the solution.

The effect of hydrogen evolution on copper electrodeposition was examined at overpotentials of 550, 650, 800, and 1,000 mV. At an overpotential of 550 mV, there was hydrogen evolution only from 0.15 M $CuSO_4$ in 1.0 M H_2SO_4 (the average current efficiency of hydrogen evolution, $\eta_{av}(H_2)$, was 0.75%).[67] The summary of

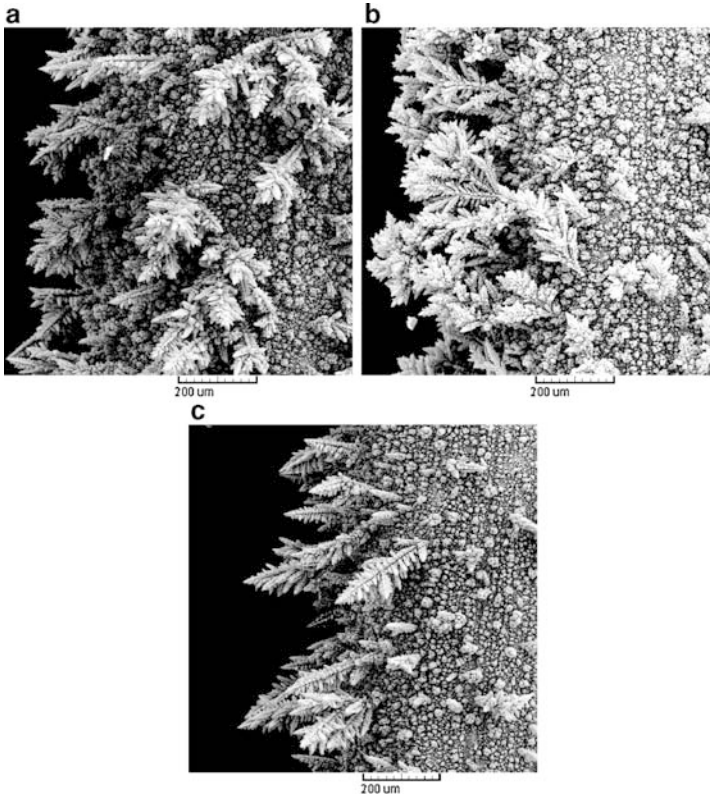

Figure 33. Copper deposits obtained at an overpotential of 650 mV from: (**a**) 0.15 M $CuSO_4$ in 0.125 M H_2SO_4, (**b**) 0.15 M $CuSO_4$ in 0.25 M H_2SO_4, and (**c**) 0.15 M $CuSO_4$ in 1.0 M H_2SO_4. Quantity of electricity: 10 mA h cm^{-2}. (Reprinted from Ref. [67] with permission from Elsevier).

the obtained values of the average current efficiencies of hydrogen evolution in the dependence of concentration of H_2SO_4 at overpotentials of 650, 800, and 1,000 mV[60,67] are given in Table 2. For all examined solutions, overpotentials of 550 and 650 mV corresponded to the plateau of the limiting diffusion current density, while overpotentials of 800 and 1,000 mV were about 50 and 250 mV outside the plateau of the limiting diffusion current density, respectively (Fig. 32).

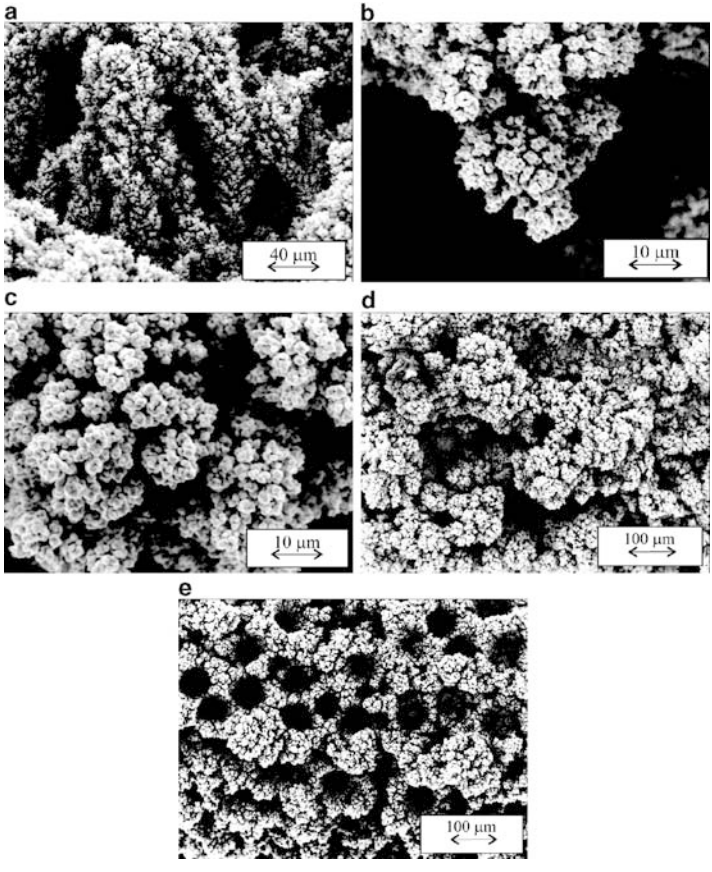

Figure 34. Copper deposits obtained at an overpotential of 800 mV from: (**a–c**) 0.15 M $CuSO_4$ in 0.125 M H_2SO_4; (**d**) 0.15 M $CuSO_4$ in 0.25 M H_2SO_4, and (**e**) 0.15 M $CuSO_4$ in 1.0 M H_2SO_4. Quantity of electricity: 10 mA h cm^{-2}. (Reprinted from Ref. [60] with permission from Elsevier).

(i) Morphologies of Copper Deposits Obtained at Overpotentials up to 800 mV

Electrodeposition of copper at an overpotential of 550 mV from 0.15 M $CuSO_4$ in 0.125 M H_2SO_4, as well as from 0.15 M $CuSO_4$ in 0.25 M H_2SO_4 led to the formation of dendritic forms with the quantity of the electricity of 10 mA h cm^{-2}.[67] The number of copper

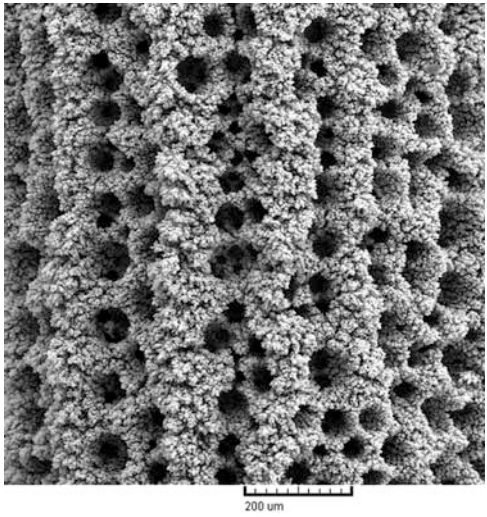

Figure 35. The copper deposit obtained at an overpotential of 1,000 mV from 0.15 M $CuSO_4$ in 1.0 M H_2SO_4. Quantity of electricity: 10 mA h cm^{-2}. (Reprinted from Ref. [67] with permission from Elsevier).

dendrites formed at a surface area of copper electrodes increased with the decrease of the H_2SO_4 concentration. Cauliflower-like forms were obtained by electrodeposition at the same overpotential from 0.15 M $CuSO_4$ in 1.0 M H_2SO_4 with the quantity of the electricity of 10 mA h cm^{-2}. Some of them were developed in dendritic forms by the electrodeposition with the double quantity of electricity.

Copper dendrites were formed by electrodeposition processes at an overpotential of 650 mV from all three solutions (Fig. 33). It can be seen from Fig. 33 that the number of formed dendritic forms increased with the decrease of H_2SO_4 concentration. Also, the branching of these forms increased with the decrease of the concentration of H_2SO_4. The corncob-like forms were grouped in flower-like or tree-like forms, or even formed individually at an electrode surface (Fig. 33).

The analysis of copper electrodeposition processes at overpotentials of 550 and 650 mV has shown that the decrease of H_2SO_4 concentration led to the shift of the formation of dendritic forms

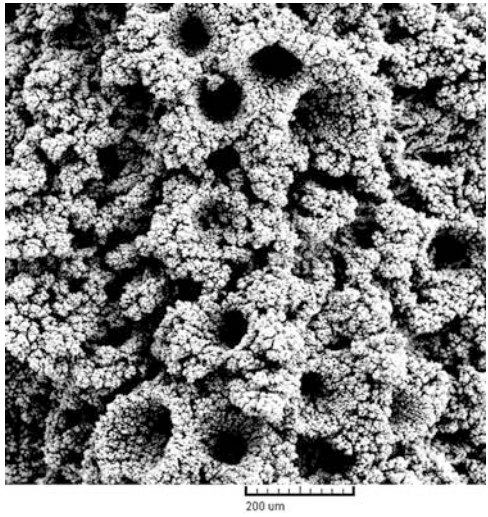

Figure 36. The copper deposit obtained at an overpotential of 1,000 mV from 0.15 M $CuSO_4$ in 0.25 M H_2SO_4. Quantity of electricity: 10 mA h cm^{-2}. (Reprinted from Ref. [67] with permission from Elsevier).

toward higher overpotentials of electrodeposition. This effect was the same as the one which had been noticed in case of the increasing concentration of Cu(II) ions,[19] as it was discussed considering minimum overpotential for dendritic growth initiation.

The morphologies of the copper deposits obtained at an overpotential of 800 mV are presented in Fig. 34. A channel structure (Fig. 34a), degenerate dendrites (Fig. 34b), and cauliflower-like forms (Fig. 34c) were formed by copper electrodeposition from 0.15 M $CuSO_4$ in 0.125 M H_2SO_4. Holes originating from attached hydrogen bubbles were formed by electrodeposition from 0.15 M $CuSO_4$ in 0.25 M H_2SO_4 (Fig. 34d). Degenerate dendrites and cauliflower-like forms, similar to those shown in Fig. 34b, c, were also formed by electrodeposition from this solution. Finally, the honeycomb-like structure, constructed from holes formed due to attached hydrogen bubbles and cauliflower-like agglomerates of copper grains between them, was formed by the electrodeposition from 0.15 M $CuSO_4$ in 1.0 M H_2SO_4 (Fig. 34e).

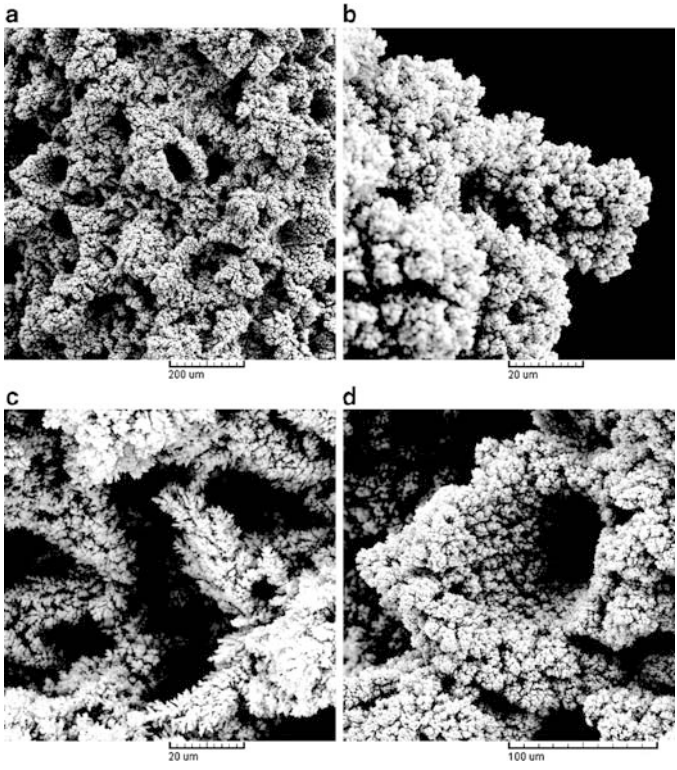

Figure 37. (**a**) The copper deposit obtained at an overpotential of 1,000 mV from 0.15 M $CuSO_4$ in 0.125 M H_2SO_4. Quantity of electricity: 10 mA h cm^{-2}, (**b–d**) details from Fig. 37a: (**b**) degenerate dendrite, (**c**) irregular channels, and (**d**) the shoulder of the hole. (Reprinted from Ref. [67] with permission from Elsevier).

Table 2.
The average current efficiencies of hydrogen evolution in the function of H_2SO_4 concentration. (Reprinted from Refs. [60,67] with permissions from Elsevier).

	The average current efficiencies of hydrogen evolution, $\eta_{av}(H_2)$ (in %), at overpotentials of:		
Solution for copper Electrodeposition	650 mV	800 mV	1,000 mV
0.15 M $CuSO_4$ in 0.125 M H_2SO_4	0	4.83	20.3
0.15 M $CuSO_4$ in 0.25 M H_2SO_4	0.32	9.05	26.4
0.15 M $CuSO_4$ in 1.0 M H_2SO_4	3.3	23.3	45.7

(ii) Morphologies of Copper Deposits Obtained at an Overpotential of 1,000 mV

Morphologies of copper deposits obtained at an overpotential of 1,000 mV from these copper solutions are shown in Figs. 35–37. The honeycomb-like structure was formed by the electrodeposition from 0.15 M $CuSO_4$ in 1.0 M H_2SO_4(Fig. 35). From Fig. 35 it can be seen that holes were lined up in parallel rows. The average diameter of formed holes was 50 μm, while the number of formed holes was 71/mm^2 surface area of the copper electrode.

The honeycomb-like structure was also formed by electrodeposition at 1,000 mV from 0.15 M $CuSO_4$ in 0.25 M H_2SO_4 (Fig. 36). However, in contrast to parallely lined up holes formed from 0.15 M $CuSO_4$ in 1.0 M H_2SO_4, holes which made this honeycomb-like structure were random oriented at the electrode surface. The number of the formed holes was 14/mm^2 surface area of the copper electrode and it was about five times smaller than the number of holes formed from 0.15 M $CuSO_4$ in 1.0 M H_2SO_4. The decrease of concentration of H_2SO_4 led to the increase of the diameter of holes, and the average diameter of holes formed from this solution was estimated to be about 110 μm.

The random-oriented holes were also formed during copper electrodeposition at 1,000 mV from 0.15 M $CuSO_4$ in 0.125 M H_2SO_4 (Fig. 37a). However, the detailed analysis of the copper deposit shown in Fig. 37a revealed the presence of morphological forms which were not obtained by electrodeposition processes from 0.15 M $CuSO_4$ in both 0.25 M and 1.0 M H_2SO_4. Aside from holes and cauliflower-like agglomerates of copper grains between them, the presence of degenerate dendrites (Fig. 37b) and irregular channels formed by evolved hydrogen around dendritic and cauliflower-like particles (Fig. 37c) were also noticed by the analysis of the copper deposit electrodeposited from 0.15 M $CuSO_4$ in 0.125 M H_2SO_4. Additionally, degenerate dendrites were formed at the shoulders of some of holes (Fig. 37d). The average diameter of the formed holes was 120 μm, while their number was estimated to be 7/mm^2 surface area of the copper electrode.

4. The Effect of Temperature on Electrodeposition of Disperse Copper Deposits

The polarization curves for the electrodeposition of copper from 0.15 M $CuSO_4$ in 0.50 M H_2SO_4 at temperatures of 14.0 ± 0.5, 35.0 ± 0.5 and 50.0 ± 0.5°C are given in Fig. 38. It can be seen from Fig. 38 that increasing the temperature leads to an increase of the limiting diffusion current density, as well as to a shift of both the beginning and the end of the plateau of the limiting diffusion current density toward lower electrodeposition overpotentials.

It is clear from Fig. 38 that an overpotential of 550 mV belongs to the plateau of the limiting diffusion current density at all analyzed temperatures. An overpotential of 650 mV belongs to the plateau of the limiting diffusion current density only at a temperature of 14.0 ± 0.5°C. This overpotential is about 50 mV outside the plateau at a temperature of 35.0 ± 0.5°C and about 100 mV outside at a

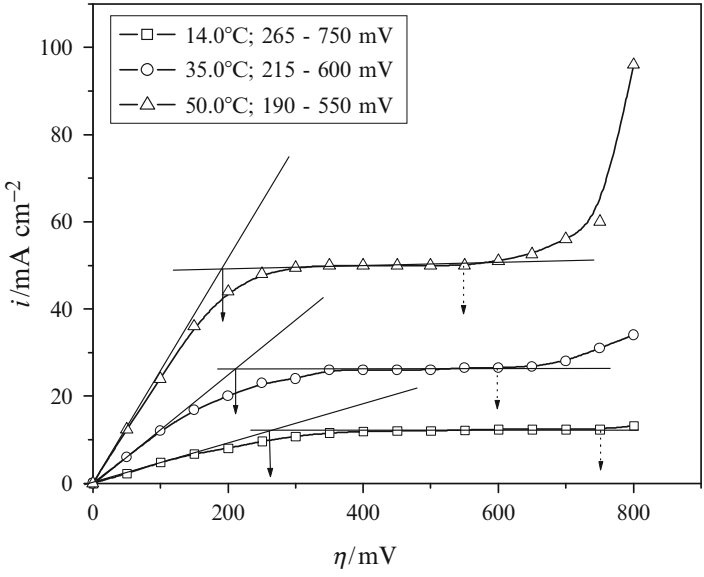

Figure 38. Polarization curves for curves for electrodeposition of copper from 0.15 M $CuSO_4$ in 0.50 M H_2SO_4 at temperatures of 14.0±0.5°C, 35.0±0.5°C, and 50.0 ± 0.5°C. (Reprinted from Ref. [68] with permission from the Serbian Chemical Society).

Table 3.
The values of the average current efficiencies of hydrogen evolution, $\eta_{av}(H_2)$ (in %) in the dependence on temperature of electrodeposition. (Reprinted from Ref. [68] with permission from the Serbian Chemical Society).

	The average current efficiencies of hydrogen evolution, $\eta_{av}(H_2)$ (in %), at overpotentials of:		
Temperature (°C)	550 mV	650 mV	800 mV
14.0 ± 0.5	0	1.6	11.1
35.0 ± 0.5	0	2.2	14.2
50.0 ± 0.5	0	3.7	18.6

temperature of 50.0 ± 0.5°C. Finally, an overpotential of 800 mV is outside the plateau of the limiting diffusion current density at all temperatures.

The average current efficiences for hydrogen evolution reaction, $\eta_{av}(H_2)$, at overpotentials of 650 and 800 mV are summarized in Table 3,[68] which also includes the values of the average current efficiences of hydrogen evolution of 0.0% obtained at an overpotential of 550 mV. It can be clearly seen from Table 3 that the electrodeposition processes at overpotentials of 650 and 800 mV are accompanied by the increase of the average current efficiencies of hydrogen evolution with increasing temperature, causing a shift of the end of the limiting diffusion current density plateau toward lower values of the overpotential. This is due to the increased rate of hydrogen evolution with increasing temperature. In totality, the three groups of the average current efficiences of hydrogen evolution are of significance in the investigation of the effect of temperture on the electrodeposition of copper at high overpotentials.

The first group is characterized by electrodeposition of copper at an overpotential of 550 mV, (potential at which there is no hydrogen evolution or hydrogen evolution was below the sensitivity of the measurement technique).

The second group is characterized by processes of electrodeposition at an overpotential of 650 mV (potential at which the average

current efficiencies of hydrogen evolution were below the critical value of the average current efficiency of hydrogen evolution of 10.0%, leading to a change of the hydrodynamic conditions in the near-electrode layer in this solution).

Finally, the third group includes electrodeposition processes at 800 mV, which are accompanied by an average current efficiency of hydrogen evolution above the critical value of 10.0%.

The morphologies of the copper deposits electrodeposited at an overpotential of 550 mV are cauliflower-like and dendritic ones.[68] The size of the cauliflower-like particles did not change with increasing temperature, but the size of sub-particles constituting the cauliflower-like forms which decreased with increasing temperature of electrodeposition. The decrease of the size of sub-particles with increasing temperature can be explained by the well-known dependence of the nucleation rate on temperature,[69] which was derived by Volmer and Weber.[70]

The morphologies of the copper deposits obtained at an overpotential of 650 mV are shown in Fig. 39, from which the strong effect of temperature on the electrodeposition of copper at an overpotential of 650 mV can immediately be clearly seen. Very branched copper dendrites were formed during electrodeposition at a temperature of 14.0°C (Fig. 39a). They were constructed of corncob-like elements (Fig. 39b). This is in accordance with the position of an overpotential of 650 mV in the limiting diffusion current density plateau. Dendritic forms were obtained during electrodeposition at a temperature of 35.0°C (Fig. 39c) but holes, the origin of which was attached hydrogen bubbles, were also formed (the part in the circle in Fig. 39d). The increased hydrogen evolution at a temperature of 50.0°C compared to that at 35.0°C led to a change of the shape of the copper dendrites, which become similar to cauliflower-like forms (Fig. 39e) or, probably, degenerate dendrites were formed. Also, the holes formed due to the attachment of hydrogen bubbles can be observed in this copper deposit (Fig. 39f). These facts were unexpected because the current efficiency of the hydrogen evolution reaction was lower than 10.0%, but it can be explained by the findings of Vogt and Balzer.[71] They showed that the bubble coverage of an electrode surface increased with temperature more than linearly. Besides, Krenz[72] observed an increase in bubble coverage of about 50% as the temperature was raised from 25 to 50°C.

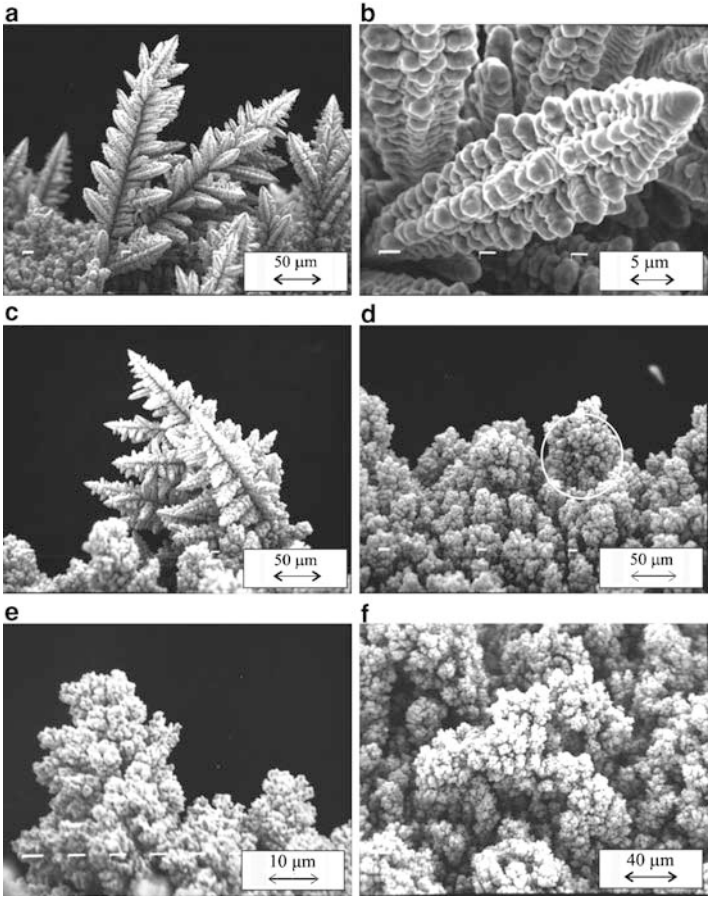

Figure 39. Morphologies of copper deposits electrodeposited at an overpotential of 650 mV at temperatures of: (**a, b**) 14.0 ± 0.5°C, (**c, d**) 35.0 ± 0.5°C, and (**e, f**) 50.0 ± 0.5°C. (Reprinted from Ref. [68] with permission from the Serbian Chemical Society).

The morphologies of the copper deposits electrodeposited at an overpotential of 800 mV are shown in Fig. 40, from which the strong effect of evolved hydrogen on the morphologies of copper deposits is visible. Very porous structures, holes formed due to the attachment of hydrogen bubbles, cauliflower-like forms, and the absence

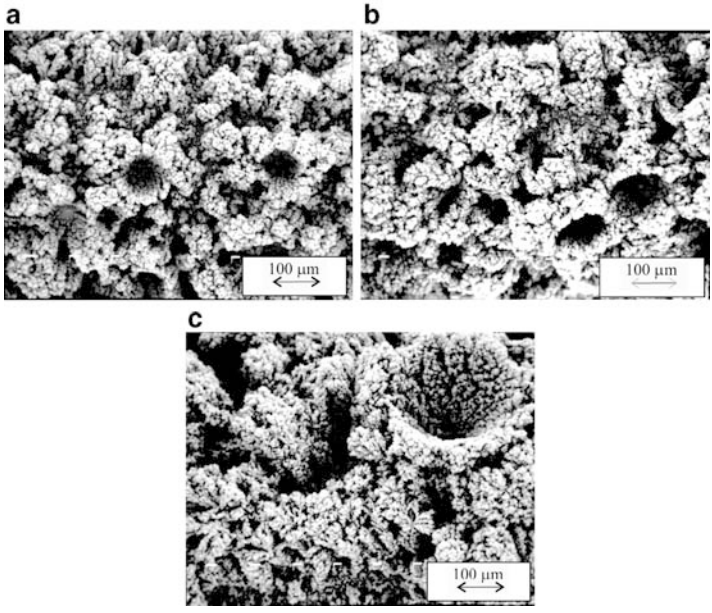

Figure 40. Morphologies of copper deposits electrodeposited at an overpotential of 800 mV at temperatures of: (**a**) $14.0 \pm 0.5°C$, (**b**) $35.0 \pm 0.5°C$, and (**c**) $50.0 \pm 0.5°C$. (Reprinted from Ref. [68] with permission from the Serbian Chemical Society).

of dendritic forms were the main characteristics of copper deposits obtained at this overpotential. A decreased number of holes per square millimeter surface area of copper electrodes and the increased diameter of the holes with increasing temperature can be observed from Fig. 40. Also, the portions of the copper structure consisting of disperse agglomerates of copper grains, among which irregular channels were formed, increased with increasing temperature of the solution.

First, it is necessary to note that the decrease of the number of holes per square millimeter surface area of the copper electrode with intensification of hydrogen evolution was very surprising. It is opposed to the already observed phenomena[10,17,18] when it was shown that intensification of hydrogen evolution reaction leads to an increase of the number of holes. Thus, the unexpected development of the copper structures with intensification of the hydrogen

evolution reaction clearly highlights the necessity to take into consideration the effect of temperature on some properties of electroplating solution, as well as the already mentioned increased bubble coverage with the increasing temperature. The properties of an electrolyte of importance in metal electrodeposition processes which are affected by a change of temperature are the viscosity[73] and surface tension of the electrolyte.[71]

In Ref.[68] are given the values of the viscosity and surface tension of a copper solution containing 0.15 M $CuSO_4$ in 0.50 M H_2SO_4 at the examined temperatures. As expected, both the viscosity and the surface tension of this solution decrease with increasing temperature. The decrease of the surface tension of the solution lowers the break-off diameter of hydrogen bubble from the electrode surface,[71] while the decreased viscosity of the solution probably facilitates the transport of the detached hydrogen bubbles through the interior of the deposit, thus forming a channel structure through it. A typical channel structure formed at an overpotential of 800 mV at a temperature of 50.0°C is shown in Fig. 41a, while the top view of this deposit shows that very disperse cauliflower-like agglomerates of copper grains were surrounded by irregular channels (Fig. 41b).

Hence, increase the temperature led to a redistribution of evolved hydrogen from those creating a honeycomb-like structure (holes formed due to the attachment of hydrogen bubbles with cauliflower-like agglomerates of copper grains between them) to those making a copper structure with the dominant presence of cauliflower-like forms and irregular channels between them.

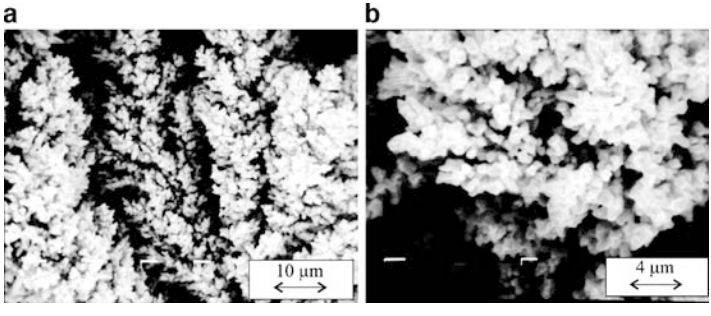

Figure 41. Morphologies of copper deposits electrodeposited at an overpotential of 800 mV at a temperature of 50.0 ± 0.5°C: (**a**) the channel structure, and (**b**) the top view of the deposit. (Reprinted from Ref.[68] with permission from the Serbian Chemical Society).

This increase of the portion of channel structure to the overall structure of the deposit in relation to the portion of holes to the overall structure is probably due to changes of the properties of the electroplating solution, caused by the dependences of the viscosity and surface tension of solution on temperature. As a result of this, the formation of holes becomes less possible and hence large holes appear only due to the edge effect, as can be clearly seen from Fig. 40c. It is obvious that the probability of the formation of the nucleus of such a structure decreases with lowering of the break-off diameter of the bubbles.

Also, it is necessary to note that increasing the temperature led to the formation of morphological forms of copper deposits characteristic for electrodeposition at higher overpotentials, probably because of the increase of bubble coverage with increasing temperature. The effect of temperature was opposite to those observed with increasing the concentration of Cu(II) ions,[19] when increasing concentration of Cu(II) ions led to a the formation of morphological forms of copper deposits characteristic for electrodeposition at lower overpotentials.[19]

5. Analysis of Deposition Conditions with the Aspect of the Honeycomb-like Structure Formation

It is obvious that the honeycomb-like structures can be considered as possible electrodes in electrochemical devices such as fuel cells and sensors due to their very open and porous structure. Analysis of the effect of different parameters of electrolysis given in this section enables to be systematized electrodeposition conditions leading to the formation of this structure type.

The acceleration of electrochemical processes through the increase of concentration of Cu(II) ions above 0.15 M $CuSO_4$ (in 0.50 M H_2SO_4) showed an unfavorable effect to the formation of the honeycomb-like structure due to the formation of dish-like holes with the higher concentrations of Cu(II) ions.[58]

The formation of degenerate dendrites (Fig. 37b), a channel structure around dendritic and cauliflower-like particles (Fig. 37c) and holes with the shoulders of degenerate dendrites (Fig. 37d) clearly points out that hydrodynamic conditions in the near-electrode layer were not changed by electrodeposition of copper from 0.15 M $CuSO_4$ in 0.125 M H_2SO_4. This was very surprising having in mind a relatively high average current efficiency of hydrogen evolution

of 20.3% by which this deposit was formed. Anyway, it is very clear that the quantity of evolved hydrogen is not the only parameter responsible for the formation of the honeycomb-like structures, and therefore, the analysis of the composition of electrodeposition solutions and electrodeposition conditions is very important. In order to explain different morphological forms obtained under hydrogen codeposition, Fritz equation,[74] modified by Stephan,[75] for the bubble break-off diameter at zero current, d_0 will be used.

This bubble break-off diameter, d_0, can be presented by (13):

$$d_0 = 1.20\vartheta\sqrt{\frac{\gamma}{g\,(\rho_L - \rho_G)}} \tag{13}$$

where ϑ is contact angle, γ is surface tension, ρ_L is a density of liquid phase, and ρ_G is a density of gaseous phase.

The bubble break-off diameter depends on a current density and as it was shown by numerous experiments,[71,76,77] it decreases with increasing current density. The fact that break-off diameter decreases with increasing current density is the result of varying electrode potential which affect the wettability and, hence, the contact angle supports the conclusion that (13) is a basic relationship to explain the dependence of the break-off diameter on the current density. Then, the bubble break-off diameter, d can be presented by (14):[71]

$$\frac{d}{d_0} = \left(1 + 0.2\frac{I/S}{\mathrm{Am}^{-2}}\right)^{-0.45} \tag{14}$$

where I/S is the superficial current density.

Using (13) and (14) as well as the fact that a contact angle decreases with lowering surface tension,[78] the formation of morphologies of copper deposits shown in Figs. 35–37 can be considered as follows. In Table 4 are given the values for a density and a surface tension of the examined solutions. As expected,[79] the density of copper solutions increased with the increase of concentration of H_2SO_4, while the increasing concentration of H_2SO_4 lowered the surface tension values of the examined solutions. The use of electroplating solution with lower surface tension generates more hydrogen bubbles during copper electrodeposition,[78] which is definitely confirmed in this investigation. It can be seen from Table 4 that the change of the density and the surface tension with increasing H_2SO_4 concentration was less than 5%.

Table 4.
The values of the density, ρ, and the surface tension, γ, of copper solutions containing 0.15 M $CuSO_4$ in 0.125, 0.25 and 1.0 M H_2SO_4. (Reprinted from Ref. [67] with permission from Elsevier).

Solution for copper Electrodeposition	ρ(kg dm^{-3})	$\gamma \times 10^3$ (J m^{-2})
0.15 M $CuSO_4$ in 0.125 M H_2SO_4	1.033	100.2
0.15 M $CuSO_4$ in 0.25 M H_2SO_4	1.038	98.7
0.15 M $CuSO_4$ in 1.0 M H_2SO_4	1.081	97.6

In order to apply (14) to potentiostatic conditions of electrodeposition, an average current density, I_{av}/S should be taken into consideration. An average current density, I_{av}/S can be presented by (15), and it was shown that the average current density increased with the increasing concentration of H_2SO_4.[67]

$$I_{av}/S = (1/t)\int_0^t i\,dt \tag{15}$$

Hence, according to (13), the increase of a density and the decrease of a surface tension of solution lead to a decrease of the bubble break-off diameter. According to (14) and (15), at the same deposition overpotential, copper electrodeposition by the higher average current density in addition decreases the break-off diameter of hydrogen bubbles. It is very clear from the above consideration that the contribiution of the average current density to the decrease of the break-off diameter is larger than the contribution of the density and the surface tension of the solutions. It can be concluded that the change of the break-off diameter of hydrogen bubbles with the change of H_2SO_4 concentration is consequence of synergetic effect of electroplating solutions properties and electrodeposition conditions. Anyway, the analysis of densities and surface tensions of the examined solutions, as well as the average current densities of electrodeposition successfully explains the change of the size of holes formed under the described hydrogen co-deposition conditions (Figs. 35–37).

Finally, the analysis of the break-off diameter (or the diameter of the detached hydrogen bubble) can give an explanation why the change of hydrodynamic conditions in the near-electrode layer is achieved from the copper solution with the lower quantity of evolved hydrogen (i.e. from 0.15 M $CuSO_4$ in 0.50 M H_2SO_4 at 800 mV

with the quantity of evolved hydrogen corresponding to $\eta_{av}(H_2)$ of 10.8%, but not from 0.15 M $CuSO_4$ in 0.125 M H_2SO_4 where the quantity of evolved hydrogen corresponded to $\eta_{av}(H_2)$ of 20.3%).

An increase of the density and the lowering of surface tension of the solution decreases the break-off diameter of bubble ((13) and (14)), and consequently, reduce the time needed for its detachment from an electrode surface. After the detachment of hydrogen bubble, the further electrodeposition process occurs by the formation of new hydrogen bubbles at an energetically active sites of electrode surface. A successive processes of the formation of hydrogen bubbles at an energetically active sites of electrode surface and their ability to relatively fast achieve the critical size for the detachment from electrode surface, produces an sufficient amount of hydrogen bubbles which can cause an effective stirring of solution in the near-electrode layer. This will lead to the decrease of the cathode diffusion layer thickness and the increase of the limiting diffusion current density, and as a result of this, the change of hydrodynamic conditions in the near-electrode layer is achieved. In this way, copper structures constructed of holes and agglomerates of copper grains between them, as well as without dendritic forms (denoted as the honeycomb-like structure) are formed.

On the other hand, the use of an electroplating solution of lower density and higher surface tension increases the break-off diameter of hydrogen bubbles. It means that during electrodeposition process from such a solution, newly formed hydrogen bubbles coalesce primarily with hydrogen bubbles formed in the initial stage of electrodeposition, increasing their diameter and prolonging a time needed for their detachment from electrode surface. In this way, the number of formed hydrogen bubbles will not be sufficient to cause an effective stirring of solution in the near-electrode layer. As a result of insufficient change of hydrodynamic conditions in the near-electrode layer, dendritic growth is not inhibited completely and degenerate dendrites as well as dendritic particles inside channels formed of evolved hydrogen were obtained.

The analysis of a number of holes formed per square millimeter surface area of copper electrodes and the average diameter of holes obtained from 0.15 M $CuSO_4$ in 0.50 M H_2SO_4 at 800 mV and from 0.15 M $CuSO_4$ in 0.125 M H_2SO_4 at 1,000 mV confirms above consideration. The number of holes formed due to the attached hydrogen bubbles from 0.15 M $CuSO_4$ in 0.50 M H_2SO_4 at 800 mV was 10/mm^2 surface area of copper electrode,[17] while their average

diameter was approximately 98.7 μm. This number was for about 40% larger than the number of holes formed from 0.15 M $CuSO_4$ in 0.125 M H_2SO_4 at 1,000 mV. The average diameter of holes formed from 0.15 M $CuSO_4$ in 0.125 M H_2SO_4 at 1,000 mV was for about 20% larger than the average diameter of those formed from 0.15 M $CuSO_4$ in 0.50 M H_2SO_4 at 800 mV.

Anyway, the results of the performed qualitative consideration clearly indicate that Fritz equation[74] modified by Stephan[75] can be applied for the examination of copper electrodeposition processes under hydrogen co-deposition in potentiostatic conditions.

The acceleration of electrochemical processes through the increase of a temperature of electrolysis showed an unfavorable effect to the formation of the honeycomb-like structures.[68] The increase of a temperature leads to the decrease of number of holes because of the effect of a temperature on some properties of solutions such as a viscosity and a surface tension.[68,71–73]

Hence, the conditions which must be fulfilled in order to get the honeycomb-like structure are: electrodeposition from the solutions with lower concentrations of Cu(II) ions (0.15 M $CuSO_4$ and less) in a concentration range from 0.25 M to 1.0 M H_2SO_4, at a temperature of 18.0 ± 1.0°C and at overpotentials outside the plateau of the limiting diffusion current density at which hydrogen evolution is vigorous enough to change hydrodynamic conditions in the near-electrode layer. The critical quantity of evolved hydrogen enabling the formation of the honeycomb-like structures under the given electrodeposition conditions corresponds to the average current efficiency of hydrogen evolution, $\eta_{av}(H_2)$ of 10.0%.[19]

The number of craters or holes forming the honeycomb-like structure increased rapidly with the quantity of evolved hydrogen, as can be seen from Fig. 42 which shows the dependence of the number of holes or craters formed due to the attachment of hydrogen bubbles on the average current efficiency of hydrogen evolution.

V. INFLUENCE OF IONIC EQUILIBRIUM IN THE $CuSO_4$–H_2SO_4–H_2O SYSTEM ON THE FORMATION OF IRREGULAR ELECTRODEPOSITS OF COPPER

The most suitable way to analyze the ionic equilibrium in the $CuSO_4$–H_2SO_4–H_2O system was the examination of electrodeposition processes at overpotentials outside the plateau of the

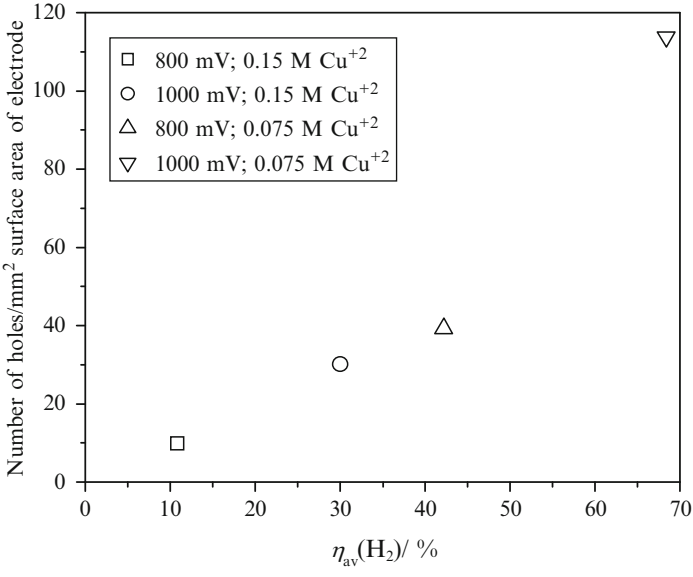

Figure 42. The dependence of the number of holes formed due to the attachment of hydrogen bubbles per square millimeter surface area of copper electrode on the average current efficiency of hydrogen evolution. (Reprinted from Ref. [19] with permission from MDPI).

limiting diffusion current density, due to the hydrogen evolution reaction which occurs parallel to the copper electrodeposition. In order to do it, two sets of acid sulfate solutions were analyzed. In one set of experiments, the concentration of $CuSO_4$ was the same (0.15 M $CuSO_4$), while the concentration of H_2SO_4 was different (0.125, 0.25, and 1.0 M H_2SO_4). The other set of experiments was performed with a constant concentration of H_2SO_4 and different concentrations of $CuSO_4$ (0.075, 0.30, and 0.60 M $CuSO_4$ in 0.50 M H_2SO_4). Then, the volumes of the evolved hydrogen (calculated as the average current efficiencies of hydrogen evolution) and the morphologies of copper deposits obtained at an overpotential of 800 mV for the same ratio of $CuSO_4/H_2SO_4$ were mutually compared and discussed in terms of the relative concentrations of hydrogen ions (H^+) as a function of the H_2SO_4 concentration.[60]

The ratios $CuSO_4/H_2SO_4$ were: 1.2 (for the copper solutions containing 0.15 M $CuSO_4$ in 0.125 M H_2SO_4 and 0.60 M $CuSO_4$

in 0.50 M H_2SO_4), 0.60 (for the copper solutions containing 0.15 M $CuSO_4$ in 0.25 M H_2SO_4 and 0.30 M $CuSO_4$ in 0.50 M H_2SO_4), and 0.15 (for the copper solutions containing 0.15 M $CuSO_4$ in 1.0 M H_2SO_4 and 0.075 M $CuSO_4$ in 0.50 M H_2SO_4).[60]

Analyzing the $CuSO_4/H_2SO_4$ ratio of 1.2 by insight into the ionic equilibrium of the species in the $CuSO_4$–H_2SO_4–H_2O system (Fig. 1), where the position of the Cu concentration of 0.15 M can easily be calculated, it can be noticed that the relative concentration of H^+ ions is larger for the copper solution containing 0.15 M $CuSO_4$ in 0.125 M H_2SO_4 than it is for the one containing 0.60 M $CuSO_4$ in 0.50 M H_2SO_4. This is confirmed by the larger average current efficiency of hydrogen evolution from 0.15 M $CuSO_4$ in 0.125 M H_2SO_4 (4.83%) than from 0.60 M $CuSO_4$ in 0.50 M H_2SO_4 (0.66%). The obtained morphologies of the copper deposits (Figs. 34a–c and 25e) also were in a good agreement with the determined average current efficiency of hydrogen evolution and this ionic equilibrium. The formation of degenerate dendrites from 0.15 M $CuSO_4$ in 0.125 M H_2SO_4 is the consequence of the larger quantity of evolved hydrogen from this solution than from 0.60 M $CuSO_4$ in 0.50 M H_2SO_4 when copper dendrites only were formed.

A similar consideration can also be applied to the $CuSO_4/H_2SO_4$ ratio of 0.60. According to the ionic equilibrium in $CuSO_4$–H_2SO_4–H_2O system, the relative concentration of H^+ ions is larger for a copper solution containing 0.15 M $CuSO_4$ in 0.25 M H_2SO_4 than for one containing 0.30 M $CuSO_4$ in 0.50 M H_2SO_4. The experimentally determined average current efficiency of hydrogen evolution and the observed morphologies of the copper deposits (Figs. 34d and 25b–d) were also in good agreement with the calculation of this ionic equilibrium. The presence of dendritic forms during electrodeposition from 0.30 M $CuSO_4$ in 0.50 M H_2SO_4 at 800 mV (Fig. 25b) clearly indicates that copper electrodeposition was accompanied by a smaller quantity of evolved hydrogen from this solution than from 0.15 M $CuSO_4$ in 0.25 M H_2SO_4.

Finally, the honeycomb-like copper structures were obtained with a $CuSO_4/H_2SO_4$ ratio of 0.15. The honeycomb-like copper structure was formed from 0.075 M $CuSO_4$ in 0.50 M H_2SO_4 under more vigorous hydrogen evolution than that formed from 0.15 M $CuSO_4$ in 1.0 M H_2SO_4, which is also in agreement with the calculation of the ionic equilibrium in the $CuSO_4$–H_2SO_4–H_2O system.

VI. THE SHAPE OF ELECTROCHEMICALLY FORMED COPPER POWDER PARTICLES AND THEIR DEPENDENCE ON THE QUANTITY OF EVOLVED HYDROGEN

In spite of detailed investigations of the formation and properties of metal powders obtained by electrolysis,[13,22–25] the first report which considered the effect of hydrogen evolution on the shape of powder particles was given recently.[80]

It was found[80] that two types of powder copper particles are formed, depending on the quantity of evolved hydrogen. The first type is formed with a quantity of evolved hydrogen which is insufficient to change the hydrodynamic conditions in the near-electrode layer ($\eta_{av}(H_2) < 10.0\%$), whereas the second type is formed when the quantity of evolved hydrogen is sufficient to change the hydrodynamic conditions in the near-electrode layer ($\eta_{av}(H_2) > 10.0\%$).

The first type of copper powder particles is shown in Fig. 43a. These particles were obtained by tapping the copper deposit obtained by electrodeposition from 0.15 M $CuSO_4$ in 0.50 M H_2SO_4 at an overpotential of 700 mV which was accompanied by $\eta_{av}(H_2)$ of 1.97%.[10] It can be seen from Fig. 43a that the copper particles were highly branched dendrites. The typical branchy from which these powder particles are constructed is presented in Fig. 43b.

The basic element from which this type of powder particles is constructed was obtained by a treatment of the copper powder

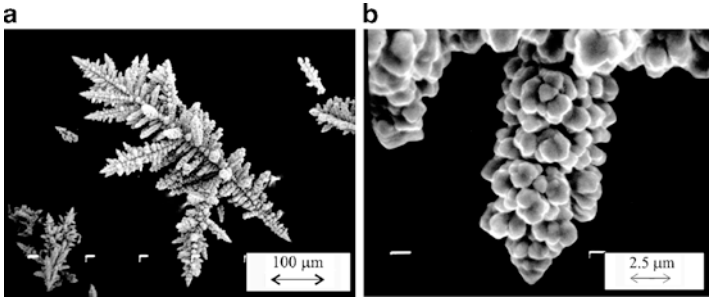

Figure 43. SEM photomicrographs of copper powder particles obtained by electrodeposition from 0.15 M $CuSO_4$ in 0.50 M H_2SO_4, at an overpotential of 700 mV: (**a**) dendritic particle, and (**b**) the detail from Fig. 43a. (Reprinted from Ref. [80] with permission from Elsevier).

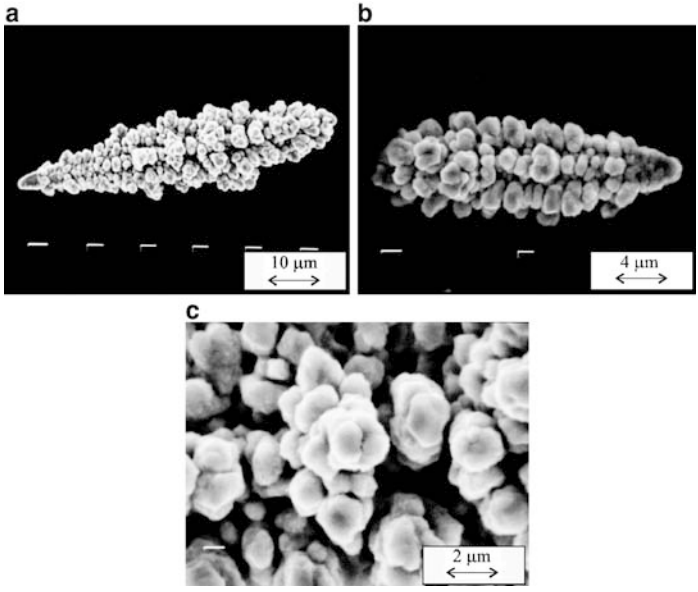

Figure 44. SEM photomicrographs of copper powder particles shown in Fig. 43 after treatment in an ultrasonic field: (**a, b**) the basic elements of the dendritic particles, and (**c**) the micro structure of the basic element. (Reprinted from Ref. [80] with permission from Elsevier).

particles shown in Fig. 43 in an ultrasonic field. The resulting particles are shown in Fig. 44. From Fig. 44a, b, it can be seen that the particles obtained had a corncob-like structure. They all took the form of branches of dendrites but, although they had the same surface structure, a difference in their size was noticeable. Analysis of these branches at the micro level revealed that the branches consisted of agglomerates of copper grains (Figs. 43b and 44c).

According to Wranglen,[81] a dendrite consists of a stalk and branches (primary, secondary, etc.). It is obvious from Figs. 43 and 44 that the corncob-like elements forming the branches constitute the dendritic character of these particles. These corncob-like elements can be grouped in different forms of dendritic particles or alternatively can be formed individually at the electrode surface. This can easily be seen from Fig. 45, which shows disperse deposits immediately before they were tapped from the electrode surface. They were all obtained by electrodeposition processes when the

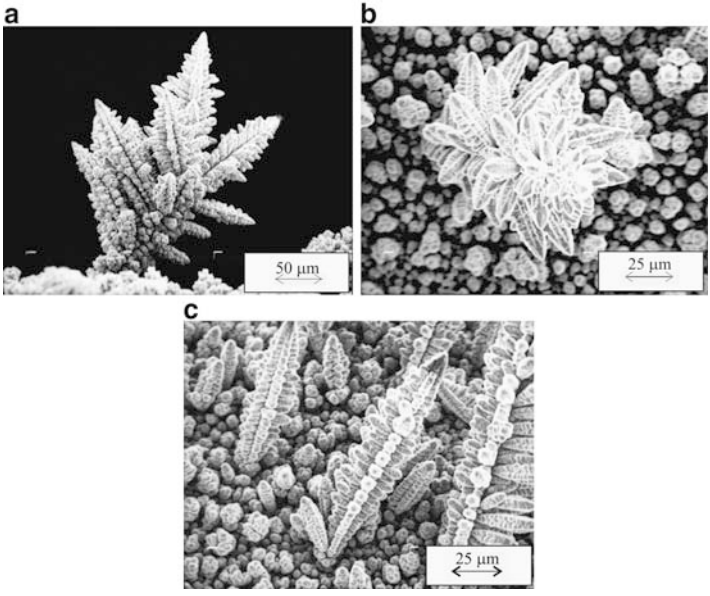

Figure 45. SEM photomicrographs of the copper powder deposits obtained by electrodeposition at an overpotential of 650 mV from: (**a**) 0.075 M $CuSO_4$ in 0.50 M H_2SO_4; (**b, c**) 0.30 M $CuSO_4$ in 0.50 M H_2SO_4. (Reprinted from Ref. [80] with permission from Elsevier).

quantities of evolved hydrogen were below the critical value for a change in the hydrodynamic conditions in the near-electrode layer. Figure 45a shows the powder deposit electrodeposited at an overpotential of 650 mV from 0.075 M $CuSO_4$ in 0.50 M H_2SO_4 ($\eta_{av}(H_2)$ was 7.5%),[19] whereas Fig. 45b, c shows the powder deposits electrodeposited at the same overpotential but from 0.30 M $CuSO_4$ in 0.50 M H_2SO_4 ($\eta_{av}(H_2)$ was 0.83%).[19] The electrodeposition process which led to the formation of the highly branched dendritic particles was controlled by the diffusion of ions to the electrode surface, rather than electron transfer control.[13]

The powder particles belonging to the second type are shown in Fig. 46a. They are obtained by tapping the copper deposit electrodeposited from 0.15 M $CuSO_4$ in 0.50 M H_2SO_4 at an overpotential of 1,000 mV at which the electrodeposition of copper was accompanied by vigorous hydrogen evolution, corresponding to

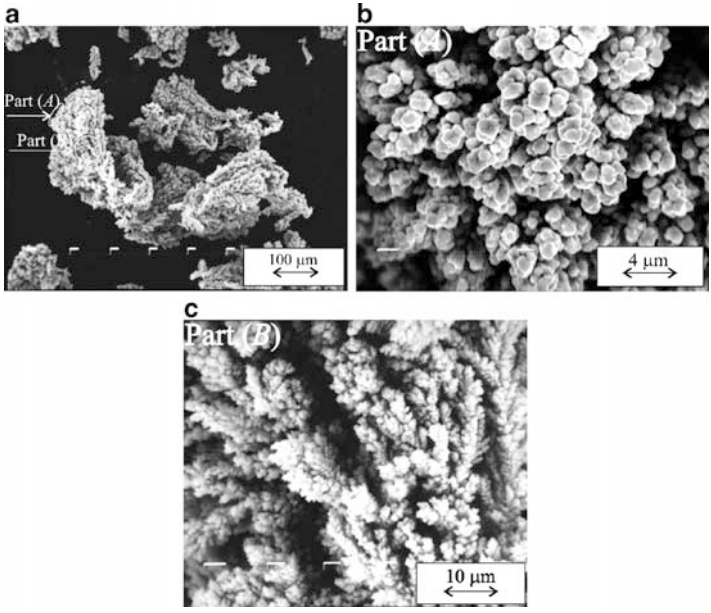

Figure 46. SEM photomicrographs of copper powder particles obtained by electrodeposition from 0.15 M $CuSO_4$ in 0.50 M H_2SO_4, at an overpotential of 1,000 mV: (**a**) sponge-like particle, and (**b, c**) *Part (A)* and *Part (B)* details from Fig. 46a. (Reprinted from Ref. [80] with permission from Elsevier).

$\eta_{av}(H_2)$ of 30.0%.[10] These powder particles were sponge-like and the difference between them and those formed when the quantity of evolved hydrogen was below the critical value for a change in the hydrodynamic conditions (Figs. 43–45) is clear. For this reason, further analysis of these particles is necessary. The parts of the powder particle denoted with *Part* (*A*) and *Part* (*B*) in Fig. 46a are shown at higher magnifications in Fig. 46b, c, respectively. It can be seen from Fig. 46b that these particles actually have a cauliflower-like structure. In Fig. 46c, a porous, channel structure through the interior of the powder particle can be seen. These channels were generated in situ by the simultaneous processes of the formation of copper particles and vigorous hydrogen evolution.

The basic element from which this type of powder particles is constructed was obtained by treatment of the particles shown in Fig. 46a in an ultrasonic field. Figure 47 shows the particles obtained

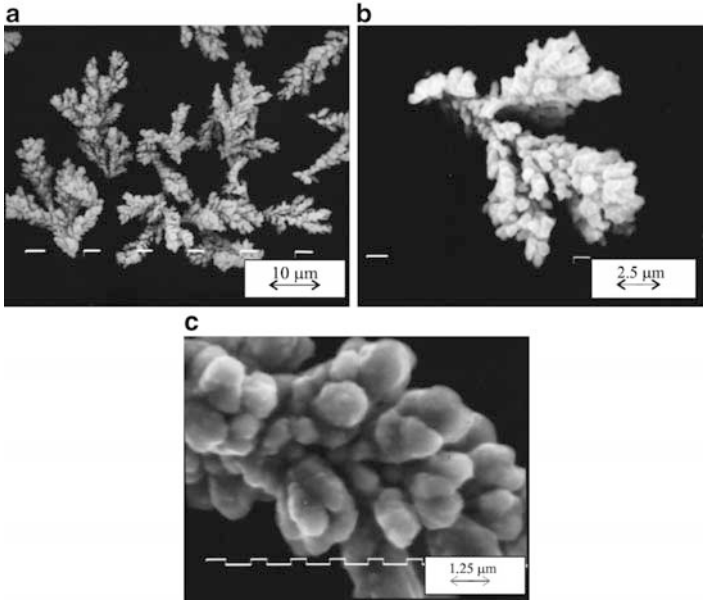

Figure 47. SEM photomicrographs of copper powder particles shown in Fig. 46 after treatment in an ultrasonic field: (**a, b**) the basic elements of the sponge-like particles, and (**c**) the micro structure of the basic element. (Reprinted from Ref. [80] with permission from Elsevier).

after treatment in an ultrasonic field. It can be seen that the structure of the basic element of which these powder particles are composed was completely different to that obtained when the amount of evolved hydrogen was below the critical value for a change in the hydrodynamic conditions in the near-electrode layer. In this case, corncob-like structures were not formed. The particles obtained had irregular shapes and had the appearance of degenerate dendrites. This shape is obviously caused by the vigorous hydrogen evolution, or hydrogen stream, which prevents the growth of the copper deposit in one direction, resulting in particles with a curvilinear form. Agglomerates of copper grains can also clearly be seen in these powder particles (Fig. 47b, c).

Although the powder particles obtained with evolved hydrogen below and above the critical value for a change in the hydrodynamic conditions were very different at the macro level, their similarity at the micro level is very clear. Both types of powder particles consisted

of agglomerates of copper grains. The only difference lay in the size of the individual copper grains of which these agglomerates were constituted – that is, the individual copper grains obtained at an overpotential of 1,000 mV were considerably smaller. This difference can be explained by the higher nucleation rate at an overpotential of 1,000 mV than at an overpotential of 700 mV.

The mechanism of electrodeposition of copper under intensive hydrogen evolution is completely different from that which led to the formation of dendritic particles. The quantity of evolved hydrogen corresponding to an average current efficiency of hydrogen evolution of 30.0% was sufficient to cause mixing of the solution in the near-electrode layer, decreasing the cathode diffusion layer thickness and increasing the limiting diffusion current density. The formation of this type of powder particle can be successfully explained by the concept of "effective overpotential."[10]

ACKNOWLEDGMENT

The work was supported by the Ministry of Science and Technological Development of the Republic of Serbia under the research project: "Deposition of ultrafine powders of metals and alloys and nanostructured surfaces by electrochemical techniques" (No. 142032G).

REFERENCES

[1]H.-C. Shin, J. Dong, and M. Liu, *Adv. Mater*. **15** (2003) 1610.
[2]D. R. Gabe, *J. Appl. Electrochem*. **27** (1997) 908.
[3]J. K. Dennis and T. E. Such, *Nickel and Chromium Plating*, Newnes–Butterworths, London (1972).
[4]R. Weiner and A. Walmsley, *Chromium Plating*, Finishing Publications Ltd., Teddington, Middlesex, England (1980).
[5]F. A. Lowenheim, *Electroplating,* McGraw-Hill Book Company, New York; St. Louis (1978).
[6]T. J. Wolery, *EQ3NR – A Computer Program for Geochemical Aqueous Speciation-Solubility Calculations: Theoretical Manual and User'guide, Version 7.0*. Lawrence Livermore National Laboratory, Livermore, CA (1992).
[7]A. Roine, *HSC Chemistry: Chemical Reaction and Equilibrium Software with Extensive Thermochemical Database. 4.0*. Outokumpu Research Oy, Finland (1999).
[8]J. M. Casas, F. Alvarez, and L. Cifuentes, *Chem. Eng. Sci*. **55** (2000) 6223.

[9]K. S. Pitzer, *Activity Coefficients in Electrolyte Solutions*, 2nd edition, CRC, Boca Raton, FL (1991).
[10]N. D. Nikolić, K. I. Popov, Lj. J. Pavlović, and M. G. Pavlović, *J. Electroanal. Chem*. **588** (2006) 88.
[11]V. D. Jović, B. M. Jović, and M. G. Pavlović, *Electrochim. Acta* **51** (2006) 5468.
[12]V. D. Jović, B. M. Jović, V. Maksimović, and M. G. Pavlović, *Electrochim. Acta* **52** (2007) 4254.
[13]K. I. Popov, S. S. Djokić, and B. N. Grgur, *Fundamental Aspects of Electrometallurgy,* Kluwer Academic/Plenum Publishers, New York (2002), and references therein.
[14]H. Vogt, *J. Appl. Electrochem*. **25** (1995) 764.
[15]J. Eigeldinger, and H. Vogt, *Electrochim. Acta* **45** (2000) 4449.
[16]H. Vogt, *Electrochim. Acta* **50** (2005) 2073.
[17]N. D. Nikolić, K. I. Popov, Lj. J. Pavlović, and M. G. Pavlović, *Surf. Coat. Technol*. **201** (2006) 560.
[18]N. D. Nikolić, K. I. Popov, Lj. J. Pavlović, and M. G. Pavlović, *J. Solid State Electrochem*. **11** (2007) 667.
[19]N. D. Nikolić, K. I. Popov, Lj. J. Pavlović, and M. G. Pavlović, *Sensors* **7** (2007) 1.
[20]G. E. Dima, A. C. A. de Vooys, and M. T. M. Koper, *J. Electroanal. Chem*. **554–555** (2003) 15.
[21]D. Pletcher and Z. Poorbedi, *Electrochim. Acta* **24** (1979) 1253.
[22]A. Calusaru, *Electrodeposition of Metal Powders*, Elsevier Scientific Publishing Company, Amsterdam; Oxford; New York (1979) 296.
[23]K. I. Popov and M. G. Pavlović, in *Modern Aspects of Electrochemistry*, Vol. 24, Ed. by R. W. White, J. O'M. Bockris, and B. E. Conway, Plenum Press, New York (1993) 299–391.
[24]N. D. Nikolić, S. B. Krstić, Lj. J. Pavlović, M. G. Pavlović, and K. I. Popov, "The Mutual Relation of Decisive Characteristics of Electrolytic Copper Powder and Effect of Deposition Conditions On Them", in *Electroanalytical Chemistry Research Trends*, Ed. by K. Hayashi, NOVA Publishers (2009) Chap. 8, 185–209.
[25]M. G. Pavlović and K. I. Popov (2005). *Metal Powder Production by Electrolysis*, Electrochemistry Encyclopedia, http://electrochem.cwru.edu/ed/encycl/art-p04-metalpowder.htm.
[26]M. G. Pavlović, N. D. Nikolić, and K. I. Popov, *J. Serb. Chem. Soc*. **68** (2003) 649.
[27]J. O'M. Bockris, Z. Nagy, and D. Dražić, *J. Electrochem. Soc*. **120** (1973) 30.
[28]K. I. Popov, M. D. Maksimović, J. D. Trnjančev, and M. G. Pavlović, *J. Appl. Electrochem*. **11** (1981) 239.
[29]N. Ibl, *Chemie Ing. Techn*. **33** (1961) 69.
[30]N. Ibl, *Chemie Ing. Techn*. **35** (1963) 353.
[31]L. J. Jenssen and J. G. Hoogland, *Electrochim. Acta* **15** (1970) 1013.
[32]J. O'M. Bockris, A. K. N. Reddy, and M. Gamboa-Aldeco, *Modern Electrochemistry 2A, Fundamentals of Electrodics*, Kluwer Academic/Plenum Publishers, New York, 2nd edition (2000).
[33]L. Martins, J. I. Martins, A. S. Romeira, M. E. Costa, J. Costa, and M. Bazzaoui, *Mater. Sci. Forum* **455–456** (2004) 844.
[34]N. D. Nikolić, H. Wang, H. Cheng, C. Guerrero, E. V. Ponizovskaya, G. Pan, and N. Garcia, *J. Electrochem. Soc*. **151** (2004) C577.
[35]N. D. Nikolic, H. Wang, H. Cheng, C. A. Guerrero, and N. Garcia, *J. Magn. Magn. Mater*. **272–276** (2004) 2436.
[36]N. D. Nikolić, *J. Serb. Chem. Soc*. **70** (2005) 1213.
[37]N. D. Nikolić, *J. Serb. Chem. Soc*. **70** (2005) 785.
[38]N. D. Nikolić, *J. Serb. Chem. Soc*. **71** (2006) 1083.

[39]N. D. Nikolić, *J. Serb. Chem. Soc*. **72** (2007) 787.
[40]M. G. Pavlović, Š. Kindlova, and I. Roušar, *Electrochim. Acta* **37** (1992) 23.
[41]R. Aogaki, K. Fueki, and T. Mukaibo, *Denki Kagaku* **43** (1975) 509.
[42]J. P. Glas and J. W. Westwater, *Int. J. Heat Mass Transf*. **7** (1964) 1427.
[43]R. Kaishew and B. Mutafctschiew, *Electrochim. Acta* **10** (1965) 643.
[44]S. Štrbac, Z. Rakočević, K. I. Popov, M. G. Pavlović, and R. Petrović, *J. Serb. Chem. Soc*. **64** (1999) 483.
[45]I. Markov, A. Boynov, and S. Toshev, *Electrochim. Acta* **18** (1973) 377.
[46]K. I. Popov, B. N. Grgur, E. R. Stojilković, M. G. Pavlović, and N. D. Nikolić, *J. Serb. Chem. Soc*. **62** (1997) 433.
[47]A. Milchev, W. S. Kruijt, M. Sluyters-Rehbach, and J. H. Sluyters, *J. Electroanal. Chem*. **362** (1993) 21.
[48]W. S. Kruijt, M. Sluyters-Rehbach, J. H. Sluyters, and A. Milchev, *J. Electroanal. Chem*. **371** (1994) 13.
[49]N. Kovarskii and A. V. Lisov, *Elektrokhimiya* **20** (1984) 221 (in Russian).
[50]N. Kovarskii and A. V. Lisov, *Elektrokhimiya* **20** (1984) 833 (in Russian).
[51]N. Kovarskii and T. A. Arzhanova, *Elektrokhimiya* **20** (1984) 452 (in Russian).
[52]K. I. Popov, Lj. J. Pavlović, M. G. Pavlović, and M. I. Čekerevac, *Surf. Coat. Technol*. **35** (1988) 39.
[53]K. I. Popov, M. G. Pavlović, Lj. J. Pavlović, M. I. Čekerevac, and G. Ž. Remović, *Surf. Coat. Technol*. **34** (1988) 355.
[54]K. I. Popov, M. G. Pavlović, E. R. Stojilković, and Z. Ž. Stevanović, *Hydrometallurgy* **46** (1997) 321.
[55]K. I. Popov, S. K. Zečević, and S. M. Pešić, *J. Serb. Chem. Soc*. **61** (1996) 583.
[56]K. I. Popov, N. D. Nikolić, and Z. Rakočević, *J. Serb. Chem. Soc*. **67** (2002) 635.
[57]K. I. Popov, N. D. Nikolić, and Z. Rakočević, *J. Serb. Chem. Soc*. **67** (2002) 769.
[58]N. D. Nikolić, Lj. J. Pavlović, M. G. Pavlović, and K. I. Popov, *Electrochim. Acta* **52** (2007) 8096.
[59]N. D. Nikolić, Lj. J. Pavlović, G. Branković, M. G. Pavlović, and K. I. Popov, *J. Serb. Chem. Soc*. **73** (2008) 753.
[60]N. D. Nikolić, Lj. J. Pavlović, S. B. Krstić, M. G. Pavlović, and K. I. Popov, *Chem. Eng. Sci*. **63** (2008) 2824.
[61]D. G. Offin, P. R. Birkin, and T. G. Leighton, *Electrochem. Commun*. **9** (2007) 1062.
[62]K. I. Popov, V. Radmilović, B. N. Grgur, and M. G. Pavlović, *J. Serb. Chem. Soc*. **59** (1994) 47.
[63]L. Barton and J. O'M. Bockris, *Proc. R. Soc*. **A268** (1962) 485.
[64]J. W. Diggle, A. R. Despić, and J. O'M. Bockris, *J. Electrochem. Soc*. **116** (1969) 1503.
[65]E. Gileadi, *Electrode Kinetics*, VCH Publishers Inc., New York, (1993) 443.
[66]K. I. Popov, N. V. Krstajić, and M. I. Čekerevac, in: *Modern Aspects of Electrochemistry*, Vol. 30, Ed. by R. E. White, B. E. Conway, and J. O'M. Bockris, Plenum Press, New York (1996) 261–311, and references therein.
[67]N. D. Nikolić, G. Branković, M. G. Pavlović, and K. I. Popov, *J. Electroanal. Chem*. **621** (2008) 13.
[68]N. D. Nikolić, Lj. J. Pavlović, M. G. Pavlović, and K. I. Popov, *J. Serb. Chem. Soc*. **72** (2007) 1369.
[69]E. Budevski, G. Staikov, and W. J. Lorenz, *Electrochemical Phase Formation and Growth, An Introduction to the Initial Stages of metal Deposition*, VCH Weinheim, New York; Basel; Cambridge; Tokyo (1996) 163.
[70]M. Volmer and A. Weber, *Z. Physik. Chem*. **119** (1926) 277.
[71]H. Vogt and R. J. Balzer, *Electrochim. Acta* **50** (2005) 2073.

[72]M. Krenz, *Untersuchung des elektrodennahen Raumes gasentwickelnder elektroden*, Dissertation A, Humboldt-Universitat, Berlin (1984).
[73]A. Amadi, D. R. Gabe, and M. Goodenough, *J. Appl. Electrochem*. **21** (1991) 1114.
[74]W. Fritz, *Phys. Z*. **36** (1935) 379.
[75]K. Stephan, *Heat Transfer in Condensation and Boiling*, Springer, Berlin (1992).
[76]N. Ibl, E. Adam, J. Venczel, and E. Schalch, *Chem. Eng. Tech*. **43** (1971) 202.
[77]H. Vogt, *Gas evolving electrodes*, in: Comprehensive Treatise of Electrochemistry, Vol. 6, Ed. by E. Yeager, J. O. M. Bockris, B. E. Conway, and S. Sarangapani, Plenum Press, New York (1983) 455.
[78]S.-C. Chang, Y.-L. Wang, C.-C. Hung, W.-H. Lee, and G.-J. Hwang, *J. Vac. Sci. Technol. A* **25** (2007) 566.
[79]D. C. Price and W. G. Davenport, *Metall. Trans. B* **11 B** (1980) 159.
[80]N. D. Nikolić, Lj. J. Pavlović, M. G. Pavlović, and K. I. Popov, *Powder Technol*. **185** (2008) 195.
[81]G. Wranglen, *Electrochim. Acta* **2** (1960) 130.

2

Noble Metal Nanoislands Decoration of Au(111) and Pt(111) Single Crystal Surfaces

Svetlana Strbac[1] and Andrzej Wieckowski[2]

[1] *ICTM-Institute of Electrochemistry, University of Belgrade, Njegoseva 12, Belgrade, Serbia*
[2] *Department of Chemistry, University of Illinois at Urbana-Champaign, Urbana, IL, USA*

I. INTRODUCTION

Platinum single crystals decorated with noble metal nanoislands have found increasing applications as model systems for highly active fuel cell catalysis due to their enhanced electrocatalytic properties.[1,2] Pt single crystals modified with Ru nanoislands were particularly explored due to the high catalytic efficiency of PtRu bimetallic electrodes with respect to the removal of CO poisoning during methanol oxidation.[1–4] The precise geometry of the Ru-modified Pt single crystals, acquired by the use of both ex situ[5–8] and in situ scanning tunneling microscopy (STM)[2–9] techniques, enabled fundamental investigations of their activity from the structural perspective.[2,5] Comprehensive in situ STM studies of Au single crystals decorated with Ru nanoislands were also undertaken

S.S. Djokić (ed.), *Electrodeposition: Theory and Practice*,
Modern Aspects of Electrochemistry 48, DOI 10.1007/978-1-4419-5589-0_2,

in order to elucidate the catalytic behavior of ruthenium nanoislands,[9–14] since the Au substrate alone was much less active towards CO adsorption or oxidation.[15]

Most of the Pt or Au single crystal-based model bimetallic electrodes were prepared by electrochemical deposition[2, 10–13] or spontaneous deposition.[1, 3–9, 14, 16–24] The spontaneous deposition method has several important advantages: it is simple, yields structurally heterogeneous surfaces decorated with three-dimensional nanoislands, and provides an excellent way for adjusting the coverage of the foreign metal nanoislands in a submonolayer deposition regime. Utilizing a "multiple spontaneous deposition" method can yield surfaces with high coverage values by repetition of the exposure to the depositing metal ion solution.[17]

Spontaneous deposition of other metal nanoislands on Pt and Au single crystal substrates has also been reported. For instance, Os deposition on single crystal platinum electrodes was studied by both ex situ[6, 7, 18] and in situ STM.[19, 20] In addition, in situ STM studies of the spontaneous depositions of Os,[21, 22] Pt,[23, 24] and Sn[25] on Au(111) single crystal as well as Pt on Ru(0001)[26] and Pb on Ru(0001)[27] were also carried out.

The oxidation state of the spontaneously deposited metal nanoislands is an important issue for interpreting the electrocatalytic activity of the bimetallic electrodes. For that, in situ X-ray photoelectron spectroscopy (XPS) was used to determine the electrode potential-dependent oxidation state of Ru[28] and Os[29] nanoislands spontaneously deposited on Pt(111). XPS data concerning the oxidation state of spontaneously deposited Pt on Au(111)[23] and Ru and Ir on Ru(0001) were reported.[30]

In this chapter, we present results obtained in two laboratories: Institute for Surface Chemistry and Catalysis, Ulm University and Department of Chemistry, University of Illinois at Urbana-Champaign. An overview of the fundamental electrochemical and structural properties of selected bimetallic electrodes obtained by both electrochemical and spontaneous deposition is reported. The chapter is organized as follows. A brief description of the electrode preparation for in situ STM[9] and electrode characterization is given first. This is followed by a presentation of a variety of surface morphologies obtained by the electrochemical deposition of Ru on Au(111) over a wide potential region.[11, 12] Next, a wide range of surface morphologies of some other selected bimetallic single crystal

electrodes, namely those obtained by the spontaneous deposition of Os on Au(111)[21,22] as well as Ru[9,16] and Os[9,19] on Pt(111) single crystal surfaces, are reported. The significance of the spontaneous deposition method leading to the formation of surface structures that cannot be obtained by other methods is highlighted. Finally, a summary of the electrocatalytic activity of selected bimetallic surfaces towards CO oxidation[9,12,22] and other small organic molecules[19,31] relevant for use in fuel cells is provided.

II. PREPARATION AND CHARACTERIZATION OF Me/Au(111) AND Me/Pt(111) SURFACES

1. Au(111) and Pt(111) Single Crystal Preparation for In Situ STM Measurements

Electrochemical STM appears to be a superior technique for studies of electrode–electrolyte interface in surface electrochemistry. In situ measurements are explored to acquire surface topography information during an electrochemical process, which enables the assessment of direct information about the surface structure of an electrode at a certain potential or about changes of the structure with potential. In situ STM is a superior technique for studies of surface structure and its changes with electrode potential and the electrode processes that occur at certain potentials. For instance, the most studied processes in the electrochemistry of single crystal electrodes were: the structure of chemisorbed inorganic and organic species, metal deposition, electrode surface reconstruction and anion adsorption, and their relation to the electrocatalytic activity of the investigated electrodes. These studies are described in several comprehensive reviews.[32–34] In situ STM measurements were used to obtain the results that will be presented in this chapter.

Before each measurement, single crystals were first electrochemically polished[35] and then flame annealed for several minutes, cooled down, and either immersed into an external electrochemical cell for cyclic voltammetry (CV) characterization or mounted into an electrochemical cell of an STM. For both CV and in situ STM results, sample potentials were measured and presented vs. Ag/AgCl reference electrode.

For instance, for in situ STM measurements with Au(111) crystal, the crystal was contacted with the solution under potential control and images were recorded at a chosen potential.

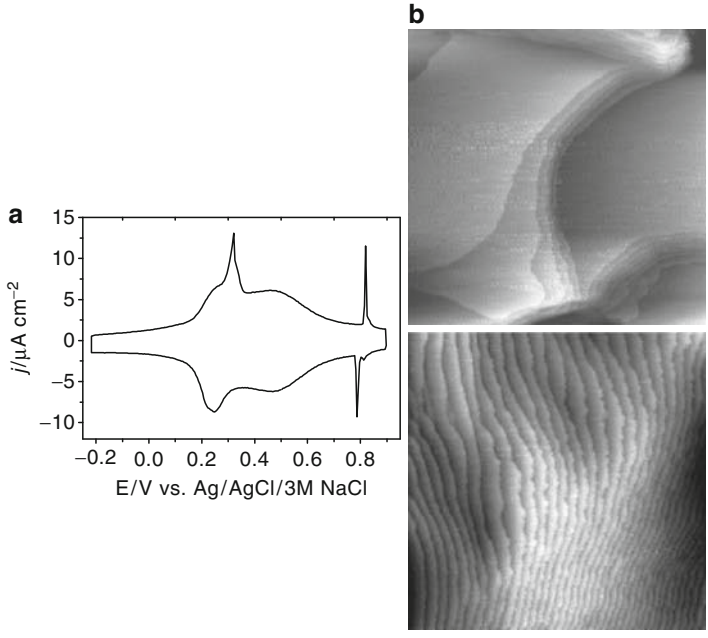

Figure 1. Characterization of the initial Au(111) surface in 0.5 M H_2SO_4: (**a**) CV in the double layer potential region; (**b**) the upper STM image ($285 \times 285\,nm^2$) shows a smooth area, while the lower one ($140 \times 140\,nm^2$) shows a highly stepped surface area. The images are recorded in 0.5 M H_2SO_4 at the open circuit potential. Reprinted from Ref. [16] with permission from Elsevier.

A representative CV and in situ STM images of the initial Au(111) surface in 0.5 M H_2SO_4 are given in Fig. 1.[16] The CV in the double layer potential region (Fig. 1a) shows the typical features of a clean Au(111) surface in sulfuric acid solutions.[36–38] At potentials negative to 0.3 V, the Au(111) surface is reconstructed and the peak at 0.3 V is associated with a lifting of the reconstruction via sulfate adsorption. Sulfate adsorption occurs over a wide potential region up to the beginning of oxide formation and the peak at approximately 0.80 V is associated with the formation of an ordered sulfate adlattice. STM images obtained in sulfuric acid solution at the open circuit potential show the unreconstructed Au(111) surface consisting of 100–200–nm-wide terraces (Fig. 1b, top image) and a highly stepped surface area with terrace widths of 2–10 nm (Fig. 1b, bottom image).

The integrity of the order of a platinum single crystal surface is highly sensitive to oxygen chemisorption and concomitant surface oxidation.[39] This creates difficulty when using STM due to the time it takes to mount the crystal in the STM cell after the flame annealing,[40] and the surface may disorder rapidly before the STM images are taken. To prevent such disordering, as well as to eliminate other possible platinum contaminations, a procedure based on surface protection by I^- adsorption[41] modified in a way which enables the crystal to be mounted in the STM cell while still maintaining the crystallographic long-range order and cleanness of the crystal surface was proposed.[9] First, the crystal is annealed in a hydrogen flame and cooled in hydrogen–argon atmosphere.[40] The crystal is subsequently protected by a drop of deaerated water and transferred to a 1 mM KI solution, where I^- adsorbs on the Pt forming an iodine adlayer which protects against platinum oxidation and contamination. Subsequently, the I-protected crystal is safely mounted in the STM cell. A CO-saturated sulfuric acid solution is then admitted to the electrochemical STM cell and the potential is held at -0.1 V for 10 min to displace the iodide with carbon monoxide.[42] The CO-saturated solution is replaced with clean sulfuric acid while still under electrode potential control, and subsequently the surface is scanned to 0.75 V in order to strip the surface of CO without causing surface disorder.[42–44]

The CV obtained after CO stripping (Fig. 2a) depicts the character of a clean, well-ordered Pt(111) substrate, with relatively "flat" hydrogen adsorption/desorption regions, a well-defined and sharp peak at ca. 0.22 V corresponding to sulfate adsorption on the (111) surface sites, and a small oxidation and reduction peak at 0.48 and 0.44 V, respectively. All these voltammetric features indicate that the Pt surface had maintained the proper purity and crystallographic order. After mounting the Pt(111) crystal in the STM cell, the surface was characterized by imaging at 0.1 V in 0.1 M H_2SO_4 (Fig. 2b). A typical STM image of the Pt(111) surface exhibits large terraces (ranging from 50 to 150 nm width) with monoatomic steps. The image demonstrates the absence of surface islands, which is characteristic of the absence of detectable contaminations and oxides.

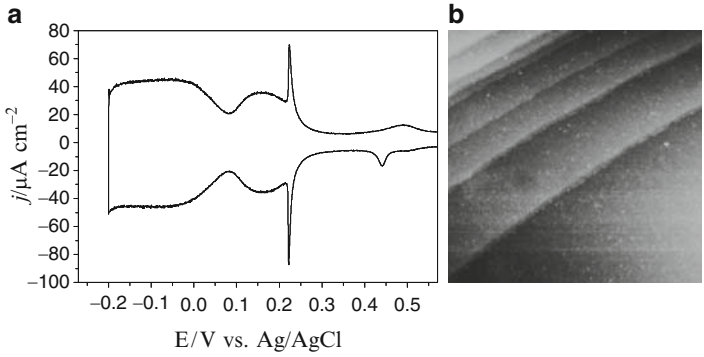

Figure 2. (**a**) Cyclic voltammogram of clean Pt(111) obtained after CO stripping in 0.1 M H_2SO_4 at a sweep rate of 50 mV/s; (**b**) STM image ($100 \times 100\,nm^2$) of the clean Pt(111) surface; the image was recorded in 0.1 M H_2SO_4 at 0.1 V. Reprinted from Ref. [9] with permission from Elsevier.

2. In Situ STM Imaging of the Au(111) and Pt(111) Single Crystals Decorated with Metal Nanoislands

Decoration of the *as prepared* Au(111) and Pt(111) single crystal surfaces with the chosen metal nanoislands was performed in the electrochemical STM cell. The electrolyte containing the metal ions to be deposited was contacted with the surface under a potential control: either at the chosen deposition potential in the case of electrochemical deposition or at the open circuit potential in the case of spontaneous deposition. After the deposition had been performed for a chosen deposition time, the electrolyte was exchanged with a pure sulfuric acid solution while keeping the potential control and STM images were recorded. Independent STM images were obtained for various deposition times, while for multiple deposition, the subsequent depositions and imaging were performed. Coverage on terrace areas was estimated as the fraction of the substrate surface area covered by overlayer structures in STM images, while coverage of steps was estimated as the fraction of step length touched by deposited metal nanoislands.

During the imaging, it was observed that the size as well as the oxidation state of the deposited metal nanoislands depended on the electrode potential.[12] In addition, interference of the tip and the deposited nanosized islands was found at higher potentials close to

the OCP. The deposited nanoislands are disturbed or moved by the tip and the islands may aggregate during prolonged scanning at the edges of the scanning area. This interference can be explained by a weakening of the bond between the deposited nanoislands and the single crystal substrate due to their partial oxidation at higher electrode potentials. Therefore, the electrode potential at which the images were taken was in the range −0.1 to 0.1 V, i.e., sufficiently negative to be sure that only metallic nanoislands were present on the surface.

III. ELECTROCHEMICAL DEPOSITION OF Ru ON Au(111)

1. The Electrodeposition of Ru on Au(111) Observed by Cyclic Voltammetry

The electrochemical deposition of Ru on an Au(111) surface was performed at various constant deposition potentials for a chosen deposition time and the obtained Ru/Au(111) surfaces were characterized by CV after the electrolyte had been changed to pure 0.1 M H_2SO_4 solution.[12] As an example, the CVs of Ru/Au(111) obtained after the electrodeposition of Ru at 0.0 V for 10 min are presented in Fig. 3a. Under these conditions, a saturation coverage close to a full coverage of the Au(111) surface by the deposited Ru was obtained (see below). The first sweep obtained in the potential limits from 0.2 up to 0.6 V was similar to those obtained under the same conditions on bulk Ru[45] and on Ru(0001) electrodes.[46] Compared to the initial Au(111), the CV of which is shown by the dotted line in Fig. 1a, the obtained Ru/Au(111) surface was characterized by an enlarged double layer current and a broad anodic peak at 0.3 V and three overlapping cathodic peaks between 0.35 and −0.1 V. With the increase of the upper potential limit, the anodic current increased, while the broad cathodic peak changed significantly. According to CV studies of Ru deposition on Pt(poly)[47,48] and on Pt single crystals,[4] and XPS studies on Pt(111),[28] these features are associated with the presence of deposited Ru in various oxidation states depending on the potential; this will be addressed in more detail below. Upon sweeping the potential further to 1.1 V, the deposited Ru began to dissolve. After about ten sweeps to the potential of Au oxidation, the deposited Ru was almost completely removed and the initial

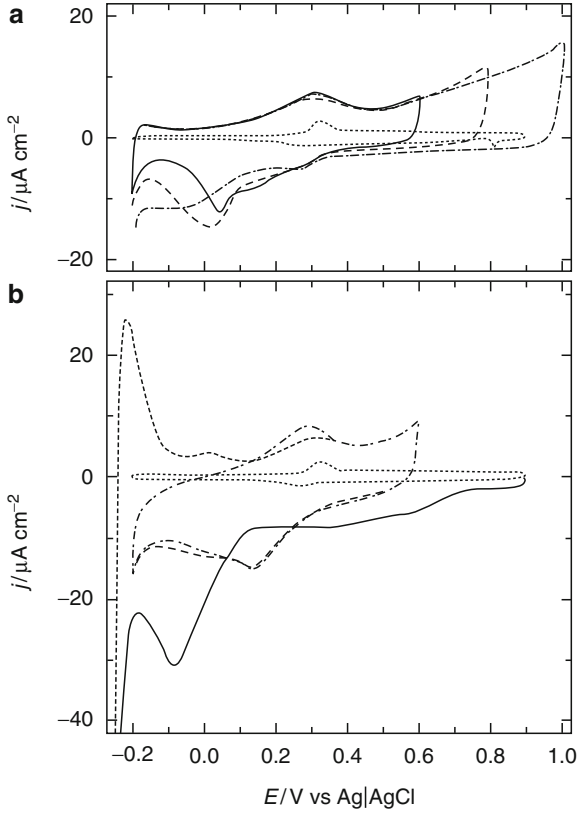

Figure 3. Cyclic voltammograms of: (**a**) a Ru monolayer on Au(111) prepared by 10-min deposition at 0.0 V in 2×10^{-4} M $RuCl_3 + 0.1$ M H_2SO_4; (**b**) Ru deposition on Au(111) directly after immersion at 0.9 V. The *solid, dashed*, and *dashed-dotted lines* correspond to the first negative sweep and the second and third potential cycles, respectively. For comparison, the CV of the bare Au(111) surface in 0.1 M H_2SO_4 is shown *(dotted line)*. The sweep rate was 10 mV/s. Reprinted from Ref. [12] with permission from Elsevier.

voltammogram of the Au(111) surface was restored. Since the Ru deposit consisted of a mixture of Ru species having various oxidation states and, moreover, Ru dissolution was accompanied with O_2 evolution on the deposited Ru and with the oxidation of the underlying Au(111) substrate, an estimation of the Ru coverage was not

possible, either from the double layer charge or from the dissolution stripping charge. Therefore, the Ru coverage was more accurately estimated from STM measurements, as demonstrated below.

The Ru deposition process itself was characterized by recording CVs in a Ru-containing solution during a potential scan starting from the initial value of 0.9 down to −0.2 V and then back to 0.9 V as shown in Fig. 3b. A closer examination of the electrodeposition of Ru on Au(111) shows that Ru is deposited not only at potentials negative to the Ru^{2+}/Ru^0 Nernst potential (0.135 V for 10^{-4} M $RuCl_3$) but also at higher potentials up to the onset of Au oxidation, although only to a limited extent.

Immediately after the immersion of the electrode at 0.9 V and scanning the potential in the negative direction, a broadening of the double layer region compared to the initial Au(111) surface (presented by the dotted line in Fig. 3b) was observed. After that, the current density increased reaching a plateau at 0.4 V. A further increase of the current occurred only at potentials negative to the Nernst potential, exhibited a peak at −0.1 V. As will be shown below, at potentials higher than the Nernst potential, Ru species are deposited in submonolayer amounts, achieving a saturation coverage which is associated with the current plateau. Completion of a monolayer occurs at potentials lower than the Nernst potential down to −0.2 V. Only at potentials lower than −0.2 V, does a bulk Ru deposition occur, which is further verified by an increase in the oxide formation peak in the second sweep.

At potentials lower than the Nernst potential, the deposited Ru species consisted mainly of metallic ruthenium.[4] In addition, certain amounts of ruthenium oxides, RuO_2 and even RuO_3, were detected. This indicates that deposition at lower potentials involved the deposition of metallic Ru, most probably according to the reactions:

$$RuO^{2+} + 2H^+ + 4e \rightarrow Au\text{-}Ru^0 + H_2O \quad (1)$$

or

$$Ru^{3+} + 3e \rightarrow Ru^0 \quad (2)$$

With an increase of the potential, the amount of metallic Ru decreases, while the amount of Ru oxides increases, particularly high-valence ruthenium(VI) oxide (RuO_3). At the potential higher than 0.6 V, only ruthenium oxides and no metallic Ru are detected by XPS.[28]

The formation of RuOH and RuO during electrochemical deposition was ascribed to the presence of $RuO[(H_2O)_4]^{2+}$ and formation of $RuO_{2,ads}$ on the surface and its further evolution according to the reactions:

$$RuO^{2+} + H^+ + A^- + 2e \rightarrow RuOH + A \quad (3)$$

and

$$RuO_{2,ads} + 2H^+ + 2e \rightarrow RuO_{ads} + H_2O \quad (4)$$

or directly

$$RuO[(H_2O)_4]^{2+} + A^- + e \rightarrow RuO_{ads} + A + 4H_2O \quad (5)$$

This would explain the high open circuit potential of 0.63 V established after the deposition. The Ru coverage is strongly dependent on the potential of its deposition and the Cl^- ion activity.[47–49] Increasing the Cl^- ion activity induces a negative shift in the potential at the beginning of Ru deposition. The rate of charge transfer is related to transport processes and adsorption. For these reasons, the Ru ions have enough time to diffuse without discharge. Hence, instead of bulk deposition, mostly an adsorbed layer is formed.

2. The Electrodeposition of Ru on Au(111) Observed by In Situ STM

At potentials negative to 0.15 V, Ru was deposited at a reconstructed surface of gold.[11] The Ru-containing electrolyte (10^{-4} M $RuCl_3$ + 0.5 M H_2SO_4) was contacted with the surface under a potential control in order to preserve the reconstruction and the deposition was performed for the chosen deposition times. Subsequently, the electrolyte was changed to pure 0.5 MH_2SO_4 solution while keeping the potential control and STM images were recorded. The STM images shown in Fig. 4a–d were obtained after the deposition had been performed for 30, 60, 120, and 180 s at 0.0 V, producing Ru/Au(111) surfaces with an estimated Ru coverage of 0.07, 0.3, 0.5, and 0.7 ML, respectively. For the relatively low Ru coverage of 0.07 ML (Fig. 4a), the average height of the deposited Ru islands was 0.22 nm, consistent with predominantly monolayer high islands, while the average width of the deposited islands was 0.74 nm. The two-dimensional (2D) Ru islands were aligned along recognizable directions, thus

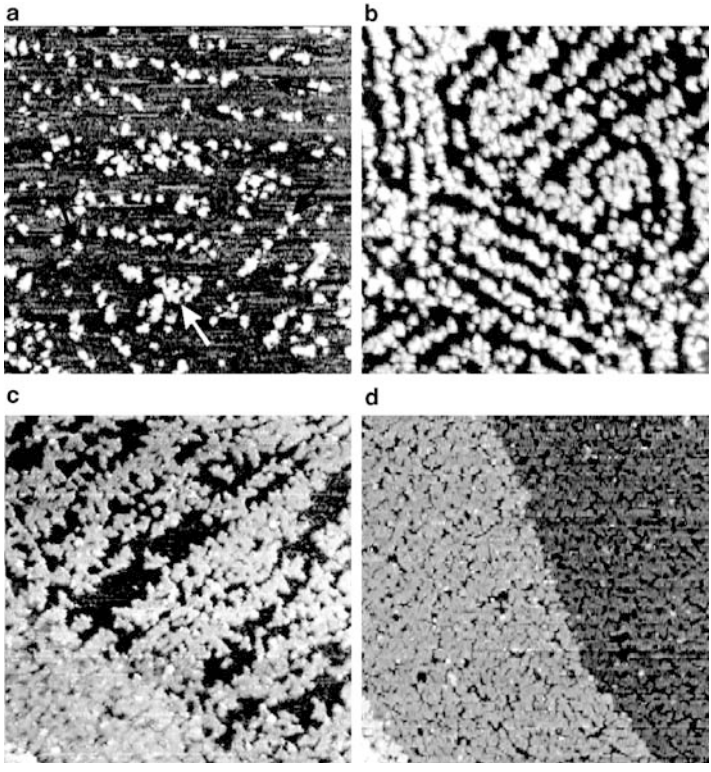

Figure 4. STM images of Au(111) recorded in 0.5 M H_2SO_4 at 0.0 V, after Ru deposition from 10^{-4} M $RuCl_3$ + 0.5 M H_2SO_4 for: (**a**) 30 s, coverage 0.07 ML ($82 \times 82\,nm^2$); (**b**) 60 s, coverage 0.30 ML ($82 \times 82\,nm^2$); (**c**) 120 s, coverage 0.55 ML ($73 \times 73\,nm^2$); (**d**) 180 s, coverage 0.7 ML ($82 \times 82\,nm^2$). Reprinted from Ref. [11] Copyright (1999) by The American Physical Society.

forming island arrays. The distance between neighboring island arrays was 6.5 nm, which corresponds to the distance between neighboring double rows on a reconstructed Au(111) surface, indicating that the deposited Ru islands were arranged along the rows of a reconstruction. In addition, three different elongations of the island arrays were observed, corresponding to deposition at three differently oriented hyperdomains of the reconstruction.

With increasing coverage up to 0.3 ML, only further arrangement of approximately the same sized deposited islands along the rows of reconstruction occurred (Fig. 4b). The fact that the mean size of Ru islands did not change despite an increase in the surface coverage by a factor of 4 is characteristic of the so-called pure nucleation regime, where additional deposition predominantly results in the formation of new nuclei. A further increase of the coverage up to 0.5 ML (Fig. 4c) led to the transition from nucleation to growth.

This was accompanied by a considerable increase in the average island size. Most islands were one layer high, although the growth of a second layer was also observed with islands nucleating on top of densely populated areas of the first layer. A further increase of the coverage up to 0.7 ML (Fig. 4d) led to exclusively island growth in the first layer. In the second layer, only the density of the islands increased, but their coalescence and growth still did not occur. Thus, the last two images (Fig. 4c,d) showed pure growth or steady-state regime, where the island density had saturated. STM images of the above-obtained deposits were also recorded at higher potentials, in order to observe the changes upon oxidation of the Ru islands. Images of the deposit shown in Fig. 4c,but obtained at various electrode potentials, are presented in Fig. 5. A break in orderliness and subsequent rearrangement of the Ru islands was observed at potentials higher than 0.3 V. With a further increase of the potential up to 0.9 V, an enlargement of the Ru islands due to their oxidation was observed (Fig. 5d). After a potential excursion to the region of oxide formation of gold (up to 1.45 V) and back to the oxide reduction potentials, the recorded STM image indicated a partial removal of Ru from the surface. After about ten sweeps, the Ru had been almost completely removed from the surface.

By following the morphological changes of the deposited Ru islands with the electrode potential, starting from the pure metallic phase at 0.0 V, it was found that a noticeable increase in the size of the deposited Ru islands began at 0.6 V, which is attributed to the formation of Ru oxide/hydroxide species. It was also found that, on increasing the potential, the fraction of Ru oxide species on the surface increased, leading to a significant change in the morphology of the deposit.

The electrochemical deposition of Ru at potentials positive to the Nernst potential, when the reconstruction of the underlying Au(111) surface had been partly or completely lifted, is illustrated

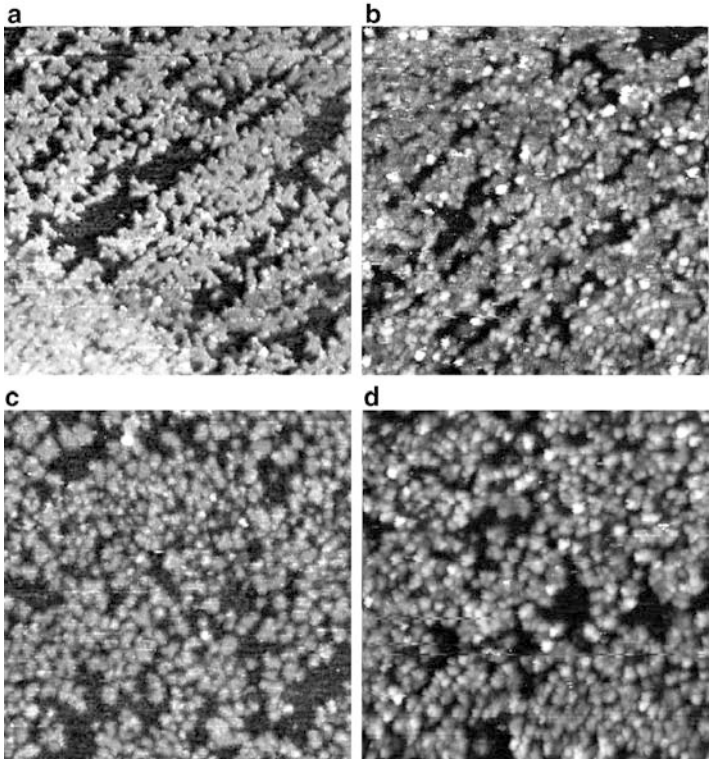

Figure 5. STM images ($140 \times 140\,nm^2$) showing the rearrangement and oxidation of Ru islands from Fig. 4c, with increasing the electrode potential from 0.0 V to: (**a**) 0.3 V; (**b**) 0.6 V; (**c**) 0.8 V; and (**d**) 0.9 V. Reprinted from Ref. [12] with permission from Elsevier.

by the STM images given in Fig. 6. For the deposition at 0.5 V, a uniform cluster size and a random distribution of the islands were obtained (Fig. 6a). For the deposition at 0.3 V, a nonuniform cluster size and a random distribution of clusters with a slight decoration of the steps were obtained (Fig. 6b). The coverage of the substrate was slightly higher than in the previous case. For the deposition at 0.1 V, a high coverage of the substrate with Ru and a nearly homogeneous distribution of the islands were obtained (Fig. 6c). The Au islands obtained after lifting of the reconstruction are clearly recognized. It should be pointed out that the coverage obtained for a

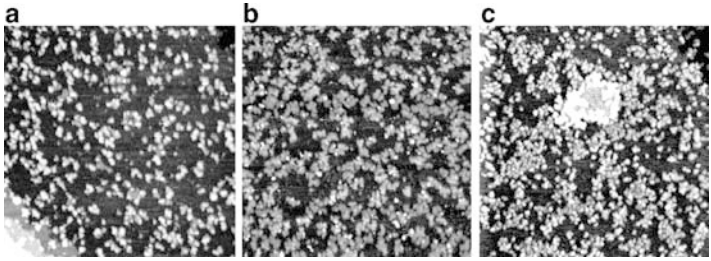

Figure 6. STM images ($120 \times 120\,nm^2$) of Au(111) recorded in 0.5 M H_2SO_4 after Ru was deposited from 10^{-4} M $RuCl_3$ + 0.5 M H_2SO_4 up to a saturation coverage at various positive potentials: (**a**) $E = 0.5$ V, $t = 30$ min, image recorded at 0.0 V, coverage 0.25 ML, (**b**) $E = 0.3$ V, $t = 3$ min, recorded at 0.3 V, coverage = 0.35 ML, (**c**) $E = 0.1$ V, $t = 1$ min, recorded at 0.1 V, coverage = 0.38 ML. Reprinted from Ref. [12] with permission from Elsevier.

deposition time of 3 min corresponded to the saturation coverage for the given deposition potential, since the coverage did not change on prolonging the deposition time up to half an hour.

IV. SPONTANEOUS DEPOSITION OF Ru ON Au(111)

Upon immersion of the Au(111) single crystal electrode in the Ru-containing solution (1 mM $RuCl_3$ in 0.5 M H_2SO_4), an immediate increase in the OCP value from 0.38 to ca. 0.72 V was observed, followed by a slow increase with increasing immersion time, as shown in Fig. 7a.[16] This shift of the open circuit potential to higher values was most likely due to the reduction of Ru^{4+} anions from $RuO[(H_2O)_2]^{2+}$ to either Ru^{3+} or Ru^0. In parallel, the $RuO[(H_2O)_2]^{2+}$ species were dehydrated to RuO_2. These surface reactions were followed by a catalytic disproportionate reaction, in which RuO_2 (or adsorbed $RuO[(H_2O)_2]^{2+}$) yields Ru^0 and RuO_3. The outcome was an adsorbate comprising Ru^0, RuO_2 and RuO_3, as confirmed by XPS measurements on platinum.[28] This is in accordance with the assumption that deposited Ru islands at the potential corresponding to the OCP are partly oxidized. The assumption was made based on the above-described in situ STM results of electrochemically deposited Ru on the Au(111) surface.

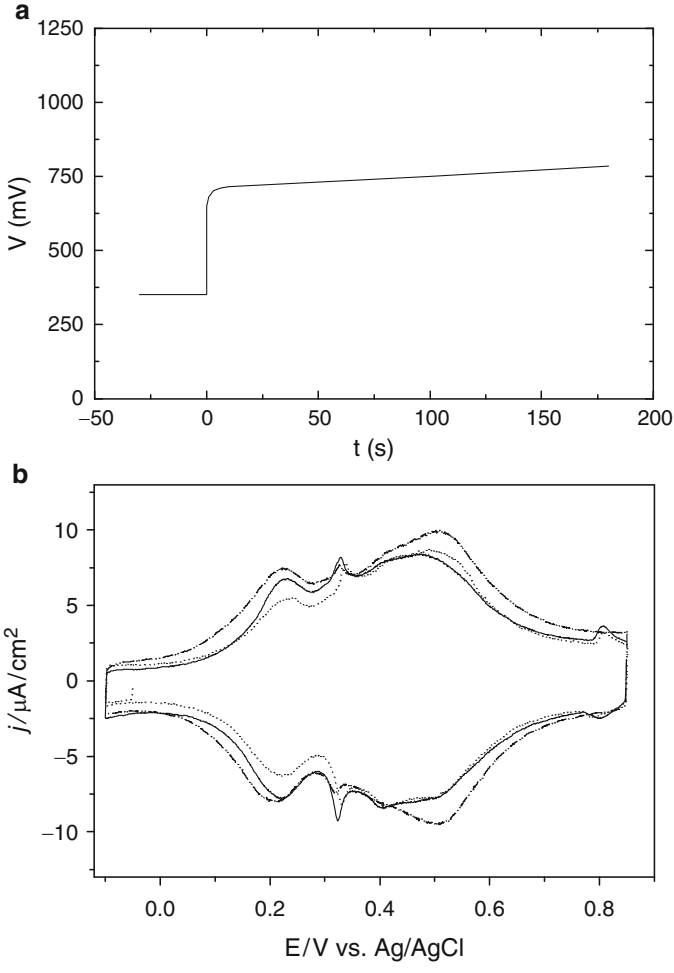

Figure 7. (**a**) Plot of the OCP vs. time of the Au(111) surface immediately upon immersion in the 1 mM $RuCl_3$ + 0.5 M H_2SO_4 solution; (**b**) cyclic voltammograms in 0.5 M H_2SO_4 of the Ru/Au(111) surface prepared by Ru deposited for 30 s *(dotted line)*, 3 min *(dashed line)*, and 3 × 2 repetitive depositions for 3 min each *(dashed-dot-dot-dashed line)*. The sweep rate was 50 mV/s. Reprinted from Ref. [16] with permission from Elsevier.

The cyclic voltammograms of the Ru/Au(111) electrodes obtained in sulfuric acid solution, after Ru had been spontaneously deposited for the given deposition times, and the potential cycled from −0.1 to 0.85 V in order to reduce the ruthenium oxide species, are shown in Fig. 7b. The formation of an ordered sulfate adlayer did not occur on the Au(111) surfaces covered by ruthenium, as can be seen by the dramatic suppression of the peak at 0.8 V (see Fig. 1a). This indicates that the formation of a ruthenium deposit irreversibly disrupted the long-range order processes. The thresholds for the oxidation of metallic ruthenium on the positive-going sweep and for the reduction of ruthenium oxide on the negative sweep are at around 0.3 V. As hydrogen does not adsorb readily on gold, the hydrogen adsorption current is absent. When ruthenium is deposited on the surface, a hydrogen evolution current was observed at an approximately 50 mV more positive potential. However, the capacitive current in the potential range from ca. −0.1 to 0.12 V did not noticeably increase on increasing the ruthenium coverage from 0.0 to approximately 0.6 ML, showing that no hydrogen was adsorbed on metallic ruthenium deposited on gold.

The STM images of the same Ru/Au(111) surfaces, recorded under potential control after the electrolyte had been replaced with a 0.5 M H_2SO_4 supporting electrolyte, are shown in Fig. 8. The STM images revealed that Ru islands were formed preferentially along the substrate steps. The Ru islands were also formed on the terraces, however, to a smaller degree. This is seen even as the deposition time was increased, i.e., the Ru islands tend to saturate the step edges. For a deposition time of 3 min, saturation coverage of the steps was achieved, as demonstrated in Fig. 8a, b, which shows several terraces separated by mono-atomically high steps. Step decoration was also observed during the electrodeposition of Ru on an Au(111) surface in HCl solution at a low Ru concentration and at a low electrode potential.[50] The coverage of the flat terraces of the Au(111) surface was ca. 5%, while the coverage of the steps appeared to be much higher. The coverage of steps corresponds to the amount of Ru islands contacting the edge of a step per unit step length, i.e., the number of deposited Ru islands per unit step length multiplied by the average island diameter. The average diameter of the mainly 2D deposited Ru islands was 1.5 nm, similar to the size observed after electrochemical deposition of ruthenium on Au(111).[11] The saturation coverage of the steps was 38% and the total coverage for a deposition time of 3 min was ca. 20%.

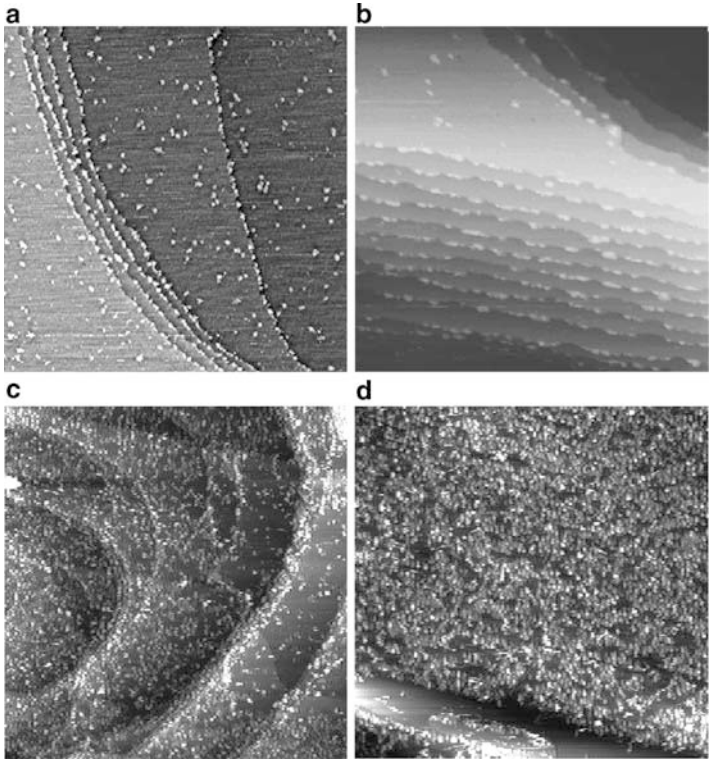

Figure 8. STM image of Ru/Au(111) recorded at 0.1 V in 0.5 M H_2SO_4 after Ru had been spontaneously deposited from 1 mM $RuCl_3 + 0.5$ M H_2SO_4 for: (**a**) 3-min 210×210 nm^2 image of a flat surface; (**b**) 100×100 nm^2 image of a highly stepped area; (**c**) 3×3 min 450×450 nm^2 image of a flat surface; (**d**) 320×320 nm^2 image of a highly stepped area. Reprinted from Ref. [16] with permission from Elsevier.

Once the saturation coverage of Ru on Au(111) had been achieved, it was possible to increase it further using a multiple spontaneous deposition method.[17] After the first deposition, the crystal was held at 0.1 V in H_2SO_4 to reduce Ru oxide, then the solution was replaced at the OCP with a ruthenium-containing solution and the deposition was performed for another 3 min, without removal of the deposited ruthenium from the previous deposition. STM images obtained after three consecutive depositions of 3 min each are shown in Fig. 8c, d.[16] An increase in the number of Ru islands

deposited on the steps, as well as an increase in the size of the islands (5–10 nm), was observed. The total coverage obtained was estimated at 35–40%, well above the coverage of 20% obtained by a single 3-min deposition. Notice that these islands now consist of two to four monolayers. Figure 8c reveals that certain areas of the electrode had higher coverage values than others, as can be seen by comparing the left side of the image to the right. It was noticed that the terrace coverage increased on the lower terraces. When analyzing the Ru coverage by section, the left side (lower terraces) had coverage close to 55%, while the coverage of the right side (higher terraces) was calculated to be 20–25%. In Fig. 8d, an image obtained while scanning over a stepped part of the surface is given to illustrate that the step edges were still the predominant nucleation sites.

Anions from the Ru-containing solution play a significant role in the spontaneous deposition process, influencing the coverage as well as the size of the deposited Ru islands. The STM images presented in Fig. 9 of Ru/Au(111) surfaces prepared by spontaneous Ru deposition from a perchlorate-containing solution (1 mM $RuCl_3$ + 0.1 M $HClO_4$), were obtained for deposition times of 30 s (Fig. 9a) and 3 min (Fig. 9b, c). The Ru islands were generally larger than those formed during deposition from a sulfate solution and grew in size with increasing deposition time. For an exposure time of 30 s, the island size was 4–6 nm, the step coverage was approximately 25%, while the total coverage was only 15%. The islands were predominately two layers high, although some islands consisted of up to four monolayers. In Fig. 9b, arrays of individual and distinguished islands were observed. The islands were densely packed along the steps, indicating that full step coverage had been achieved after 3 min of the deposition. While the density of islands on the terraces did not increase significantly with deposition time, the size of the islands was higher, namely 6–10 nm.

The step decoration obtained during spontaneous deposition of Ru on the Au(111) surface indicates that the steps were the active sites for the chemical reactions involving the formation of solid RuO_2 species and subsequent chemical disproportionate reaction discussed above. This reveals that, for a particular concentration of the solution, the density of the steps is the main factor determining the Ru coverage. A higher density of steps or active sites can be achieved either by multiple deposition, whereby the deposited Ru islands take over the role of active sites in the deposition (see

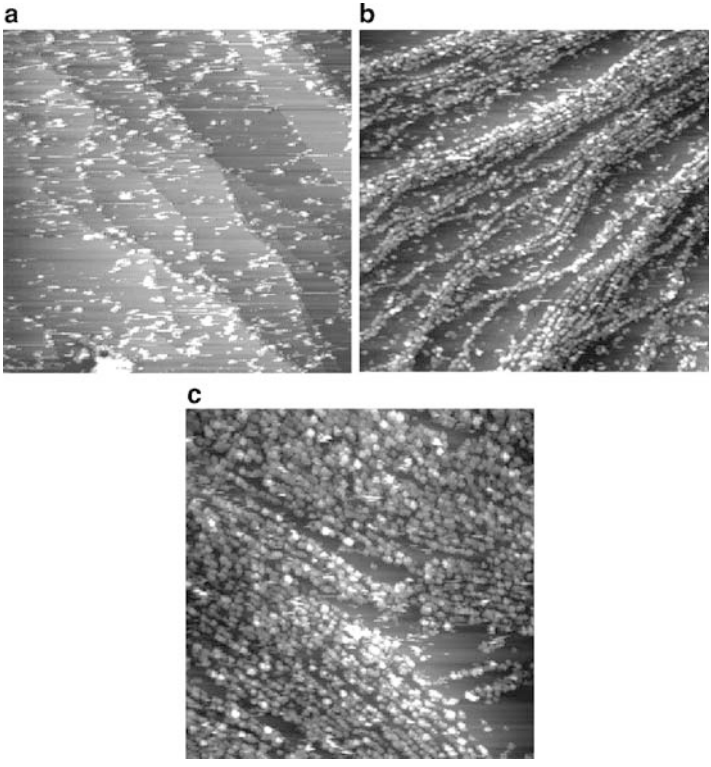

Figure 9. STM images of Ru-modified Au(111) recorded at 0.1 V in 0.5 M H_2SO_4 after Ru had been spontaneously deposited from 1 mM $RuCl_3$ in 0.1 M $HClO_4$ for: (**a**) 30 s (330 × 330 nm^2); (**b**) 3 min (360 × 360 nm^2); (**c**) 3 min (230 × 230 nm^2), obtained on a highly stepped area of the Au(111) surface. Reprinted from Ref. [16] with permission from Elsevier.

above), or by choosing an appropriate orientation of the Au surface. The stepped faces vicinal to the (111) orientation exhibited a higher activity for the spontaneous deposition of Ru than the flat Au(111) surface, as was indicated by the decoration of the vicinal steps which could also be found on the flat Au(111) surface, as illustrated in Fig. 9c.

On the smaller scale STM images (Fig. 10) the hexagonal shape of the Ru islands and their uniformity in size are clearly resolved. Moreover, the islands are regularly arranged one beside another

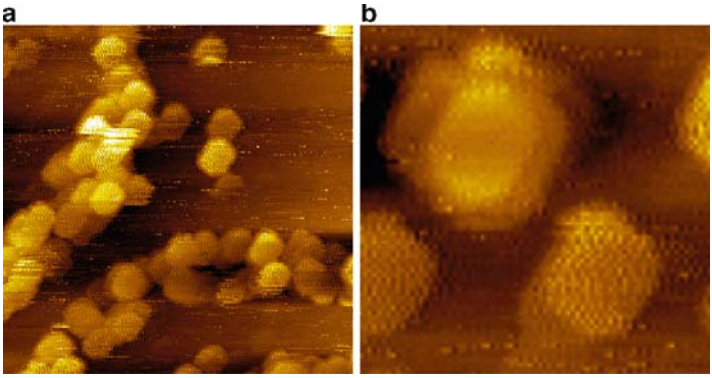

Figure 10. Smaller scale STM images of Ru/Au(111) from Fig. 9b: (**a**) $65 \times 65\ nm^2$; (**b**) $20 \times 20\ nm^2$. Reprinted from Ref. [16] with permission from Elsevier.

along the steps into arrays (Fig. 10a). Also, the formation of two distinguished arrays of Ru islands is noticed on some steps. The multilayer nature of the Ru islands is depicted in Fig. 10b, where the larger central island (10 nm) consists of six monolayers, while the bottom two islands (6 nm) consist of four monolayers.[16]

Evidently, the STM image provides details of the crystallographic nature of the cluster growth under multiple spontaneous deposition of ruthenium on gold. The image indicates that, with the deposition of Ru from perchloric acid solution, not only are the islands larger, but they consist of more layers. The lower saturation coverage with respect to the step coverage obtained when the spontaneous deposition was performed from sulfate solution alludes to the blocking effect of sulfate anions. It is assumed that sulfate anions form a shell around Ru^{3+} as well as around Ru^{4+} in solution, slowing down ruthenium deposition (see reactions 1 and 2).

V. SPONTANEOUS DEPOSITION OF Os ON Au(111)

Spontaneous deposition of Os on Au(111) was performed by exposure of a clean Au(111) electrode for a range of deposition times and concentrations of the Os-containing solution (0.01, 0.1, or 1 mM), $OsCl_3$ + 0.1 M H_2SO_4.[21] The CVs recorded in 0.1 M H_2SO_4, after the potential had been cycled several times from −0.20 to 0.50 V to

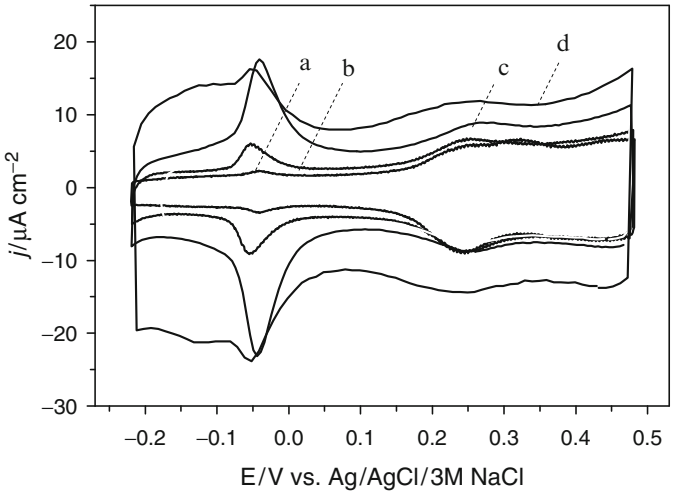

Figure 11. Cyclic voltammograms recorded in 0.1 M H_2SO_4 of an Au(111) surface after Os had been spontaneously deposited from 0.1 M H_2SO_4 containing: (**a**) 0.01 mM $OsCl_3$ for 1 min; (**b**) 0.1 mM $OsCl_3$ for 1 min; (**c**) 1 mM $OsCl_3$ for 5 min; (**d**) 1 mM $OsCl_3$ for 30 min. Reprinted with permission from Ref. [21] Copyright 2005 American Chemical Society.

reduce the adsorbed Os species of high valence to stable, metallic Os islands,[29] are presented in Fig. 11. The CVs show a clear increase in the area of the peaks at −40 mV and the double layer thickness with increasing amount of the Os deposit. Comparing the CVs in Fig. 11 with the CV of the initial Au(111) electrode (Fig. 1a), the peak at ca. 0.3 V is suppressed by the added Os. This shows that the electrochemically induced surface reconstruction was inhibited by the presence of the deposited Os.[16,37]

STM images of the same Os/Au(111) bimetallic surfaces recorded in 0.1 M H_2SO_4 after cycling the potential from −0.2 to 0.5 V are shown in Fig. 12. During the imaging, the electrode potential was held at −0.15 V in order to have metallic Os on the surface.[29] The STM images show that the Os coverage increased with increasing concentration of the Os deposition solution, and also with increasing deposition time. A slight step preference, indicative of heterogeneous nucleation, was observed at lower Os coverage (Fig. 12a,b). The deposition was faster and more homogeneous when

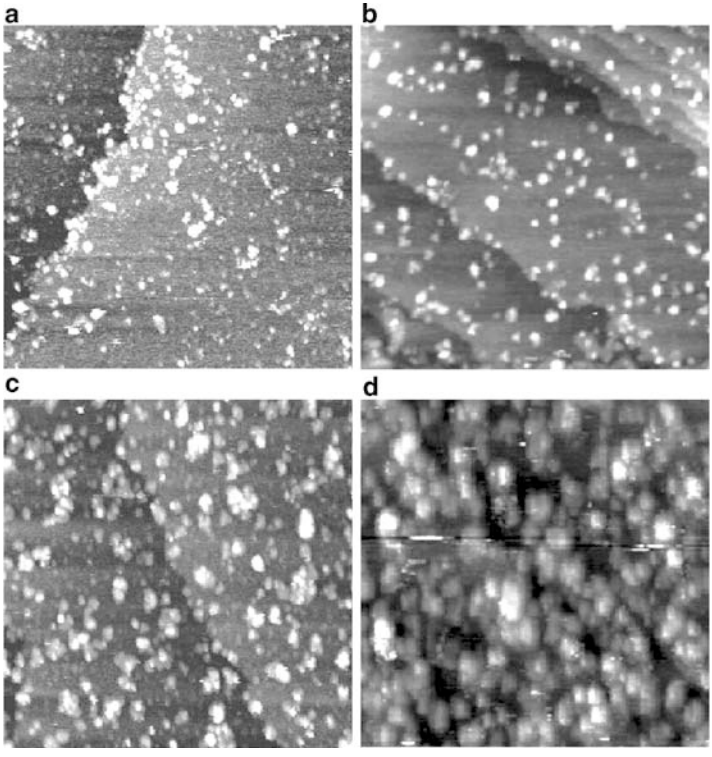

Figure 12. STM images ($80 \times 80\,nm^2$) of Os-modified Au(111) recorded in 0.1 M H_2SO_4 at −0.15 V after Os had been spontaneously deposited from 0.1 M H_2SO_4 containing: (**a**) 0.01 mM $OsCl_3$ for 1 min, coverage = 9 ± 2%; (**b**) 0.1 mM $OsCl_3$ for 1 min, coverage = 17 ± 3%; (**c**) 1 mM $OsCl_3$ for 5 min, coverage = 26 ± 5%; (**d**) 1 mM $OsCl_3$ for 30 min, coverage = 60 ± 7%. Reprinted with permission from Ref. [21] Copyright 2005 American Chemical Society.

the more concentrated Os-containing solution was used (Fig. 12c). The coverage was much higher after prolonged deposition, achieving saturation at 30 min (Fig. 12d).

The deposited Os islands were not uniform in size. As the Os solution concentration and the deposition time were increased, the widths and heights of the Os islands increased.[21] The range of island widths increased from 1 to 3 nm for 1-min deposition from 0.01 mM $OsCl_3$ solution up to 2–6 nm for 30-min deposition

from 1 mM $OsCl_3$ solution. While the surface of the lowest Os coverage (Fig. 12a) showed predominantly monolayer high islands (about 80%), about 50% of the islands on the other three surfaces had multiple layers (Fig. 12b–d). The three later surfaces showed similar distributions with respect to the height of the total Os deposit area: 70–75% of the total Os area had one Os layer, 20–25% had two Os layers, and more than 5% had 3–5 layers.

Once a certain coverage of high valency Os precursors from the Os solution was attained,[29] the electroreductive formation of Os islands from the precursors resulted in a relatively constant distribution of the surface area of the islands having different height ranges. Compared to Ru islands on Au(111) surface area (see Fig. 8), more of the Os islands had multiple layers. The Os islands are also very irregular compared to the flat, hexagonal shape of the Ru islands. Higher resolution STM images showing the structure of the Os islands in more detail are given below.

The cyclic voltammograms of Os/Au(111) prepared by 5-min Os deposition from a 1 mM $OsCl_3$ solution are presented in Fig. 13, which show Os oxidation/reduction and the subsequent gradual dissolution by extending the positive potential limit. The potential window was extended positively by intervals of 100 mV and three cycles

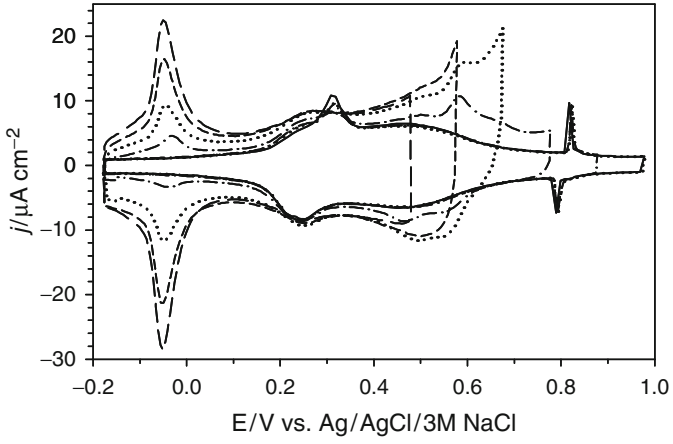

Figure 13. Gradual dissolution of Os from the Os/Au(111) surface shown in Fig. 12c by extending the positive potential limit. Reprinted with permission from Ref. [21] Copyright 2005 American Chemical Society.

up to each new potential were performed. The third cycle of each set is shown. The oxidation and dissolution of Os are evidenced by the rise in the current as the potential was swept positive by 0.5 V and the decrease in the size of the oxidation/reduction peak couple at −40 mV. A small peak at 0.5 V on the negative sweep indicates that the remaining, highly oxidized Os was reduced again. Os was being removed with each set of cycles and it was almost completely removed by sweeping to 0.9 V. The original CV of the Au(111) surface was then nearly restored.

STM images showing the structure of the same Os/Au(111) surface after the opening of the potential limit to various potentials are presented in Fig. 14. The images were taken at −0.15 V after three potential cycles from −0.2 V to the chosen positive potential limit and back. Cycling up to −0.5 V can be repeated without changing the island morphology.[21] After cycling to higher potentials, the STM images show the appearance of several 1–1.5 nm islands that are dispersed between the main island groupings (Fig. 14a). The deposit had reorganized during the Os oxidation and reduction and/or dissolution and redeposition processes, although the surface coverage remains similar at 28 ± 4%, due to the simultaneous, compensating effects of Os dissolution and the formation of smaller, one-layer-high islands at the expense of the taller islands. When the positive potential limit was increased to higher values, more significant structural changes of the Os deposit occurred (Fig. 14b). The overall Os coverage remained about the same at 28 ± 4%, but the island morphology was different. Although most of the islands were still 1–1.5 nm wide and one layer high, there were also several large 8–20-nm-wide islands. These islands had a smooth, one-layer-high base, on top of which were 2–4 layers high structures. The tallest spots (3–4 layers) accounted for only about 1–3% of the surface, whereas 80–90% of the total island area was now only one layer high due to the loss of Os. A possible explanation for the formation of the smooth domains is that the highly mobile Os species created by the oxidation process form larger Os islands at the expense of smaller Os islands by an Ostwald ripening mechanism.[51] Unfortunately, it was not possible to obtain STM images after the potential had been cycled to higher values, most likely due to the deposition of dissolved Os on the tip, which caused noise and decreased the tip quality.

STM images recorded on a smaller scale of $27 \times 27\ nm^2$, shown in Fig. 14c, d, enabled a closer examination of the structure and

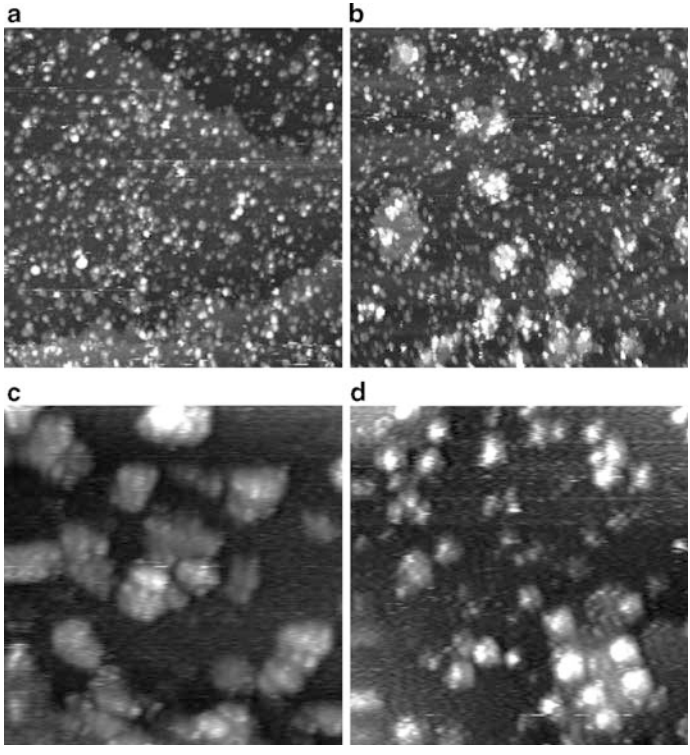

Figure 14. STM images of Os/Au(111) surfaces from Fig. 12c, showing the change in Os deposit morphology due to the opening of the positive potential limit. Potential was cycled from -0.2 V to: (**a**) 0.7 V ($100 \times 100\,nm^2$); (**b**) 0.75 V ($100 \times 100\,nm^2$); (**c**) 0.5 V ($27 \times 27\,nm^2$); (**d**) 0.75 V ($27 \times 27\,nm^2$). The sweep rate was 50 mV/s. Reprinted with permission from Ref. [21] Copyright 2005 American Chemical Society.

distribution of the islands over the Au(111) surface before and after oxidation/reduction cycles up to 0.75 V. Before the partial dissolution of Os, the islands were mostly 1–4 nm wide and many were grouped closely together. The image reveals that these Os islands were composed of even smaller parts that were about 1 nm wide. These Os islands were completely rearranged and partly dissolved by the oxidation/reduction cycles up to 0.75 V, as shown in Fig. 14d. The islands were less tightly clustered together and most of them were smaller, 1–1.5 nm wide. Smaller parts of width of about 1 nm

are again visible within the islands. These substructures are too large to be single Os atoms of 0.27 nm diameter and may represent ordered clusters of Os atoms.

VI. SPONTANEOUS DEPOSITION OF Ru ON Pt(111)

Cyclic voltammograms of the Ru/Pt(111) surfaces in 0.1 M H_2SO_4 solution are shown in Fig. 15. Spontaneous deposition of Ru on Pt(111) was performed from a ruthenium-containing solution (1 mM $RuCl_3$ in 0.1 M $HClO_4$) using the multiple deposition method.[17] For comparison, a typical CV profile of a clean Pt(111) surface in 0.1 M H_2SO_4 is presented (see the solid line in Fig. 15). The CV of Ru/Pt(111) obtained by 3-min Ru deposition is shown as the dotted line and the one obtained by two sequential 3-min depositions is shown by the dashed-dotted line. The characteristic "butterfly" feature[52] is suppressed after one deposition, indicating that obtaining a long-range ordered sulfate adlayer, demonstrated on Pt(111),[53,54] is no longer possible on the Ru/Pt(111) surface.[9,17] Additionally, the surface exhibited a noticeable increase in the double layer capacity.

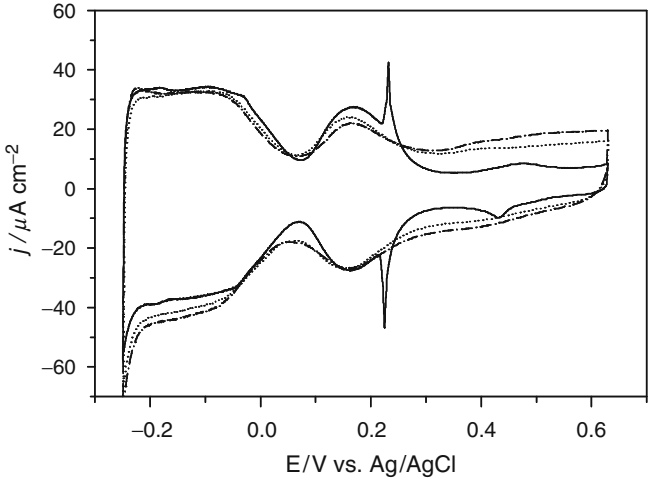

Figure 15. Cyclic voltammograms recorded in 0.1 M H_2SO_4 of the clean Pt(111) surface *(solid line)*, after 3 min of a single spontaneous Ru deposition *(dotted line)*, and after 2 × 3 min of multiple deposition *(dash-dot-dashed line)*. Reprinted from Ref. [9] with permission from Elsevier.

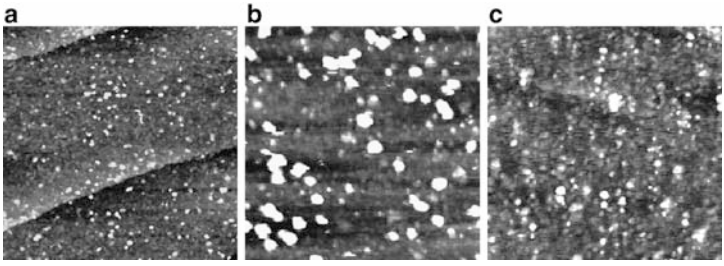

Figure 16. In situ STM images ($40 \times 40\,nm^2$) of Ru/Pt(111) surfaces recorded at 0.1 V in 0.5 M H_2SO_4, obtained by the spontaneous deposition of Ru from 1 mM $RuCl_3$ + 0.1 M $HClO_4$ for: (**a**) 3 min, coverage = 0.19 ML; (**b**) 2 × 3 min; (**c**) 2 × 3 min (recorded after a potential cycle from 0.1 to 0.7 V and back to 0.1 V), coverage = 0.25 ML. Reprinted from Ref. [9] with permission from Elsevier.

Representative STM images of the same Ru/Pt(111) surfaces obtained in 0.1 M H_2SO_4 under electrode potential control[9] are shown in Fig. 16. The in situ STM image obtained after the first deposition at the saturation coverage of 18 ± 3% revealed that ruthenium islands nucleate homogeneously over the Pt(111) surface (Fig. 16a). This is in agreement with the results of previous ex situ STM investigations of iodine-protected Pt(111)/Ru surfaces.[5,17] The average diameter of the mainly 2D Ru islands was in the range of 1–3 nm. Most of the islands have a monolayer height (76 ± 5%), but a clearly detectable amount of multilayer growth appeared as well. In contrast to the spontaneous deposition of ruthenium on Au(111), no preferential deposition along the Pt(111) steps was found. It seems therefore, that the diffusion of Ru adatoms over an Au(111) surface is much faster than over Pt(111), enabling the adatoms to diffuse towards and along the steps whereby the observed step decoration morphology is obtained. The hexagonal shape of the growing islands indicates that adatoms diffuse along atomic rows as well as along the edges of the growing Ru islands, i.e., that there is no preferential direction of diffusion.

After imaging the deposit obtained from the first deposition, the crystal was held at −0.1 V in H_2SO_4 for a short time to ensure that only metallic Ru was present. The H_2SO_4 solution was then replaced by a ruthenium-containing solution (1 mM $RuCl_3$ in 0.1 M $HClO_4$) at the OCP and a second deposition was performed for a further 3 min. The STM image of the resulting surface recorded at 0.1 V is

presented in Fig. 16b. The coverage now obtained was 22 ± 3%, and the size of the islands had increased vs. the data obtained during a single deposition, with most islands having a width between 2 and 5 nm. However, a significant increase in the average island height was observed. Only 50 ± 5% of the islands were now of monolayer height, while the remaining islands consisted of two to four monolayers. The data show a high preference for the ruthenium islands to predominantly form on top of the previously adsorbed islands, indicating the capability of ruthenium to spontaneously deposit on a ruthenium surface. Notice that the border sites of the formerly deposited Ru islands also acted as nucleation centers for the subsequent depositions, as some increase in the island size was observed.

Using the Pt(111) electrode covered by Ru via two spontaneous depositions, it was found that a major factor determining the size of the ruthenium islands was the ruthenium oxidation state, as the size depended on the electrode potential at which the STM imaging was performed.[9] An increase of the electrode potential led to an increase in the island lateral size and height. These new features may be attributed to the transformation of metallic Ru to Ru oxides.[28]

With a further increase of the electrode potential, disintegration of the Ru islands into smaller islands began.[9] Breaking of the Ru islands upon their oxidation becomes even more pronounced upon their subsequent reduction with the potential drive back to 0.1 V. On increasing the potential to 0.7 V, the originally oxidized and partially disintegrated islands become smaller in size and more dispersed upon their reduction with a potential drive back to 0.1 V (Fig. 16c). Namely, while the island width before the oxidation was 2–5 nm, it was now reduced to 1–2 nm. Simultaneously, the island density was higher, while the island height decreased (with 79 ± 5% of the islands displaying only a monolayer height). As a consequence, the Ru surface coverage increased to 25 ± 3%. It can be concluded that a significant change in surface morphology and an increase in the island dispersion were obtained after the redox sequence invoked from 0.1 to 0.7 V and back to 0.1 V.

VII. SPONTANEOUS DEPOSITION OF Os ON Pt(111)

The CV obtained after exposing a Pt(111) electrode to a 0.1 mM $OsCl_3$ + 0.1 M H_2SO_4 solution for 1 min is shown in Fig. 17. The feature at −75 mV on going in the negative direction is attributed to

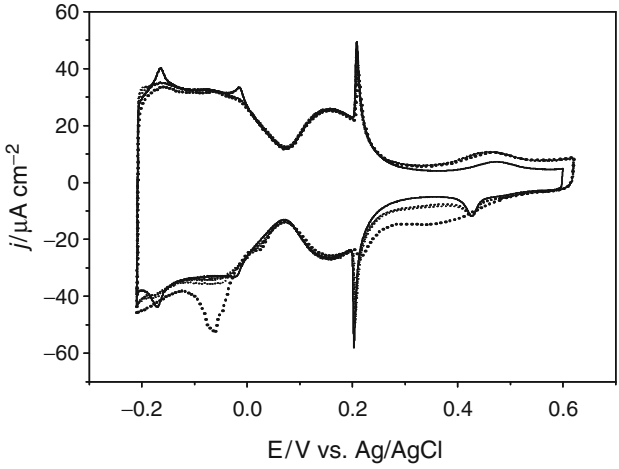

Figure 17. Cyclic voltammograms recorded in 0.1 M H_2SO_4 of a clean Pt(111) surface *(solid line)*, and after exposure of the electrode to a 0.1 mM $OsCl_3$ + 0.1 M H_2SO_4 solution for 1 min (*dotted lines*, four cycles). Reprinted from Ref. [9] with permission from Elsevier.

the reduction of Os oxides/hydroxides obtained during spontaneous deposition.[29] After several sweeps, a stable voltammogram was obtained; four cycles are shown by the dotted line in Fig. 17. The characteristic "butterfly" peak at 0.24 V was only slightly suppressed by Os deposition, although complete suppression can be obtained with a deposition from a 1 mM Os solution for 5 min.[19]

A single deposition was performed for 1 min from a 0.1 mM $OsCl_3$ + 0.1 M H_2SO_4 solution at the open circuit potential, after which the solution was changed to 0.1 M H_2SO_4. The potential was cycled several times from −0.2 to 0.6 V in order to stabilize the Os deposit, whereby a complete reduction of the osmium precursor to metallic Os was attained. An STM image was obtained at 0.1 V, at which potential the Os deposit is in its metallic state, as determined by XPS[29] (Fig. 18a). The total coverage obtained from the STM image was 22 ± 3%.

For 1-min deposition from 0.1 mM Os solution, only 39 ± 5% of the islands are one layer high, and there is a significant multilayer growth even up to 5 monolayer height.[19] In general, the tallest islands are the widest islands as well. One layer high islands typically

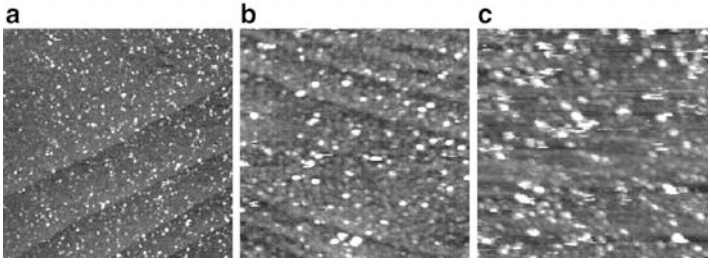

Figure 18. STM images of Os/Pt(111) recorded at 0.1 V in 0.1 M H_2SO_4 after Os had been spontaneously deposited from 0.1 M H_2SO_4 containing: (**a**) 10^{-4} M $OsCl_3$ solution for 1 min (150 × 150 nm^2); (**b**) 10^{-3} M $OsCl_3$ solution for 1 min (60 × 60 nm^2); (**c**) 10^{-3} M $OsCl_3$ solution for 5 min (65 × 65 nm^2). Reprinted with permission from Ref. [19] Copyright 2006 American Chemical Society.

are of only 1.5–2.5 nm width, whereas islands 2–4 layers high were 2.0–3.5 nm wide. The tallest islands (5 monolayer or higher) are even larger at 3.0–5.5 nm wide.

The image of Os/Pt(111) obtained after 1-min deposition from 1 mM Os solution is shown in Fig. 18b. Osmium covered a much larger area of 0.60 ± 0.08 ML. After a 5-min deposition from 1 mM Os solution, the area coverage of Os increased further to 0.7 ±0.1 ML, as shown in Fig. 18c. The island heights and the island widths showed little change as compared to imaging data in Fig. 18a, while the island density had increased, thus contributing to the overall increase in the coverage.

The deposition of Os on Pt(111) occurred much faster than that of Ru. Comparing the surfaces obtained under the deposition conditions of 1 min from a 0.1 mM Os solution and 3 min from a 1 mM Ru solution (see Fig. 16a), a similar Os coverage vs. the Ru coverage limit was attained even though the concentration of Os in the depositing solution was ten times lower than that of Ru and the deposition time was shorter. This was observed irrespective of the electrolyte composition or upon the change from perchloric to sulfuric acid medium.

The multilayer growth appeared more significantly with Os, with 61 ± 5% after only 1-min deposition from a 0.1 mM Os solution vs. only 24 ± 3% multilayer growth on Ru/Pt(111) after 1-min deposition from a 1 mM Ru solution. There was a wider distribution of the island width and height for a single deposition of Os

vs. a single deposition of Ru on Pt(111), and the islands were, on average, wider and taller. The islands were in fact more comparable to those obtained from two Ru depositions. Many of the larger Os islands were composed of smaller, rounded units of 1–2 nm width, whereas segmented growth was not pronounced for Ru. As with the Ru/Pt(111) surfaces, osmium was deposited homogeneously without any preference for the steps.

VIII. APPLICATIONS OF SELECTED BIMETALLIC SURFACES FOR THE ELECTROCATALYTIC PURPOSES

1. CO Oxidation on Ru/Au(111) Prepared by Electrochemical Ru Deposition

CO oxidation was studied on Ru decorated Au(111) electrodes in order to clarify the effect caused by the substrate and the electronic modification by nanosized Ru islands.[12–14,16] Since the Au(111) surface is inactive for CO adsorption or oxidation at potentials lower than 1.0 V,[15,55,56] the reaction on Ru/Au(111) was limited to the Ru nanoislands themselves. CO stripping voltammetry curves of Ru/Au(111) surfaces prepared by electrochemical Ru deposition, obtained after 5-min CO adsorption at −0.25 V and subsequent purging of the solution with argon,[12,16] are presented in Fig. 19.

CO stripping curves for an approximately 10-ML-thick Ru deposit (Fig. 19a) for a monolayer film at the saturation coverage of 0.85 ML (Fig. 19b) and for a submonolayer deposit with Ru coverage of 0.15 ML are shown to illustrate the effect of Ru coverage and morphology on the activity of Ru/Au(111) surfaces towards CO oxidation. The anodic sweeps recorded directly after CO adsorption (solid lines) exhibit pronounced stripping currents, while the second cycles (dotted lines) are, for all three deposits, the same as the baseline CVs obtained in a CO-free solution. This verifies that the electrolyte is free of CO and that the adsorbed CO was completely oxidized. On the multilayer deposit, a pronounced stripping peak exhibiting a maximum at 0.3 V was observed, which is in a very good agreement with CO stripping experiments on bulk Ru,[45] although a certain CO oxidation current also appeared at more positive potentials. On the Au(111) surface covered by a monolayer Ru deposit, only a broad current plateau was observed, while a particularly interesting

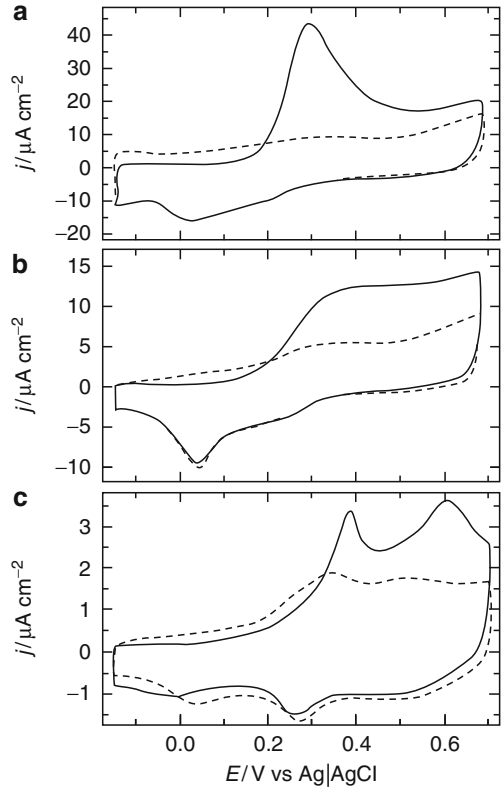

Figure 19. CO stripping voltammograms of Ru/Au(111) (*solid line*) and the baselines obtained on CO free surfaces (*dotted line*) obtained in 0.1 M H_2SO_4 for: (**a**) a multilayer deposit; (**b**) a saturated monolayer (0.85 ML coverage); (**c**) a submonolayer deposit (0.15 ML coverage). Reprinted from Ref. [12] with permission from Elsevier.

behavior was found for the Ru/Au(111) with a 0.15 ML Ru coverage, which consisted of well-separated Ru islands. In the last case (Fig. 19c) two CO stripping peaks were resolved, which were centered at 0.38 and 0.60 V, respectively, at significantly more positive potentials than the stripping peak on bulk Ru.

To explain the quite complex CO stripping behavior, various aspects have to be taken into consideration, including: the adsorption

of oxygen species, the CO adsorption geometry, and the effect of the Au(111) substrate. At potentials coinciding with CO oxidation, the increase of the double layer current in the base CVs suggests that this current is associated with O or OH adsorption,[4,57] i.e., with a partial oxidation of the deposited Ru islands, which increased with increasing potential[28] (as described above). In addition, the process depends strongly on the CO adsorption energy, i.e., on the CO adsorption sites. The existence of different CO adsorption sites on the Ru-decorated Au(111) surfaces is apparent from the STM images presented above. For a submonolayer Ru coverage, the deposit consisted of well-separated Ru monolayer nanoislands, which gives rise to the two types of adsorption sites, i.e., on top of the Ru islands and at Ru/Au edges. A stronger CO adsorption on the step sites, as was observed for CO on the other metal surfaces,[58,59] would explain two distinct stripping peaks in Fig. 19c. At higher coverage, the Ru islands start to merge (see Fig. 4c), resulting in a highly defective Ru adlayer that exhibits various other types of adsorption sites. As a consequence, a broad plateau in the CO stripping curves appeared. The positive shift of the CO stripping on Au(111) decorated by a submonolayer to a monolayer of Ru nanoislands as compared to a Ru multilayer or bulk Ru suggests a stronger binding of CO to Ru nanoislands on the Au(111) substrate. This is similar to previous findings for CO adsorption on expanded monolayer films under ultrahigh vacuum conditions.[60] This effect was explained by strain-induced electronic modifications of the Ru film, which resulted in an increase of the CO adsorption energy and, consequently, in a higher oxidation potential.

2. CO Oxidation on Ru/Au(111) Prepared by Spontaneous Ru Deposition

The CO stripping voltammetry for Ru/Au(111) prepared by 3-min spontaneous deposition from 1 mM $RuCl_3$ in 0.1 M $HClO_4$ is depicted in Fig. 20. The CO stripping is shown as a solid line, whereas the second sweep, which is shown as a dotted line, indicates the complete removal of CO from the solution and represents CV of the Ru/Au(111) surface in 0.5 M H_2SO_4 (see also Fig. 1a).

The observed CO stripping currents from Ru/Au(111) surfaces are attributed to partially oxidized Ru islands,[9] as in the above-described case of Ru/Au(111) surfaces obtained by electrochemical deposition. Two main peaks associated with CO stripping were

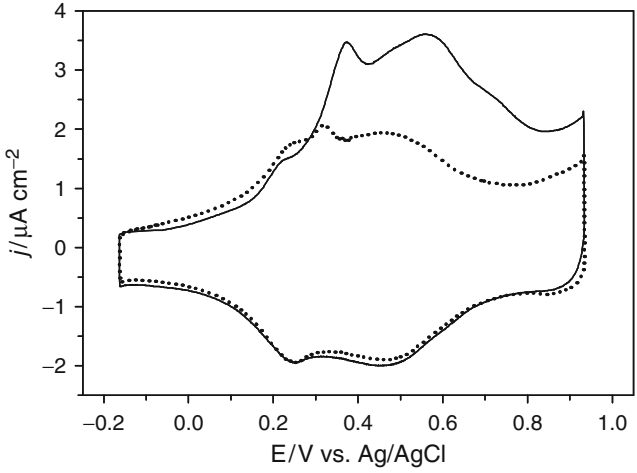

Figure 20. Cyclic voltammetry of Ru/Au(111) in 0.1 M H_2SO_4 after Ru had been spontaneously deposited from 1 mM $RuCl_3$ in 0.1 M $HClO_4$ for 3 min (*dotted line*) and CO stripping voltammogram of the same surface, obtained after 5-min CO adsorption at −0.25 V and subsequent purging of the solution with argon (*solid line*). Reprinted from Ref. [9] with permission from Elsevier.

observed at 0.37 and 0.56 V. The peak positions were significantly more positive than the single peak at 0.30 V for CO oxidation on bulk Ru[45] or on thick electrodeposited Ru layers on Au(111).[12] As in the case of electrodeposited Ru adatoms, the shift indicates a stronger bond between CO and Ru due to the pseudomorphic expansion of the Ru lattice relative to bulk Ru. The two peaks observed for CO oxidation on Ru/Au(111) produced by spontaneous 3-min deposition were attributed to the presence of two different types of Ru sites, most likely sites on top of the islands and sites on the island edges.

3. Formaldehyde Oxidation on Ru/Au(111) Prepared by Spontaneous Ru Deposition

It was recently reported[31] that deposited Ru islands play a significant role in promoting the electrocatalytic activity of Au(111) towards formaldehyde oxidation in sulfuric acid media. Cyclic voltammograms of the electrochemical oxidation of formaldehyde on Au(111)

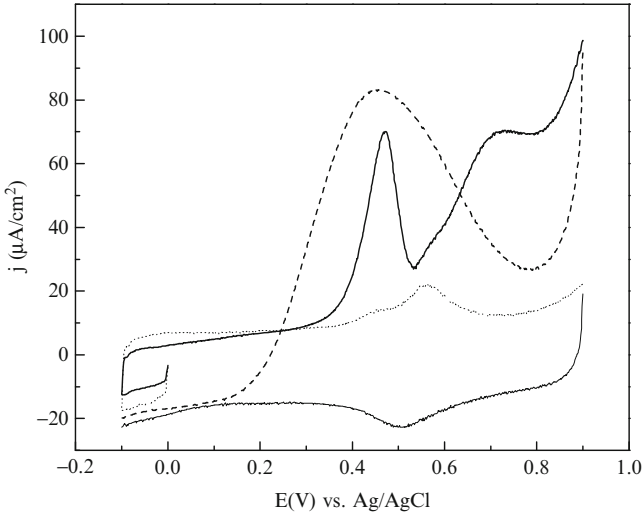

Figure 21. Oxidation of formaldehyde on Ru/Au(111) in 0.5 M H_2SO_4 containing 0.25 M HCHO; the first sweep in the anodic direction (*solid line*); the reverse sweep (*dashed line*); cyclic voltammetry of the Ru/Au(111) bimetallic surface in 0.5 M H_2SO_4 (*dotted line*). The sweep rate was 50 mV/s. Reprinted from Ref. [31] with permission from Elsevier.

modified by 3-min spontaneous Ru deposition from 1 mM $RuCl_3$ + 0.1 M $HClO_4$, recorded in 0.5 M H_2SO_4 solution containing 0.25 M HCHO, are presented in Fig. 21. The anodic sweep is presented by a solid line, while the reverse sweep is presented by a dashed line. For comparison, the CV of the Ru/Au(111) surface in pure 0.5 M H_2SO_4 solution is presented by a dotted line.

There was no HCHO oxidation on the Ru/Au(111) electrode up to a potential of 0.25 V. Starting from a potential of 0.25 V, the reaction occurred with increasing current up to a potential of 0.55 V, showing a peak with a maximum current density of 0.07 mA/cm^2 at a potential of 0.43 V. At higher potentials, as well as in the reverse sweep, the HCHO oxidation occurred following the same path as on the pure Au(111) surface, although with smaller currents, most likely due to the inhibiting effect of the present oxidized Ru species.

For comparison, the anodic sweeps of HCHO oxidation on Ru/Au(111) (from Fig. 21) and on pure Au(111) in the same solution are presented in Fig. 22 by a solid line and by a dotted line, respectively.

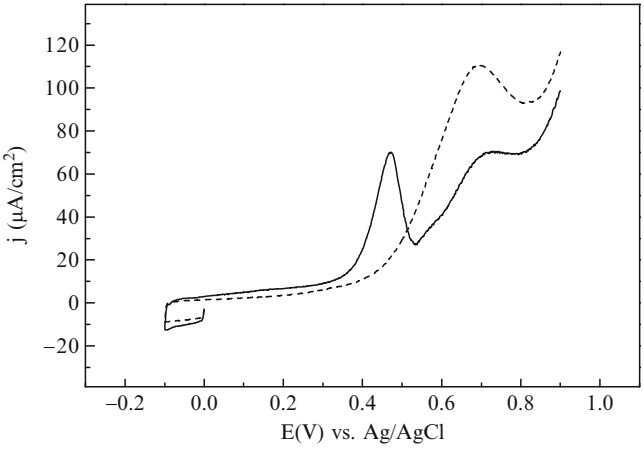

Figure 22. Oxidation of formaldehyde on Ru/Au(111) (*solid line*) and pure Au(111) (*dashed line*) in 0.5 M H_2SO_4 containing 0.25 M HCHO; the first sweep in the anodic direction is presented. The sweep rate was 50 mV/s. Reprinted from Ref. [31] with permission from Elsevier.

The oxidation of HCHO on Ru/Au(111) commenced at a 0.1 V more negative potential than on pure Au(111). The increased anodic activity of the Ru/Au(111) surface in the potential region from 0.25 to 0.55 V is, most likely, associated with the oxidation of some adsorbed intermediates assisted by the presence of Ru. In this potential range, the Ru deposit consisted mainly of metallic Ru together with Ru species partially oxidized to RuO_2, the amount of which increases with increasing potential.[4,28] It is assumed that the presence of chemisorbed water on metallic Ru[28] facilitates the oxidation of some adsorbed intermediates at lower potentials compared to Au(111), giving rise to the prepeak at approximately 0.43 V. This intermediate might be CO adsorbed on the Ru/Au edge sites (as the CO oxidation occurs in the same potential range on Ru/Au(111) as illustrated above). At potentials higher than 0.43 V, the fraction of metallic Ru decreased, while the fraction of RuO_2 prevailed. On increasing the potential further, the presence of Ru in higher oxidation states, such as RuO_2 and RuO_3,[28] caused a partial inhibition of HCHO oxidation. This also coincides with the inactivity of Ru/Au(111) for CO oxidation at higher potentials.

4. CO Oxidation on Os/Au(111) Prepared by Spontaneous Os Deposition

CO stripping measurements on an Os/Au(111) electrode surface prepared by spontaneous Os deposition for 5 min from a 1 mM $OsCl_3$ + 0.1 M H_2SO_4 solution[22] did not show a distinct CO stripping peak, but rather a broad stripping region from 0.05 to 0.70 V as shown in Fig. 23. The CO stripping peak overlapped the Os stripping peak to some extent, so the difference between the two stripping curves was taken as the CO charge. The CO stripping charge of ca. 70 $\mu C/cm^2$ corresponds to about 50% CO coverage of the Os islands, which covered 26 ± 5% of the Au(111) substrate. From the catalytic perspective, the Os deposits showed very small activity to CO oxidation and they sustained very low rates of methanol electrooxidation.

5. CO Oxidation on Ru/Pt(111) Prepared by Spontaneous Ru Deposition

CO stripping voltammetry measurements were performed using Ru/Pt(111), prepared by spontaneous Ru deposition. A typical CV curve for CO stripping on Ru/Pt(111), showing a clear split in the

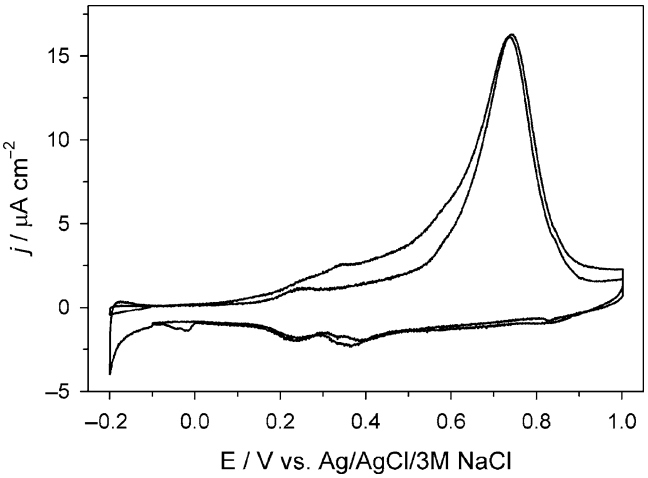

Figure 23. CO stripping curve for Os/Au(111) obtained by a 5-min spontaneous deposition from a 1 mM Os solution. Sweep 2 shows the removal of CO by oxidation, while sweep 1 shows the CO-free surface.

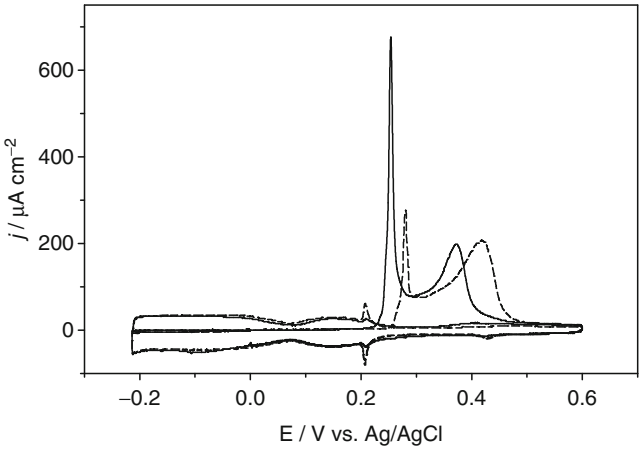

Figure 24. CO stripping from a Ru/Pt(111) surface in 0.1 M H_2SO_4 prepared by a 2-min spontaneous deposition from a 1 mM $RuCl_3$ + 0.1 M $HClO_4$ solution, with (*solid line*) and without (*dashed line*) the stabilization of the Ru deposit by three voltammetric cycles between −0.2 and 0.6 V before CO dosing. The sweep rate was 50 mV/s. Reprinted from Ref. [9] with permission from Elsevier.

CO stripping profile, is presented in Fig. 24. It is well known that the first CO oxidation peak on Ru/Pt(111) originates from CO oxidation on the Ru adislands.[61] Indeed, previous XPS results demonstrated that Ru showed oxide formation already at 0.12 V.[28]

CO is also a good probe to test the stability[62,63] of the Ru deposits before undergoing the electrochemical stabilization–reduction cycles. Such a behavior is of interest in order to enhance the understanding of the spontaneous deposition reaction per se. Thus, Ru/Pt(111) was first obtained after a single Ru spontaneous deposition and successive voltammetric stabilization–reduction of the Ru deposit.

The solid line in Fig. 24 shows the CO stripping reaction from this surface. Subsequently, the experiment was restarted, and a new Pt(111) surface was exposed to the Ru-containing solution, rinsed, and transferred to the electrochemical cell. Such a freshly prepared Ru/Au(111) electrode was exposed to CO without electrochemical stabilization of the deposit. The dashed line in Fig. 24 shows the CO oxidation features obtained from this procedure. The data clearly indicate that most of the freshly prepared Ru precursor was

displaced from the electrode by CO chemisorption, similar to the CO displacement of some underpotentially deposited, apparently unstable metals.[63,64] This gives additional credit to the idea that electrochemical stabilization is an essential step in the utilization of spontaneous deposition for the preparation of stable bimetallic Ru/Pt electrodes. In addition, assuming that CO is displacing, but not reacting with the Ru precursors, the data showed that the amount of metallic ruthenium in the deposit was very low, as only loosely bound surface complexes of ruthenium[4] can be displaced by CO. It conclusively documents that the main mechanism of the formation of the deposit precursor is the one involving chemisorption rather than the disproportionate reaction.[4]

Comparison of the data of CO stripping from Ru/Au(111) (Figs. 19 and 20) with that from Ru/Pt(111) (Fig. 24) demonstrates an interesting feature. Namely, the CO stripping peak from Ru/Pt(111) at 0.23 V, which was previously attributed to the oxidation of CO at Ru sites and adjacent Pt sites, is negatively shifted with respect to bulk Ru,[45] by ca. 0.30 V, in contrast to the positive shift observed for Ru/Au(111). As noted above, the Au(111) substrate seems to increase the strength of the Ru–CO bond,[61] whereas modification of Ru by the Pt(111) substrate appears to weaken the Ru–CO bond.

6. Methanol Oxidation on Pt(111) Modified by Spontaneously Deposited Ru

The increase in the island dispersion, as it increases the ruthenium coverage, removes platinum sites that were present on the bimetallic surface before the experiment reported above was executed. In other words, the number of "ensembles" of Pt sites available,[65,66] e.g., for chemisorption on the Pt sites of the Pt(111)/Ru surface was reduced. A typical case where this development is important is the process of dissociative chemisorption of methanol, as it requires as many as three adjacent sites for methanol dissociation (dehydrogenation) to chemisorbed CO[65–67] As methanol oxidation to CO_2 predominantly occurs via the CO formation process,[67,68] the overall rate of methanol oxidation may be affected by an increase in ruthenium coverage at the expense of the number of collective Pt sites required for methanol decomposition to CO.[65,66]

Chronoamperometric measurements in a methanol-containing solution (0.6 M CH_3OH + 0.1 M H_2SO_4 solution) were performed

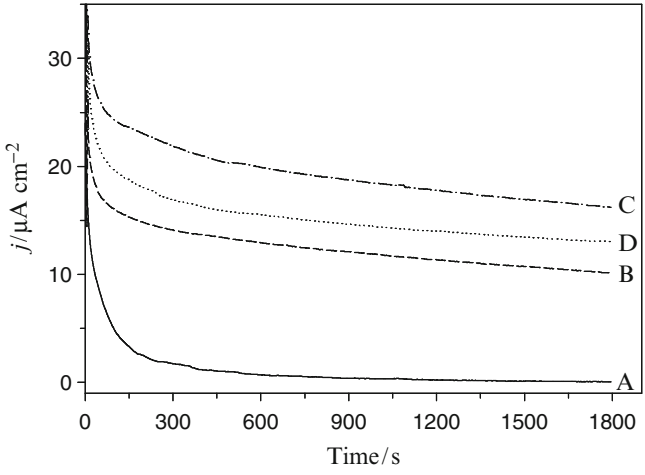

Figure 25. Current–time transient curves for: (**a**) clean Pt(111); (**b**) modified by 3 min of Ru deposition; (**c**) 2 × 3 min Ru deposition before methanol oxidation; (**d**) 2 × 3 min Ru deposition, but the potential was increased to 0.7 V and subsequently returned to 0.1 V. The current–time transient curves were recorded at 0.16 V in 0.6 M CH_3OH + 0.1 M H_2SO_4. Reprinted from Ref. [9] with permission from Elsevier.

at a constant electrode potential using several Ru/Pt(111) surfaces prepared as described above. The electrode was immersed in the solution at −0.1 V for 1 min to ensure that the Ru deposit was initially metallic and that the decomposition of methanol was very slow.[69] Current–time decays were then collected at 0.16 V, which are representative of the kinetics of methanol oxidation at this electrode potential.[69]

Four chronoamperometric methanol oxidation curves are displayed in Fig. 25. Curve A was obtained with clean Pt(111), i.e., with no ruthenium on the surface. The low current at the end of the decay (after 30 min)[68] is due to Pt site blocking by adsorbed CO from methanol dehydrogenation.[67] The Ru/Pt(111) surface obtained after the first Ru deposition with 18 ± 3% ruthenium coverage (see Fig. 16a) exhibited a much higher methanol oxidation current (curve B), showing the large catalytic enhancement of the Ru/Pt(111) electrode in comparison to clean Pt(111). The current measured for the Ru/Pt(111) surface obtained after two consecutive Ru depositions (see Fig. 16b) was 1.6 times higher than that obtained after

the single spontaneous deposition (curve C). However, after the surface had been perturbed by oxidizing the Ru islands at 0.70 V and subsequently reducing them again at 0.1 V (see Fig. 16c), the methanol oxidation current decreased to 1.3 times that measured after the first Ru deposition, as shown in curve D. This conforms well to the bifunctional methanol oxidation mechanism[70] that optimization requires an appropriate balance of the Pt and Ru sites on the surface.[65–67,69]

7. CO Oxidation on Os/Pt(111) Prepared by Spontaneous Os Deposition

CV curve for CO stripping from Os/Pt(111) is shown in Fig. 26. As in the case of CO stripping from Ru/Pt(111), a clear split in the CO stripping profile was observed, although the separation was less pronounced, and the threshold for CO oxidation shifted by 70 mV in the positive potential direction. The shift in the CO oxidation threshold is indicative of Os/Pt(111) being less active in CO oxidation and generally in the oxidation of organic molecules that proceed via a pathway involving surface CO as an intermediate. This can be linked to

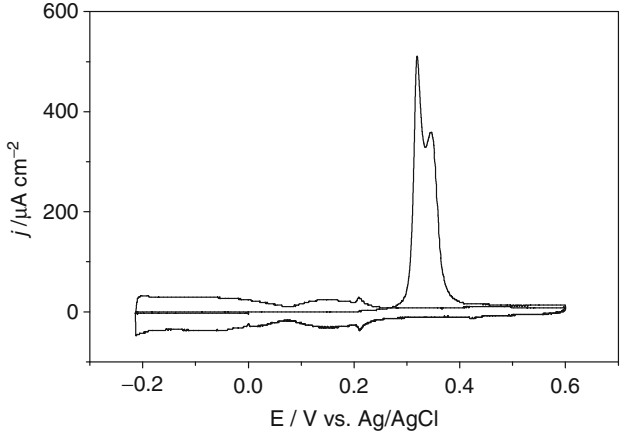

Figure 26. CO stripping from an Os/Pt(111) surface in 0.1 M H_2SO_4, prepared by 30-s Os deposition from 0.5 mM $OsCl_3$ + 0.1 M $HClO_4$. The sweep rate was 50 mV/s. Reprinted from Ref. [9] with permission from Elsevier.

the difference in the oxophilicity of the two metals and their relative ability to provide oxygen-containing species for CO oxidation.

XPS results demonstrated that Os is less oxophilic than Ru on Pt(111): Os is entirely metallic at potentials lower than 0.31 V, whereas Ru shows oxide formation already at 0.12 V.[28] This is in accordance with the expectation based on the work function or electronegativity difference between Os and Ru.

The oxophilicity difference between Ru and Os may also account for the observed better performance of Ru/Pt(111) for methanol oxidation at potentials below 0.21 V.[71,72] However, the Os/Pt(111) system is more active for methanol oxidation than Ru/Pt(111) at higher potentials.[19]

IX. CONCLUSIONS

We have presented an overview of our results that marked the progress made in the development of model bimetallic electrocatalysts for a possible application in syntheses of fuel cell catalysts. Our research effort over a decade was focused on monitoring the processes of the nucleation and growth of a foreign metal on single crystal substrates by means of in situ STM, during electrochemical and spontaneous deposition. The understanding of these processes enabled us to tailor bimetallic surfaces of desired well-defined structure and composition. This finally led us to achieving the ultimate goal, namely to establishing a direct correlation between surface structure and its electrocatalytic activity for the reactions relevant for fuel cells.

We have found that the structure of bimetallic surfaces, where foreign metal nanoislands are deposited on a single crystal substrate at submonolayer coverage, depends on the deposition procedure. That was particularly well illustrated on the Ru/Au(111) system for which both electrochemical and spontaneous deposition methods were used. It was shown that, during electrochemical Ru deposition, metallic Ru islands were obtained at potentials lower than the Nernst potential, while at higher potentials mixed Ru oxides were formed. A variety of structures, including the long-range ordered Ru structures, were obtained by controlling the structure of the substrate, and by the electrode potential. One-layer-high Ru islands were obtained up to a full coverage of Ru on the substrate. The Ru islands were found uniform in size in all cases examined. Since the reaction took

place in a wide potential region, it was not possible to establish a proper control of the reaction progress over time. On the other hand, during spontaneous deposition, the saturation coverage for a particular concentration of the depositing species was achieved, which enabled the satisfactory deposition time control. Since the deposition occurs at an open circuit potential, mixed Ru/Ru oxide islands were formed on the Au(111) surface. Additional stabilization of the deposit on the surface was achieved by potential cycling. As the deposited Ru prevented Au(111) surface reconstruction, the structure of the underlying Au(111) surface remained the same and independent of the potential as long as it was kept lower than the Au(111) oxidation potential. Step decoration was observed on Au(111) by deposited multilayer high Ru islands mostly uniform in size. We have also shown that, to a certain extent, the surface structure depends on the carrying electrolyte–ion effect. The same applies for Os spontaneously deposited on the Au(111), although the deposition proceeds faster and gives rise to the large variation of island sizes and to higher number of taller islands. Spontaneous deposition method was also explored for the deposition of Ru and Os on the Pt(111) single crystal. Both have shown a homogeneous deposition, with no specific step decoration. The increase of the Pt(111) surface coverage by the deposit was successfully achieved utilizing a multiple deposition method. Compared to Ru/Pt(111), however, Os was deposited on Pt(111) at a much higher rate and it formed predominantly multilayer islands within only a single deposition. These structural examinations contributed significantly to the understanding of the role of deposited nanoislands in the electrocatalytic activity of bimetallic electrodes. The exceptional activity of Ru/Pt(111) and Os/Pt(111) electrodes for CO and methanol oxidation as well as the activity of Ru/Au(111) for formaldehyde oxidation has been directly related to the coverage, size and distribution of the deposited nanoislands over the electrode surface.

In terms of the catalytic aspects of this review, we have found that the oxidation state of the deposited nanoislands, as precisely determined by separate XPS measurements and observed by in situ STM imaging, contributed significantly to the overall activity of examined bimetallic surfaces. For instance, it was found that Ru nanoislands showed oxide formation at lower potentials than Os nanoislands. Therefore, we conclude that the oxophilicity difference between Ru and Os may account for the observed better performance

of Ru/Pt(111) for methanol oxidation at nearly 0.2 V. Overall, we believe that our investigations have contributed to the understanding of the principles of reactivity at single crystal electrodes modified by metal nanoislands, adding to the progress in heterogeneous catalysis research.

ACKNOWLEDGMENTS

Svetlana Strbac acknowledges support by the Ministry of Science of the Republic of Serbia (project 06-141001). Andrzej Wieckowski acknowledges support by the National Science Foundation (grant NSF CHE06-51083).

REFERENCES

[1]Herrero, K. Franaszczuk, and A. Wieckowski, *J. Electroanal. Chem*. **361** (1993) 269.
[2]K. A. Friedrich, K. P. Geyzers, U. Stimming, and R. Vogel, *Z. Phys. Chem*. **208** (1999) 137.
[3]W. Chrzanowski, H. Kim, and A. Wieckowski, *Catal. Lett*. **50** (1998) 69.
[4]W. Chrzanowski and A. Wieckowski, *Langmuir* **13** (1997) 5974.
[5]E. Herrero, J. M. Feliu, and A. Wieckowski, *Langmuir* **15** (1999) 4944.
[6]A. Crown and A. Wieckowski, *Phys. Chem. Chem. Phys*. **3** (2001) 3290.
[7]A. Crown, I. R. Moraes, and A. Wieckowski, *J. Electroanal. Chem*. **500** (2001) 333.
[8]V. D. Colle, M. J. Giz, and G. Tremiliosi-Filho, *J. Braz. Chem. Soc*. **14** (2003) 601.
[9]S. Strbac, C. M. Johnston, G. Q. Lu, A. Crown, and A. Wieckowski, *Surf. Sci*. **573** (2004) 80.
[10]F. Maillard, G.-Q. Lu, A. Wieckowski, and A. Stimming, *J. Phys. Chem. B* **109** (2005) 16230.
[11]S. Strbac, O. M. Magnussen, and R. J. Behm, *Phys. Rev. Lett*. **83** (1999) 3246.
[12]S. Strbac, F. Maroun, O. M. Magnussen, and R. J. Behm, *J. Electroanal. Chem*. **500** (2001) 479.
[13]S. Strbac, O. M. Magnussen, and R. J. Behm, *J. Serb. Chem. Soc*. **66** (2001) 119.
[14]S. Strbac, O. M. Magnussen, and R. J. Behm, *J. Serb. Chem. Soc*. **66** (2001) 281.
[15]S. C. Chiang, A. Hamelin, and M. J. Weaver, *J. Phys. Chem*. **95** (1991) 5560.
[16]S. Strbac, R. J. Behm, A. Crown, and A. Wieckowski, *Surf. Sci*. **517** (2002) 207.
[17]A. Crown, C. M. Johnston, and A. Wieckowski, *Surf. Sci*. **506** (2002) L268.
[18]V. Pacheco Santos, V. Del Colle, R. M. Bazerra, and G. Tremiliosi-Filho, *Electrochim. Acta* **49** (2004) 1221.
[19]C. M. Johnston, S. Strbac, A. Lewera, E. Sibert, and A. Wieckowski, *Langmuir* **22** (2006) 8229.
[20]B. Ku, C. Jung, and C. K. Rhee, *J. Phys. Chem. B* **110** (2006) 13425.
[21]C. M. Johnston, S. Strbac, and A. Wieckowski, *Langmuir* **21** (2005) 9610.
[22]S. Strbac, C. M. Johnston, and A. Wieckowski, Russ. *J. Electrochem*. **42** (2006) 1244.

[23]S. Strbac, S. Petrovic, R. Vasilic, J. Kovac, A. Zalar, and Z. Rakocevic, *Electrochim. Acta* **53** (2007) 998.
[24]J. Kim, C. Jung, C. K. Rhee, and T-H. Lim, *Langmur* **23** (2007) 10831.
[25]L. A. Meier, D. R. Salinas, J. M. Feliu, and S. G. Garcia, *Electrochem. Commun*. **10** (2008) 1583.
[26]S. R. Brankovic, J. McBreen, and R. R. Adzic, J. *Electroanal. Chem*. **503** (2001) 99.
[27]S. R. Brankovic, J. McBreen, and R. R. Adzic, *Surf. Sci*. **479** (2001) L363.
[28]H. Kim, I. Rabelo de Moraes, G. Tremiliosi-Filho, R. Haasch, and A. Wieckowski, *Surf. Sci*. **474** (2001) L203.
[29]C. K. Rhee, M. Wakisaka, Y. V. Tolmachev, C. M. Johnston, R. Haasch, K. Attenkofer, G. Q. Lu, H. You, and A. Wieckowski, *J. Electroanal. Chem*. **554–555** (2003) 367.
[30]S. Manandhar and J. A. Kelber, *Electrochim. Acta* **52** (2007) 5010.
[31]S. Strbac and M. Avramov Ivic, *Electrochim. Acta* **54** (2009) 5408.
[32]K. Itaya, Prog. *Surf. Sci*. **58** (1998) 232.
[33]A. A. Gewirth and B. K. Niece, *Chem. Rev*. **97** (1997) 1129.
[34]O. M. Magnussen, *Chem. Rev*. **102** (2002) 679.
[35]S. Strbac, R. R. Adzic, and A. Hamelin, *J. Electroanal. Chem. Interfacial Electrochem*. **249** (1988) 291.
[36]D. A. Scherson and D. M. Kolb, *J. Electroanal. Chem. Interfacial Electrochem*. **176** (1984) 353.
[37]A. S. Dakkouri and D. M. Kolb, in *Interfacial Electrochemistry: Experimental, Theory and Applications*, Ed. by A. Wieckowski, Marcel Dekker, New York (1999) 151.
[38]O. M. Magnussen, J. Hagebock, J. Hotlos, and R. J. Behm, *Faraday Discuss*. **94** (1992) 329.
[39]J. Clavilier, in I*nterfacial Electrochemistry: Experimental, Theory and Applications*, Ed. by A. Wieckowski, Marcel Dekker, New York (1999) 231.
[40]D. Zurawski, L. Rice, M. Hourani, and A. Wieckowski, *J. Electroanal. Chem*. **230** (1987) 221.
[41]A. T. Hubbard, *Chem. Rev*. **88** (1988) 633.
[42]B. Love and J. Lipkowski, in *Electrochemical Surface Science; Molecular Phenomena at Electrode Surfaces*, Vol. 378, Ed. by M. P. Soriaga, ACS Symposium Series, Washington, DC (1988) 484.
[43]D. Zurawski, M. Wasberg, and A. Wieckowski, *J. Phys. Chem*. **94** (1990) 2076.
[44]N. M. Markovic, C. A. Lucas, A. Rodes, V. Stamenkovic, and P. N. Ross, *Surf. Sci*. **499** (2002) L149.
[45]H. Gasteiger, N. M. Marković, and P. N. Ross Jr., *J. Phys. Chem*. **99** (1995) 8290.
[46]N. S. Marinkovic, J. X. Wang, H. Zajonz, and R. R. Adzic, *Electrochem. Solid State Lett*. **3** (2000) 508.
[47]S. Szabo and I. Bakos, *J. Electroanal. Chem*. **230** (1987) 233.
[48]S. Szabo, I. Bakos, and F. Nagy, *J. Electroanal. Chem*. **271** (1989) 269.
[49]K. A. Friedrich, K.-P. Geyzers, U. Stimming, J. Stumper, and R. Vogel, *J. Phys. Chem*. **208** (1998) 137.
[50]F. Maroun, S. Morin, A. Lachenwitzer, O. M. Magnussen, and R. J. Behm, *Surf. Sci*. **460** (2000) 249.
[51]J. A. Venables, *Introduction to Surfaces and Thin Film Processes*, Cambridge University Press, Cambridge, UK (2000).
[52]J. Clavillier, *J. Electroanal. Chem*. **107** (2002) 211.
[53]A. M. Funtikov, U. Stimming, and R. Vogel, *J. Electroanal. Chem*. **428** (1997) 147.
[54]A. M. Funtikov, U. Linke, U. Stimming, and R. Vogel, *Surf. Sci*. 324 (1995) L 343.
[55]M. W. Hsiao, R. R. Adzic, and E. Yeager, *Electrochim. Acta* **37** (1992) 357.

[56]R. R. Adzic, J. X. Wang, O. M. Magnussen, and B. M. Ocko, *Langmuir* **12** (1996) 513.
[57]W. F. Lin, M. S. Zei, Y. D. Kim, H. Over, and G. Ertl, *J. Phys. Chem. B* **104** (2000) 6040.
[58]M. Ruff, S. Frey, B. Gleich, and R. J. Behm, *Appl. Phys. A* **66** (1998) S513.
[59]B. Hamer, O. H. Nielsen, and J. K. Norskov, *Catal. Lett*. **46** (1997) 31.
[60]J. A. Rodriges, *Surf. Sci. Rep*. **24** (1996) 223.
[61]G. Q. Lu, P. Waszczuk, and A. Wieckowski, *J. Electroanal. Chem*. **532** (2002) 49.
[62]B. Hammer, Y. Morikawa, and J. K. Norskov, *Phys. Rev. Lett*. **76** (1996) 2141.
[63]N. M. Markovic, B. N. Grgur, C. A. Lucas, and P. N. Ross Jr., *Langmuir* **16** (2000) 1998.
[64]N. M. Markovic and P. N. Ross Jr., *Surf. Sci. Rep*. **45** (2002) 117.
[65]H. A. Gasteiger, N. Markovic, P. N. Ross Jr., and E. J. Cairns, *J. Phys. Chem*. **97** (1993) 12020.
[66]H. A. Gasteiger, N. M. Markovic, P. N. Ross Jr., and E. J. Cairns, *J. Phys. Chem*. **98** (1994) 617.
[67]A. Hamnett, in *Interfacial Electrochemistry: Experimental, Theory and Applications*, Ed. by A. Wieckowski, Marcel Dekker, New York (1999) 843.
[68]W. Chrzanowski and A. Wieckowski, in *Interfacial Electrochemistry: Theory, Experiment, and Applications*, Ed. by A. Wieckowski, Marcel Dekker, New York (1999) 937.
[69]W. Chrzanowski and A. Wieckowski, *Langmuir* **14** (1998) 1967.
[70]M. Watanabe and S. Motoo, *J. Electroanal. Chem. Interfacial Electrochem*. **60** (1975) 275.
[71]W. Chrzanowski, H. Kim, and A. Wieckowski, *Catal. Lett*. **50** (1998) 69.
[72]A. Crown, I. R. Moraes, and A. Wieckowski, *J. Electroanal. Chem*. **500** (2001) 333.

3

Electrodeposition for Electrochemical Energy Conversion and Storage Devices

Nima Shaigan

National Research Council of Canada, Institute for Fuel Cell Innovation, Vancouver, BC, Canada V6T 1W5

I. INTRODUCTION

Electrodeposition of metals, alloys, metal oxides, conductive polymers, and their composites plays a pivotal role in fabrication processes of some recently developed electrochemical energy devices, most particularly fuel cells, supercapacitors, and batteries. Unique nanoscale architectures of electrocatalysts for low temperature fuel cells, including proton exchange membrane fuel cell (PEMFC) and direct methanol fuel cell (DMFC), can only be obtained through electrodeposition processes. Promising, cost-effective conductive/protective coatings for stainless steel interconnects used in solid oxide fuel cells (SOFCs) have been achieved employing a variety of electrodeposition techniques. In supercapacitors, anodic deposition of metal oxides, conductive polymers, and their composites is a versatile technique for fabrication of electrodes with distinctive morphology and exceptional specific capacitance. Electrodeposition is also very recently employed for preparation of Sn-based anodes for lithium ion batteries.

S.S. Djokić (ed.), *Electrodeposition: Theory and Practice*,
Modern Aspects of Electrochemistry 48, DOI 10.1007/978-1-4419-5589-0_3,

This chapter concerns with theory and application of electrodeposition techniques used for fabrication of components for high and low temperature fuel cells, supercapacitors, and lithium ion batteries. Recent progress and possible future research directions in each field will be discussed.

II. PROTON EXCHANGE MEMBRANE FUEL CELLS

PEMFCs, classified as low temperature fuel cells, operate at temperatures normally below 80°C and consume hydrogen as the fuel. A single PEMFC is capable of producing voltage up to 1 V and power densities of up to about 1 W cm^{-2}.[1] The main application of PEMFCs is in electric vehicles. The electrolyte used in PEMFCs is a proton conducting, ion exchange polymer membrane.[1–3] Fluorinated sulfonic acid polymers (e.g., Nafion from DuPont) are the main electrolyte materials. Electrodes in PEMFCs are composed of a gas porous material, i.e., carbon, and a carbon supported electrocatalyst. The membrane conducts the protons only in the presence of liquid water and, therefore, the operating temperature must not exceed 100°C even under high operating pressures.[1] Due to low operating temperatures, use of an efficient electrocatalyst system is indispensable to obtain an acceptable performance. Platinum is the most promising electrocatalyst for reduction of oxygen in PEMFCs.

1. Membrane Electrode Assembly

Catalyst layers used in PEMFCs electrodes are commonly carbon substrates (e.g., Vulcan XC-72) containing dispersed nanoscale Pt particles.[4] Porous carbon-based films are used as gas diffusion layers (GDL) on the sides of the carbon-supported catalyst layer to transport gases.[5] The electrodes, consisting of catalyst layer, GDL, and a current collector, are assembled on each side of the polymer membrane (e.g., Nafion) to form a membrane electrode assembly (MEA).[5] Catalytic activity of the electrodes, especially on the cathode side where oxygen reduction reaction occurs, is a critical factor determining the cell performance.[4] Catalytic activity increases with increasing of the Pt loading of the electrode resulting in high costs of raw materials.[4] Simultaneous maximizing of the catalytic activity and minimizing of the Pt loading is the focus of recent research

on low temperature fuel cells. Increasing the effective surface area and homogeneity of the dispersed catalyst particles can reduce the required Pt loading by increasing its utilization.

There are two main techniques for fabrication of MEAs, powder and nonpowder methods.[6] In the traditional powder process, introduced by Uchida et al.,[7] the carbon supported catalyst is obtained by means of mixing suspended carbon support particles with a platinum compound and an organic solvent. Addition of reducing agents such as hydrazine, formaldehyde, or borohydrides and increasing the solution pH leads to chemical reduction of Pt on the surface of carbon particles. The obtained carbon supported catalyst is then mixed with an organic binder and Nafion and the resulting paste is applied on the membrane and/or GDL. It has been shown by Taylor et al.[8] that the Pt particles which are in intimate contact with the active membrane are the only ones acting as actual electrocatalysts, and, therefore, Pt particles covered with binder do not contribute to the electrocatalytic reactions. In nonpowder techniques for fabrication of MEAs, Pt particles are deposited directly on the carbon supports, eliminating the need for binders and pastes. Sputtering of Pt has been reported as a technique for formation of Pt on the carbon supports.[9] This technique, nevertheless, is costly and does not prevent wasting of Pt. Alternatively, Pt particles can be electrochemically deposited.[8, 10–15]

2. Electrodeposition of Pt Electrocatalysts for MEAs

Taylor et al.[8] were the first to report an electrochemical method for preparation of MEAs for PEMFCs. In their technique, Pt was electrochemically reduced and deposited at the electrode membrane interface, where it was actually utilized as an electrocatalyst. Nafion, which is an ion exchange polymer membrane, is first coated on a noncatalyzed carbon support. The Nafion-coated carbon support is then immersed into a commercial acidic Pt plating solution for electrodeposition. Application of a cathodic potential results in diffusion of platinum cations through the active Nafion layer. The migrated platinum species are reduced and form Pt particle at the electrode/membrane interface only on the sites which are both electronically and ionically conductive. The deposition of Pt particles merely at the electrode/membrane interface maximizes the Pt utilization. The Pt particles of 2–3.5 nm and a Pt loading of less than $0.05\,\mathrm{mg\,cm^{-2}}$ were obtained employing this technique.[8] The limitation of this method is the difficulty of the diffusion of platinum

species through the ionic channels of Nafion. Furthermore, the Pt loading of $0.05\,\mathrm{mg\,cm^{-2}}$ does not provide sufficient electroactivity for oxygen reduction.[16] To overcome the aforementioned limitations, alternative electrochemical techniques for direct deposition of Pt on carbon supports, without Nafion coating, have been developed and studied.[6,14,17–24] Almost in all cases, pulsating current deposition technique is used.

The purpose of application of pulsating current is to achieve a fine grained Pt deposit. As opposed to direct current (DC), pulse plating allows the use of higher peak current densities, which result in deposit grain refinement. The effect of high deposition current densities on grain refinement can be explained by dependency of the nucleation rate on the overpotential, which, in turn, depends on the current density. According to (1), the nucleation rate increases with increasing the overpotential:

$$J = K \exp\left(-\frac{bs\varepsilon^2}{zekT\eta}\right), \tag{1}$$

where K is the rate constant, b a geometrical factor, s the area occupied by an atom on the surface of a nucleus, ε the specific edge energy, e the electron charge, k the Boltzman constant, T the absolute temperature and η is the deposition overpotential.[25]

For large cathodic current densities smaller than the limiting current density, the deposition overpotential increases with increasing current density and vice versa, according to the Bulter–Volmer equation:

$$i = -i_\mathrm{o} \exp\left(-\frac{\alpha zF\eta}{RT}\right), \tag{2}$$

where i is the current density, i_o the exchange current density, α the transfer coefficient, z the number of transferred electrons, F the Faraday constant, η the deposition overpotential, R the gas constant, and T is the absolute temperature.[25]

Increasing the current density, however, increases the deposition overpotential unless the limiting current density is reached. Beyond the limiting current density, the controlling step changes from charge transfer to mass transfer, and the extra current will not entirely contribute to the deposition. The limiting current density depends on the Nernst diffusion layer thickness according to (3):

$$i_\mathrm{L} = \frac{nFDC_\mathrm{b}}{\delta_\mathrm{N}}, \tag{3}$$

where i_L is the limiting or maximum current density contributing to deposition, n the number of electrons involved in the reaction, D the diffusion coefficient of ions in the electrolyte, C_b concentration of ions in the bulk electrolyte, and δ_N is the Nernst diffusion layer thickness.[25]

In contrast to DC plating, pulsating current deposition includes both current on-time and off-time intervals, induced by the wave shape. While the current is off, the reduced, consumed metal ions at the electrode surface are replenished by those migrating from the bulk of electrolyte. The Nernst diffusion layer, thus, breaks down during the off-time and is rebuilt during the on-time periods.[26] Formation and collapse of this layer harmonizes with the pulsating current and a quasisteady state will be established.[26] The Nernst diffusion layer then splits into two inner and outer layers.[25,26] The inner layer, so-called pulse diffusion layer, is located in the immediate vicinity of the electrode surface.[25,26] The outer layer, which is limited to the bulk from one end and the inner layer from the other end, is referred to as stationary diffusion layer.[25,26] The thickness of the pulse diffusion layer (δ_p), which is much smaller than that of the Nernst diffusion layer (δ_N), determines the distance for the ions to diffuse across and reach the electrode surface. This facilitates the ion transport and enables a higher rate of metal ion consumptions, implying higher limiting current densities, at the electrode surface. Due to higher limiting current densities in pulsating current electrodeposition in comparison with DC deposition, a higher nucleation rate and finer deposit crystallites can be obtained.

Kim et al.[6,14] have deposited Pt directly on a carbon support surface from a chloroplatinic acid electrolyte by means of pulsating current electrodeposition. They investigated the effect of peak current density on Pt grain refinement and performance of PEMFCs using so obtained electrodes. It was shown that with an identical charge density, the Pt particle size achieved with pulsating current was smaller to a great extent in comparison with those obtained by application of DC. The difference between Pt particle size deposited via pulsating and direct current is clearly seen in transmission electron microscope (TEM) images shown in Fig. 1. Correspondingly, the cell performance determined from polarization curves showed superiority of the pulse electrodeposition technique. The polarization curves for the PEMFC utilizing electrodeposited Pt catalysts obtained via DC and pulsating current methods are shown in Fig. 2.

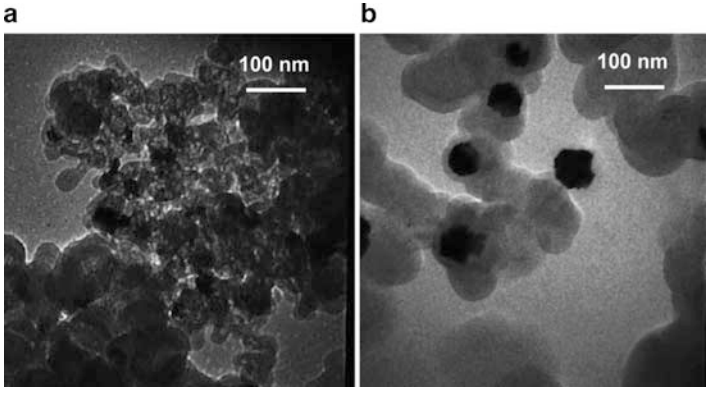

Figure 1. TEM images of Pt deposited on carbon under different electrodeposition conditions: (**a**) 200 mA cm^{-2} of peak pulsating current; (**b**) 10 mA cm^{-2} of DC. Reprinted from Kim et al. [6] with permission from Elsevier.

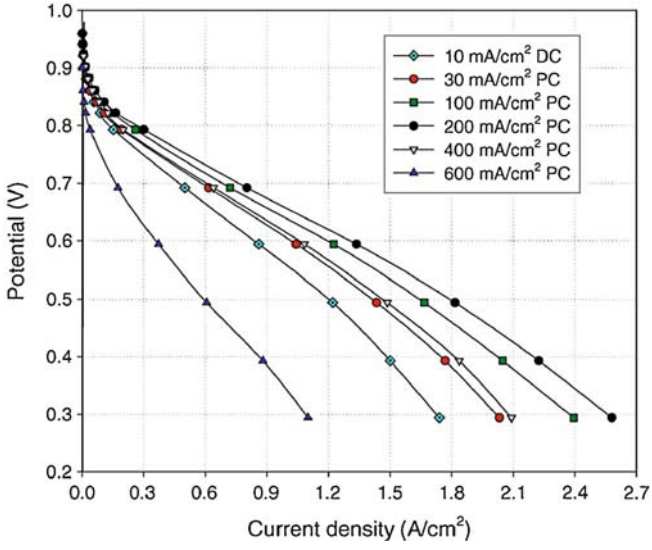

Figure 2. Polarization curves for the PEMFC using electrodeposited Pt obtained via pulsating current, with various peak current densities, and DC methods. Reprinted from Kim et al. [6] with permission from Elsevier.

The cell performance greatly depends on the peak current density for up to 200 mA cm^{-2}, which is probably the limiting peak current density. The other critical factor determining the size of Pt particles was found to be the off-time period. The longer the duration of the off time was, the larger Pt grains and lower cell performance were obtained. Kim et al.[6] have attributed this effect to a smaller mass transport overpotential with longer off times that leads to a smaller overall overpotential and, consequently, a decreased nucleation rate according to (1). The authors also pointed out that beyond a critical charge density (8 C cm^{-2}), the increase in charge density and Pt loading does not enhance the cell performance to any further.

The catalytic activity of carbon supported electrodes was further improved by replacing the conventional carbon supports like Vulcan XC-72R with carbon nanotubes (CNTs) and carbon nanofibers (CNFs). Carbon nanostructures including CNT and CNF have extremely higher electronic conductivity and specific surface area in comparison with the carbon black.[4] The traditional Vulcan XC-72R exhibits an electronic conductivity of 4.0 S cm^{-1}, while the electronic conductivity of CNT and CNF are in the range of 103–104 S cm^{-1}. The high electronic conductivity of CNT and CNF ensures a reliable conductive path connecting Pt particles to supporting electrodes and increases the Pt utilization.[27]

Electrodeposition of Pt on multiwall carbon nanotubes (MWNT) has been reported by Wang et al.[27] In their process, a layer of Co was first electrodeposited on a carbon paper. The purpose of Co film was to catalyze the growth of the subsequent MWNTs layer. A chemical vapor deposition (CVD) technique was used to deposit MWNTs on the Co film. Platinum was then electrodeposited on the MWNT layer. The electrolyte used contained H_2PtCl_6 and H_2SO_4. The electrodeposition of Pt was performed under potentiostatic condition using 0 V vs. saturate calomel electrode (SCE). The particle size achieved with this technique was approximately 25 nm that is too large in comparison with other chemical and electrochemical methods.

3. Electrodeposition of Carbon Monoxide Tolerant Electrocatalysts

Application of liquid fuels in fuel cells is attracting attention mostly for transportation and portable applications. A DMFC uses methanol, water vapor, and air. The MEAs used in DMFCs are

similar to those in PEMFC. For this type of fuel cell, however, the main technological challenges are poor kinetic of methanol dehydrogenation in addition to poisoning of Pt catalysts by carbon monoxide. Carbon monoxide poisoning also affects PEMFCs if the fuel contains even traces of CO. More active catalysts are required to electrooxidize the adsorbed CO to CO_2 gas and mitigate the CO poisoning issue.[28] Electrodeposition of Pt particles with an extremely small size range on carbon nanostructures is considered as a solution to enhance the kinetic of methanol oxidation.

A three-step process for deposition of Pt nanoparticles on single-wall carbon nanotubes (SWNTs) has been reported by Guo et al.[29] Mineral oil was mixed with SWNTs and the resulting paste was electrochemically activated through potential cycling from $+1.8$ to -0.4 V vs. SCE with the scan rate of 200 mV S^{-1} in Na_2SO_4 solution to form functional groups (i.e., carbonyl, carboxylate, and/or hydroxide) on the defective sites on the surface of SWNTs. The second step involved potential cycling in K_2PtCl_4 and K_2SO_4 from $+0.3$ to 1.3 V vs. SCE. Potential cycling in this range produces octahedral Pt(IV) complexes, but does not reduce the Pt ions to metallic Pt. The final step included electrochemical reduction of the octahedral complexes of Pt(IV) to metallic Pt on SWNTs. The final Pt particle size was 4–6 nm. The catalyst so obtained showed an excellent catalytic activity toward electrooxidation of methanol in addition to a good stability.

Alloying of Pt with other metals has been considered as an approach to enhance electrooxidation of CO and alleviate the CO poisoning issue in PEMFCs and DMFCs. It has been reported that Pt–Ru alloys have significantly greater activity toward electrooxidation of methanol than pure Pt.[30,31] Two mechanisms including the bifunctional[30–32] effect and the ligand model[33] have been proposed to explain the beneficial effect of Ru addition. The bifunctional theory assumes that Ru atoms react with water molecules to form Ru–OH.[30–32] The Ru–OH then reacts with poisoned Pt (i.e., Pt–CO) to release CO_2 according to the following reactions:[30–32]

$$\mathrm{Ru^{\circ} + H_2O \rightarrow Ru - OH + e^- + H^+}$$
$$\mathrm{Pt - CO + Ru - OH \rightarrow CO_2 + Ru^{\circ} + Pt^{\circ} + e^- + H^+}$$

According to the ligand model, Ru atoms interact with the conduction band of Pt surface and weaken the Pt–CO bonds and, thus,

result in an enhanced oxidation and release of CO.[33] The bifunctional mechanism has been reported to be four times more effectual than the ligand model.[33]

Ra et al.[34] have reported a process for electrodeposition of Pt–Ru particles on Nafion(Na^+)-bonded carbon layer to enhance CO tolerance of the catalyst layers. The electrolyte for alloy deposition was a proton-free composition containing 20 mM K_2PtCl_6, 10–40 mM K_2RuCl_5, 0.4 M ethanol, and 0.5 M NaCl. Application of a pulsating current with peak current density of 300 mA cm^{-2} and 10:100 on-time:off-time intervals yielded a particle size average of 3–4 nm. A Pt:Ru atomic ratio of 1:1 was obtainable by keeping the concentration of K_2RuCl_5 constant at 30 mM. CO stripping voltammetry showed that such a composition has highest electrochemical surface area in comparison with various Pt:Ru ratios achievable.

Although powder routes have been successfully developed for synthesis of catalysts used in low temperature fuel cells, electrodeposition offers the highest noble metal utilization and is preferred over the alternative chemical methods. Electrodeposition enables the formation of catalyst particles on specific sites where they can be essentially utilized, i.e., the triple phase boundary where the membrane (ionic conductor), electrode (electronic conductor), and reactants meet. Powder methods do not guarantee that all catalyst particles are in contact with both electrode and membrane materials, and therefore, a portion of catalyst particles may remain inactive.

III. SOLID OXIDE FUEL CELLS

In SOFCs, as the name implies, a solid, ion conducting ceramic material is used as the electrolyte, in contrast to other types of fuel cells that function with liquid electrolytes. An individual SOFC consists of a solid electrolyte [e.g., yttria stabilized zirconia (YSZ)], a permeable cathode [e.g., lanthanum strontium manganite (LSM)], and a porous anode (e.g., Ni/ZrO_2 cermet).[1,35] Oxygen or air is fed to the cathode where the oxygen is reduced to oxygen anions. Oxygen anions then migrate through the solid electrolyte and reach the anode where hydrogen or a hydrocarbon oxidizes. The operating temperature range is 600–1,000°C, depending on cell design and materials.

1. Ferritic Stainless Steel Interconnects for SOFCs

The maximum obtainable voltage produced by each individual cell does not practically exceed 1 V, which is not adequate for commercial applications. Consequently, single cells are electrically and mechanically interconnected in series to form stacks, which will be capable of producing the required voltage, current, and power. In a stack, individual cells are interconnected by a component termed the interconnect (or bipolar plate). Since the interconnect must operate in both oxidizing and reducing atmospheres at high temperatures (i.e., 600–1,000°C), the material selected for this purpose must meet some stringent criteria to guarantee the expected cell stability and performance for the target service time of 40,000 h.[36] The interconnect material must be impermeable to gases and ions, exhibit sufficient chemical and physical stability, and provide adequate electronic and thermal conductivity. Furthermore, since the interconnect is in direct contact with other ceramic cell components, the candidate material must also be compatible with these parts in terms of exhibiting good thermal coefficient of expansion (CTE) match.[37–41] Recent interconnect research studies have concentrated almost exclusively on various grades of ferritic stainless steels due to several advantages. The most prominent advantage of ferritic stainless steels over other chromia forming alloys is their excellent CTE match with other ceramic components of the SOFCs. Also, these steels are low cost and easily fabricated into complex forms. The commercially available grades of ferritic stainless steels, nevertheless, do not meet all the interconnect criteria.

2. Conductive/Protective Coatings for Ferritic Stainless Steel Interconnects

Since ferritic stainless steels are chromia forming alloys, high temperature formation of a chromia layer under SOFC operating conditions is unavoidable. Chromia is p-type semiconductor with relatively poor electronic conductivity ($\sim 0.01\ S\ cm^{-1}$ at 800°C).[42] Therefore, the area specific resistance (ASR) of the steel interconnect increases as the chromia layer grows continuously. In addition, Cr(VI) species (e.g., CrO_3) easily vaporize from chromia scales, deposit on cathode/electrolyte interface, and poison the electrochemical activity of the cathode.[43,44] Coatings with materials possessing high electronic conductivity and low ionic diffusivity are considered

as a solution to mitigate these issues. Among various coating materials studied so far, conductive spinels have proven to be the most effective ones.

3. Spinel Coating via Electrodeposition/Heat Treatment

Although screen printing and spray coatings have been the original application methods for spinel coating, complete coverage of the substrate with such methods directly depends on the line of sight. Hence, complex shapes such as corrugated metal sheets cannot be entirely coated by employing such techniques. Spinel coatings can also be achieved through electrodeposition of metals/alloys followed by oxidation in air. Feasibility of coating on complex shapes is considered as a unique advantage of electrodeposition.

Cobalt–Mn and Cu–Mn spinels are the most attractive binary spinels in terms of both electronic conductivity and CTE compatibility with ferritic substrates.[45] However, electrodeposition of Mn and its alloys presents challenges due to very negative electrode potential of Mn in aqueous solutions as well as brittleness of the metallic Mn.[46] Although at high current densities, Mn can be electrodeposited; the deposits are readily soluble in the electrolytes. This is particularly attributed to presence of impurities, from the electrolyte and anode oxidation products, which may be incorporated in the deposit and form local galvanic cells.[46] The most important contaminant is known to be iron ions, which reduce to the lower valance and deposit iron hydroxide on the cathode surface.[47] Electrodeposition of Mn is conventionally performed in a two compartment bath.[46] The anode and cathode compartments are separated by means of a diaphragm to avoid contamination of the electrolyte in the cathode compartment (catholyte).[46] In addition, Mn hydroxide precipitates in the solution and changes the electrolyte pH and its conductivity.[47] Precipitation of Mn hydroxide can be inhibited by addition of ammonium ions.[46,47] Ammonium ions function as buffer at pH values ranging from 2 to 3.5 and 6 to 7, enhance the reduction ability of Mn, reduce the hydrogen evolution rate, and, thus, increase the current efficiency.[47,48] It has been shown that addition of Se and S facilitates the deposition of Mn and increases the current efficiency.[46,47,49] However, these elements incorporate into Mn deposits and change the film properties.[46] Also, electrodeposition of Mn alloys requires high current densities often higher than the second metal's limiting current density.[46] Addition of complexing

agents will not solve the problem as complexing agents also inhibit the deposition of Mn.[46] Despite some insignificant improvements achieved, obtaining smooth, ductile, and well adherent Mn or Mn alloy coatings is still facing challenges.

Application of electrodeposition for spinel coatings was first reported by Bateni et al.[50] and characterized by Wei et al.[51] from the same research group. In their work, Co–Mn and Cu–Mn were sequentially electrodeposited on AISI-SAE 430 stainless steel substrates. The Mn plating bath used was a two compartment cell in which the compartments were separated by glass frit tubes. The cathode and anode compartments contained ammonium and Mn sulfates and ammonium sulfate, respectively. Platinum was used as the anode. A chloride based electrolyte was used for Co deposition, and a Cu sulfate/sulfuric acid based bath was used for Cu plating. To form an alloy from sequentially plated Mn–Co/Cu deposits, the coatings were annealed in argon for 2 h at 800°C. The formation of Mn–Co/Cu spinels upon oxidation in air at 750°C was observed. Both Mn–Co and Mn–Cu oxidized coatings exhibited a stably low ASR of 0.003 $\Omega\,cm^2$ at 750°C after 1,500 h of oxidation, while the ASR measured for uncoated steels under identical condition was 0.189 $\Omega\,cm^2$.[51] Both coatings were highly effective in inhibiting Cr outward diffusion during oxidation.

Electrodeposition of Mn–Co alloys using both DC and pulsating current has been investigated by Wu et al.[52–54] The electrolyte contained Co and Mn sulfates with a molar ratio of 0.02:0.2, boric acid, gluconate, and ammonium sulfate. However, their efforts did not entirely succeed. The standard electrode potentials for Co is −0.277 vs. standard hydrogen electrode (SHE) while that for Mn is −0.180 vs. SHE, and high current densities are needed to obtain coatings with adequate Mn concentrations. Increasing the current density, however, is not desirable as high current densities may result in precipitation of Mn hydroxide and formation of powdery, spongy deposits. Rapid depletion of Co in the electrolyte and need for continuous monitoring and replenishing the consumed Co are other disadvantages of this process. Using pulsating current, electrodeposition did not offer any significant improvement as Mn dissolves instantly during the current off-time periods.[53]

Pure Co spinel (i.e., Co_3O_4) also exhibits good high temperature electronic conductivity and CTE compatibility with ferritic steels.[45] Deng et al.[55] used a sulfate/chloride-based Co plating bath to coat

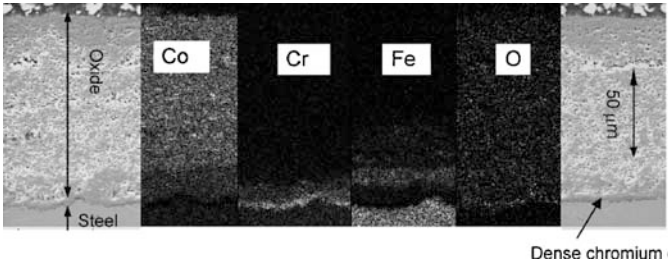

Figure 3. SEM image and EDX elemental maps for electrodeposited Co oxidized at 800°C for 1,900 h in air. Reprinted from Deng et al.[55] with permission from Elsevier.

AISI-SAE 430 ferritic steels with 20–40 µm-thick Co layers. The oxidation of Co coated samples in air at 800°C resulted in growth of a triple layer oxide scale with a top layer of Co_3O_4, a midlayer of a spinel solid solution containing Co, Cr, and Fe, and an inner layer of a relatively thick Cr-rich oxide (~5–7 µm). Figure 3 shows the scanning electron microscope (SEM) images and energy dispersive X-ray (EDX) elemental maps for Co, Cr, Fe, and O after oxidation at 800°C for 1,900 h. The coating effectively inhibited the Cr outward diffusion from the Cr-rich inner oxide layer. The coating exhibited a very stable, low ASR of 0.025 Ω cm^2 after 1,900 h of oxidation at 800°C in air.

(i) Drawbacks of Spinel Coatings via Electrodeposition/oxidation

There are, however, a number of potential deficiencies associated with the spinel coating via electrodeposition/oxidation process that must be accounted for. During high temperature oxidation, interdiffusion of coating and substrate elements occurs. Elements from steel substrates (i.e., Fe, Mn, and to a lesser extent Cr) diffuse into electrodeposited layers and change the coating composition before the entire metallic coating is transformed to oxides. Likewise, electrodeposited metals diffuse into the substrate and result in substrate compositional changes and dilution of the alloy surface region in Cr. The latter case is extremely important for long-term high-temperature stability. It is well known that, in order for a protective, dense chromia layer to grow, a minimum, critical Cr concentration

is required in the steel composition. Although at Cr concentrations slightly lower than Cr threshold, a chromia layer may form, it becomes instable, relative to Fe oxides, due to lack of a sufficient Cr supply from the alloy.[56,57] In addition, the situation worsens as the oxidation proceeds for long periods. For long oxidation times, if the bulk of alloy is unable to replenish the Cr consumed by the scale, due to slow diffusion of Cr in the alloy, the surface region becomes gradually more depleted in Cr. This results in severe instability of chromia and its breakdown. In such circumstances, any mechanical damage, as a result of thermal shocks, to chromia scale cannot be self-repaired due to inadequate Cr concentration in the substrate surface in contact with oxide scale.[56,57] As a result, Fe from the steel starts to oxidize and form large, localized hematite nodules on the surface. This phenomenon is referred to as breakaway type of oxidation and certainly is a drawback for long-term high-temperature stability. The Cr threshold depends on a number of factors including oxide scale growth rate and interdiffusion coefficient.[56,57] Using substrate alloys with a sufficient Cr concentration and reactive elements, which reduce the Cr concentration threshold, therefore, seems necessary.

In Wei et al.'s work,[51] after 7 days of oxidation at 750°C, a relatively thick layer (~5–10 μm) of Cr-rich oxide formed under the Co–Mn and Cu–Mn spinel layers. Although such thick chromia scales are likely vulnerable to break down in long term or at higher temperatures, no anomalous oxidation behavior was reported. Similarly, in Deng et al.'s work[55] from the same research group, ~5–7-μm-thick Cr-rich oxides formed under the Co spinel layer.

Shaigan et al.[58–60] have developed and studied composite spinels obtained via composite electrodeposition/oxidation. The metal matrix was Ni or Co and the second phase in the electrodeposited composite was $LaCrO_3$. The purpose of use of $LaCrO_3$ particles was to improve the oxidation properties of coatings. Lanthanum (or other reactive elements like Y, Ce, Hf, etc.) containing oxide particles have proven to dramatically reduce the oxidation rate and increase the metal to scale adhesion.[61] The coatings were applied on AISI-SAE 430 stainless steel substrates. Coelectrodeposition of inert particles with metals can be simply conducted by suspending the particles in the plating electrolyte and is studied and modeled in many works.[62] Oxidation of the as-deposited $Ni/LaCrO_3$ coating resulted in growth of a double layer oxide scale consisting of a Cr-rich subscale, with embedded $LaCrO_3$ particles,

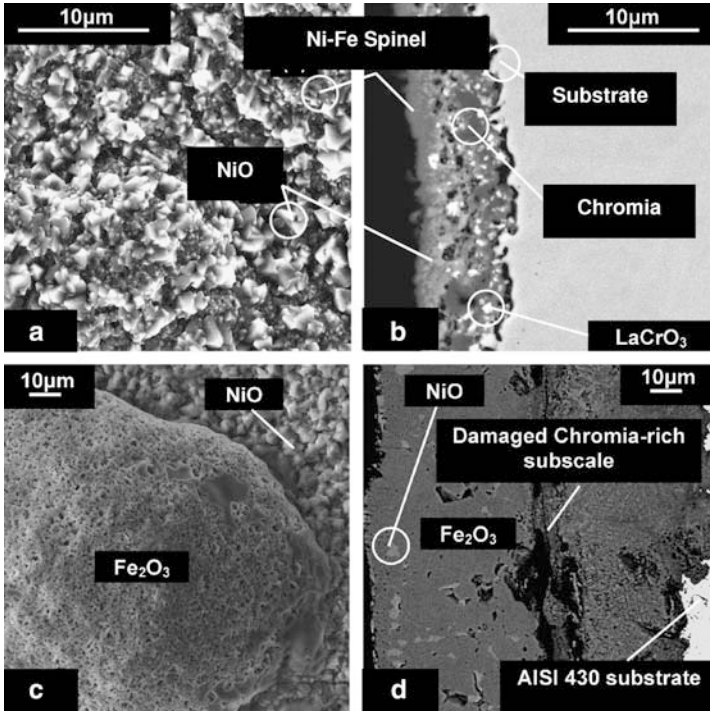

Figure 4. SEM images of oxidized electrodeposited $Ni/LaCrO_3$ [(**a**) and (**b**)] and Ni [(**c**) and (**d**)] after 2,040 h oxidation at 800°C in air. [58] Reprinted from Shaigan et al. [58] with permission from Elsevier.

and an outer scale composed of Ni/Fe-rich spinel in addition to NiO particles (Fig. 4a, b).[58] It was observed that in the absence of $LaCrO_3$ particles, Ni-plated steels exhibited breakaway type oxidation (Fig. 4c, d).[58] Hematite nodules started to form and grow after 600 h of oxidation in air at 800°C.[58] The breakaway oxidation was attributed to dilution of the substrate surface in Cr and high consumption rate of Cr ions in the scale in the absence of particles, as discussed previously.[58]

In the case of $Co/LaCrO_3$,[60] a triple layer scale consisting of a Cr-rich subscale, a Co–Fe spinel midlayer, and a Co_3O_4 spinel top layer was observed after oxidation at 800°C in air.[60] It was determined that $LaCrO_3$ particles significantly decrease the specific

weight gain and oxide scale thickness of Co coatings. Partial spallation of the oxide scale was observed in the absence of particles and after 1,000 h oxidation at 800°C in air.[60] Spallation occurred at the chromia silica interface.[60] Breakaway oxidation, however, did not occur for pure Co coatings without particles as opposed to Ni coatings.

Both $Ni/LaCrO_3$ and $Co/LaCrO_3$ coatings performed as reliable barriers against Cr outward diffusion. Low, stable ASR values of 0.005 $\Omega\,cm^2$ (after 400 h) and 0.02 $\Omega\,cm^2$ (after 900 h) at 800°C in air were reported for $Ni/LaCrO_3$[58] and $Co/LaCrO_3$[60] composite coatings, respectively.

4. Anodic Deposition of Co–Mn Spinels

Anodic deposition of oxides followed by a subsequent heat treatment is an alternative route for spinel coating. Metal oxides can be anodically deposited on the steel surfaces from aqueous solutions containing metal salts and with or without complexing agents. The oxide layers so obtained are usually nanocrystalline or amorphous with metastable phases which transform to crystalline spinel structures upon a subsequent heat treatment.[63–65] The coating thickness is limited due to poor conductivity of the deposited oxides. Anodic deposition of Co-rich, Co–Mn oxides on a ferritic stainless steel for the purpose of high-temperature oxidation protection was first practiced by Wei et al.[64] The electrolyte was a solution of Co and Mn sulfates and ethylenediaminetetraacetic acid (EDTA) as the complexing agent. The deposition temperature and current density were set above 70°C and below $\sim$5 mA cm^{-2}, respectively. Deposition at lower temperatures and higher current densities resulted in crack formation, the mechanism of which was not described by Wei et al. It was found that the composition of the coating can be easily adjusted by controlling the deposition temperature, the ratio of the metal salts in the electrolyte, and the current density. The Co content of the oxide film increased by increasing current density up to 30 mA cm^{-2}. The as-deposited films consisted of nanocrystals with a metastable, defective sodium chloride structure. Changing of the deposition condition and film composition did affect the crystal structure. As a result of annealing at temperatures above 500°C, the metastable sodium chloride phase transformed to spinels of either face centered cubic (FCC) or tetragonal. Deposits with higher Co:Mn ratios

transformed to FCC spinel while those rich in Mn yielded a tetragonal spinel phase upon annealing. The protective properties and electronic conductivity of anodically deposited Mn–Co oxides were studied by the same investigators.[66] In their work, two different annealing atmospheres including air and forming gas ($5\%H_2$–N_2) were used for annealing. The time and temperature of annealing (800°C for 10 h) were identical for both annealing processes. Annealing in air led to spallation and cracking of the coating while the same process in forming gas resulted in reduction of Co oxide to metallic Co particles embedded in a Mn_3O_4 matrix. The coatings annealed in forming gas also adhered well to the substrate and slightly reduced the ASR values relative to the uncoated substrates.

Electrodeposition is a unique technique that enables the application of protective/conductive coatings on complex interconnect configurations, for example, corrugated metallic sheets. In addition, the oxidation protection ability of the electrodeposited coating can be greatly improved by moving from plain metal plating to metal/reactive element oxide composite electrodeposition. The next research direction in the field of coatings for metallic interconnect would be spinal coating via electrodeposition for recently developed alloys that contain less amounts of impurities (e.g., Si, Al, S, C, etc.), higher Cr concentrations, and smaller amounts of reactive elements (e.g., La). Such alloys are now commercially available.

IV. ELECTROCHEMICAL SUPERCAPACITORS

Supercapacitors are energy storage devices with exceptionally high capacitance, long cycle life, and high power density. Supercapacitors possess higher power density but lower energy density in comparison with batteries.[67] In general, the cycle life of the supercapacitors is more than hundred times longer than that of batteries.[67] The main application of supercapacitors is in electric vehicles to boost the power density when peak power pulses are required.[67,68]

1. Faradic and Non-Faradic Supercapacitors

Supercapacitors are categorized into two classes based on their charge storage mechanisms.[67,68] Electric charge may be stored in a capacitor through charge separation at the electrode–electrolyte

interface without any electron transfer. This mechanism of charge storage is known as the non-Faradic capacitance, and the supercapacitors based on this mechanism are classified as electric double layer capacitor (EDLC). The alternative mechanism of electric charge storage is based on reversible redox or electrosorption reactions occurring in the electroactive electrode materials during charge and discharge cycles. This process of charge storage is associated with charge transfer and is known as Faradic capacitance. The supercapacitors based on Faradic capacitance are referred to as pseudocapacitors.

Electrodes in EDLCs consist of highly porous, conductive materials mounted on a metallic sheet, known as current collector.[69] The electrodes are separated by means of a porous insulating sheet impregnated with an organic or aqueous electrolyte. The porous electrode material used in commercially available supercapacitors is activated carbon[70–76] or carbon nanostructures such as nanotubes[69,77–83] and aerogels.[70,79,84–90] Instead, pseudocapacitors use transition metal oxides,[91–97] and/or conductive polymers,[98–102] as electroactive electrode materials. In both cases, the electrode material must be sufficiently porous with a proper pore size distribution to provide high surface area for electrolyte access. Electric double layer supercapacitors are commercially available and are not subject to discussion in this chapter. Pseudocapacitors, in contrast, have been attracting a considerable attention in the recent years due to their excellent capacitance and power density.

2. Metal Oxide Electrodes

Among various metal oxides, hydrous or anhydrous RuO_2 is found to exhibit the greatest specific capacitance (i.e., $760\,F\,g^{-1}$) and electronic conductivity along with the longest cycle life.[103–106] Ruthenium, nonetheless, is a precious metal and its commercial use is, hence, limited. Many studies have been conducted to find a metal oxide capable of exhibiting capacitive properties analogous to RuO_2. Among a variety of examined metal oxides and hydroxides of Ni,[93,94,107–126] Co,[94,127–140] Fe,[141] In,[142] Sn,[143–146] V,[147,148] and Mn,[95–97,149–195] hydrous MnO_2 is the most attractive candidate due to its reasonable specific capacitance (the practically attainable capacitance range is $\sim$100–$200\,F\,g^{-1}$[196]), its low cost, and being environmentally friendly.

Nonetheless, MnO_2-based electrodes possess lower specific capacitance and electronic conductivity in addition to a narrower potential window in comparison with their RuO_2-based counterparts. Many recent research studies have concentrated on novel synthesis methods for preparation of MnO_2 with various crystal structures, morphologies, and architectures to improve the capacitive behavior.

There are two theories developed to explain the processes for charge storage in MnO_2.[197] One theory suggests that proton (H^+) and alkali metal cations (C^+), present in the electrolyte, can be reversibly intercalated into the bulk of MnO_2 through a reduction reaction and deintercalated via an oxidation reaction:[198]

$$MnO_2 + H^+ + e^- \leftrightarrow MnOOH$$
$$MnO_2 + C^+ + e^- \leftrightarrow MnOOC$$
$$\left(Mn^{+4} + e^- \leftrightarrow Mn^{+3}\right)$$

The other theory is based on surface electrosorption of cations on MnO_2 according to the following reaction:[199]

$$(MnO_2)_{surface} + C^+ + e^- \leftrightarrow \left(MnO_2{}^- C^+\right)_{surface}$$
$$\left(Mn^{+4} + e^- \leftrightarrow Mn^{+3}\right)$$

For both cases, a reversible redox reaction between Mn^{+4} and Mn^{+3} occurs to maintain the electroneutrality of the electrode material.

3. Electrodeposition of Manganese Oxides

Although chemical techniques, including sol gel,[198–201] thermal decomposition,[199] and hydrothermal[201,202] methods, have been used for preparation of MnO_2 powders, anodic[95,97,150,153,157,173,196,203] and less often cathodic[163,177,185] electrodeposition of MnO_2 is the preferred route for synthesizing of MnO_2-based electrodes. The main advantage of electrodeposition is feasibility of the direct growth of MnO_2 on the surface of conductive substrates without need for any binder or other inactive additives.

Manganese oxide can be anodically deposited on various conductive substrates from aqueous solutions containing simple or chelated Mn salts with or without buffers and surfactants.

Manganese ions hydrolyze under anodic potentials to deposit MnO_2 according to the following reaction:

$$Mn^{2+} + 2H_2O \rightarrow MnO_2 + 4H^+ + 2e^-$$

The morphology, electronic conductivity, exposed specific surface area, crystal structure, and defect chemistry (cation distribution and oxidation states) of the manganese oxides considerably influence the performance of pseudocapacitor (capacitance, cycle life, and charge/discharge rate).[153,156,157,173,180,186,188] All these features may be modified by varying the deposition parameters and/or heat treatment.

Crystal structure and defect chemistry determine the dimensions of crystal tunnels, which are the transport pathways for protons and alkali metal cation intercalation.[204] Wei et al.[95,196] have studied the effect of two complexing agents including disodium salt of ethylenediaminetetraacetic acid (EDTA) and sodium citrate on crystal structure, defect chemistry, and electrochemical behavior of the MnO_2 and oxidation state of Mn in the deposited film. In their work, anodic deposition of manganese oxide was performed in neutral aqueous solutions containing $MnSO_4$ with or without complexing agents. The electrolyte without any complexing agent led to deposition of loosely aggregated nanofibers of MnO_2. The TEM selected area diffraction (SAD) patterns from the film showed that the crystal structure is hexagonal ε-MnO_2 with Mn^{4+} cations distributed in half of the octahedral sites of the hexagonal close packed (HCP) of the oxygen sublattice. Addition of EDTA resulted in a slight change in the arrangement of the nanofibers. As opposed to complexing agent free electrolyte, the deposit achieved with EDTA was a metastable, defective sodium chloride type with an FCC oxygen anion arrangement and Mn cations occupying the octahedral interstices with a large number of cation vacancies. With use of sodium citrate, the crystal structure obtained was a defective antifluorite with Mn cations randomly occupying the eight tetrahedral interstices in the oxygen unit cell. In this case, the film was composed of small, agglomerated particles instead of fibers. The diameter of the particles was determined to be ~5 nm. Regardless of the presence and type of the complexing agent used in electrodeposition, the valance of Mn cations in the oxide was +4, determined by X-ray photoelectron spectroscopy (XPS). It was concluded that the use of a complexing agent in the electrolyte leads to unique, highly defective structures. The authors pointed out that

the other deposition parameters including solution temperature, pH, and current density did not influence the crystal structure of the anodically deposited MnO_2 films. The specific capacitance of the deposited films was analyzed by means of cyclic voltammetry (CV) in 0.5 M Na_2SO_4. The following equation may be used to calculate the specific capacitance from voltammograms:

$$C_{sp} = \frac{Q}{m_e \times \Delta E} = \frac{\int I \mathrm{d}t}{m_e \times \Delta E} = \frac{\int I \mathrm{d}v}{m_e \times \Delta E \times S_r} (\mathrm{F\,g^{-1}}), \quad (4)$$

where Q is the total charge (F), m_e the active electrode mass (g), ΔE the width of the potential window (V), I the current (A), v the potential (V), S_r the scan rate ($\mathrm{V\,S^{-1}}$), and $\int I \mathrm{d}v$ represents the area under either cathodic or anodic voltammogram.

As seen in Fig. 5, defective Mn oxides including rock salt and antifluorite structures show a higher specific capacitance than hexagonal ε-MnO_2 for all scanning rates examined. The improvement was attributed to the greater number of unoccupied interstices, considered as electrochemically active sites, for rapid ionic transportation in defective structures obtained by addition of complexing agents to the electrolyte. Regardless of the MnO_2 structure, increasing the scan rate results in a decrease in the specific capacitance.

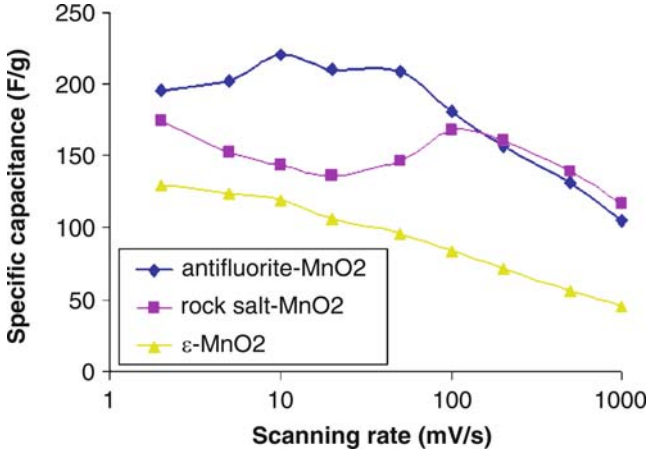

Figure 5. Specific capacitance of MnO_2 deposits derived from the cyclic voltammograms (second cycle) at various cycling rates. Courtesy of Wei et al.[95] Reprinted with permission from Wei et al.[95] Copyright 2008 American Chemical Society.

4. Conductive Polymer Electrodes

The alternative materials of interest for use in supercapacitor electrodes are conductive polymers. These materials were first introduced in 1971 when Shirakawa et al.[205] synthesized polyacetylene. Recently, conductive polymers including polyaniline (PANI), poly[3,4-ethylenedioxythiophene] (PEDOT), and polypyrrole (PPY) are used for their special properties including electroactivity, semiconductivity, conductivity, electrochromism, ion exchange ability, and being electrochemically catalytic.[206] They are used for fabrication of numerous products such as sensors, energy storage devices, optical and electroluminescence devices, diodes, transistors, display devices, smart windows, ion exchange membranes, and catalyzing electrodes.[206] Delocalized electrons in π conjugated system along the polymer chains result in a high electronic conductivity.[206] Conductive polymers are also capable of undergoing reversible redox reactions upon application of an external potential.[207,208] Redox reactions in conductive polymers are associated with diffusion of ions in and out of the polymer (doping and undoping) to maintain the electroneutrality.[208] It has been shown that the specific capacitance of the conductive polymers can reach somewhat close to that of RuO_2. The specific capacitances for PANI, PPY, and PEDOT have been reported to be $815\,F\,g^{-1}$,[209] $400\,F\,g^{-1}$,[210] and $250\,F\,g^{-1}$,[211] respectively. Although PANI and PPY exhibit higher specific capacitances than PEDOT, the cycle life of PEDOT is notably longer than the other two polymers due to its superior chemical stability.[208,212]

5. Electrodeposition of Conductive Polymers

Conductive polymers may be synthesized via either chemical or electrochemical polymerization methods. Electrodeposition of conductive polymers from electrolytes is, thus, feasible provided that the depositing polymer is not soluble in the electrolyte.[206] Conductive polymers can be deposited from the electrolytes containing the monomers via either electrooxidation or electroreduction, based on the monomer type used. Similar to that of metals, the electrodeposition of polymers is based on nucleation and growth. The deposition mechanism involves oxidation of monomers adsorbed on the electrode surface, diffusion of the oxidized monomers and oligomerization, formation of clusters, and eventually film growth.[213]

Aniline, pyrrole, and 3,4-ethylenedioxythiophene (EDOT) can be electroploymerized by electrooxidation to deposit polyaniline, polypyrrole, and PEDOT films.[206] Electrodeposition of polyaniline and polypyrrole from aqueous electrolytes is feasible.[214,215] Electrodeposition of PEDOT from aqueous electrolytes, however, presents challenges due to insolubility of thiophene and its derivatives in water, higher oxidation potential of thiophene than water, and formation of thienyl cation radicals that inhibit the electropolymerization.[214] One approach is use of organic electrolytes (e.g., acetonitrile-based electrolytes). Alternatively, addition of a significant amount of anionic surfactants [i.e., sodium dodecyl sulfate (SDS)] increases the solubility of thiophene and lowers its oxidation potential.[214] Formation of micelles leads to dissolution of the water insoluble compounds. In addition, a micellar media changes the electrolyte/electrode interface, via irreversible adsorption of the surfactant, and affects the electrochemical reactions.[214] Furthermore, charged radicals may be stabilized by surfactants.[214] According to Sakmeche et al.,[214] addition of 0.01 M SDS lowers the oxidation potential of EDOT by 90 and 130 mV in water and acetonitrile media, respectively. The reason behind this is believed to be formation of a pseudocomplex between dodecyl sulfate (DS^-) and $EDOT^+$ cation radicals.[214]

In spite of having high specific capacitance, conductive polymers are not absolutely promising for use in supercapacitors owing to their slow ion transport while undergoing redox reactions. The sluggish ion transfer adversely affects the charge/discharge rate and power density of the supercapacitor.[208] Shortening of the ionic diffusion distances in conductive polymers by exploiting nanostructures, in particular nanotubules, has been considered as a solution to overcome this issue.[216] Nanostructures can be electrodeposited using templates (hard templates), pseudotemplates (soft templates including polymer and surfactants), or template free methods.[216] Template electrosynthesis is the most often used technique for deposition of nanostructures. This method is based on electrodeposition within the ordered channels (or pores) of a membrane. Sputter or evaporation coatings of metals, commonly gold, are applied on one side of the nonconductive templates which will be in contact with the electrode. The purpose of this step is to provide conductive sites for electrodeposition to initiate from the bottom of the template's channels. Depending on the electrodeposition conditions, either hollow

nanotubules or solid nanofibrils can be deposited within the channels of a membrane.[217] Anodized aluminum oxide (AAO) and track etched polycarbonate are the most commonly used template materials for template electrosynthesis.[217] AAO membranes consist of thin wall, normal to the surface channels arranged in a hexagonal manner. The thickness of the membrane and diameter of the channels may be straightforwardly controlled by adjusting the anodizing parameters. Furthermore, easy dissolution of AAO in hydroxide solutions to release the nanowires is another benefit of using AAO membranes.

Template synthesis of nanotubular structures of conductive polymers were first introduced by Martin's group.[217] It was discovered that by using a track-etched polycarbonate membrane in short polymerization times, thin wall tubules of polymers grow preferentially on the walls of the membrane channels. Thick wall tubules or solid fibrils (in the case of PPY), however, were obtained by increasing the polymerization time.[217] According to Martin et al.'s hypothesis, preferential growth of polymer on the walls of pores is, in part, due to existence of a "solvophobic" effect stemming from insolubility of polycationic forms of the polymer. Additionally, electrostatic forces between the negatively charged wall of the pores and cationic polymers result in adsorption of the polymer preferentially on the wall surfaces. This effect is referred to as "molecular anchor."[217] The conductivity of polymers obtained through template synthesis was greatly improved and was attributed to a high degree of polymer chain alignment on the outer surface of tubules or fibrils.[217] Following the Martin's discovery, many research endeavors were devoted to improve the capacitive behavior of conductive polymers by modifying the morphology of the polymer deposits.

Cho et al. were the first to electrosynthesize nanotubular PEDOT using alumina templates for application in electrochromic devices and supercapacitors.[216] In their study, a mechanism based on competition between diffusion rate of monomer into the pore and polymerization reaction rate was proposed for tubule formation within the walls of the template pores. The effect of monomer concentration (10–100 mM) and applied potential (1.0–1.8 V vs. Ag/AgCl) on inner morphologies of PEDOT structures was investigated. The electrolyte used was acetonitrile with 0.1 M $LiClO_4$. The tubular portion of the polymer wires (R = tubular length/total wire length) as a function of applied potential at given monomer

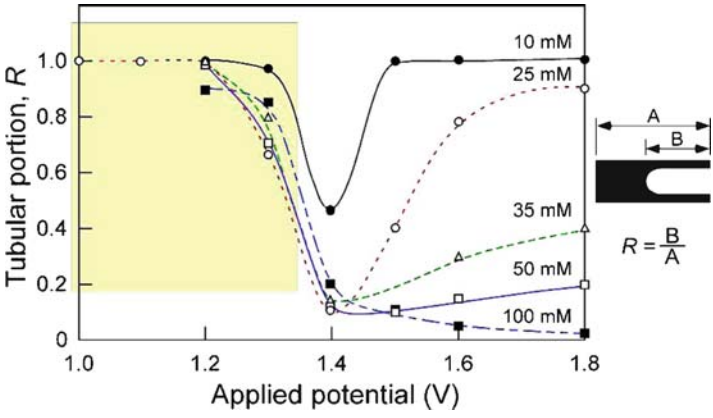

Figure 6. Tubular portion of PEDOT nanostructures vs. applied potential for various monomer concentrations. Monomer concentration does not affect the tubular portion at very low oxidation potentials. Courtesy of Il Cho et al. Reprinted with permission from Il Cho and Lee. [216] Copyright 2008 American Chemical Society.

concentration was measured (Fig. 6). As seen in Fig. 6, at high applied potentials, greater than 1.4 V, the tubular portion increases with increasing potential and decreases with increasing monomer concentration. This effect was attributed to the slow deposition rate and long time required for diffusion of monomers into the bottom of the pores so that there is no concentration gradient of monomers along the pore length, which may result in a preferential growth on the wall surfaces. In the case of high potential and low monomer concentration, the deposition rate is so fast that there is a deficit of monomer at the bottom of the pores due to insufficient monomer diffusion. This results in faster growth of polymer on the wall surfaces, where concentration of monomer is high enough, as opposed to the bottom of the pores. Under this condition, hollow tubes form within channels of the membrane. The effect of potential and monomer concentration for the applied potentials above 1.4 V for two extreme cases of monomer concentration is schematically presented in Fig. 7. For the applied potentials below 1.4 V, however, the tubular portion is almost independent of the monomer concentration. This effect cannot be explained by the mechanism previously described and is attributed to the presence of annular gold active sites at the bottom of the pores as the result of gold sputtering intrusions inside the walls. Use of flat

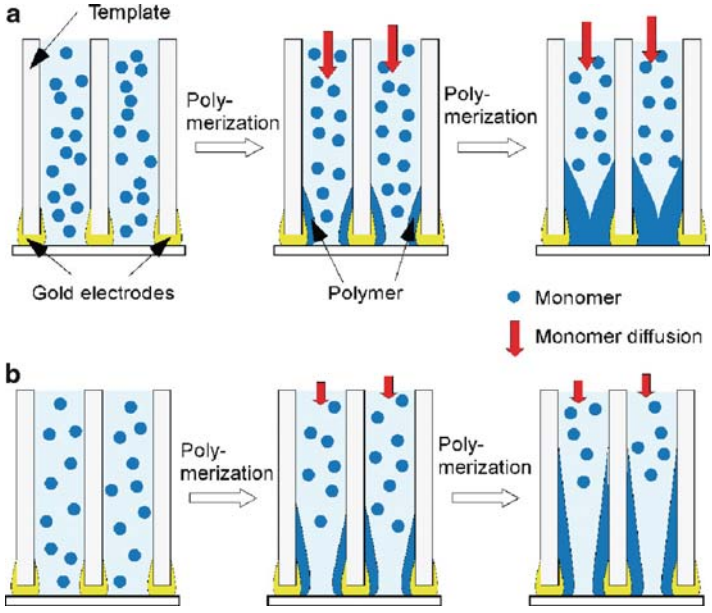

Figure 7. Schematic representation of growth mechanism of PEDOT nanostructures for high oxidation potential (1.4 V): (**a**) slow reaction rate at high monomer concentration and (**b**) fast reaction rate at low monomer concentration. Courtesy of Il Cho et al. Reprinted with permission from Il Cho and Lee. [216] Copyright 2008 American Chemical Society.

top template, obtained with further electrodeposition of gold, at low applied potential of 1.2 V produces solid wires instead of tubules. This supports effect of annular active sites at the bottom of the pores. The schematic SEM and TEM images of PEDOT electrodeposited under low potentials are depicted in Fig. 8.

The capacitive properties of nanotubes obtained with Cho et al.'s method have been studied by Liu et al. from the same research group.[208] Tubular structures were obtained with electrodeposition in acetonitrile solution containing 20 mM EDOT under potentiostatic condition at 1.6 V vs. Ag/AgCl while nanofibers were synthesized in 100 mM EDOT and at 1.4 V applied potential. Thin wall nanotubes of PEDOT exhibited a stable specific capacitance of 140 Fg^{-1}, while the specific capacitance for the solid nanofibers was 50 Fg^{-1}, under the identical test conditions. Figure 9 compares the

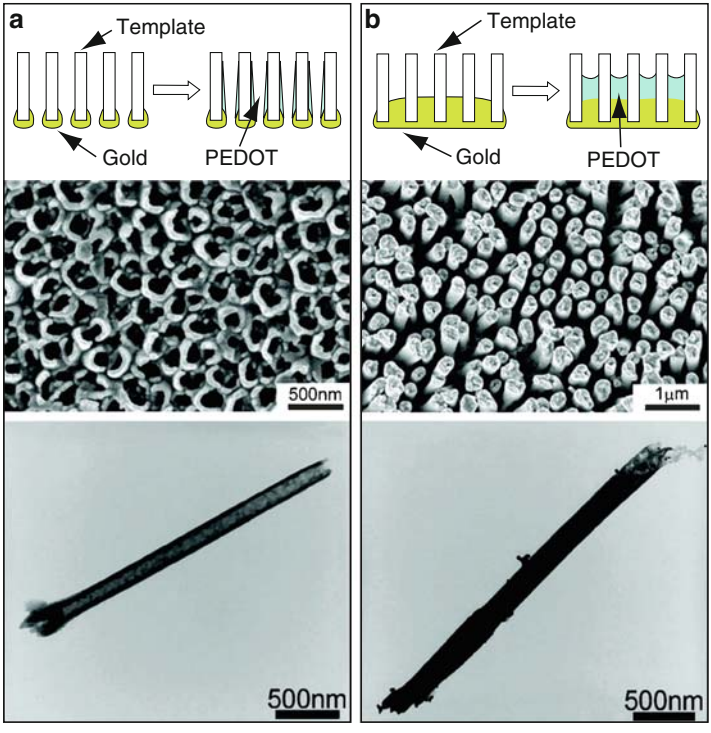

Figure 8. At low anodic potentials (<1.4 V), the electrochemically active sites on sharp electrode edges determine the growth mechanism and morphology of PEDOTs. Part (**a**) shows the PEDOT deposited on annular and (**b**) for flat top templates. SEM images show the morphologies and TEM images show a PEDOT nanostructure obtained in each case. Courtesy of Il Cho et al. Reprinted with permission from Il Cho and Lee. [216] Copyright 2008 American Chemical Society.

cyclic voltammograms of solid nanofibers and nanotubes of PEDOT obtained with identical deposition charge density and deposit mass. A notably smaller capacitive current is observed for solid nanofibers than that for nanotubes under the same scan rate. Furthermore, non-ideal, potential-dependent capacitive behavior is realized from the highly distorted rectangular voltammogram of the nanofibers. The specific capacitance and capacitive behavior of electrodeposited PEDOT is, therefore, highly related to the morphology and the length of diffusion paths for doping/undoping of counter ions.

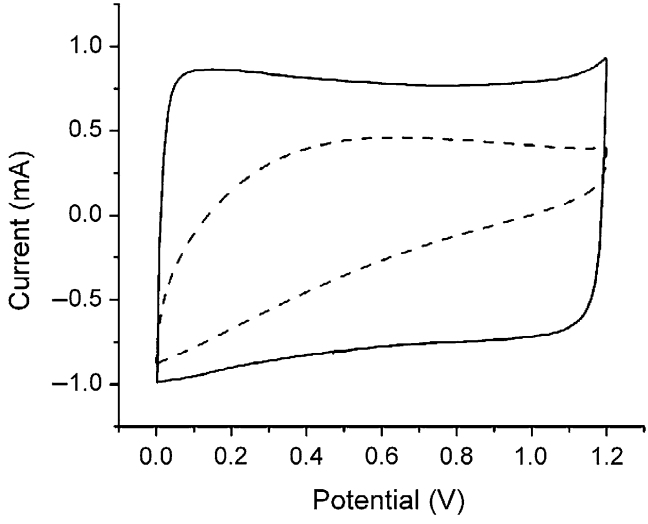

Figure 9. Cyclic voltammograms for shielded (*dashed line*) and unshielded (*solid line*) nanowires. The charge density was 500 mC cm^{-2}, scan rate was 100 mV s^{-1}, and the potential was cycled between 0 and 1.2 V. Reprinted from Liu et al. [208] with permission from IOP Publishing Ltd.

6. Composite Electrodeposition of Metal Oxides/Polymers

Nanocomposites of metal oxides/polymers in a shell/core configuration have been recently developed and studied for application in supercapacitors. Although PEDOT possesses a high electronic conductivity, stability, and mechanical flexibility,[218,219] it suffers from low electrochemical energy density.[220] Manganese oxide, on the other hand, provides high energy density, but exhibits low electronic conductivity.[220] A composite of MnO_2 and PEDOT with MnO_2 as the core and PEDOT as the shell can facilitate electronic and ionic transport into the core MnO_2 and improve its structural stability to avoid mechanical breakdown of the composite nanostructures.[220] Liu and Lee[220] have developed a method for electrocodeposition of MnO_2 and PEDOT in a coaxial nanowire configuration using alumina membrane. The electrolyte used contained 80 mM EDOT and 10 mM manganese acetate. The anodic deposition potential was constant and selected in the range between 0.6 and 0.85 V vs. Ag/AgCl for the codeposition of both PEDOT and MnO_2 to be

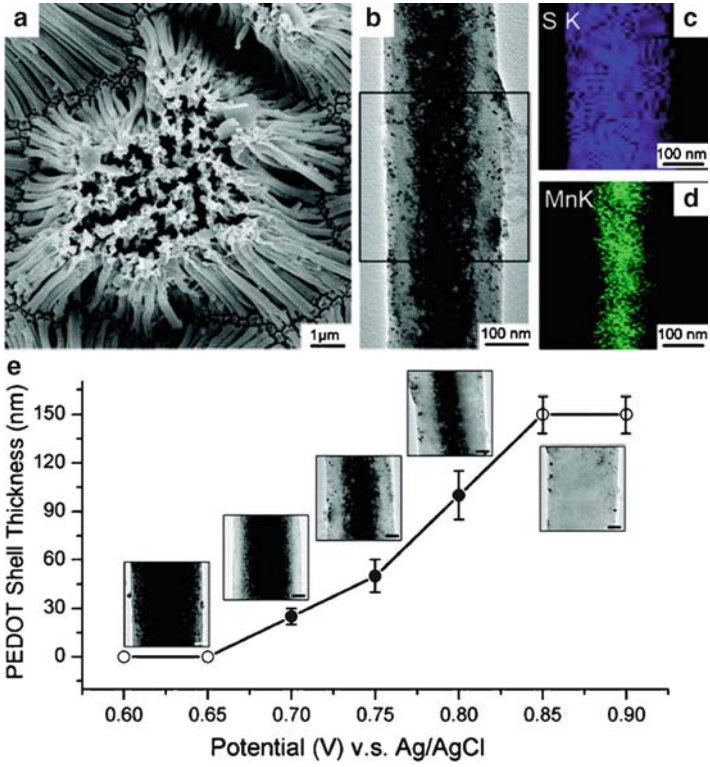

Figure 10. SEM image of MnO_2/PEDOT nanowires deposited at 0.75 V (**a**), TEM image of a nanowire (**b**), EDS elemental maps for S and Mn [(**c**) and (**d**)], and PEDOT shell thickness variations as a function of potential (**e**) (Scale bar: 50 nm). Courtesy of Liu et al. Reprinted with permission from Liu and Lee.[220] Copyright 2008 American Chemical Society.

possible. Deposition potential determines the PEDOT shell thickness and MnO_2 core diameter. The effect of depositing potential on microstructure of the wires and the PEDOT shell thickness is shown in Fig. 10. Superior specific capacitance and stability of capacitance with current density was achieved with the coaxial nanowires in comparison with either of the individual materials. The specific capacitance for MnO_2 nanowires, PEDOT nanowires, MnO_2 thin film, and MnO_2/PEDOT coaxial nanowires as a function of current density is shown in Fig. 11.

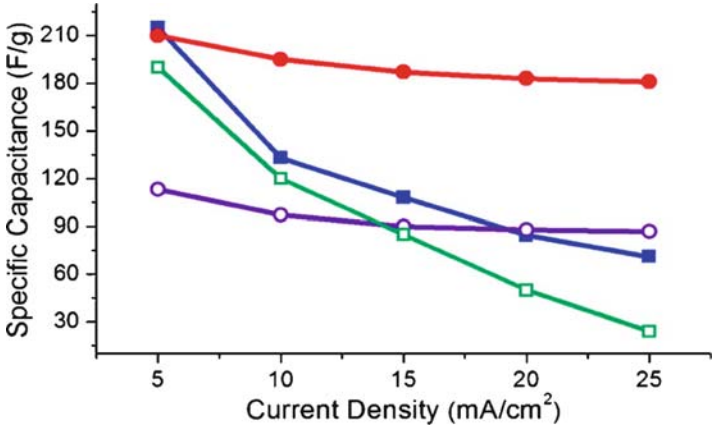

Figure 11. Specific capacitance as a function of charge/discharge current density for MnO_2 nanowires (*solid squares*), PEDOT nanowires (*hollow circles*), MnO_2 thin film (*hollow squares*), and MnO_2/PEDOT nanowires (*solid circles*). Courtesy of Liu et al. Reprinted with permission from Liu and Lee. [220] Copyright 2008 American Chemical Society.

Despite the limited improvements in material development for supercapacitor electrodes, the specific capacitance and life cycle of the newly developed materials cannot be compared with those of RuO_2.

Electrodeposition is a unique, versatile technique for fabrication of metal oxide, polymer, and composite electrodes for electrochemical supercapacitors. Composition, crystal structure, and morphology of the deposits can be easily manipulated by adjusting the electrodeposition parameters to achieve improved capacitive behavior. Current progress, however, is far from the commercial expectations for electrochemical supercapacitors.

V. LITHIUM ION BATTERIES

Rechargeable lithium ion batteries are of great importance at the present time due to their superiority in terms of volumetric and gravimetric energy density and cycle life, in comparison with their traditional counterparts including value regulated lead acid (VRLA), nickel cadmium (Ni–Cd), and nickel metal hybrid

(Ni–MH) secondary cells.[221] In addition to their conventional use in mobile electronics, telecommunications, and computing, lithium ion batteries have gained a significant consideration for application in hybrid and electric vehicles.[221,222] A single cell of lithium ion battery is composed of an electrolyte, anode (negative electrode) and a cathode (positive electrode). The electrolyte is conventionally an ion conducting solid polymer with a negligible electronic conductivity [e.g., crystalline complexes of poly(ethylene oxide) and $LiXF_6$ (X = P, As, Sb)].[222] The anode is either Li metal or a compound which acts as a host for Li via undergoing highly reversible insertion (e.g., LiC_6, LiAl, Li_3As, Li_2Si_5, Li_2Sn_5, etc.) or conversion reactions (e.g., CoO, CuO, NiO, Co_3O_4, etc.).[222] The cathode is also a lithium accepting material, but with a greater positive redox potential (e.g., TiS_2, MnO_2, $LiMn_2O_4$, $LiCoO_2$, etc.).[222] In lithium insertion reactions, Li^+ is incorporated into the electrode material; while in conversion reactions, the metal oxide is fully reduced to metallic nanoparticles by Li^+ ions, which form a layer of Li_2O surrounding the reduced metal particles. The followings are the examples of insertion and conversion overall cell reactions during charge/discharge:

$$\text{Insertion: } LiCoO_2 + C \underset{\leftarrow \text{ discharge}}{\overset{\text{charge} \rightarrow}{\rightleftharpoons}} Li_xC + Li_{1-x}CoO_2$$

$$\text{Conversion: } Co_3O_4 + 8Li \underset{\leftarrow \text{ discharge}}{\overset{\text{charge} \rightarrow}{\rightleftharpoons}} 3Co + 4Li_2O$$

1. Tin-Oxide-Based Anodes

Among various anode materials capable of lithium insertion, Sn-based materials offer marked advantages particularly in terms of specific capacity and energy density. Lithium can be inserted into Sn to form $Li_{22}Sn_5$ with a theoretical specific capacity of 992 A h kg^{-1} which is noticeably higher than that of graphite (372 A h kg^{-1}).[223,224] In 1997, the first Sn-based lithium ion battery was introduced by Fuji Photo Film Celtech Co. (Japan) under the trademark of Stalion®.[225–227] The anode material used in Stalion® was an amorphous Sn-based composite oxide (abbreviated as TCO). This composite also contained Al_2O_3, B_2O_3, and Sn phosphate, as a glassy, inactive matrix.[228] Initial, irreversible reaction of tin oxide with Li results in reduction of SnO to Sn, as metallic nanoparticles,

and formation of Li_2O.[228] This step irreversibly consumes Li and leads to a capacity loss during the first conversion cycle. The metallic nanoparticles of Sn, in the second step, can accept Li^+ ions up to $Li_{22}Sn_5$.[228] The following reactions correspond to the first and second steps:

$$SnO_x + 2xLi^+ + 2xe^- \rightarrow xLi_2O + Sn \text{ (first step: irreversible)}$$
$$xLi_2O + Sn + yLi^+ \leftrightarrow xLi_2O + Li_ySn \text{ (second step: cycling)}$$

Formation of the electrochemically reduced nanoscale Sn particles is the main purpose of using tin oxide instead of metallic Sn. The nanoscale Sn particles facilitate insertion/deinsertion of lithium ions by shortening of the diffusion paths for lithium ions.

Nevertheless, in addition to the irreversible capacity loss during the first discharge cycle, Sn-based anodes suffer from poor cycle life. Li insertion/deinsertion in anode material is associated with volume variations. Huge changes in volume upon cycling induce severe mechanical stresses which, in turn, lead to damaging of the brittle, ionic electrode material.[229] Such a mechanical damage significantly affects the cycle life. This issue not only affects Sn-based anodes but also all other intermetallic anode materials and is considered as the main drawback of such materials in comparison with graphite which only exhibits 10% volume change during cycling.[222] Although the volume change problem can be alleviated by addition of inactive materials acting as buffer to accommodate the strains, the energy density of the battery will be adversely affected due to a load of additional inactive materials. One potential solution to the volume variation issue is to move from flat, thin films to special micro/nanoarchitectures that are capable of providing free spaces to accommodate the strains. The active materials can be synthesized using template or template-free methods. Cathodic deposition of Sn followed by a subsequent oxidation in air[230] or anodic deposition of tin oxides[231] have been very recently developed and studied.

Ortiz et al. have developed and studied a nanocomposite of SnO in a TiO_2 nanotube network using a two-step electrochemical synthesis method.[230] The TiO_2 matrix was fabricated via electrochemical oxidation of a Ti substrate. The TiO_2 matrix provides a reasonably conductive substrate for the subsequent electrodeposition of Sn. The conductivity of TiO_2 can be further improved

by Li insertion. Tin was electrodeposited from a nitrate containing chloride-based bath using Pt as the anode. The current density was 5 mA cm^{-2} and the deposition time was 6 min. The total thickness of the film was 1.6 µm. The electrodeposited Sn/TiO_2 composite film was subsequently annealed in air at 350°C for 3 h to oxidize Sn to SnO. The capacity per unit area of SnO/TiO_2 and Sn/TiO_2 (as deposited) films was measured as a function of cycle number for up to 50 cycles. Both films showed reasonably stable capacity during cycling, but a superior capacity was observed for the annealed (SnO/TiO_2) anode (Fig. 12). The large drop in capacity after the first discharge was attributed to the irreversible consumption of Li as Li_2O as well formation of an ionically conductive, passivating reaction layer on the electrode surface, conventionally referred to as solid electrolyte interface (SEI). Although a 53% drop in capacity was observed after the second discharge cycle, these composites exhibited a relatively stable cycling behavior.

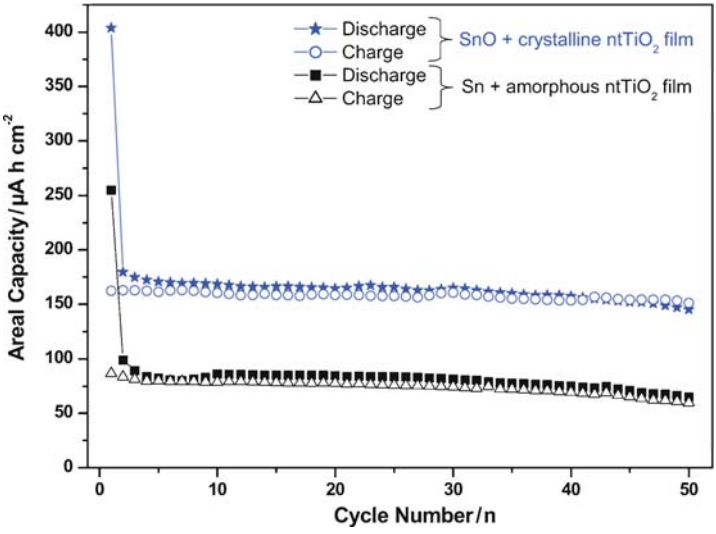

Figure 12. Specific capacity of the SnO/TiO_2 and Sn/TiO_2 films as a function of cycle number. *Hollow and solid symbols* represent the charge and discharge, respectively. The current density for both charge and discharge was 100 µA cm^{-2}. Courtesy of Ortiz et al.[230] Reproduced by permission of ECS – The Electrochemical Society.

Chou et al. were the first to report a template-free, one-step method for synthesizing SnO_2 mesoscale tubes via an anodic deposition process.[231] The anodic deposition of SnO_2 was conducted in a nitrate containing, chloride-based Sn bath with Pt as both cathode and anode substrate. The electrodeposition was performed under potentiostatic condition.

The following reactions were suggested to be involved in this anodic deposition process at potentials greater than 1.6 V vs. SCE (the redox potential for oxygen):

$$Sn^{2+} + 4H_2O \rightarrow Sn(OH)_4 + 2e^- + 4H^+$$
$$2Sn(OH)_4 \rightarrow Sn_2O(OH)_6 + H_2O \rightarrow SnO_2 + 4H_2O$$
$$2H_2O \rightarrow O_2 + 4H^+ + 4e^-$$
$$2Sn^+ + O_2 + 6H_2O \leftrightarrow 2Sn(OH)_4 + 4H^+$$
$$2Sn(OH)_4 \rightarrow Sn_2O(OH)_6 + H_2O \rightarrow SnO_2 + 4H_2O$$

Anodic deposition of SnO_2 at potentials greater than 1.6 V vs. SCE is associated with evolution of oxygen bubbles, which act as pseudotemplates to manipulate the SnO_2 morphology. The deposition potential that determines the rate of oxygen liberation is a key parameter controlling the morphology of the film. At low potentials, insufficient for oxygen evolution, no significant nanoscale morphology was observed. Conversely, application of a high potential (i.e., 2.0 V vs. SCE) well above that for oxygen generation resulted in a bowl-like morphology. The optimal potential to obtain uniform mesoscale tubes was determined to be 1.8 V vs. SCE. The deposition time influenced the length of mesoscale tubes. For short deposition times (e.g., initial 5 min), spherical/half-spherical morphology was obtained. For longer deposition times (e.g., 15 min), hollow spheres grew to a tubular structure. Excessively long deposition times (e.g., 10 h), however, resulted in 10-μm long tubes, which collapsed due to their mechanical instability. The deposit morphology obtained at 1.8 V for 60 min is represented in Fig. 13.

It was observed that mesoscale tubes show superior specific capacity and Coulombic efficiency in comparison with the microbowls of SnO_2. The specific capacity and Coulombic efficiency at 2-C ($C = 790\,mA\,g^{-1}$) charge/discharge rate for mesoscale tubes were $1{,}164\,mA\,h\,g^{-1}$, 35.3% for the first cycle and $462\,mA\,h\,g^{-1}$, 98.9% after 150 cycles, respectively. These values for microbowls were $909\,mA\,h\,g^{-1}$, 25.0% for the first cycle and $261\,mA\,h\,g^{-1}$, 98.0%

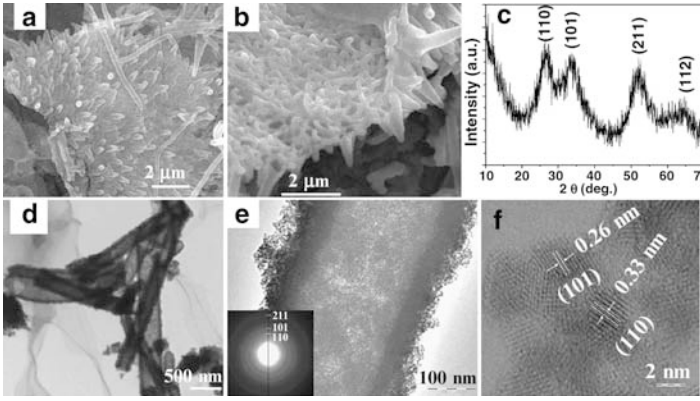

Figure 13. SEM image of the surface (**a**), the underside of the peeled film (**b**), the X-ray diffraction pattern (XRD) (**c**), and TEM images of the as-deposited SnO_2 [(**d**)–(**f**)]. The tube walls are composed of ~4-nm SnO_2 particles. Courtesy of Chou et al. Reprinted from Chou et al.[231] with permission from Elsevier.

after 150 cycles, respectively. The improvement achieved was attributed to the shorting of diffusion paths and lower activation energy for Li insertion/deinsertion in mesoscale structure in comparison with microbowl morphology of the SnO_2 film.

2. Tin and Tin Intermetallic Anodes

Since metallic Sn has a high capacity for reversible Li insertion, pure Sn as well as its intermetallic compounds have been considered as promising anode materials in lithium ion batteries. In intermetallic compounds of Sn, the second metal is normally electrochemically inactive and cannot be alloyed with Li. Such an inactive metal performs as a buffer to accommodate volume variations during Li insertion/deinsertion in Sn.[224] Among various Sn intermetallic compounds, Ni_3Sn_4[232–235] and Cu_6Sn_5[236,237] are the most commonly studied materials. Intermetallic compounds of Sn with Ni and Cu can be electrochemically deposited. Templates are conventionally used to improve the morphological properties and, thus, the electrochemical behavior of the electrodeposited Sn and Sn intermetallic compounds. Copper nanopillars can be electrodeposited within alumina templates on a Cu foil to provide a unique template for the subsequent electrodeposition of Sn or its intermetallic compounds.

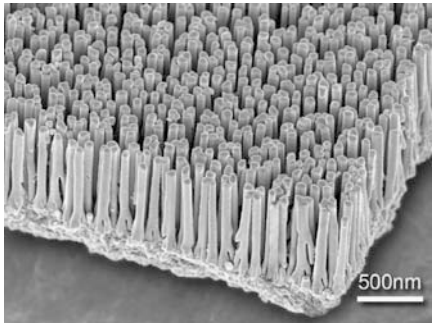

Figure 14. A Cu template consisting of electrodeposited Cu nanopillars on a Cu foil. Courtesy of Bazin et al. Reprinted from Bazin et al.[239] with permission from Elsevier.

These nanopillars not only provide free space for volume variations but also act as a promising current collector. Synthesis of such Cu templates was first introduced by Taberna et al. for use as the substrate/current collector for electrodeposition of Fe_3O_4, as a conversion type anode material.[238] A typical structure of a Cu template is illustrated in Fig. 14.

Bazin et al. developed and studied a process for electrodeposition of pure Sn onto Cu templates.[239] The electrodeposition was performed from a solution containing $SnCl_2$, methane sulfonic acid, and β-naphthol and gelatin as additives. The deposition time was adjusted to 5 min to inhibit extra deposition, which led to filling of the gaps among the Cu pillars and formed a planar surface. It was hypothesized that Sn alloys with Cu form a thin Cu_6Sn_5 intermetallic layer on the surface of Cu pillars. This further assists the accommodation of the volume variations during discharge process. It was observed that the thick Sn films on planar Cu (electrodeposited for 5 min) show rapid capacity degradation over cycling, while Sn covered Cu nanopillars show a good cycling behavior (Fig. 15a). Very thin films of Sn on planar Cu (electrodeposited for 5 min), however, exhibited a similar cycle stability to the Sn covered nanopillars (Fig. 15b). Nevertheless, the specific capacity of Sn on planar Cu was five times smaller than that for Sn covered nanopillars. The improved stability of Sn thin films on planar Cu was attributed to a better accommodation of strains, while the higher capacity of the Sn covered nanopillars was ascribed to a greater surface area.

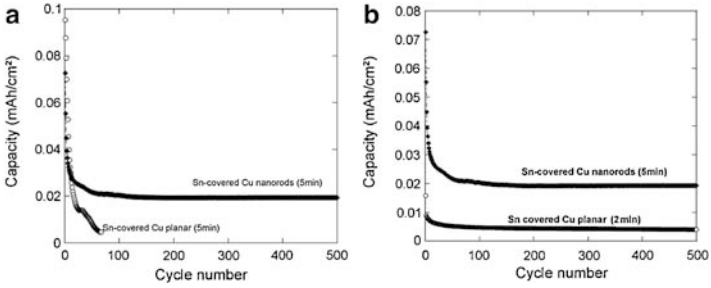

Figure 15. Specific capacity of Sn covered Cu nanopillars and thick planar Cu (**a**) and (**b**) Sn covered Cu thin film as a function of cycle number. Courtesy of Bazin et al. Reprinted from Bazin et al.[239] with permission from Elsevier.

Electrodeposition of Ni_3Sn_4 onto a Cu nanopillar template has been recently reported by Hassoun et al.[240] The deposition bath contained $NiCl_2$ (0.075 M), $SnCl_2$ (0.175 M), $K_2P_2O_7$, glycine, and NH_4OH, and the anode used was Pt. The authors of this work studied the effect of morphology on electrochemical behavior of the Ni_3Sn_4 deposits by comparing two specimens both deposited onto Cu template but with varying deposition times. Long deposition times for one sample resulted in filling of the spaces among the pillars, while short deposition time for the sample almost retained the original morphology of the Cu pillars. The initial specific capacity of the flat samples was 400 mA h g^{-1} (40% of the theoretical value), but a severe decay after 50th cycle was observed. The specific capacity for Ni_3Sn_4 on the sample with pillar morphology was 500 mA h g^{-1}, and no indication of decay was observed for more than 200 cycles. The SEM images of the Ni_3Sn_4 samples deposited on the planar surface and pillar morphology after 200 cycles are represented in Fig. 16a, b, respectively. Structural damage is evidently seen for the sample deposited on a planar surface, while the sample with pillar morphology retained its pristine shape to some extents.

To achieve a stably high specific capacity, the anode material's intrinsic properties and the morphology of film and its ability to accommodate the volume variations during charge/discharge processes are equally important. Electrodeposition is a practical technique for synthesizing promising structure capable of providing long cycle life for anodes used in lithium ion batteries. Recent research and the direction for the future developments have concentrated on

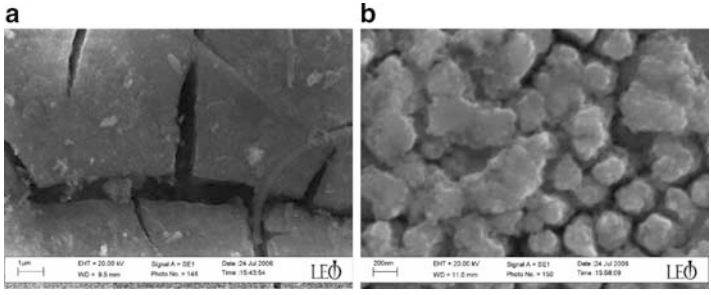

Figure 16. SEM images of electrodeposited Ni_3Sn_4 after 200 cycles on Cu template (**a**) flat surface and (**b**) nanopillar morphology. Courtesy of Hassoun et al. Reprinted from Hassoun et al.[240] Copyright Wiley-VCH Verlag GmbH & Co. KGaA. Reproduced with permission.

manipulating material morphology to improve the cycle life for the future generation of lithium ion batteries. Electrodeposition of alloys, in particular Sn intermetallic compounds, plays a critical role to achieve this goal.

VI. CONCLUSIONS

Novel electrochemical devices require components with special architectures to enhance the performance and reduce the manufacturing costs. Although such unique structures can be achieved through a variety of techniques, electrodeposition offers distinct advantages of being straightforward yet versatile and cost effective. In low temperature fuel cells, electrodeposition of Pt and its alloys, in comparison with alternative chemical techniques, significantly increases the Pt utilization, lowers the raw material costs, and enhances the performance of membrane electrode assemblies. Highly conductive/protective coatings for stainless steel interconnects used in high temperature SOFCs can only be applied on complex configurations by means of electrodeposition. For supercapacitor electrodes, composites of metal oxide/polymer with unique, core/shell structures; high capacitance; charge/discharge rate; and long cycle life have been attained using electrodeposition with or without use of templates. In rechargeable lithium ion batteries with Sn-based anodes, the issue of volume variations and premature anode degradation can

be mitigated using an electrodeposited Cu template, which provides free spaces to accommodate volume changes. The current research is advancing toward manipulation of materials' morphology and structure to enhance mass and charge transfer. In this way, electrodeposition plays a key role.

ACKNOWLEDGMENTS

The author is thankful to his former colleagues from the Department of Chemical and Materials Engineering at the University of Alberta, Dr. D.G. Ivey and Ms. Banafsheh Babakhani who assisted him with preparation of materials for a portion of this chapter.

REFERENCES

[1]M. C. Williams, *Fuel Cell Handbook*, U.S. Department of Energy, Morgantown (2000).
[2]E. Chen, *Fuel Cell Technology Handbook,* CRC Press, Boca Raton (2003).
[3]M. C. William, in *ASM Handbook,* Vol. 13A, Ed. by S. D. Carmer and B. S. Covino, ASM International, Materials Park, OH (2003) 178.
[4]K. Lee, J. J. Zhang, H. J. Wang, and D. P. Wilkinson, *J. Appl. Electrochem.* **36** (2006) 507.
[5]S. Litster and G. McLean, *J. Power Sources* **130** (2004) 61.
[6]H. S. Kim, N. P. Subramanian, and B. N. Popov, *J. Power Sources* **138** (2004) 14.
[7]M. Uchida, Y. Aoyama, N. Eda, and A. Ohta, *J. Electrochem. Soc.* **142** (1995) 4143.
[8]E. J. Taylor, E. B. Anderson, and N. R. K. Vilambi, *J. Electrochem. Soc.* **139** (1992) L45.
[9]S. Hirano, J. Kim, and S. Srinivasan, *Electrochim. Acta* **42** (1997) 1587.
[10]J. Martin, A. M. Chaparro, B. Gallardo, M. A. Folgado, and L. Daza, *J. Power Sources* **192** (2009) 14.
[11]J. J. Li, F. Ye, L. Chen, T. T. Wang, J. L. Li, and X. D. Wang, *J. Power Sources* **186** (2009) 320.
[12]S. M. Ayyadurai, Y. S. Choi, P. Ganesan, S. P. Kumaraguru, and B. N. Popov, *J. Electrochem. Soc.* **154** (2007) B1063.
[13]Z. D. Wei, S. H. Chan, L. L. Li, H. F. Cai, Z. T. Xia, and C. X. Sun, *Electrochim. Acta* **50** (2005) 2279.
[14]H. Kim and B. N. Popov, *Electrochem. Solid-State Lett.* **7** (2004) A71.
[15]S. D. Thompson, L. R. Jordan, and M. Forsyth, *Electrochim. Acta* **46** (2001) 1657.
[16]O. Antoine and R. Durand, *Electrochem. Solid-State Lett.* **4** (2001) A55.
[17]F. Ye, T. T. Wang, J. J. Li, Y. L. Wang, J. L. Li, and X. D. Wang, *J. Electrochem. Soc.* **156** (2009) B981.
[18]F. Ye, J. J. Li, T. T. Wang, Y. Liu, H. J. Wei, J. L. Li, and X. D. Wang, *J. Phys. Chem. C* **112** (2008) 12894.
[19]Y. J. Song, J. K. Oh, and K. W. Park, *Nanotechnology* **19** (2008).
[20]S. Kim and S. J. Park, *Electrochim. Acta* **53** (2008) 4082.

[21]F. Ye, L. Chen, J. J. Li, J. L. Li, and X. D. Wang, *Electrochem. Commun.* **10** (2008) 476.
[22]T. Selvaraju and R. Ramaraj, *J. Electroanal. Chem.* **585** (2005) 290.
[23]M. Pan, H. L. Tang, S. P. Jiang, and Z. C. Liu, *J. Electrochem. Soc.* **152** (2005) A1081.
[24]N. Rajalakshmi and K. S. Dhathathreyan, *Int. J. Hydrogen Energy* **33** (2008) 5672.
[25]M. Paunovic and M. Schlesinger, *Electrochemical Deposition,* Wiley, Hoboken, NJ (2006) 77.
[26]N. Kanani, *Electroplating – Basic Principles, Processes and Practice,* Elsevier, Oxford (2004) 88.
[27]C. Wang, M. Waje, X. Wang, J. M. Tang, R. C. Haddon, and Y. S. Yan, *Nano Lett.* **4** (2004) 345.
[28]C. R. K. Rao and D. C. Trivedi, *Coord. Chem. Rev.* **249** (2005) 613.
[29]D. J. Guo and H. L. Li, *J. Electroanal. Chem.* **573** (2004) 197.
[30]H. A. Gasteiger, N. Markovic, P. N. Ross, and E. J. Cairns, *J. Phys. Chem.* **97** (1993) 12020.
[31]H. A. Gasteiger, N. Markovic, P. N. Ross, and E. J. Cairns, *J. Phys. Chem.* **98** (1994) 617.
[32]K. Wang, H. A. Gasteiger, N. M. Markovic, and P. N. Ross, *Electrochim. Acta* **41** (1996) 2587.
[33]P. Waszczuk, G. Q. Lu, A. Wieckowski, C. Lu, C. Rice, and R. I. Masel, *Electrochim. Acta* **47** (2002) 3637.
[34]Y. Ra, J. Lee, I. Kim, S. Bong, and H. Kima, *J. Power Sources* **187** (2009) 363.
[35]N. Q. Minh, *J. Am. Ceram. Soc.* **76** (1993) 563.
[36]P. Singh and N. Q. Minh, *Int. J. Appl. Ceram. Technol.* **1** (2004) 5.
[37]W. Z. Zhu and S. C. Deevi, *Mater. Sci. Eng., A* **362** (2003) 228.
[38]J. H. Zhu, Y. Zhang, A. Basu, Z. G. Lu, M. Paranthaman, D. F. Lee, and E. A. Payzant, *Surf. Coat. Technol.* **177** (2004) 65.
[39]K. Kendall, *Int. Mater. Rev.* **50** (2005) 257.
[40]Z. G. Yang, K. S. Weil, D. M. Paxton, and J. W. Stevenson, *J. Electrochem. Soc.* **150** (2003) A1188.
[41]Z. G. Yang, M. S. Walker, P. Singh, J. W. Stevenson, and T. Norby, *J. Electrochem. Soc.* **151** (2004) B669.
[42]W. Z. Zhu and S. C. Deevi, *Mater. Sci. Eng., A* **348** (2003) 227.
[43]Y. Matsuzaki and I. Yasuda, *J. Electrochem. Soc.* **148** (2001) A126.
[44]H. Yokokawa, T. Horita, N. Sakai, K. Yamaji, M. E. Brito, Y. P. Xiong, and H. Kishimoto, *Solid State Ionics* **177** (2006) 3193.
[45]A. Petric and H. Ling, *J. Am. Ceram. Soc.* **90** (2007) 1515.
[46]A. Brenner, *Electrodeposition of Alloys Principles and Practice,* Academic, New York and London (1963).
[47]P. Wei, O. E. Hileman, M. R. Bateni, X. H. Deng, and A. Petric, *Surf. Coat. Technol.* **201** (2007) 7739.
[48]J. Gong and G. Zangari, *J. Electrochem. Soc.* **149** (2002) C209.
[49]J. E. Lewis, P. H. Scaife, and D. A. J. Swinkels, *J. Appl. Electrochem.* **6** (1976) 453.
[50]M. R. Bateni, P. Wei, X. H. Deng, and A. Petric, *Surf. Coat. Technol.* **201** (2007) 4677.
[51]P. Wei, X. Deng, M. R. Bateni, and A. Petric, *Corrosion* **63** (2007) 529.
[52]J. W. Wu, Y. L. Jiang, C. Johnson, and X. B. Liu, *J. Power Sources* **177** (2008) 376.
[53]J. W. Wu, C. D. Johnson, Y. L. Jiang, R. S. Gemmen, and X. B. Liu, *Electrochim. Acta* **54** (2008) 793.

[54]J. W. Wu, C. D. Johnson, R. S. Gemmen, and X. B. Liu, *J. Power Sources* **189** (2009) 1106.
[55]X. H. Deng, P. Wei, M. R. Bateni, and A. Petric, *J. Power Sources* **160** (2006) 1225.
[56]N. Birks, G. H. Meier, and F. S. Pettit, *Introduction to the High-Temperature Oxidation of Metals*, Cambridge University Press, New York (2006).
[57]D. J. Young, Editor, *High Temperature Oxidation and Corrosion of Metals, Elsevier*, Amsterdam (2008).
[58]N. Shaigan, D. G. Ivey, and W. X. Chen, *J. Power Sources* **183** (2008) 651.
[59]N. Shaigan, D. G. Ivey, and W. X. Chen, *J. Electrochem. Soc.* **155** (2008) D278.
[60]N. Shaigan, D. G. Ivey, and W. X. Chen, *J. Power Sources* **185** (2008) 331.
[61]D. P. Whittle and J. Stringer, *Philos. Trans. R. Soc. Lond A* **295** (1980) 309.
[62]A. Hovestad and L. J. J. Janssen, in *Modern Aspects of Electrochemistry,* Vol. 38, Ed. by B.E. Conway, C.G. Vayenas, and R. White, Kluwer/Plenum, New York (2005).
[63]W. F. Wei, W. X. Chen, and D. G. Ivey, *J. Phys. Chem. C* **111** (2007) 10398.
[64]W. F. Wei, W. Chen, and D. G. Ivey, *Chem. Mater.* **19** (2007) 2816.
[65]W. F. Wei, W. X. Chen, and D. G. Ivey, *Chem. Mater.* **20** (2008) 1941.
[66]W. F. Wei, W. X. Chen, and D. G. Ivey, *J. Power Sources* **186** (2009) 428.
[67]S. Arico, P. Bruce, B. Scrosati, J. M. Tarascon, and W. Van Schalkwijk, *Nat. Mater.* **4** (2005) 366.
[68]E. Conway, *Electrochemical Supercapacitors*, Kluwer/Plenum, New York (1999).
[69]V. V. N. Obreja, *Physica E* **40** (2008) 2596.
[70]E. Frackowiak and F. Beguin, *Carbon* **39** (2001) 937.
[71]J. Gamby, P. L. Taberna, P. Simon, J. F. Fauvarque, and M. Chesneau, *J. Power Sources* **101** (2001) 109.
[72]T. Osaka, X. J. Liu, M. Nojima, and T. Momma, *J. Electrochem. Soc.* **146** (1999) 1724.
[73]D. Y. Qu, *J. Power Sources* **109** (2002) 403.
[74]T. Saito, Y. Kibi, M. Kurata, J. Tabuchi, and A. Ochi, *NEC Res. Dev.* **36** (1995) 193.
[75]H. Shi, *Electrochim. Acta* **41** (1996) 1633.
[76]N. L. Wu and S. Y. Wang, *J. Power Sources* **110** (2002) 233.
[77]K. H. An, W. S. Kim, Y. S. Park, J. M. Moon, D. J. Bae, S. C. Lim, Y. S. Lee, and Y. H. Lee, *Adv. Funct. Mater.* **11** (2001) 387.
[78]K. H. An, K. K. Jeon, J. K. Heo, S. C. Lim, D. J. Bae, and Y. H. Lee, *J. Electrochem. Soc.* **149** (2002) A1058.
[79]T. Bordjiba, M. Mohamedi, and L. H. Dao, *Adv. Mater.* **20** (2008) 815.
[80]Y. H. Lee, K. H. An, S. C. Lim, W. S. Kim, H. J. Jeong, C. H. Doh, and S. I. Moon, *New Diam. Front. Carbon Technol.* **12** (2002) 209.
[81]K. Liang, A. Chen, Z. S. Feng, and Z. X. Ye, *Acta Phys. Chim. Sin.* **18** (2002) 381.
[82]G. Liu, M. Liu, M. Z. Wang, and H. M. Cheng, *New Carbon Mater.* **17** (2002) 64.
[83]J. Yoon, S. H. Jeong, K. H. Lee, H. S. Kim, C. G. Park, and J. H. Han, *Chem. Phys. Lett.* **388** (2004) 170.
[84]P. Gouerec, D. Miousse, F. Tran-Van, and L. H. Dao, *J. New Mater. Electrochem. Syst.* **2** (1999) 221.
[85]S. J. Kim, S. W. Hwang, and S. H. Hyun, *J. Mater. Sci.* **40** (2005) 725.
[86]J. Li, X. Y. Wang, Q. H. Huang, S. Gamboa, and P. J. Sebastian, *J. Power Sources* **158** (2006) 784.
[87]Q. H. Meng, L. Liu, H. H. Song, R. Zhang, and L. C. Ling, *J. Inorg. Mater.* **19** (2004) 593.
[88]H. Probstle, C. Schmitt, and J. Fricke, *J. Power Sources* **105** (2002) 189.
[89]H. Probstle, M. Wiener, and J. Fricke, *J. Porous Mater.* **10** (2003) 213.

[90]J. H. Zhou, Y. J. Ji, J. P. He, C. X. Zhang, and G. W. Zhao, *Microporous Mesoporous Mater.* **114** (2008) 424.
[91]S. B. Ma, K. W. Nam, W. S. Yoon, X. Q. Yang, K. Y. Ahn, K. H. Oh, and K. B. Kim, *Electrochem. Commun.* **9** (2007) 2807.
[92]S. Wen, J. W. Lee, I. H. Yeo, J. Park, and S. Mho, *Electrochim. Acta* **50** (2004) 849.
[93]D. Zhao, M. W. Xu, W. H. Zhou, J. Zhang, and H. L. Li, *Electrochim. Acta* **53** (2008) 2699.
[94]M. B. Zheng, Z. X. Ling, S. T. Liao, Z. J. Yang, G. B. Ji, J. M. Cao, and J. Tao, *Acta Chim. Sin.* **67** (2009) 1069.
[95]W. F. Wei, X. W. Cui, W. X. Chen, and D. G. Ivey, *J. Phys. Chem. C* **112** (2008) 15075.
[96]W. F. Wei, X. W. Cui, W. X. Chen, and D. G. Ivey, *J. Power Sources* **186** (2009) 543.
[97]W. F. Wei, X. W. Cui, W. X. Chen, and D. G. Ivey, *Electrochim. Acta* **54** (2009) 2271.
[98]W. K. Li, J. Chen, J. J. Zhao, J. R. Zhang, and J. J. Zhu, *Maters. Lett.* **59** (2005) 800.
[99]K. S. Ryu, Y. G. Lee, Y. S. Hong, Y. J. Park, X. L. Wu, K. M. Kim, M. G. Kang, N. G. Park, and S. H. Chang, *Electrochim. Acta* **50** (2004) 843.
[100]J. Wang, Y. L. Xu, X. Chen, and X. F. Du, *J. Power Sources* **163** (2007) 1120.
[101]M. White and R. C. T. Slade, *Electrochim. Acta* **49** (2004) 861.
[102]Y. L. Xu, J. Wang, W. Sun, and S. H. Wang, *J. Power Sources* **159** (2006) 370.
[103]T. R. Jow and J. P. Zheng, *J. Electrochem. Soc.* **145** (1998) 49.
[104]J. P. Zheng, P. J. Cygan, and T. R. Jow, *J. Electrochem. Soc.* **142** (1995) 2699.
[105]J. P. Zheng and T. R. Jow, *J. Electrochem. Soc.* **142** (1995) L6.
[106]R. Rolison, R. W. Long, J. C. Lytle, A. E. Fischer, C. P. Rhodes, T. M. Mcevoy, M. E. Bourga, and A. M. Lubers, *Chem. Soc. Rev.* **38** (2009) 226.
[107]S. H. Lee, C. E. Tracy, and J. R. Pitts, *Electrochem. Solid-State Lett.* 7 (2004) A299.
[108]K. Liang, A. Chen, L. He, and W. Wang, *J. Mater. Sci. Technol.* **18** (2002) 383.
[109]K. W. Nam and K. B. Kim, *Electrochemistry* **69** (2001) 467.
[110]K. W. Nam, W. S. Yoon, and K. B. Kim, *Electrochim. Acta* **47** (2002) 3201.
[111]K. R. Prasad and N. Miura, *Appl. Phys. Lett.* **85** (2004) 4199.
[112]X. F. Wang, D. Z. Wang, and J. Liang, *Acta Phys. Chim. Sin.* **21** (2005) 117.
[113]M. Q. Wu, J. H. Gao, S. R. Zhang, and A. Chen, *J. Porous Mater.* **13** (2006) 407.
[114]M. S. Wu, Y. A. Huang, C. H. Yang, and H. H. Jow, *Int. J. Hydrogen Energy* **32** (2007) 4153.
[115]M. S. Wu and H. H. Hsieh, *Electrochim. Acta* **53** (2008) 3427.
[116]M. S. Wu, Y. A. Huang, and C. H. Yang, *J. Electrochem. Soc.* **155** (2008) A798.
[117]M. S. Wu, C. Y. Huang, and K. H. Lin, *J. Power Sources* **186** (2009) 557.
[118]W. Yang, C. L. Xu, and H. L. Li, *Chem. Commun.,* (2008) 6537.
[119]D. D. Zhao, W. J. Zhou, and H. L. Li, *Chem. Mater.* **19** (2007) 3882.
[120]Y. Z. Zheng, H. Y. Ding, and M. L. Zhang, *Mater. Res. Bull.* **44** (2009) 403.
[121]X. M. Liu, X. G. Zhang, and S. Y. Fu, *Mater. Res. Bull.* **41** (2006) 620.
[122]K. W. Nam and K. B. Kim, *J. Electrochem. Soc.* **149** (2002) A346.
[123]U. M. Patil, R. R. Salunkhe, K. V. Gurav, and C. D. Lokhande, *Appl. Surf. Sci.* **255** (2008) 2603.
[124]X. F. Wang and X. H. Kong, *J. Inorg. Mater.* **16** (2001) 815.
[125]Y. Y. Xi, D. Li, A. B. Djurisic, M. H. Xie, K. Y. K. Man, and W. K. Chan, *Electrochem. Solid-State Lett.* **11** (2008) D56.
[126]B. Zhang, Y. K. Zhou, and H. L. Li, *Mater. Chem. Phys.* **83** (2004) 260.
[127]M. J. Deng, F. L. Huang, I. W. Sun, W. T. Tsai, and J. K. Chang, *Nanotechnology* **20** (2009) 175602 (5pp).
[128]S. G. Kandalkar, C. D. Lokhande, R. S. Mane, and S. H. Han, *Appl. Surf. Sci.* **253** (2007) 3952.

[129]S. G. Kandalkar, J. L. Gunjakar, and C. D. Lokhande, *Appl. Surf. Sci.* **254** (2008) 5540.
[130]S. G. Kandalkar, J. L. Gunjakar, C. D. Lokhande, and O. S. Joo, *J. Alloys Compd* **478** (2009) 594.
[131]J. Kim and S. G. Park, *Electrochemistry* **69** (2001) 848.
[132]K. Kim, T. Y. Seong, J. H. Lim, W. I. Cho, and Y. S. Yoon, *J. Power Sources* **102** (2001) 167.
[133]S. Lichusina, A. Chodosovskaja, A. Selskis, K. Leinartas, P. Miecinskas, and E. Juzeliunas, *Chemija* **19** (2008) 7.
[134]C. Lin, J. A. Ritter, and B. N. Popov, *J. Electrochem. Soc.* **145** (1998) 4097.
[135]V. Gupta, S. Gupta, and N. Miura, *J. Power Sources* **177** (2008) 685.
[136]P. K. Nayak and N. Munichandraiah, *J. Electrochem. Soc.* **155** (2008) A855.
[137]W. J. Zhou, D. D. Zhao, M. W. Xu, C. L. Xu, and H. L. Li, *Electrochim. Acta* **53** (2008) 7210.
[138]W. J. Zhou, J. Zhang, T. Xue, D. D. Zhao, and H. L. Li, *J. Mater. Chem.* **18** (2008) 905.
[139]V. R. Shinde, S. B. Mahadik, T. P. Gujar, and C. D. Lokhande, *Appl. Surf. Sci.* **252** (2006) 7487.
[140]S. L. Xiong, C. Z. Yuan, M. F. Zhang, B. J. Xi, and Y. T. Qian, *Chem. Eur. J.* **15** (2009) 5320.
[141]N. Nagarajan and I. Zhitomirsky, *J. Appl. Electrochem.* **36** (2006) 1399.
[142]J. Chang, W. J. Lee, R. S. Mane, B. W. Cho, and S. H. Han, *Electrochem. Solid-State Lett.* **11** (2008) A9.
[143]Z. A. Hu, Y. L. Xie, Y. X. Wang, L. P. Mo, Y. Y. Yang, and Z. Y. Zhang, *Mater. Chem. Phys.* **114** (2009) 990.
[144]R. S. Mane, J. Chang, D. Ham, B. N. Pawar, T. Ganesh, B. W. Cho, J. K. Lee, and S. H. Han, *Curr. Appl. Phys.* **9** (2009) 87.
[145]R. K. Selvan, I. Perelshtein, N. Perkas, and A. Gedanken, *J. Phys. Chem. C* **112** (2008) 1825.
[146]S. W. Hwang and S. H. Hyun, *J. Power Sources* **172** (2007) 451.
[147]Q. T. Qu, Y. Shi, L. L. Li, W. L. Guo, Y. P. Wu, H. P. Zhang, S. Y. Guan, and R. Holze, *Electrochem. Commun.* **11** (2009) 1325.
[148]H. M. Zeng, Y. Zhao, Y. J. Hao, Q. Y. Lai, J. H. Huang, and X. Y. Ji, *J. Alloys Compd* **477** (2009) 800.
[149]M. Toupin, T. Brousse, and D. Belanger, *Chem. Mater.* **14** (2002) 3946.
[150]C. C. Hu and T. W. Tsou, *Electrochem. Commun.* **4** (2002) 105.
[151]B. Djurfors, J. N. Broughton, M. J. Brett, and D. G. Ivey, *Acta Mater.* **53** (2005) 957.
[152]X. Y. Wang, X. Y. Wang, W. G. Huang, P. J. Sebastian, and S. Gamboa, *J. Power Sources* **140** (2005) 211.
[153]K. Chang, Y. L. Chen, and W. T. Tsai, *J. Power Sources* **135** (2004) 344.
[154]B. Djurfors, J. N. Broughton, M. J. Brett, and D. G. Ivey, *J. Mater. Sci.* **38** (2003) 4817.
[155]V. Subramanian, H. W. Zhu, R. Vajtai, P. M. Ajayan, and B. Q. Wei, *J. Phys. Chem. B* **109** (2005) 20207.
[156]J. N. Broughton and M. J. Brett, *Electrochim. Acta* **50** (2005) 4814.
[157]J. K. Chang and W. T. Tsai, *J. Electrochem. Soc.* **152** (2005) A2063.
[158]S. Devaraj and N. Munichandraiah, *Electrochem. Solid-State Lett.* **8** (2005) A373.
[159]C. Ye, Z. M. Lin, and S. Z. Hui, *J. Electrochem. Soc.* **152** (2005) A1272.
[160]Z. A. Zhang, B. C. Yang, M. G. Deng, and Y. D. Hu, *J. Inorg. Mater.* **20** (2005) 529.

[161]B. Djurfors, J. N. Broughton, M. J. Brett, and D. G. Ivey, *J. Power Sources* **156** (2006) 741.
[162]A. Taguchi, S. Inoue, S. Akamaru, M. Hara, K. Watanabe, and T. Abe, *J. Alloys Compd* **414** (2006) 137.
[163]N. Nagarajan, H. Humadi, and I. Zhitomirsky, *Electrochim. Acta* **51** (2006) 3039.
[164]B. Djurfors, J. N. Broughton, M. J. Brett, and D. G. Ivey, *J. Electrochem. Soc.* **153** (2006) A64.
[165]W. Nam and K. B. Kim, *J. Electrochem. Soc.* **153** (2006) A81.
[166]E. Machefaux, T. Brousse, D. Belanger, and D. Guyomard, *J. Power Sources* **165** (2007) 651.
[167]K. W. Nam, M. G. Kim, and K. B. Kim, *J. Phys. Chem. C* **111** (2007) 749.
[168]A. Zolfaghari, F. Ataherian, M. Ghaemi, and A. Gholami, *Electrochim. Acta* **52** (2007) 2806.
[169]S. Devaraj and N. Munichandraiah, *J. Electrochem. Soc.* **154** (2007) A80.
[170]V. Subramanian, H. W. Zhu, and B. Q. Wei, *J. Power Sources* **159** (2006) 361.
[171]S. E. Chun, S. I. Pyun, and G. J. Lee, *Electrochim. Acta* **51** (2006) 6479.
[172]R. K. Sharma, H. S. Oh, Y. G. Shul, and H. Kim, *J. Power Sources* **173** (2007) 1024.
[173]T. Lee, J. K. Chang, and W. T. Tsai, *J. Electrochem. Soc.* **154** (2007) A875.
[174]C. H. Liang, C. L. Nien, H. C. Hu, and C. S. Hwang, *J. Ceram. Soc. Jpn* **115** (2007) 319.
[175]N. Nagarajan, M. Cheong, and I. Zhitomirsky, *Mater. Chem. Phys.* **103** (2007) 47.
[176]M. W. Xu, D. D. Zhao, S. J. Bao, and H. L. Li, *J. Solid State Electrochem.* **11** (2007) 1101.
[177]J. Wei, N. Nagarajan, and I. Zhitomirsky, *J. Mater. Process. Technol.* **186** (2007) 356.
[178]S. B. Ma, K. W. Nam, W. S. Yoon, X. Q. Yang, K. Y. Ahn, K. H. Oh, and K. B. Kim, *J. Power Sources* **178** (2008) 483.
[179]Y. C. Hsieh, K. T. Lee, Y. P. Lin, N. L. Wu, and S. W. Donne, *J. Power Sources* **177** (2008) 660.
[180]J. K. Chang, S. H. Hsu, W. T. Tsai, and I. W. Sun, *J. Power Sources* **177** (2008) 676.
[181]S. Devaraj and N. Munichandraiah, *J. Phys. Chem. C* **112** (2008) 4406.
[182]X. H. Yang, Y. G. Wang, H. M. Xiong, and Y. Y. Xia, *Electrochim. Acta* **53** (2007) 752.
[183]S. Devaraj and N. Munichandraiah, *J. Solid State Electrochem.* **12** (2008) 207.
[184]C. J. Xu, B. H. Li, H. D. Du, F. Y. Kang, and Y. Q. Zeng, *J. Power Sources* **180** (2008) 664.
[185]J. Wei and I. Zhitomirsky, *Surf. Eng.* **24** (2008) 40.
[186]J. K. Chang, C. H. Huang, W. T. Tsai, M. J. Deng, I. W. Sun, and P. Y. Chen, *Electrochim. Acta* **53** (2008) 4447.
[187]L. Athouel, F. Moser, R. Dugas, O. Crosnier, D. Belanger, and T. Brousse, *J. Phys. Chem. C* **112** (2008) 7270.
[188]J. K. Chang, C. H. Huang, W. T. Tsai, M. J. Deng, and I. W. Sun, *J. Power Sources* **179** (2008) 435.
[189]P. Staiti and F. Lufrano, *J. Power Sources* **187** (2009) 284.
[190]B. Yuan, M. L. Wang, Y. Q. Wang, and J. Hu, *Electrochim. Acta* **54** (2009) 1021.
[191]J. P. Ni, W. C. Lu, L. M. Zhang, B. H. Yue, X. F. Shang, and Y. Lv, *J. Phys. Chem. C* **113** (2009) 54.
[192]C. J. Xu, B. H. Li, H. D. Do, F. Y. Kang, and Y. Q. Zeng, *J. Power Sources* **184** (2008) 691.
[193]M. Cheong and I. Zhitomirsky, *Surf. Eng.* **25** (2009) 346.

[194]R. R. Jiang, T. Huang, J. L. Liu, J. H. Zhuang, and A. S. Yu, *Electrochim. Acta* **54** (2009) 3047.
[195]K. Nayak and N. Munichandraiah, *Electrochem. Solid-State Lett.* **12** (2009) A115.
[196]W. F. Wei, *Thesis*, University of Alberta, Canada (2009).
[197]M. Toupin, T. Brousse, and D. Belanger, *Chem. Mater.* **16** (2004) 3184.
[198]S. C. Pang, M. A. Anderson, and T. W. Chapman, *J. Electrochem. Soc.* **147** (2000) 444.
[199]H. Y. Lee and J. B. Goodenough, *J. Solid State Chem.* **144** (1999) 220.
[200]C. K. Lin, K. H. Chuang, C. Y. Lin, C. Y. Tsay, and C. Y. Chen, *Surf. Coat. Technol.* **202** (2007) 1272.
[201]J. W. Long, A. L. Young, and D. R. Rolison, *J. Electrochem. Soc.* **150** (2003) A1161.
[202]X. Y. Chen, X. X. Li, Y. Jiang, C. W. Shi, and X. L. Li, *Solid State Commun.* **136** (2005) 94.
[203]M. Nakayama, S. Konishi, H. Tagashira, and K. Ogura, *Langmuir* **21** (2005) 354.
[204]T. Brousse, M. Toupin, R. Dugas, L. Athouel, O. Crosnier, and D. Belanger, *J. Electrochem. Soc.* **153** (2006) A2171.
[205]H. Shirakawa and S. Ikeda, *Polym. J.* **2** (1971) 231.
[206]T. Osaka, S. Komaba, and T. Momma, in *Modern Electroplating*, Ed. by M. Paunovic and M. Schlrsinger, Wiley, New York (2000) 623.
[207]Z. H. Cai and C. R. Martin, *J. Electroanal. Chem.* **300** (1991) 35.
[208]R. Liu, S. Il Cho, and S. B. Lee, *Nanotechnology* **19** (2008) 215710.
[209]K. R. Prasad and N. Munichandraiah, *J. Electrochem. Soc.* **149** (2002) A1393.
[210]K. Sharma, A. C. Rastogi, and S. B. Desu, *Electrochem. Commun.* **10** (2008) 268.
[211]S. Patra and N. Munichandraiah, *J. Appl. Polym. Sci.* **106** (2007) 1160.
[212]G. Heywang and F. Jonas, *Adv. Mater.* **4** (1992) 116.
[213]M. A. del Valle, P. Cury, and R. Schrebler, *Electrochim. Acta* **48** (2002) 397.
[214]N. Sakmeche, E. A. Bazzaoui, M. Fall, S. Aeiyach, M. Jouini, J. C. Lacroix, J. J. Aaron, and P. C. Lacaze, *Synth. Met.* **84** (1997) 191.
[215]N. Sakmeche, J. J. Aaron, M. Fall, S. Aeiyach, M. Jouini, J. C. Lacroix, and P. C. Lacaze, *Chem. Commun.* **24** (1996) 2723.
[216]S. Il Cho and S. B. Lee, Acc. *Chem. Res.* **41** (2008) 699.
[217]C. R. Martin, *Science* **266** (1994) 1961.
[218]X. Crispin, S. Marciniak, W. Osikowicz, G. Zotti, A. W. D. Van der Gon, F. Louwet, M. Fahlman, L. Groenendaal, F. De Schryver, and W. R. Salaneck, *J. Polym. Sci. Part B – Polym. Phys.* **41** (2003) 2561.
[219]L. Groenendaal, G. Zotti, P. H. Aubert, S. M. Waybright, and J. R. Reynolds, *Adv. Mater.* **15** (2003) 855.
[220]R. Liu and S. B. Lee, *J. Am. Chem. Soc.* **130** (2008) 2942.
[221]R. J. Brodd, in *Lithium-Ion Batteries Science and Technology,* Ed. By M. Yoshio, R. J. Brodd, and A. Kozawa, Springer, New York (2009) 1.
[222]A. Patil, V. Patil, D. W. Shin, J. W. Choi, D. S. Paik, and S. J. Yoon, *Mater. Res. Bull.* **43** (2008) 1913.
[223]Y. Idota, T. Kubota, A. Matsufuji, Y. Maekawa, and T. Miyasaka, *Science* **276** (1997) 1395.
[224]M. Winter and J. O. Besenhard, *Electrochim. Acta* **45** (1999) 31.
[225]Y. Idota, *Nonaqueous Secondary Battery,* U.S. Patent 5478671 (1995).
[226]*Nippon Denki Shimbun,* March 11 (1996)
[227]H. Tomyama, Japanese Patent 07-029608 (1995).
[228]N. Dimov, in *Lithium-Ion Batteries Science and Technology,* Ed. by M. Yoshio, R. J. Brodd, and A. Kozawa, Springer, Berlin (2009) 241.

[229]M. M. Thackeray, J. T. Vaughey, C. S. Johnson, A. J. Kropf, R. Benedek, L. M. L. Fransson, and K. Edstrom, *J. Power Sources* **113** (2003) 124.
[230]G. F. Ortiz, I. Hanzu, P. Knauth, P. Lavela, J. L. Tirado, and T. Djenizian, *Electrochem. Solid-State Lett.* **12** (2009) A186.
[231]S. L. Chou, J. Z. Wang, H. K. Liu, and S. X. Dou, *Electrochem. Commun.* **11** (2009) 242.
[232]H. Mukaibo, T. Momma, and T. Osaka, *J. Power Sources* **146** (2005) 457.
[233]Z. P. Guo, Z. W. Zhao, H. K. Liu, and S. X. Dou, *Carbon* **43** (2005) 1392.
[234]X. Z. Liao, Z. F. Ma, H. H. Hu, Y. Z. Sun, and X. X. Yuan, *Electrochem. Commun.* **5** (2003) 657.
[235]H. Y. Lee, S. W. Jang, S. M. Lee, S. J. Lee, and H. K. Baik, *J. Power Sources* **112** (2002) 8.
[236]G. X. Wang, L. Sun, D. H. Bradhurst, S. X. Dou, and H. K. Liu, *J. Alloys Compd* **299** (2000) L12.
[237]K. D. Kepler, J. T. Vaughey, and M. M. Thackeray, *J. Power Sources* **81** (1999) 383.
[238]L. Taberna, S. Mitra, P. Poizot, P. Simon, and J. M. Tarascon, *Nat. Mater.* **5** (2006) 567.
[239]L. Bazin, S. Mitra, P. L. Taberna, P. Poizot, M. Gressier, M. J. Menu, A. Barnabe, P. Simon, and J. M. Tarascon, *J. Power Sources* **188** (2009) 578.
[240]J. Hassoun, S. Panero, P. Simon, P. L. Taberna, and B. Scrosati, *Adv. Mater.* **19** (2007) 1632.

4

The Effect of Morphology of Activated Electrodes on Their Electrochemical Activity

Konstantin I. Popov,[1,2] Predrag M. Živković,[2] and Nebojša D. Nikolić[1]

[1] *ICTM-Institute of Electrochemistry, University of Belgrade, Njegoševa 12, Belgrade, Serbia*
[2] *Faculty of Technology and Metallurgy, University of Belgrade, Karnegijeva 4, Belgrade, Serbia*

I. INTRODUCTION

The noble metals or their oxides are the most convenient substrates for most electrochemical reactions taking place in fuel cells or in industrial electrolysis, for example. Because of this, the "activated" electrodes are introduced, consisting of a conducting, inert support coated with a thin layer of electrocatalyst. In this way, not only the chemical nature of the electrode can be modified but also its morphology and structure in dependence on the procedure of preparation.[1]

The transformation of the properties of an electrode surface from those of an inexpensive inert substrate to those of an active one with a small quantity of an expensive active metal is one of the most important problems of electrocatalysis today. Numerous papers substantiate that different catalyst for different electrochemical

S.S. Djokić (ed.), *Electrodeposition: Theory and Practice*,
Modern Aspects of Electrochemistry 48, DOI 10.1007/978-1-4419-5589-0_4,

reactions have been developed by placing appropriate active nanoparticles, usually of noble metals, on a carbon support, for example, for the electrochemical oxidation of methanol,[2] the electrochemical reduction of oxygen,[3] the electrochemical oxidation of oxalic acid,[4] etc. Naturally, the catalyst can also be placed on metal or carbon substrate by electrodeposition. Formerly, metallic supports were the only substrates used in cathodic formation of electrodeposits. Nowadays, various exotic conductive materials are also experimented.[5]

According to Bockris et al.,[6] the cell voltage of a self-driving cell, U_s, is given by

$$U_s = U_e - \Delta U \tag{1}$$

and the cell voltage of a driven cell, U_d, by

$$U_d = U_e + \Delta U. \tag{2}$$

The power P_s, which can be obtained from self-driving cells, like batteries and fuel cells, is

$$P_s = (U_e - \Delta U)I \tag{3}$$

and the power P_d, required for driving the cells in, for example, electrowining of metals, is

$$P_d = (U_e + \Delta U)I, \tag{4}$$

where

$$\Delta U = \eta_a + \eta_c + IR \tag{5}$$

and U_e is the equilibrium cell potential, η_a and η_c the absolute values of overpotentials of both electrodes, and I and R are the cell current and cell Ohmic resistance, respectively.

The overpotential η in mixed activation–diffusion control is given by

$$\eta = \eta_{ac} + \eta_d, \tag{6}$$

where η_{ac} and η_d are the activation and diffusion overpotential, respectively. It follows from (3) to (6) that ΔU, P_s, and P_d depend on both activation and diffusion overpotentials and on Ohmic voltage drop in the cell.

The activation overpotential mainly depends on the kinetic parameters of processes under consideration on the given substrate

and on the actual current density. The diffusion overpotential mainly depends on the actual current density to the limiting current density ratio, and the Ohmic voltage drop depends on the current in the cell, the composition of the solution, and geometry of the system.

Obviously, ΔU represents the losses of energy, and making U near U_e, or ΔU as low as possible, is the crucial problem of the applied electrochemistry.

There are two basic problems in activation of inert substrates by electrodeposition: first, the effect of the structure of the active surface film on the transformation of electrode from inert to active one[7] and second, effect of the surface morphology on the polarization characteristics of activated electrodes.[8,9] Obviously, in the last case, the nature of the initial substrate is not important. The analysis of both of them is the aim of this chapter. It will be performed for the cathodic reactions. Obviously, the corresponding analysis for the anodic processes can be performed in the similar way.

Metallic electrodeposits allow surfaces with a variety of morphological characteristics to be obtained. The granular electrodeposits represent the model of the partially covered inert substrate.[7] Deposits with a high roughness factor and good mechanical resistance are of particular interest. These two important aspects are usually mutually exclusive, as high values of the roughness factor are mainly obtained through growth of dendrites that have low mechanical resistance.[10] Hence, such coverings are unsuitable as electrocatalysts. On the other hand, the dendritic deposits are the best-known form of the disperse deposits,[11–13] being the most suitable for theoretical analysis. The dendrites are used here as an example of the disperse deposit characterized with large roughness factor during the analysis of the polarization behavior of activated electrodes. This is because this chapter is written in order to explain the polarization behavior of activated electrodes, not to give some concrete technical solutions.

II. MICRO- AND MACROELECTRODES

In all actual electrochemical converters, the electrodes are three-dimensional, porous structures, the pores of which contain the catalyst material to and from which electric charge transfer occurs.[14]

The electrodic catalyst consists of active nanoparticles. The distribution of the active material on the surface inside the pores is very

important for obtaining the necessary activity of the solid phase. This is because the activity of a porous structure depends on both mass transfer through it and on the electrochemical properties of the surface.[7]

Mass transfer in a porous structure strongly depends on macrogeometric parameters, but the electrochemical properties of the surface of the solid phase depend on the mutual relation of the active particles on it, being independent of the macrogeometry of the system.

In spite of some specific characteristics of nanoparticles, this can also be treated as the case of an inert substrate modified with active grains in general. Naturally, for the sake of simplicity, this analysis can be performed for planar electrodes.

According to Scharifker and Hills,[15] in systems where the charge transfer is fast, the rates of growth of nuclei are well described in terms of control by mass transfer of the electrodepositing ions to the growth centers.

During this stage of the growth of the deposit, the nuclei develop diffusion zones around themselves, and as these zones overlap, the hemispherical mass transfer gives way to linear mass transfer to an effectively planar surface. The current then falls, and the transient approaches that corresponding to the total electrode surface.

Similarly, it was shown by Gilleadi[16] that the development of a diffusion field near the surface of an ensemble of microelectrodes occurs in the four successive steps, assuming total diffusion control of the process. The ensemble of microelectrodes consists of microelectrodes placed on the inert surface at distances between their centers larger than their diameter. The first, planar diffusion to the microelectrodes; the second, spherical diffusion with no overlap; the third, spherical diffusion with substantial overlap; and finally, total overlap, equivalent to planar diffusion to the whole surface.

Stonehart and Wheeler[17] and Popov et al.[7] correlated the current densities on the microelectrodes, taking into account the change of concentration around them, with the current density on the macroelectrode. This is because the charge transfer occurs on the microelectrodes, while the mass-transfer limitations are related to the diffusion layer of the macroelectrode. In this chapter, the model of the surface of Popov et al.[7] will be used to describe the polarization behavior of previously activated inert macroelectrode with active microelectrodes.

The cathodic polarization curve equation for flat or large spherical electrode is given by

$$j = \frac{j_0(f_c - f_a)}{1 + \frac{j_0 f_c}{j_L}}, \tag{7}$$

where j, j_0, and j_L are the current density, exchange current density, and limiting diffusion current density, respectively, and

$$f_c = 10^{\frac{\eta}{b_c}}, \tag{8}$$

$$f_a = 10^{-\frac{\eta}{b_a}}, \tag{9}$$

where b_c and b_a are the cathodic and anodic Tafel slopes and η is the overpotential. Equation (7) is modified for use in electrodeposition of metals by taking cathodic current density and overpotential as positive. Derivation of (7) is performed under assumption that the concentration dependence of j_0 can be neglected.[12,18,19]

It is known[12] that electrochemical processes on microelectrodes in bulk solution can be under activation control at overpotentials, which correspond to the limiting diffusion current density plateau of the macroelectrode. The cathodic limiting diffusion current density, $j_{L,Sp}$, for steady-state spherical diffusion is given by:

$$j_{L,Sp} = \frac{nFDC_0}{r} \tag{10}$$

and for steady-state linear diffusion, j_L, by:

$$j_L = \frac{nFDC_0}{\delta}, \tag{11}$$

where n is the number of transferred electrons, F the Faraday constant, D and C_0 the diffusion coefficient and bulk concentration of the depositing ion, respectively, r the radius of the spherical microelectrode, and δ is the diffusion layer thickness of the macroelectrode. It follows from (10) and (11) that:

$$\frac{j_{L,Sp}}{j_L} = \frac{\delta}{r}. \tag{12}$$

An electrode around which the hydrodynamic diffusion layer can be established, being considerably lower than dimensions of it, could be considered as a macroelectrode. An electrode, mainly spherical, whose diffusion layer is equal to the radius of it, satisfying

$$\delta \gg r \tag{13}$$

can be considered as a microelectrode.[11]

According to (7) for

$$f_c \gg f_a \text{ and } \frac{j_0 f_c}{j_L} \gg 1, \tag{14}$$

the cathodic process on the macroelectrode enters full diffusion control, i.e.,

$$j \cong j_L. \tag{15}$$

Simultaneously, the cathodic current density on the hemispherical microelectrode, j_{Sp}, is given by:

$$j_{Sp} = \frac{j_0(f_c - f_a)}{1 + \dfrac{j_0 f_c}{j_{L,Sp}}} \tag{16}$$

or, because of (12)

$$j_{Sp} = \frac{j_0(f_c - f_a)}{1 + \left(\dfrac{j_0}{j_L}\right)\left(\dfrac{r}{\delta}\right) f_c} \tag{17}$$

and, if condition (14) is also valid, but

$$\frac{r}{\delta} \to 0. \tag{18}$$

Equation (17) can be rewritten in the form

$$j = j_0 f_c. \tag{19}$$

This means that the process on the microelectrode in the bulk solution can be under complete activation control at the same overpotential at which the same process on the macroelectrode is simultaneously under full diffusion control.

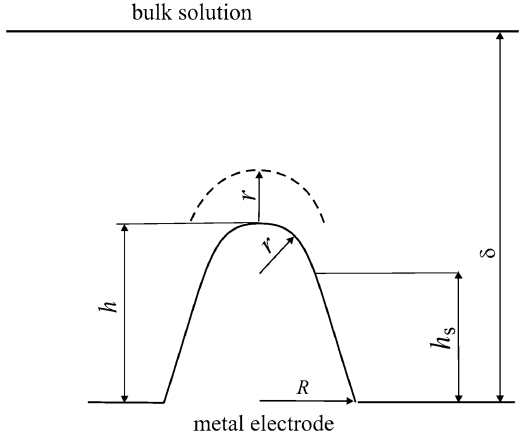

Figure 1. Model of a paraboloidal surface protrusion; h is the height of the protrusion relative to the flat portion of the surface, h_S is the corresponding local side elongation, r is the radius of the protrusion tip, R is the radius of the protrusion base, δ is the thickness of the diffusion layer and $\delta \gg h$. Reprinted from ref. [7] with permission of Elsevier.

Naturally, the microelectrodes can be placed on the macroelectrodes inside their diffusion layers. Let us consider the model of surface irregularities shown in Fig. 1. The electrode surface irregularities are buried deep in the diffusion layer, which is characterized by a steady linear diffusion to the flat portion of the surface.[7,20]

At the side of an irregularity, the limiting diffusion current density, $j_{L,S}$, is given as:

$$j_{L,S} = \frac{nFDC_0}{\delta - h_s} = j_L \frac{\delta}{\delta - h_s}. \tag{20}$$

Obviously, this is valid if the protrusion height does not affect the outer limit of the diffusion layer, and that a possible lateral diffusion flux supplying the reacting ions can be neglected. At the tip of an irregularity, the lateral flux cannot be neglected and the situation can be approximated by assuming a spherical diffusion current density, $j_{L,tip}$, given by:[20]

$$j_{L,tip} = \frac{nFDC^*}{r} \tag{21}$$

where C^* is the concentration of the diffusing species at a distance r from the tip, assuming that around the tip a spherical diffusion layer having a thickness equal to the radius of the protrusion tip is formed. If deposition to the macroelectrode is under full diffusion control, the distribution of the concentration C inside the linear diffusion layer is given by:[12]

$$C = C_0 \frac{h}{\delta}, \tag{22}$$

where $0 \leq h \leq \delta$. Hence,

$$C^* = C_0 \frac{h + r}{\delta} \tag{23}$$

and

$$j_{L,tip} = j_L \left(1 + \frac{h}{r}\right) \tag{24}$$

because of (11), (21), and (23).

The tip radius of the paraboloidal protrusion is given by[11–13]

$$r = \frac{R^2}{2h} \tag{25}$$

and substitution of r from (25) in (24) gives

$$j_{L,tip} = j_L \left(1 + \frac{2h^2}{R^2}\right) \tag{26}$$

or

$$j_{L,tip} = j_L(1 + 2k^2), \tag{27}$$

where

$$k = \frac{h}{R}. \tag{28}$$

If $h = R$, $k = 1$, hence for a hemispherical protrusion,

$$j_{L,tip} = 3j_L \tag{29}$$

If $h \ll R$, $k \to 0$,

$$j_{L,tip} \to j_L \tag{30}$$

and if $R \ll h$, $k \to \infty$ and

$$j_{L,tip} \to \infty. \tag{31}$$

Substitution of $j_{L,tip}$ from (27) instead of j_L in (7) and further rearranging give:

$$j_{tip} = \frac{j_0(f_c - f_a)}{1 + \left(\frac{j_0}{j_L} \cdot \frac{1}{1 + 2k^2} f_c\right)}. \tag{32}$$

The current density on the tip of a protrusion, j_{tip}, is determined by k, hence by the shape of the protrusion. If $k \to 0$, $j_{tip} \to j$ (see (7)) and if $k \to \infty$, $j_{tip} \to j_0(f_c - f_a) \gg j$. The electrochemical process on the tip of a sharp needle-like protrusion can be under pure activation control outside the diffusion layer of the macroelectrode. Inside it, the process on the tip of a protrusion is under mixed control, regardless it is under complete diffusion control on the flat part of the electrode for $k \to 0$. If $k = 1$, hence for hemispherical protrusion, j_{tip} will be somewhat larger than j, but the kind of control will not be changed. It is important to note that the current density to the tip of hemispherical protrusion does not depend on the size of it if $k = 1$. This makes a substantional difference between spherical microelectrodes in bulk solution and microelectrodes inside diffusion layer of the macroelectrode.[16] In the first case, the limiting diffusion current density depends strongly on the radius of the microelectrode.

Taking into account that the exchange current density depends on the concentration of reacting ion, it follows that the growth of dendrites[12,21,22] inside the diffusion layer of the macroelectrode is in fact under mixed activation–diffusion control. Hence, it can be expected that the process on the microelectrodes placed on the surface of the inert macroelectrode can be under mixed control. This is because the charge transfer occurs on the microelectrodes, while the mass-transfer limitations are related to the diffusion layer of the macroelectrode.

III. INERT MACROELECTRODE PARTIALLY COVERED WITH HEMISPHERICAL ACTIVE MICROELECTRODES

1. Mathematical Model

The use of microelectrodes is impractical, but the use of ensembles of microelectrodes can be a real option. The ensemble of microelectrodes consists of microelectrodes placed on the inert surface at distances between their centers larger than their diameter.

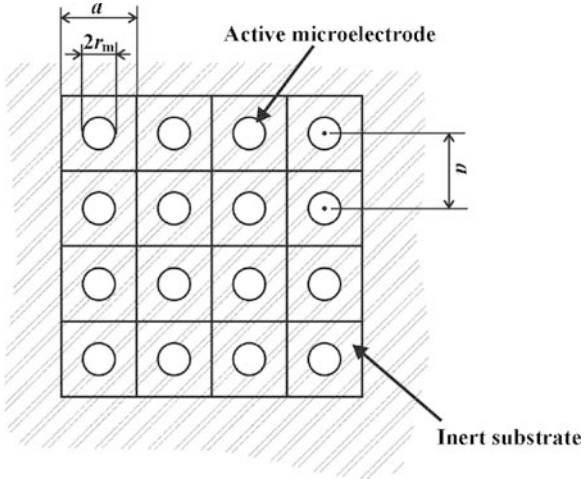

Figure 2. A schematic presentation of the top view of the surface of an inert macroelectrode modified with microelectrodes of catalyst. Reprinted from ref. [7] with permission of Elsevier.

Assuming homogeneously distributed, equal to each other, hemispherical grains of the catalyst on an inert substrate, in a way similar to that used by Gileadi[16] to describe an ensemble of microelectrodes, the surface of the macroelectrode can be presented by an idealized model, as in Fig. 2, and the number of grains per square centimeter is given by:

$$N = \frac{1}{a^2}. \tag{33}$$

It is obvious from Fig. 2 that the edge size, a, of a square of the surface of the inert macroelectrode belonging to one such particle is equal to the distance between the centers of the closest particles. If

$$a = x \cdot 2r_{\mathrm{m}}, \tag{34}$$

where r_{m} is the radius of the microelectrode and x is the ratio of the distance between the centers of the particles and the particle diameter, and (33) can be rewritten in the form

$$N = \frac{1}{4r_{\mathrm{m}}^2 \cdot x^2}. \tag{35}$$

The surface of each hemispherical microelectrode, S_m, is

$$S_m = 2r_m^2 \cdot \pi \,, \tag{36}$$

and the working surface of catalyst per square centimeter of macroelectrode, S_w, is then

$$S_w = N \cdot S_m = \frac{\pi}{2x^2} \tag{37}$$

or

$$S_w = \frac{2r_m^2 \pi}{a^2} \tag{38}$$

if (34) is taken into account, being dependent on the ratio r_m/a.

A schematic presentation of the cross section of the diffusion layer of an inert macroelectrode partially covered with small active hemispherical particles is shown in Fig. 3, taking into account that $\delta \gg r_m$.

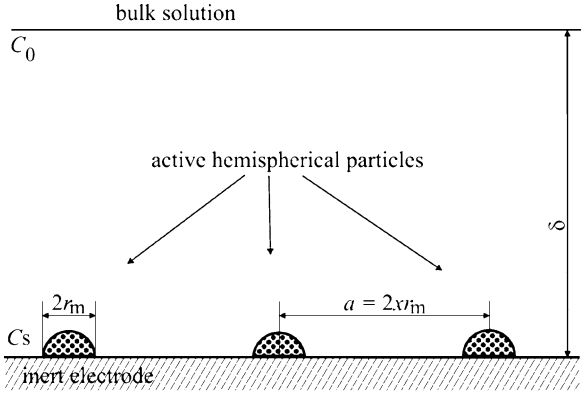

Figure 3. Schematic presentation of the cross section of the diffusion layer of a partially covered inert electrode with hemispherical active particles, where r_m is the radius of the microelectrodes, δ is the diffusion layer thickness of the macroelectrode, C_0 and C_S are the bulk and the surface concentrations of reacting ions, respectively, x is the ratio of the distance between the centers of neighboring particles and the particle diameter, and $\delta \gg r$. Reprinted from ref.[7] with permission of Elsevier.

A mathematical model can be derived under the assumption that the electrochemical process on the microelectrodes inside the diffusion layer of a partially covered inert macroelectrode is under activation control, despite the overall rate being controlled by the diffusion layer of the macroelectrode. The process on the microelectrodes decreases the concentration of the electrochemically active ions on the surfaces of the microelectrodes inside the diffusion layer of the macroelectrode, and the zones of decreased concentration around them overlap, giving way to linear mass transfer to an effectively planar surface.[15] Assuming that the surface concentration is the same on the total area of the electrode surface, under steady-state conditions, the current density on the whole electrode surface, j, is given by:

$$j = \frac{nFD(C_0 - C_S)}{\delta}, \tag{39}$$

where n is the number of transferred electrons, F the Faraday constant, and D is the diffusion coefficient of the reacting ion. Obviously, the current density from (39) is due to the difference in the bulk, C_0, and surface concentration, C_S, of the reactive ion. The concentration dependence of the exchange current density[22] is expressed as

$$j_{0,S} = \left(\frac{C_S}{C_0}\right)^{\gamma} j_0, \tag{40}$$

where

$$\gamma = \frac{d \log j_0}{d \log C_0} \tag{41}$$

and j_0 is the exchange current density for a surface concentration C_0 equal to that in the bulk, and $j_{0,S}$ is the exchange current density for a surface concentration C_S.

The current density on the macroelectrode can also be written as:

$$j = S_w j_0 \left(\frac{C_S}{C_0}\right)^{\gamma} (f_c - f_a) \tag{42}$$

assuming a reversible activation controlled electrode process on the hemispherical active microelectrodes on an inert substrate, where S_w is the active surface per square centimeter of the macroelectrode and j_0 is the exchange current density on the massive active electrode, standardized to the apparent electrode surface.

The current densities given by (39) and (42) are mutually equal and substitution of C_S/C_0 from (39) into (42), taking also into account (11) gives:

$$j = S_w j_0 \left(1 - \frac{j}{j_L}\right)^{\gamma} (f_c - f_a) \tag{43}$$

or, for $\gamma = 1$, after rearranging

$$j = \frac{S_w j_0 (f_c - f_a)}{1 + \dfrac{S_w j_0 (f_c - f_a)}{j_L}}, \tag{44}$$

where j_L is the limiting diffusion current density on the macroelectrode, standardized to the apparent electrode surface.

It is necessary to note that (44) is an approximation, because the value of γ is lower than unity. This approximation is widely used in qualitative discussions, because it permits the simple mathematical treatment of electrochemical processes with relatively small errors and with clear physical meaning. If $\gamma \neq 1$ is included in the derivation of the general polarization curve equation, simple analytical solutions are not available and numerical solutions are required.

It is obvious that

$$j_{0,\mathrm{eff}} = S_w j_0 \tag{45}$$

is the effective value of the exchange current density relative to the total surface of a partially covered electrode. It was shown[23] that the activity of a gold electrode modified with platinum 3D islands with 72% active Pt sites on the electrode is approximately 25% smaller than with pure platinum. This result is in excellent agreement with (45).

As stated earlier, (44) with $\gamma = 1$ is more suitable for discussion, but the calculation will be performed using (43) and the value of $\gamma = 0.5$ for the one-electron transfer process.[7]

Equation (44) is the polarization curve equation for a modified inert electrode for $\gamma = 1$. It is valid for inert substrates modified by active microparticles or nanoparticles as well as by 2D and 3D islands of active metal.

If

$$f_c \gg f_a \text{ and } \frac{S_w j_0 f_c}{j_L} \ll 1. \tag{46}$$

Equation (44) becomes:

$$j = S_w j_0 f_c \tag{47}$$

and for

$$f_c \gg f_a \text{ and } \frac{S_w j_0 f_c}{j_L} \gg 1. \tag{48}$$

Equation (44) becomes:

$$j \cong j_L \tag{15}$$

meaning that j_L does not depend on S_w.

If

$$f_c > f_a \text{ and } \frac{S_w j_0 (f_c - f_a)}{j_L} \gg 1. \tag{49}$$

Equation (15) is also valid, meaning that the process is under complete diffusion control at all overpotentials when $j_0 \to \infty$ if $j_L > 0$ and $S_w > 0$.

An important conclusion can be drawn from the above derivations. If (46) and (47) are valid, only a part of the surface covered with catalyst is active, with an exchange current density corresponding to the massive catalyst which makes all the electrode surface active but with a proportionally lower exchange current density.

If (48) and (15) are valid, the process enters complete diffusion control, and overpotential required increases with a decrease of S_w.

If (49) and (15) are valid, even for small S_w and overpotentials, all the surface behaves as an active one if $j_0/j_L \to \infty$. This means that the application of a partially covered inert substrate with active micro and nanoparticles will be more effective for the cases of fast electrochemical reactions. It is obvious that the above reasoning is valid not only for an inert substrate covered with microparticles, but also for any kind of partially covered electrode.

2. Polarization Curves

(i) Calculated Polarization Curves Without Included Ohmic Potential Drop

The real situation can be estimated by digital simulation.[7,24] It will be performed for example for one-electron transfer process and $\beta = 0.5$ and $\gamma = 0.5$.[7] In all cases, the apparent current density is standardized to the apparent surface of modified electrode.

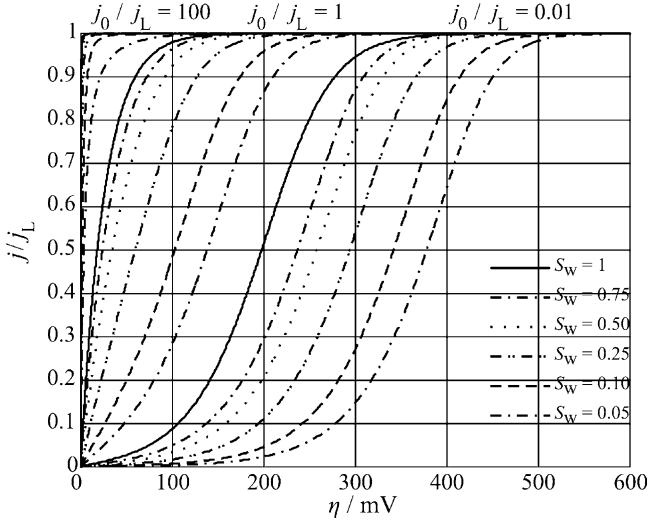

Figure 4. Dependences $j/j_L - \eta$ calculated from (43), using $j_0/j_L = 100$, 1 and 0.01, $S_w = 0.05$, 0.1, 0.25, 0.5, 0.75 and 1, and $f_c = 10^{\frac{\eta}{120}}$, $f_a = 10^{-\frac{\eta}{120}}$, and $\gamma = 0.5$ (Reprinted from ref. [7] with permission from Elsevier).

Using (43) with $\gamma = 0.5$ and $j_0/j_L = 100$, 1, and 0.01, $S_w = 0.05$, 0.1, 0.25, 0.5, 0.75, and 1, and $f_c = 10^{\eta/120}$ and $f_a = 10^{-\eta/120}$, the diagrams presented in Fig. 4 are obtained. The current density–overpotential dependence above each set of polarization curves corresponds to $S_w = 1$. It follows from Fig. 4. that for large values of $j_{0,eff}/j_L$, electrochemical polarization can probably be neglected and that complete Ohmic control of the deposition process can be expected, for $j_{0,eff}/j_L \geq 100$ up to a current density about $0.95 j_L$ and for $j_{0,eff}/j_L = 0.5$ for current densities lower than $0.3 j_L$.

As told earlier, the shape of polarization curves does not depend strongly on S_w at large j_0/j_L ratios. At lower ones, the important effect arises.

In Fig. 5, polarization curves for $j_0/j_L = 100$, 1, and 0.01 and $S_w = 1$ (other parameters as in the caption of Fig. 4) were calculated using (43) and (44).

It can be seen from Fig. 5 that the approximation of (43) by (44) is acceptable at all overpotentials and ratios j_0/j_L, being completely

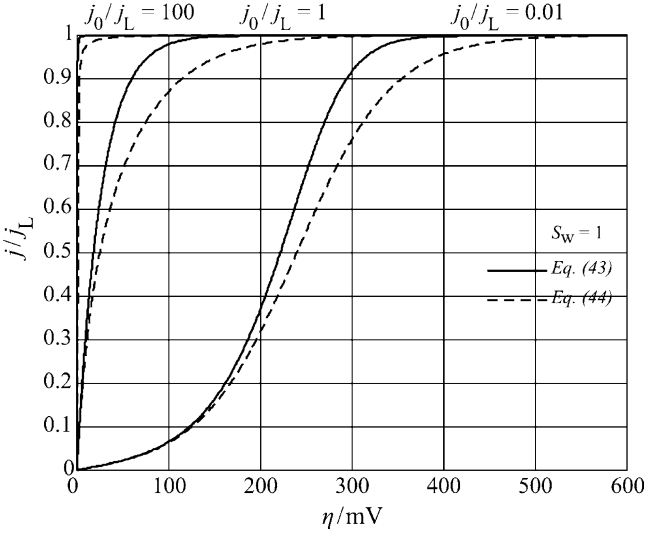

Figure 5. The same as in Fig. 4 but for $j_0/j_L = 100$, 1 and 0.01, $S_w = 1$, using (43) and $\gamma = 0.5$ as well as (44). Reprinted from ref. [7] with permission from Elsevier.

correct at low overpotentials for low exchange current densities (the Tafel region) and at large values of j_0/j_L at all overpotentials.

Finally, (7) and (44) should be compared with each other. Taking $j_0/j_L = 100$, 10, 1, 0.1, and 0.01, $S_w = 1$, and $f_c = 10^{\eta/120}$ and $f_a = 10^{-\eta/120}$, the diagrams presented in Fig. 6 are obtained. It can be seen that for $j_0/j_L \leq 1$ diagrams computed using (7) and (44) are the same. This can be explained in the following way.

Equation (7) is valid for the complete active electrode surface. On the other hand, if the inert substrate is partially covered with the same active material, the polarization curve equation is given by (44).[7]

Using the recently derived equation (44), it was possible to elucidate the Ohmic-controlled electrodeposition of metals by the consideration of silver electrodeposition on the graphite electrode, where each microelectrode was independent relative to the other ones.

At larger values of j_0/j_L ratio, the polarization curves calculated by (7) exhibit complete diffusion control being practically the same as follows from (7) when $j_0/j_L \to \infty$, for $f_c > f_a$. On the other

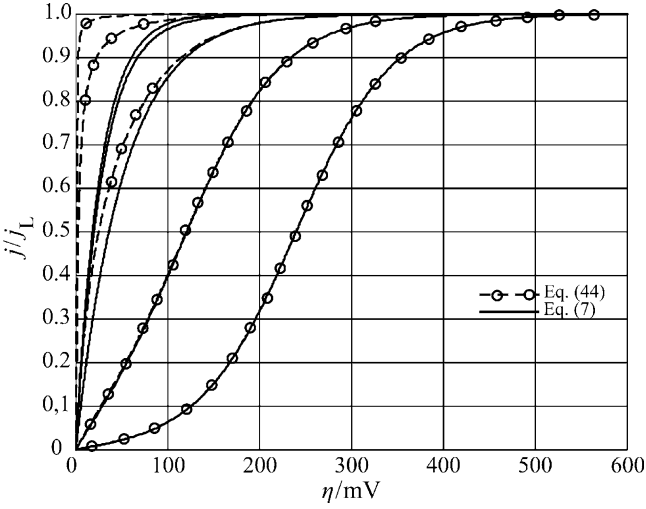

Figure 6. The comparison of polarization curves calculated using (7) and (44). From left to right side of diagram j_0/j_L ratio corresponds to 100, 10, 1, 0.1 and 0.01, respectively; $f_c = 10^{\frac{\eta}{120}}$, $f_a = 10^{-\frac{\eta}{120}}$, and $S_w = 1$. Reprinted from ref. [8] with permission of Elsevier.

hand, polarization curves calculated using (44) under the same conditions become

$$j \cong j_L. \tag{15}$$

The current densities on the massive electrode of the active material and on the inert electrode activated with microelectrodes of the same material become equal at

$$S_w = \frac{1}{1 + \frac{j_0}{j_L} f_a} \tag{50}$$

as follows from (7) and (44), being strongly dependent on the j_0/j_L ratio.[8] Obviously, for electrochemical processes characterized with $j_0/j_L \gg 1$, the inert electrode will behave as a massive active one even at low coverage. On the other hand, if $j_0/j_L \ll 1$, it follows from (50) that inert electrode will behave as activated one at $S_w = 1$.

Naturally, during deposition on the same substrate, it can be expected that only small part of the electrode surface will be active

and that for $j_0/j_L \rightarrow \infty$ (44) is valid on both the inert and the same active substrate. It can be seen from Fig. 6 that the increase of the value of j_0/j_L ratio leads to the decrease of the electrochemical overpotential. The activation part of overpotential is lost at j_0/j_L values larger than 10, while both activation and diffusion overpotential vanish at j_0/j_L values larger than 100 (Fig. 6). In the second case, the Ohmic-controlled electrochemical reaction can occur.

The Ohmic potential drop is not included in the polarization curves depicted in Figs. 4–6.

The increase of the value of the j_0/j_L ratio produces large saving of energy.

(ii) Calculated Polarization Curves With Included Ohmic Potential Drop

The polarization curves for the electrodeposition process, which include the Ohmic voltage drop, can be obtained as follows, assuming $S_w = 1$ in all cases.[7,9,24] This will be performed for a one-electron transfer process and $\beta = 0.5$, meaning $\gamma = 0.5$.[7]

Using (43) with $\gamma = 0.5$ and $j_0/j_L = 100$, 10, 1, and 0.01, $f_c = 10^{\eta/120}$ and $f_a = 10^{-\eta/120}$, and $j_L = 50$ and 10 mA cm^{-2}, the dependences presented by the dashed line in Figs. 7–10 are obtained. The Ohmic potential drop is not included in the calculated polarization curves depicted in Figs. 7–10 by the dashed line. It follows from Figs. 7–10 that for large values of j_0/j_L, electrochemical polarization can probably be neglected but mass-transfer limitations are present in all cases, which can also be shown by differentiation of (7).

On the other hand, the measured value of overpotential, η_m, is given by:

$$\eta_m = \eta + j\frac{L}{\kappa} \tag{51}$$

due to the *IR* error,[25] where L is the length of the electrolyte column between the tip of a liquid capillary and the electrode and κ is the specific conductivity of the electrolyte.

For a 1 M solution of a typical fully dissociated electrolyte, the value of κ is around 0.1 S cm^{-1}, L can be taken as 0.2 cm, and $j_L = 50$ mA cm^{-2} and 10 mA cm^{-2}. Using these given values, as well as $\kappa = 0.033$ S cm^{-1}, (51), and the diagrams presented in Figs. 7–10 by the dashed line, polarization curves including the Ohmic potential drop can be obtained, as shown in Figs. 7–10 by the solid line.

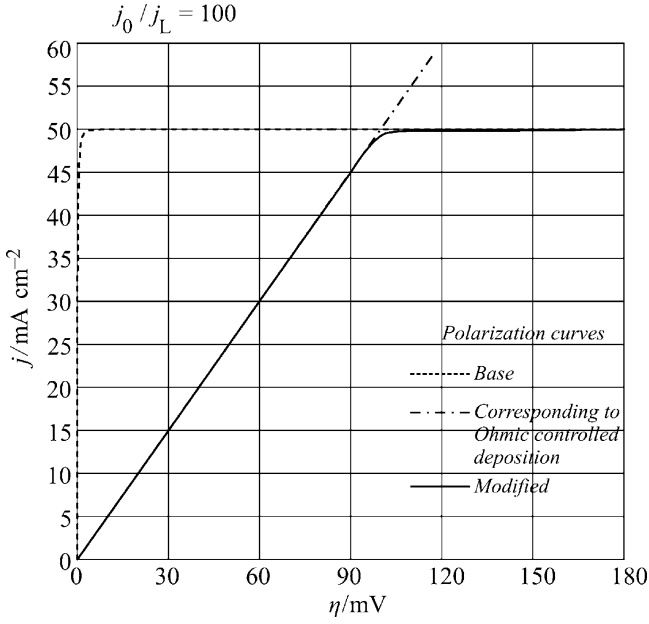

Figure 7. The dependence $j - \eta$ calculated using (43), $j_0/j_L = 100$, $f_c = 10^{\frac{\eta}{120}}$, $f_a = 10^{-\frac{\eta}{120}}$, $\gamma = 0.5$, $S_w = 1$ and $j_L = 50\,\text{mA cm}^{-2}$, and one modified using (51), $L = 0.2\,\text{cm}$, $\kappa = 0.1\,\text{s cm}^{-1}$. Reprinted from ref. [9] with permission from Elsevier.

Naturally, the condition of Ohmic-controlled electrochemical process can be derived from (51) as:

$$\eta \ll j\frac{L}{\kappa} \tag{52}$$

or

$$\eta \leq 0.01\, j\frac{L}{\kappa}. \tag{53}$$

In the case under consideration, complete Ohmic control of the deposition process can be expected for $j_0/j_L \geq 100$ up to a current density about $0.95\, j_L$ (Fig. 7) and for $j_0/j_L = 10$ up to $0.6\, j_L$ (Fig. 9). It is obvious from Figs. 7–10 that, regardless of the shape of the polarization curve, which depends on the j_0/j_L ratio and κ, a limiting diffusion current density plateau is present in all cases.

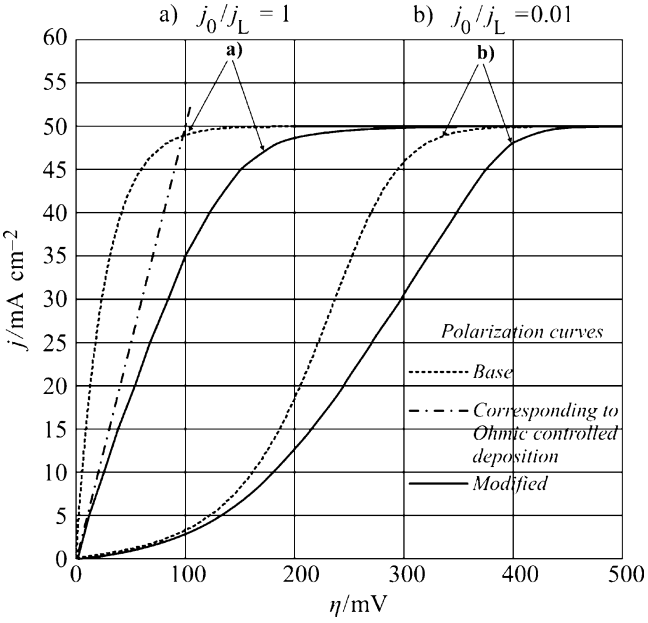

Figure 8. The dependences $j - \eta$ calculated using (43), $j_0/j_L = 1$ and 0.01, $f_c = 10^{\frac{\eta}{120}}$, $f_a = 10^{-\frac{\eta}{120}}$, $\gamma = 0.5$, $S_w = 1$ and $j_L = 50\,\text{mA cm}^{-2}$, and ones modified using (51), $L = 0.2\,\text{cm}$, $\kappa = 0.1\,\text{s cm}^{-1}$. Reprinted from ref. [9] with permission from Elsevier.

Obviously, increasing the concentration of the reacting ion and decreasing the concentration of the supporting electrolyte in a simple salt solution stimulates Ohmic control of the deposition process, but a large value of the exchange current density seems to be the most important for it (Figs. 9 and 10).

It can be noted that before the increase of the current density, over the value of the limiting diffusion one, the first part of the polarization curve for silver deposition from nitrate solution[7] has practically the same shape as that from Fig. 7 and that those from Fig. 8 are very similar to the ones for Cd and Cu deposition.[26] The value of j_0 for Ag deposition is very large.[27] In the cases of both Cd[28] and Cu[29] deposition, j_0 is considerably lower than in the case of Ag deposition.

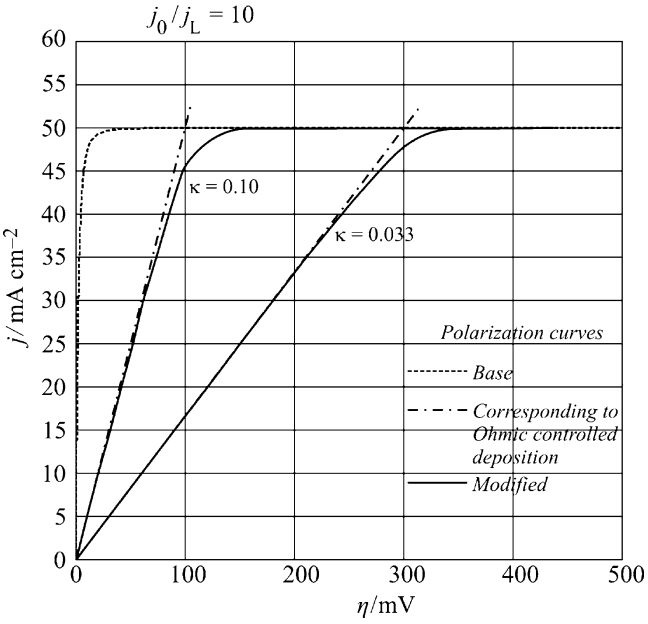

Figure 9. The dependences $j - \eta$ calculated using (43), $j_0/j_L = 10$, $f_c = 10^{\frac{\eta}{120}}$, $f_a = 10^{-\frac{\eta}{120}}$, $\gamma = 0.5$, $S_w = 1$ and $j_L = 50\,\text{mA cm}^{-2}$, and ones modified using (51), $L = 0.2\,\text{cm}$, $\kappa = 0.1$ and $0.033\,\text{S cm}^{-1}$. Reprinted from ref.[9] with permission from Elsevier.

The increase in the current density over the limiting diffusion current in the absence of some other electrochemical process indicates a decrease of the mass transport limitations, due to initiation of growth of dendrites and further dendritic growth.

3. Experimental Verification

The polarization characteristic of a partially covered inert macroelectrode is easy to determine, but it is very difficult or even impossible to do the same for microelectrodes placed on it. On the other hand,[30] the morphology of metal electrodeposits indicates the conditions of deposition. Hence, the type of process control on the microelectrodes can be derived from their morphology and correlated with the polarization curve for the partially covered macroelectrode.

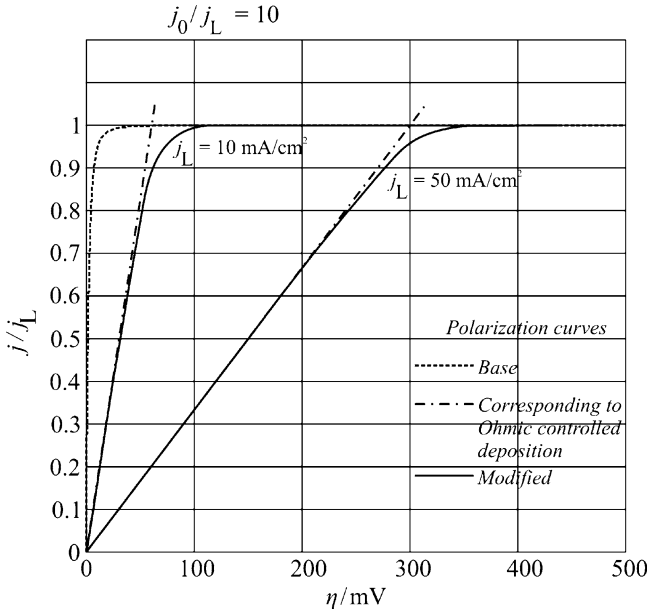

Figure 10. The dependences $j/j_L - \eta$ calculated using (43), $j_0/j_L = 10$, $f_c = 10^{\frac{\eta}{120}}$, $f_a = 10^{-\frac{\eta}{120}}$, $\gamma = 0.5$, $S_w = 1$, $j_L = 10\,\mathrm{mA\,cm^{-2}}$ and $j_L = 50\,\mathrm{mA\,cm^{-2}}$, and ones modified using (51), $L = 0.2\,\mathrm{cm}$, $\kappa = 0.033\,\mathrm{S\,cm^{-1}}$. Reprinted from ref. [9] with permission from Elsevier.

There are two conditions under which the particles of active metal placed on the surface of a macroelectrode can represent microelectrodes. The first condition is that the substrate is conducting but inert relative to the process under consideration. The second one is that the grains are sufficiently small to permit activation control of the electrochemical process on them, making thus, mixed overall control, as in the case of the tips of growing dendrites,[11,12,31] or during the induction time of the formation of spongy deposits.[32–34]

As already stated, the nuclei behave as microelectrodes in the initial stage of electrodeposition of metals onto inert substrates.[33] If nucleation exclusion zones around nuclei are formed,[35,36] an inert substrate can be partially covered even at long deposition times, due to the nucleation exclusion zones overlapping, which results in the formation of granular electrodeposits.[37,38] In this way, a granular

silver deposit on a platinum or graphite electrode can represent the ideal physical model of an inert substrate covered by nanoparticles.

It was shown earlier[32,33] that the mechanism of spongy deposit formation can be successfully illustrated by a physical model and that the calculations derived for the real system can be applied for the model and vice versa. The formation of nucleation exclusion zones is illustrated by the physical model[35] as well as by the effect of the exchange current density of the deposition process on the radii of them[36,39] with fair agreement with the experimental data. In addition, the physical simulation[40,41] of the periodicity in the surface structure of a polycrystalline electrolytic deposit[42] is also possible. As nucleation rings appear due to the supersaturation zones,[40] the mutual effect of the nuclei at the moment of their formation confirms directly that the process on the nanoscale can also be elucidated by an appropriate physical model. Besides, even the electrochemical treatment of tumors in human tissue can be simulated by the electrochemical model.[43] Hence, it can be expected that physical modeling will also be useful in the consideration of mass transfer on an inert electrode partially covered with small particles of an active metal. The kind of a process control on the microelectrodes inside the diffusion layer of a partially covered inert electrode could be estimated, and a mathematical model of the overall process on a partially covered electrode proposed.

The electrolyte solutions used in further experiments were: 0.5 M $AgNO_3$ in 0.2 M HNO_3 (nitrate bath) and 0.1 M $AgNO_3$ in 0.5 M $(NH_4)_2SO_4$ (ammonium bath). The overpotential was increased from initial to the final value and held for 30 s before measurement in all cases during the polarization measurements.

The polarization curves for silver electrodeposition are presented in Fig. 11.

It is obvious from Fig. 11 that the polarization curves for deposition on the compact silver layer and on the uncovered graphite electrode are practically the same. In both cases, the Ohmic-controlled deposition is obvious. This can mean that the deposition on the graphite electrode coated with silver also initiates by nucleation. Besides, the grain of silver can be seen from Fig. 12a. In both cases, an overpotential of 120 mV belongs to the region in which a slight decline in the slope of the polarization curve indicates an increased degree of diffusion control. At overpotentials larger than 140 mV, a strong increase in the current density with increasing overpotential occurs because of the initiation of dendritic growth.[11,12]

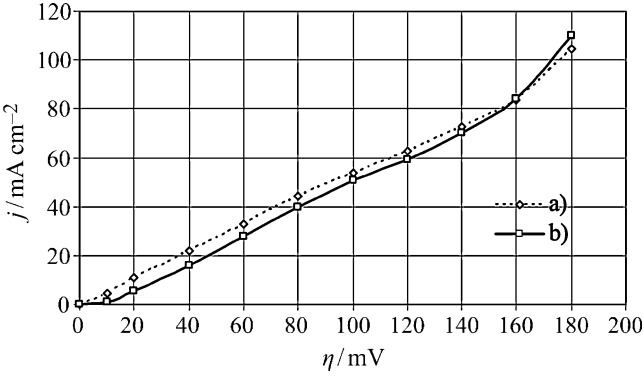

Figure 11. Polarization curves for silver electrodeposition from the nitrate solution on: (**a**) a graphite electrode previously plated with silver from the ammonium solution; (**b**) on an uncovered graphite electrode. Reprinted from ref. [7] with permission from Elsevier.

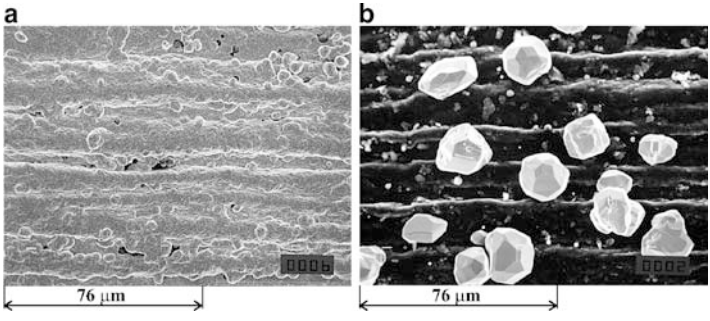

Figure 12. The physical model of a partially covered inert electrode with active grains and a completely covered inert electrode: (**a**) a graphite electrode completely covered by deposition from the ammonium bath; current density on the electrode completely covered with silver was 62.5 mA cm^{-2} at an overpotential of 120 mV in the nitrate solution; magnification 500×; (**b**) the silver deposit on the graphite electrode after the polarization measurements ended at an overpotential of 120 mV in the nitrate solution; magnification 500×; current density on such electrode was 59.4 mA cm^{-2} at the same overpotential in the nitrate solution. Reprinted from ref. [7] with permission of Elsevier.

The polarization curves on platinum electrodes were very similar to those obtained on graphite ones.[7]

An SEM microphotograph of the silver deposit obtained after polarization measurement up to an overpotential of 120 mV on an

uncovered graphite electrode is shown in Fig. 12b. The electrode surface is partially covered because of the overlapping of the nucleation exclusion zones, being, as already told, the ideal physical model of a partially covered inert electrode.

The surface of completely covered graphite electrode by deposition from ammonium bath is shown in Fig. 12a. The regular crystal form of the grains in Fig. 12b confirms that the deposition on the microelectrodes is not under diffusion control,[44,45] despite the overall deposition rate being determined by diffusion to the macroelectrode.

The current density on the electrode from Fig. 12b, with a coverage of about 20%, is practically the same as on a completely covered graphite electrode, as can be seen from Fig. 11 at an overpotential of 120 mV. This is because the exchange current density for the silver electrodeposition process from nitrate baths is extremely large.[27,46]

A similar situation appears in silver electrodeposition on platinum.[7]

The surface layers of silver obtained by electrodeposition from an ammonium bath on a graphite electrode are shown in Fig. 13.

The S_W in Fig. 13a is about 20% and the current density at 30 mV is about 40% of the current density on a completely covered

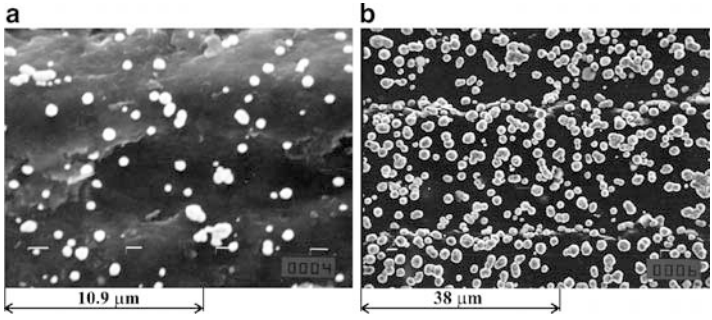

Figure 13. The silver layer on a graphite electrode obtained by electrodeposition from the ammonium solution at an overpotential of 100 mV for: (**a**) 2.5 s. The current density on this electrode in the ammonium solution at an overpotential of 30 mV was 0.5 mA cm^{-2}. Magnification 3,500×; (**b**) 60 s. The current density on this electrode in the ammonium solution at an overpotential of 30 mV was 1.0 mA cm^{-2}. The current density on a completely covered graphite electrode after a pulse of an overpotential of 150 mV for 3 s and deposition at an overpotential of 100 mV for 10 min was 1.25 mA cm^{-2} at the same potential. Magnification 1,000×. Reprinted from ref. [7] with permission from Elsevier.

inert substrate in ammonium solution. In Fig. 13b, the S_w is more than 90% and current density is 80% of the current density on a completely covered electrode. This is in accordance with (44) and (47), because the exchange current density for the silver electrodeposition process from ammonium solutions is considerably lower than the corresponding limiting diffusion current density.[47]

The above facts are a fair illustration of the concluding remarks in the previous section. It is necessary to note that the uncovered part of the inert substrate after nucleation at larger potentials negative to the reference electrode remains inert at lower ones.

4. The Required Quantity of Active Substance

Finally, the required quantity of catalyst for the activation of an inert substrate can now be estimated as follows. The volume of hemispherical microelectrode, V_m, is given by

$$V_m = \frac{2}{3} r_m^3 \cdot \pi \tag{54}$$

and the mass of such a grain is then

$$m_m = \rho \cdot V_m = \frac{2}{3} r_m^3 \cdot \pi \cdot \rho \tag{55}$$

where ρ is the density of catalyst, and the mass of catalyst per square centimeter of the inert electrode, m, is

$$m = N \cdot m_m = \frac{r_m \cdot \pi \cdot \rho}{6x^2} \tag{56}$$

or, taking into account (37) and (50)

$$m = \frac{r_m \cdot \rho}{3} S_w = \frac{r_m \cdot \rho}{3} \cdot \frac{1}{1 + \frac{j_0}{j_L} f_a}. \tag{57}$$

Equation (57) is valid for the cathodic processes. In similar way, the corresponding equation for the anodic ones can be derived.

It is obvious from (57) that the quantity of catalyst in the form of small hemispherical grain required to transform an inert electrode into an active one decreases rapidly with decrease in size of the particles, for one and the same S_w, as well as with the increase of the

j_0/j_L value for the process taking place on it. Hence, (57) can be considered as fundamental one for electrocatalysis by active particles on inert electrodes.

The current density on the graphite electrode partially covered with silver grains obtained from the nitrate solution by a pulse of an overpotential of 100 mV for 20 ms and by further growth at an overpotential of 40 mV for 30 s (Fig. 14a) is practically the same as the current density on a massive silver electrode at an overpotential of 40 mV. The same occurs with a graphite electrode covered with silver grains by a pulse of an overpotential of 500 mV for 5 ms and by further growth at an overpotential of 40 mV for 5 s (Fig. 14b). It can be seen that the deposits depicted in Fig. 14a and this in Fig. 14b,

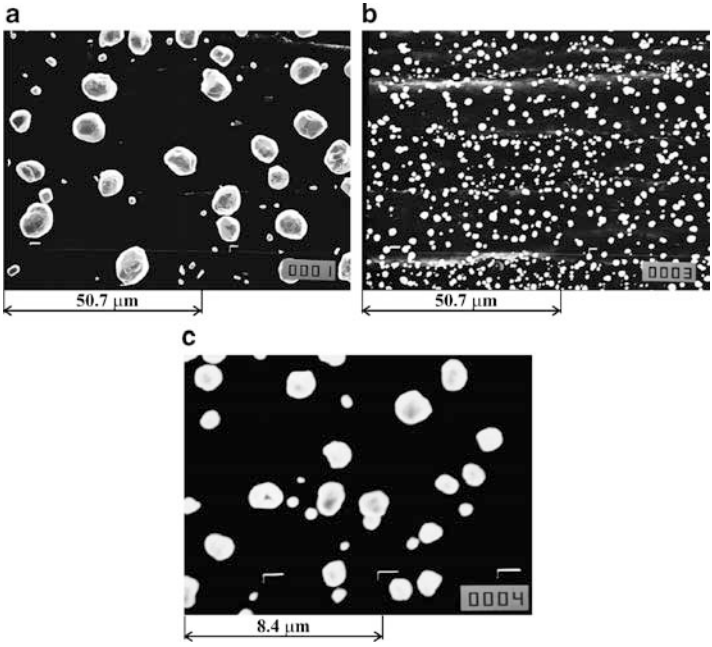

Figure 14. Silver electrodeposits on a graphite electrode obtained from the nitrate solution: (**a**) pulse of an overpotential of 100 mV for 20 ms and further growth at an overpotential of 40 mV for 30 s. Magnification 750×; (**b**) pulse of an overpotential of 500 mV for 5 ms and further growth at an overpotential of 40 mV for 5 s; magnification 750×; (**c**) the same as in (**b**), but under a magnification of 4,500×. Reprinted from ref. [7] with permission of Elsevier.

under the same magnification, are very different. In Fig. 14c, the deposit from Fig. 14b, but under a considerably larger magnification, is shown, being very similar to that depicted in Fig. 14a.

It seems to be practically identical with the deposit shown in Fig. 14a, which can also be concluded from calculated $x/2r_m$ values, being 2.5 for the deposit shown in Fig. 14a and 2.9 for that shown in Fig. 14b. It is obvious that despite the grains being many times smaller, their mutual relations are similar to those shown in Fig. 14a, producing the same activity with a many times lower quantity of electrodeposited metal, which is in the accordance with (37) and (38).

In both cases, the current density on the partially covered electrode was 21 mA cm^{-2}. The current density on a completely covered graphite electrode in the nitrate solution was 22 mA cm^{-2} at an overpotential of 40 mV.

The electrodeposition of metals on inert substrates by fast electrochemical reactions permits the physical modeling of processes on partially covered inert substrates due to formation of nucleation exclusion zones around the growing grains. Regardless of the continuous change of the size of the microelectrodes during the deposition process, the current density and morphology can be correlated to each other after any deposition time. It is also the only way of determining the type of process control on the microelectrodes.

Hence, the procedure described above could be unavoidable for the elucidation of the polarization behavior of an inert electrode partially covered with small active grains, probably with nanoparticles, too.

IV. INERT ELECTRODES ACTIVATED WITH DENDRITES

1. Large Level of Coarseness

From the electrochemical point of view, a dendrite can be defined as an electrode surface protrusion that grows under activation or mixed control, while deposition to the flat part of the electrode surface is under complete diffusion control.[11–13,48]

Considering the model of surface irregularities shown in Fig. 1, the surface irregularities are buried deep in the diffusion layer, which is characterized by a steady linear diffusion to the flat portion of completely active surface.

If the protrusion does not affect the outer limit of the diffusion layer, i.e., if $\delta \gg h$, the limiting diffusion current density to the tip of the protrusion from Fig. 1, $j_{L,tip}$, is given by[20]

$$j_{L,tip} = j_L \left(1 + \frac{h}{r}\right). \tag{24}$$

Substitution of $j_{L,tip}$ from (24) into (7) produces for $h/r \gg 1$:

$$j_{tip} = j_{0,tip}(f_c - f_a), \tag{58}$$

where $j_{0,tip}$ is the exchange current density at the tip of a protrusion.

Obviously, deposition to the tip of such protrusion inside the diffusion layer is activation controlled relative to the surrounding electrolyte, but it is under mixed activation–diffusion control relative to the bulk solution.

If deposition to the flat part of electrode is a diffusion-controlled process and assuming a linear concentration distribution inside the diffusion layer, the concentration C at the tip of a protrusion can be given by (22).[12]

$$C = C_0 \frac{h}{\delta}. \tag{22}$$

According to Newman,[22] the exchange current density at the tip of a protrusion is given by

$$j_{0,tip} = j_0 \left(\frac{C}{C_0}\right)^{\gamma} \tag{59}$$

or

$$j_{0,tip} = j_0 \left(\frac{h}{\delta}\right)^{\gamma} \tag{60}$$

because of (22).

Taking into account (58), the current density to the tip of a protrusion is then given by

$$j_{tip} = j_0 \left(\frac{h}{\delta}\right)^{\gamma} (f_c - f_a), \tag{61}$$

being under mixed control due to the $(h/\delta)^{\gamma}$ term, which takes into account the concentration dependence of $j_{0,tip}$, expressing in this way a mixed-controlled electrodeposition process.

Outside the diffusion layer $h \geq \delta$, and (61) becomes:

$$j_{\text{tip}} = j_0(f_c - f_a) \tag{62}$$

indicating pure activation control, as the $(h/\delta)^{\gamma}$ term is absent.

On the other hand, according to Wranglen,[49] a dendrite is a skeleton of a monocrystal and consists of a stalk and branches, thereby resembling a tree.

Dendritic growth occurs selectively at three types of growth sites: at screw dislocations[12] on the indestructible reentrant groove formed in the twinning process[50] and, in the case of a hexagonal close-packed lattice, growth leading to the formation of low index planes.[51] Deposition to the tip of a screw dislocation can be theoretically considered as diffusion to a point and in other two cases as diffusion to a line. In any case, the conditions requested for activation-controlled deposition are fulfilled.[12,52–54]

The current density to the tip of a protrusion formed on the flat part of the electrode surface growing inside the diffusion layer should be larger than the corresponding limiting diffusion current density.[21] Hence, if $\delta \gg h$ and

$$j_L < j_{\text{tip}}, \tag{63}$$

the protrusion grows as a dendrite.

In accordance with (63), instantaneous dendrite growth is possible at overpotentials larger than some critical value, η_{cr}, which can be derived from (61) as shown by Popov et al.[55]

$$\eta_{cr} = \frac{b_c}{2.3} \ln \frac{j_L}{j_0} \left(\frac{\delta}{h}\right)^{\gamma} \tag{64}$$

for $f_c \gg f_a$, where h and δ are the protrusion height and the diffusion layer thickness, respectively. For very fast processes, when $j_0/j_L \gg 1$, i.e., if $f_c \approx f_a$ but $f_c > f_a$, (61) becomes:

$$\eta_{cr} = \frac{RT}{nF} \frac{j_L}{j_0} \left(\frac{\delta}{h}\right)^{\gamma} \tag{65}$$

meaning that in the case of Ohmic-controlled reactions, dendritic growth can be expected at very low overpotentials, or better to say, if $j_0 \to \infty$, instantaneous dendritic growth is possible at all overpotentials if only mass-transfer limitations are taken into consideration.

In fact, dendrite propagation under such conditions is under diffusion and surface energy control and η_{cr} is then given by:[11,21]

$$\eta_{cr} = \frac{8\sigma V}{nFh}, \tag{66}$$

where σ is the metal surface energy and V is the molar volume of the metal.

Hence, a critical overpotential for initiation dendritic growth is also expected in such cases, being of the order of few millivolts.[21,56]

The initiation of dendritic growth is followed by an increase of the deposition current density, and the overall current density will be larger than the limiting diffusion current on a flat active electrode. Based on the above discussion, the polarization curve equation in the Ohmic-controlled electrodeposition of metals can be determined now by:[9]

$$j = \frac{\kappa\eta}{L} \quad \text{for } 0 \le \eta < j_L\frac{L}{\kappa}, \tag{67a}$$

$$j = j_L \quad \text{for } j_L\frac{L}{\kappa} \le \eta < \eta_{cr} + j_L\frac{L}{\kappa}, \tag{67b}$$

$$j = j_L\theta + (1-\theta)j_0\frac{(f_c - f_a)}{N}\sum_{i=1}^{i=N}\left(\frac{h_i}{\delta}\right)^{\gamma} \quad \text{for } \eta_{cr} \le \eta, \tag{67c}$$

where $N = N(t)$ is the number of dendrites and $\theta = \theta(t) \le 1$, where θ is the coverage of the electrode surface with dendrites.

Equation (67a) describes the linear part of the polarization curves for tin,[57] silver,[7] and lead[58] deposition and (67b) foresees the inflection point in the cases when η_{cr} is low and the resistance of the electrolyte large. Finally, (67c) describes the part of the polarization curve after initiation of dendrite growth.

It is interesting to note that (67c) describes qualitatively the increase of the apparent current density over the value of the limiting diffusion current density after initiation of dendritic growth, since the quantitative treatment of the polarization characteristics in the presence of dendrite growth is simply impossible. This is because dendrites can have a variety of unpredictable structures. In this way, the results of Ibl and Schadegg,[59] Diggle et al.,[12] and Popov et al.,[21] as well as the Ohmic-controlled deposition of tin,[57] silver,[7] and lead,[58] could be explained qualitatively.

Thus, instead of a limiting diffusion current density plateau, a curve inflection point or a short inclined plateau can be expected on the polarization curve in Ohmic-controlled electrodeposition of metals, as observed in the case of silver electrodeposition from nitrate solutions. The exchange current density of the silver reaction in nitrate electrolytes is sufficiently large to permit Ohmic-controlled deposition as well as dendritic growth at low overpotentials.[27] After a linear increase of the deposition current density with increasing overpotential, an exponential increase after the inflection point appears, meaning the elimination of mass-transfer limitations due to the initiation of dendritic growth.

The polarization curve for silver electrodeposition from nitrate solution, 0.5 M $AgNO_3$ in 0.2 M HNO_3, onto a graphite electrode is shown in Fig. 15. As shown earlier,[7] the polarization curves for silver deposition from nitrate solution onto a graphite electrode and on graphite covered with a nonporous surface film of silver (hence, on a massive silver electrode) are practically the same. The polarization curve in Fig. 15 is very similar to that in Fig. 7, which means that mass-transfer limitations were decreased or even eliminated. The SEM photomicrographs of the deposit corresponding to the points from Fig. 15 are shown in Fig. 16.

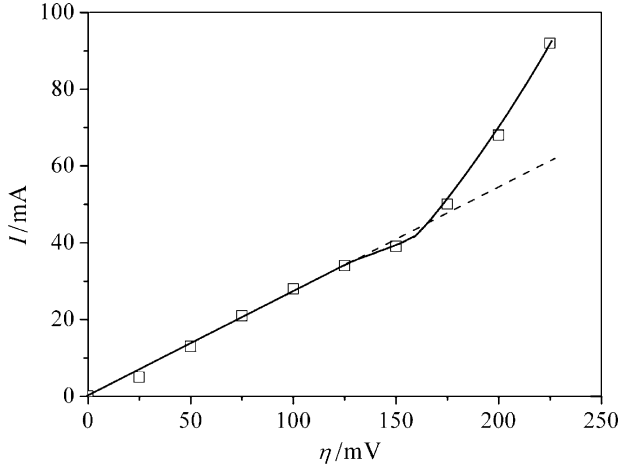

Figure 15. The polarization curve for silver electrodeposition from nitrate solution on a graphite electrode. Reprinted from ref. [9] with permission from Elsevier.

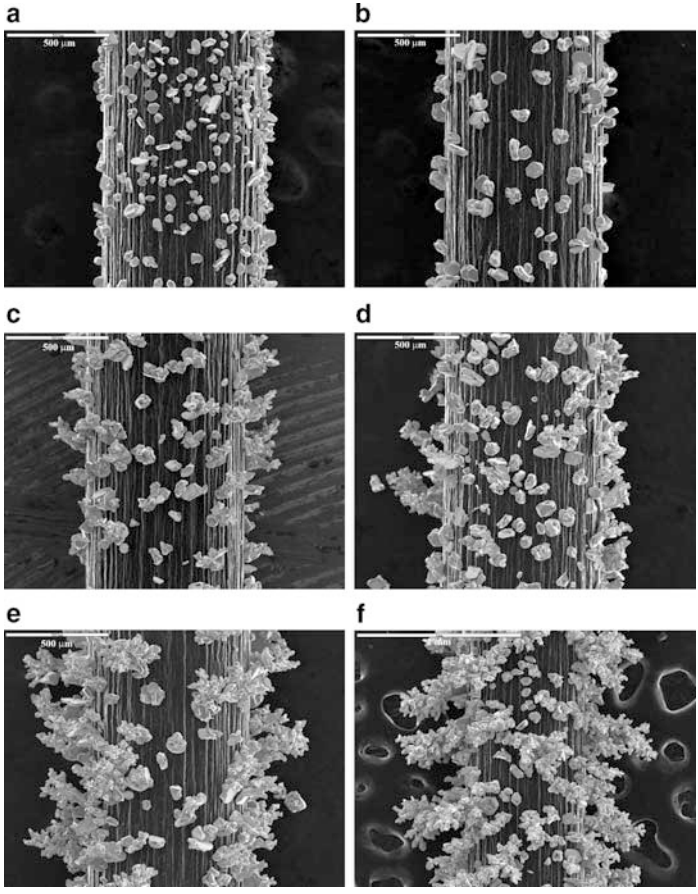

Figure 16. The SEM photomicrographs of the silver deposit obtained on a graphite electrode obtained after the recording of the current at different overpotentials in polarization measurements: (**a**) 100; (**b**) 125; (**c**) 150; (**d**) 175; (**e**) 200; and (**f**) 225 mV. Reprinted from ref. [9] with permission from Elsevier.

It can be seen from Figs. 15 and 16a that at an overpotential of 100 mV, only grains[9] can be seen, which means that the deposition was not under diffusion control. It follows from Figs. 15 and 16b that deposition at an overpotential of 125 mV is still out of diffusion control. At 150 mV, the current density is somewhat lower than that which could be expected from the linear dependence of current

on overpotential. This indicates not only the initiation of diffusion control of the deposition process but also the initiation of dendrite growth, which compensates the mass-transfer limitations, as can be seen from Figs. 15 and 16c. The point corresponding to an overpotential of 150 mV can be considered as the inflection point of the polarization curve in Fig. 15.

At overpotentials larger than 175 mV, the current density is considerably larger than the one expected from the linear dependence of current on overpotential. The formation of dendritic deposits (Fig. 16d–f) confirms that the deposition was dominantly under activation control. Thus, the elimination of mass transport limitations in the Ohmic-controlled electrodeposition of metals is due to the initiation of dendritic growth at overpotentials close to that at which complete diffusion control of the process on the flat part of the electrode surface occurs.

It is necessary to note that the silver deposits shown in Fig. 16d–f are not similar to ideal silver dendrites,[49] but they behave as dendritic ones in regard to their electrochemical properties. Hence, they can be considered as degenerate dendritic deposits.

Occasionally, the needle-like dendrites can also be formed.

On the other hand, due to the overlapping of the nucleation exclusion zones,[7,35,36] deposition on the partially covered graphite electrode is an excellent illustration of the above discussion. Namely, the diffusion layer on the inert electrode partially covered with grains of active metal can be formed and diffusion control established in the same way as on an electrode of massive active metal if the deposition process is characterized by a large j_0/j_L.[7] If dendrites are formed on the grains, their tips enter the bulk solution and overall control of the deposition process becomes activation or mixed controlled.

Naturally, the same effect can be expected if some very fast electrochemical process, other than electrodeposition, occurs on the inert electrode partially covered by dendrites of active catalyst, especially if concentration of reacting ion is low.[60] This could be of great importance for the activation of inert substrates for catalytic purposes.

It is clear that mass-transfer limitation can be avoided if the deposition process is carried out on dendritic electrodes. In order to illustrate this, the electrode shown in Fig. 17 was used. This is a dendrite electrode. It was obtained by deposition of copper on the tip of a copper wire at an overpotential of 650 mV during 20 min from 0.15 M $CuSO_4$ in 0.50 M H_2SO_4.

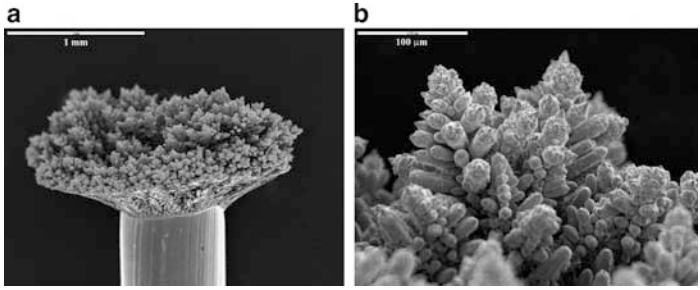

Figure 17. (**a**) The agglomerate of dendrites obtained by deposition of copper on the tip of a copper wire electrode at 650 mV for 20 min; (**b**) the outer limit of the dendritic electrode. Reprinted from ref. [9] with permission from Elsevier.

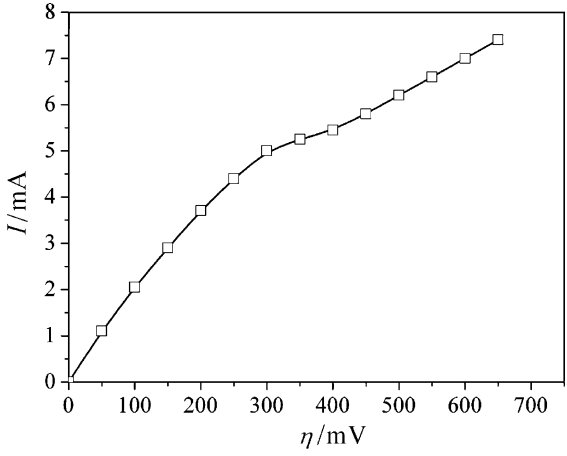

Figure 18. The polarization curve for copper deposition on the electrode from Fig. 17. Reprinted from ref. [9] with permission from Elsevier.

The polarization curve obtained on it from the same solution is shown in Fig. 18.

The shape of polarization curve in Fig. 18 clearly indicates that after the inflection point, activation control becomes dominant.

It also seems that the only way to obtain an ensemble of microelectrodes[16] working independently under activation control is to form an agglomerate of dendrites, the tips of which represent microelectrodes working in the bulk solution outside any diffusion

layer as well as outside the bulk of the agglomerated dendrites. This could be of great importance in the activation of an inert electrode surface by partial covering with dendrites of an active catalyst.

In practice, deposits with high roughness factor and good mechanical resistance are of particular interest. Dendrites have low mechanical resistance and they are unsuitable as electrocatalysts, but the elucidation of the Ohmic-controlled electrodeposition of metals due to the dendritic growth is of a great theoretical importance.

2. Low Level of Coarseness

Any solid metal surface that represents a substrate for electrochemical reactions possesses a certain roughness. The roughness factor is determined as the ratio of atomic scale real area to the geometrically measured apparent one.[61] In addition, it may appear coarse or smooth, and this is not necessarily related to the roughness. It is the level of coarseness that determines the appearance of the metal surface, while even with considerable roughness, if below the visual level, the surface may appear smooth. It is convenient to define the surface coarseness as the difference in thickness of the metal at the highest and lowest point above a reference plane facing the solution. Figure 19 show cases of surfaces with (a) equal roughness and profoundly different coarseness and (b) vice versa.[62]

The apparent surface of polycrystals, measured geometrically, is often two to three times smaller than the real area, because the latter is relatively rough – even if its hills and valleys are invisible to unaided sight. Because various metals and different samples of the same metal may have different roughness factor and because the velocity of an electrode reaction has to be standardized to the real area, the roughness factor has to be determined.[61,62]

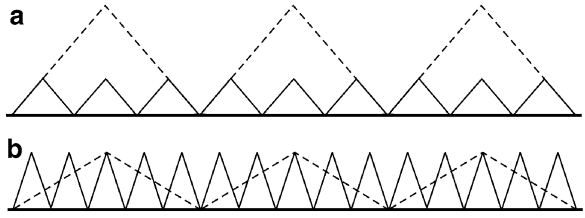

Figure 19. Models of surfaces with: (**a**) equal surface roughness with different coarseness and (**b**) vice versa. Reprinted from ref. [8] with permission of Elsevier.

The standardized values of velocity of electrochemical reactions, expressed by the values of exchange current density standardized to real area, can be compared with each other.

Since both the exchange current density and the limiting diffusion current density are included in the general cathodic polarization curve equation given by (7), it is necessary to standardize them in the same way, hence, to the apparent surface area. In that case, the exchange current density has some effective value, $j_{0,\mathrm{eff}}$, given by (68)

$$j_{0,\mathrm{eff}} = f_{\mathrm{r}} j_0, \tag{68}$$

where f_{r} is the roughness factor and j_0 is the value of the exchange current density standardized to the ideally smooth electrode surface. In similar way, the $j_{0,\mathrm{eff}}$ was defined earlier for the partially covered inert electrode with active catalyst[7] and j on porous electrodes.[63]

Electrocatalysts are produced in different ways, on different substrates, and for different purposes,[10,64–72] but almost in all cases the electrochemical characterization was performed by using the cyclic voltammetry observations. In this way, it was not possible to analyze the effects of the mass-transfer limitations on the polarization characteristics of electrochemical processes. As shown recently,[7,9] the influence of both kinetic parameters and mass-transfer limitations can be taken into account using the exchange current density to the limiting diffusion current density ratio, j_0/j_{L}, for the process under consideration. Increased value of this ratio leads to the decrease of the overpotential at one and the same current density and, hence, to the energy savings.

The basic idea of this section lies in the following facts. In the general polarization curve equation,[61] both exchange and limiting diffusion current densities are standardized to the apparent electrode surface area. Hence, if the electrode surface roughness is increased, the effective value of exchange current density for process under consideration, standardized to the apparent electrode surface area, is also increased. At the same time, if the level of the electrode surface coarseness remains low, the change of the limiting diffusion current density can be neglected. In this way, the value of j_0/j_{L} ratio is increased, what can produce the decrease of overpotential at fixed current density.

At significantly low level of coarseness, the limiting diffusion current does not depend on it, being the same as on the flat

electrode surface. On the contrary, even at significantly low level of coarseness, the surface roughness can be considerably increased as well as the value of the effective exchange current density.

Then, (7) modified with (68) can be used for calculation of the polarization curves for the same electrochemical process at different values of electrode surface roughness at low level of coarseness.

Using (7) and (68), and $f_c = 10^{\eta/120}$ and $f_a = 10^{-\eta/40}$, $j_0/j_L = 0.01$ and 0.1, and $f_r = 1, 2, 5$, and 10, the dependences presented in Fig. 20 are obtained, being valid for copper electrodeposition reaction. The strong decrease of overpotential at the same current densities with increase of the roughness factor of the electrode surface can be seen.

The Ohmic drop is not included in the polarization curve from Fig. 20. The dependences of overpotential at fixed current density on f_r are derived from the diagrams in Fig. 20 and presented in Fig. 21. It can be seen from Fig. 21 that the values of overpotential strongly decrease with increase of f_r.

There are three possibilities for the increase of both the surface roughness and coarseness during electrodeposition of metals. In the activation-controlled electrodeposition the regular crystal grains

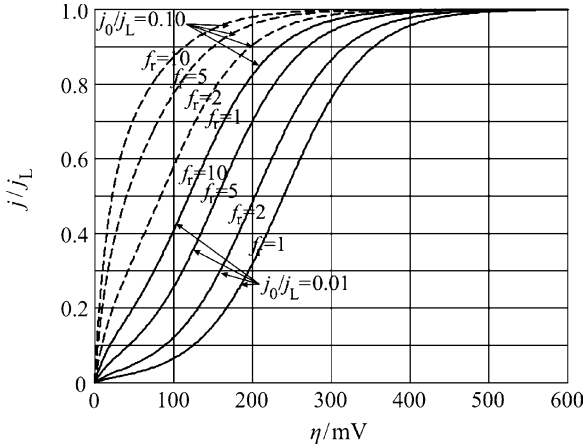

Figure 20. Dependences of $j/j_L - \eta$ calculated from (7) and (68) using $j_0/j_L = 0.1$ and 0.01, $f_r = 1, 2, 5, 10$ and $f_c = 10^{\eta/120}$ and $f_a = 10^{-\eta/40}$. Reprinted from ref. [8] with permission of Elsevier.

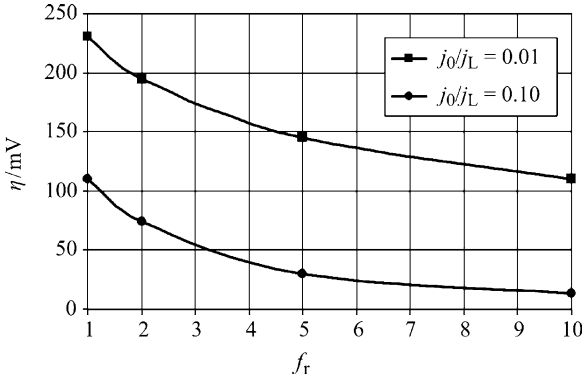

Figure 21. Dependences of overpotential on roughness factor for $j/j_L = 0.5$ and different j_0/j_L ratios. Data derived from Fig. 20. Reprinted from ref. [8] with permission of Elsevier.

grow, in the region of mixed activation–diffusion control there is a nondendritic surface coarseness amplifications, and in the complete diffusion control dendritic deposition appears.[30,48]

It is obvious that in the first case the situation like that from Fig. 19a can be expected, leading to the increase of surface coarseness, i.e., the size of crystal grains, but without considerable change of the surface roughness. In the region of the mixed control, as well as of the diffusion control at overpotentials lower than the overpotential required for dendritic growth initiation, the cauliflower-like forms are mainly formed, and they can be approximated by hemispherical protrusions. Finally, at overpotentials higher than the one required for dendritic growth initiation, dendrites are formed, and they can be approximated by cones. It is easy to show that for $\delta \gg r$, the surface roughness does not depend on the radius of the cauliflower-like particle.[30] A schematic presentation of the top view of the flat surface covered with homogeneously distributed equal hemispherical protrusions and corresponding cross section is presented in Fig. 22.

It is easy to show that roughness factor $f_{r,h}$ in this case is given as

$$f_{r,h} = 1 + \frac{\pi}{4}, \tag{69}$$

being independent on the radius of hemispherical protrusions.

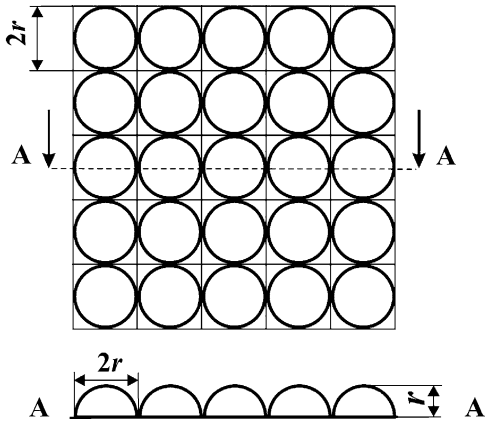

Figure 22. A schematic representation of the top view of the electrode surface modified with equal spherical protrusions and of corresponding cross-section. Reprinted from ref. [8] with permission of Elsevier.

If instead of hemispherical protrusions, the conic ones are used, characterized by radius of base r and the height h, the roughness factor $f_{\mathrm{r,c}}$ is given as

$$f_{\mathrm{r,c}} = 1 - \frac{\pi}{4} + \frac{\pi}{2r}(h^2 + r^2)^{\frac{1}{2}}, \tag{70}$$

being strongly dependant on the h/r ratio. Corresponding schematic presentation is given in Fig. 23.

Although the above illustration is a qualitative one, it can be concluded by the analysis of (69) and (70) that the roughness factor during nondendritic surface roughness amplification can be enlarged about two times. On the other hand, during dendritic growth, amplification can be many times larger than in the nondendritic one.

Hence, the activation overpotential can be considerably decreased by appropriate preparation of electrode surface morphology, especially by formation of disperse deposits at low level of coarseness. Obviously, the roughness factor can be increased many times in real situations. It is well known that the surface morphology exerts a marked influence on the electrocatalytic activity of an electrode.[73] At a microscopic level, the existence of pores, crevices, microcavities, etc. favors the increase of the electrodic surface area, though

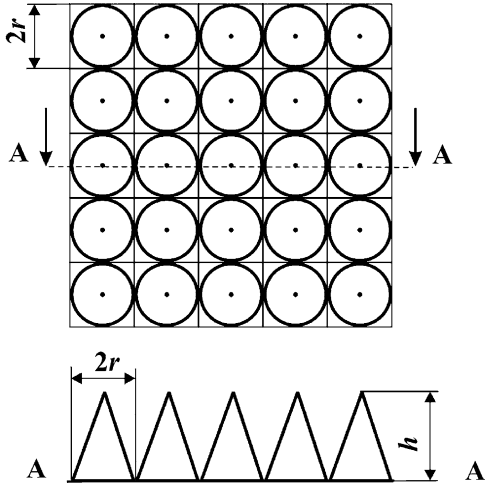

Figure 23. A schematic representation of the top view of the electrode surface modified with equal conical protrusions and of corresponding cross-section. Reprinted from ref. [8] with permission of Elsevier.

mass transfer, Ohmic, and bubble overvoltages prevent the rates of electrochemical reactions from increasing proportionally.[10] An example is the Raney-Nickel electrode used as cathodic material for the hydrogen evolution reaction, for which it has been found that in certain cases only 1.5% of the available area is used.[74] In order to avoid the discrepancy between the overall electrode surface and the part of it at which the electrochemical process occurs in prolonged electrolysis, the procedure of the determination of the effective value of roughness factor has been developed.[75] This is done by determining the exchange current densities from stationary polarization curves. The roughness factors were determined as ratios of the values of exchange current densities on different substrates and on the reference one. In this way, the differences in surface areas taking place in determination of roughness factor and in prolonged electrolysis process are avoided.

The copper deposit obtained by electrodeposition at an overpotential of 300 mV during 2 min at copper cylindrical electrode from 0.15 M $CuSO_4$ in 0.50 M H_2SO_4 is shown in Fig. 24a. Copper deposits electrodeposited at overpotentials of 550 and 650 mV on the

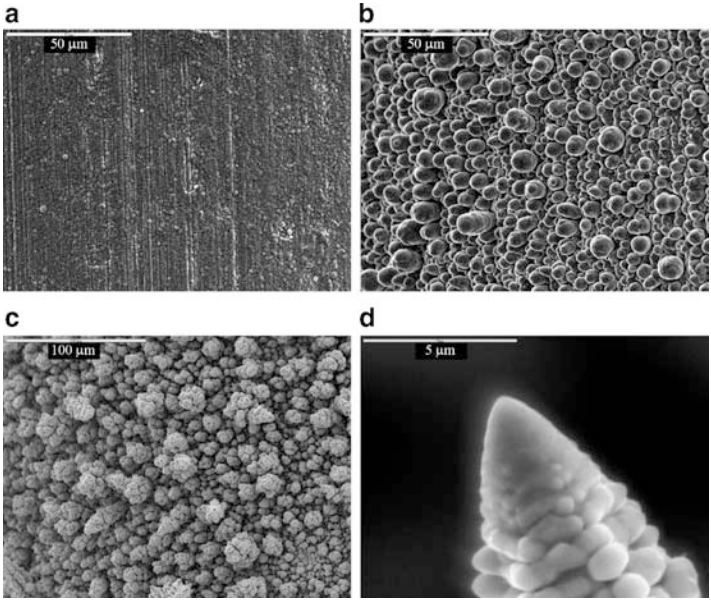

Figure 24. (**a**) The copper deposit electrodeposited at an overpotential of 300 mV during 2 min on the cylindrical copper electrode; and copper deposits electrodeposited with 5.0 mA h cm^{-2} on the copper substrate from (**a**) at overpotentials of: (**b**) 550 mV and (**c**) 650 mV; (**d**) the top of copper dendrite electrodeposited at an overpotential of 650 mV with a deposition time of 32 min. Reprinted from ref. [8] with permission of Elsevier.

copper electrode presented in Fig. 24a with a quantity of electricity of 5.0 mA h cm^{-2} are shown in Fig. 24b and c, respectively.

The polarization curves recorded on the cylindrical platinum electrodes treated in the same way as the cylindrical copper electrodes in Fig. 24 are shown in Fig. 25. There is not any difference between polarization curves obtained on the copper and platinum substrates.

The mutual position of the polarization curves from Fig. 25 indicates that the exchange current density corresponding to the substrate from Fig. 24c is considerably larger than other ones. The conclusion can be derived by the comparison of Figs. 20 and 25, because the Ohmic voltage drop in the polarization curves from Fig. 25 does

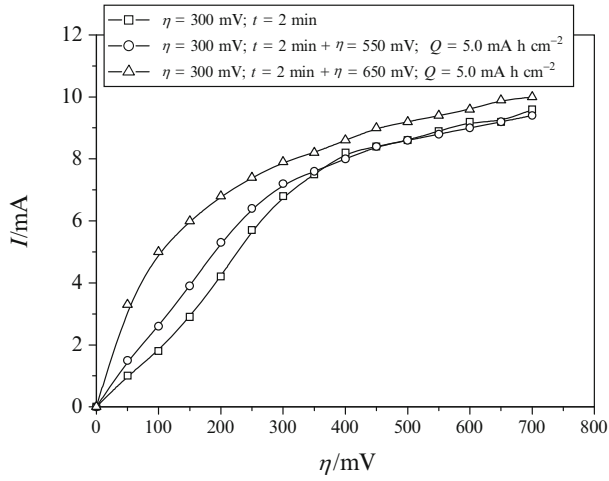

Figure 25. Polarization curves for copper electrodeposition on the cylindrical platinum electrodes treated by copper electrodeposition under the same conditions shown in Fig. 24a–c. Reprinted from ref. [8] with permission of Elsevier.

not affect the mutual position of polarization curves in which the Ohmic voltage drop is not included.[9]

On the other hand, as was shown recently,[75] the value of j_0 can be estimated using j_L value extracted from the polarization curve and known value of the cathodic Tafel slope b_c by (71)

$$j_0 = \frac{j_L}{10^{\frac{\eta_{1/2}}{b_c}}} \tag{71}$$

if the Ohmic voltage drop can be neglected, where $\eta_{1/2}$ is the value of overpotential corresponding to the half of limiting diffusion current density value. For electrode surfaces presented in Fig. 24a–c, using $b_c = 120\,\mathrm{mV\,dec^{-1}}$ and j_L from polarization curves presented in Fig. 25, exchange current density values can be estimated as $j_0 = 0.14$, 0.27, and $1.8\,\mathrm{mA\,cm^{-2}}$, respectively. This method can be applied here because the Ohmic voltage drop can be neglected for the electrode whose surface is presented in Fig. 24a. Increasing surface roughness decreases the overpotential at fixed value of apparent current density and the contribution of Ohmic voltage drop

to the measured overpotential increases. Because of this, the value of j_0 calculated by (71) can become lower than the real value, and, hence, it can be used in this qualitative discussion.

Equation (68) can be rewritten in the form

$$f_r = \frac{j_{0,\text{eff}}}{j_0}. \tag{72}$$

Assuming that j_0 corresponds to the substrate from Fig. 24a and that exchange current density values corresponding to the other substrates are the effective values, roughness factors of 1.9 and 13 for substrates shown in Fig. 24b, c, respectively, are obtained. The copper deposit formed by the nondendritic surface coarseness amplification at an overpotential of 550 mV (Fig. 24b) is well described by Fig. 22, and calculated value of 1.9 is close to the one predicted by (69). The copper deposit obtained at an overpotential of 650 mV (Fig. 24c) represents the precursors of dendrites which can be described, more or less successfully, by cones from Fig. 23. It is necessary to note that different forms on such surface are formed, from the dendritic precursor to completely formed dendrite. Also, it can be clearly seen from Fig. 24d that the top of the dendrite formed at an overpotential of 650 mV was like a cone. Anyway, inhomogeneous surface with different levels of coarseness was obtained, regardless of the limiting diffusion current density value, which was not considerably increased. The roughness factor for this electrode, calculated by (72), is $f_r = 13$, being considerably larger than the previous one.

The formation of the smaller (and less different to each other) dendrites could be obtained by the increase of deposition overpotential. Unfortunately, the increased overpotential produces the hydrogen evolution in this system and the formation of degenerate dendrites and honeycomb-like deposits.[76,77] Nevertheless, the dendritic growth in this system at larger overpotentials is possible by the application of appropriate square-wave pulsating overpotential (PO) regime. For example, the well-developed dendrites were formed with amplitude overpotential of 1,000 mV, deposition pulse of 10 ms, and pause of 100 ms (the pause to pulse ratio: 10) (Fig. 26a). They can be well approximated by the cones shown in Fig. 23. Also, superficial holes due to attached hydrogen bubbles were formed between these dendrites, as can be seen from ref. [78]

The precursors of dendrites, like a cone, were also formed by the square-wave PO with the same amplitude overpotential and the

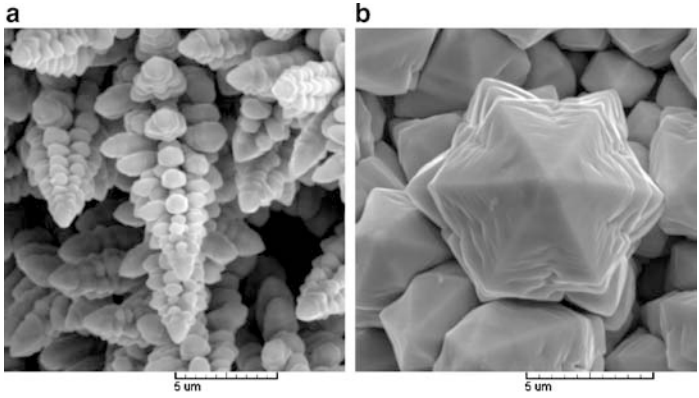

Figure 26. (**a**) The copper dendrites formed by the pulsating overpotential (PO) regime: deposition pulse of 10 ms, pause duration of 100 ms; deposition time: 18 min; (**b**) The precursor of copper dendrite obtained by PO regime: deposition pulse of 1 ms, pause duration of 10 ms; deposition time: 24 min. In both cases amplitude overpotential used was 1,000 mV. Reprinted from ref. [8] with permission of Elsevier.

pause to pulse ratio of 10, but by applying deposition pulse of 1 ms and pause of 10 ms (Fig. 26b). In this square-wave PO, hydrogen evolution was avoided.[79]

The polarization curves for copper deposition on the electrodes whose surfaces are shown in Fig. 24a and 26a are given in Fig. 27. It is obvious that the noticeable increase of the exchange current density attained by the application of the PO regime ($j_{0,\mathrm{eff}} = 3.3\,\mathrm{mA\,cm^{-2}}$; $f_r = 23.5$) is followed by the minimal increase of limiting diffusion current density, relative to the one corresponding to the substrate from Fig. 24a.

The same polarization characteristics exhibit the platinum electrode modified with copper dendrites formed by the use of the PO regime described in caption of Fig. 26a. It can be seen from Fig. 27 that the process on the electrode with increased surface roughness takes place at considerably lower overpotential than on the smoother one.

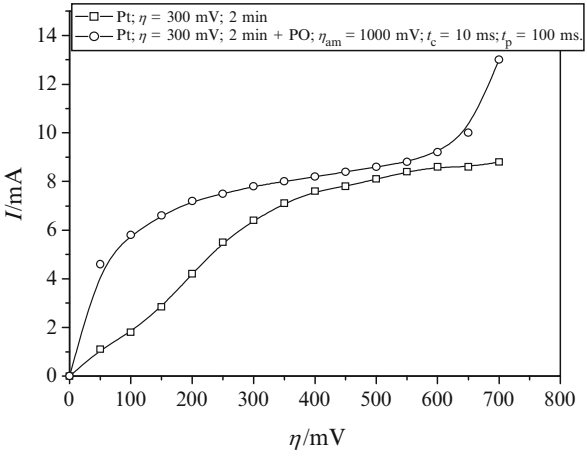

Figure 27. Polarization curves for copper electrodeposition on the substrates from Figs. 24a and 26a. Reprinted from ref. [8] with permission of Elsevier.

V. APPLIED ASPECTS

The discussion presented in this chapter is new, and it is difficult to relate it to some current applications. However, some important conclusions and recommendations can be suggested from this chapter.

First, it is possible to produce the copper dendrites by the PO deposition at the overpotential amplitude at which in a constant current regime the honeycomb-like deposits are formed. The dendrites produced by the PO regime were very small but well developed, increasing considerably the electrode surface roughness even at low level of coarseness. In other words, the apparent exchange current density of the electrochemical process occurring on such electrode can be increased for more than 20 times in comparison with one occurring at the smooth electrode surface. This result suggests that important saving in energy can be achieved. A nondendritic surface roughening does not produce significant increase in the exchange current density.

Second, as it was recently shown,[2,9] the ratio of the exchange current density and the limiting diffusion current density, j_0/j_L, determines the polarization characteristics of an electrochemical processes. Increased value of this ratio leads to a decrease of the

activation overpotential at the same applied current density. If $j_0/j_L \geq 100$, the process becomes Ohmic controlled. In this situation, not only the activation overpotential is lost, but also the diffusion overpotential at current densities lower than the limiting diffusion is lost. This means that the electrochemical process on the smooth electrode surface characterized by the value of $j_0/j_L < 5$ can be transformed to Ohmic-controlled one on the electrode surface from Fig. 26a.

As already shown, for selected set of operating conditions, the $j_{0,\text{eff}}/j_L$ value can be only altered by a change of the electrode surface roughness. The j_0/j_L ratio for the electrode whose surface is presented in Fig. 24a is 0.018 and for that presented in Fig. 26a is 0.40. It can be seen from Fig. 27 that at same current densities, belonging to the operating region of current density, about 70% of overpotential, hence energy, can be saved by using electrode with larger surface roughness at approximately the same surface coarseness. As explained earlier, the Ohmic voltage drop is neglected in this case.

Copper shows a high activity for nitrate ion reduction[80,81] as well as for a reaction in which nitrate is reduced to ammonia with a high yield from aqueous acidic perchlorate and sulphate solutions.[82] In the future, the comparison of the polarization characteristics of the mentioned reactions on a smooth electrode surface and on the rough one at low level of coarseness should be investigated in detail.

The electrode surface roughness at low level of coarseness can be increased in some different ways other than dendrites (spongy-like deposit,[33] honeycomb-like structure,[76,77] pyramid-like deposit,[83] etc.) on the microscale. The properties of electrodeposits on nanoscale should be also taken into consideration.[84,85] Further investigation will show which one of them is the best for this purpose. This chapter is written in order to initiate it.

VI. CONCLUSIONS

A completely new approach to the analysis of experimental data is introduced by the use of the complete polarization curve equation and by the method of digital simulation. It was possible in this way to elucidate the polarization behavior of the partially covered inert

electrodes, the essence of the Ohmic-controlled electrodeposition of metals, and the electrocatalytic properties of disperse electrodeposits formed at low level of the electrode coarseness.

Doubtless, the main contribution of this chapter is (57), which correlates the quantity of catalyst required for complete activation of inert electrode with size and density of hemispherical active grain and parameters of electrochemical process taking place on them.

ACKNOWLEDGMENTS

The work was supported by the Ministry of Science and Technological Development of the Republic of Serbia under the research projects: "Deposition of ultrafine powders of metals and alloys and nanostructured surfaces by electrochemical techniques" (No. 142032G) and "Modification of metal and nonmetal materials by electroconductive polymer for application in new technologies" (No. 142044).

REFERENCES

[1]S. Trasatti, "*Electrocatalysis in Water Electrolysis*", *Book of Abstracts, 1st Regional Symposium on Electrochemistry of South-East Europe*, Rovinj, Croatia (2008) 1.
[2]Y. Takasu, T. Kawaguchi, W. Sugimoto, and Y. Murakami, *Electrochim. Acta* **48** (2003) 3861.
[3]Y. Takasu, N. Ohashi, X. -G. Zhang, Y. Murakami, H. Minagawa, S. Sato, and K. Yahikozawa, *Electrochim. Acta* **41** (1996) 2595.
[4]N. Pron'kin, O. A. Petrii, G. A. Tsirlina, and D. J. Schiffrin, *J. Electroanal. Chem.* **480** (2000) 112.
[5]L. Nzoghe-Mendome, A. Aloufy, J. Ebothe, M. El Messiry, and D. Hui, *J. Cryst. Growth* **311** (2009) 1206.
[6]J. O'M. Bockris, A. K. N. Reddy, and M. Gamboa-Aldeco, *Modern Electrochemistry 2 A*, 2nd edition, Kluwer/Plenum, New York (2000) 1361.
[7]K. I. Popov, P. M. Živković, and B. N. Grgur, *Electrochim. Acta* **52** (2007) 4696.
[8]K. I. Popov, N. D. Nikolić, P. M. Živković, and G. Branković, *Electrochim. Acta* **55** (2010) 1919.
[9]K. I. Popov, P. M. Živković, S. B. Krstić, and N. D. Nikolić, *Electrochim. Acta* **54** (2009) 2924.
[10]C. A. Marozzi and A. C. Chialvo, *Electrochim. Acta* **45** (2000) 2111.
[11]J. L. Barton and J. O'M. Bockris, *Proc. R. Soc. A* **268** (1962) 485.
[12]J. W. Diggle, A. R. Despić, and J. O'M Bockris, *J. Electrochem. Soc.* **116** (1969) 1503.

[13]A. R. Despić, J. W. Diggle, and J. O'M Bockris, *J. Electrochem. Soc*. **116** (1969) 507.
[14]J. O'M. Bockris and A. K. N. Reddy, *Modern Electrochemistry 2 B*, 2nd edition, Kluwer/Plenum, New York (2000) 1811.
[15]B. Scharifker and G. Hills, *Electrochim. Acta* **28** (1983) 879.
[16]E. Gilleadi, *Electrode Kinetics*, VCH Publishers, New York (1993) 443.
[17]P. Stonehart and D. Wheeler, "*Phosphoric Acid Fuel Cells (PAFCs) for vehicles; Electrocatalyst Crystalite Design, Carbon Support, and Matrix Materials Challenges*" in *Modern Aspects of Electrochemistry*, Vol. 38, Ed. by B. E. Conway, Kluwer/Plenum, New York (2005) Chapter 4, 385.
[18]J. O'M. Bockris, A. K. N. Reddy, and M. Gamboa-Aldeco, *Modern Electrochemistry 2 A*, 2nd edition, Kluwer/Plenum, New York (2000) 1248.
[19]K. I. Popov, S. S. Djokić, and B.N. Grgur, *Fundamental Aspects of Electrometallurgy*, Kluwer/Plenum, New York (2002) Chapter 3, 14.
[20]K. I. Popov, N. V. Krstajić, and M. I. Čekerevac, "*The Mechanism of Formation of Coarse and Disperse Electrodeposits*" in Ed. by R. E. White, B. E. Conway, and J. O'M. Bockris, *Modern Aspects of Electrochemistry*, Vol. 30, Plenum, New York (1996) Chapter 3, 262.
[21]K. I. Popov, M. D. Maksimović, J. D. Trnjavčev, and M. G. Pavlović, *J. Appl. Electrochem*. **11** (1981) 239.
[22]J. S. Newman, *Electrochemical Systems*, Prentice-Hall, Engelwood Cliffs, NJ (1973) 177.
[23]M. N. Dešić, M. M. Popović, M. D. Obradović, Lj. M. Vračar, and B. N. Grgur, *J. Serb. Chem. Soc*. **70** (2005) 231.
[24]P. M. Živković, B. N. Grgur, and K. I. Popov, *J. Serb. Chem. Soc*. **73** (2008) 227.
[25]J. O'M. Bockris, A. K. N. Reddy, and M. Gamboa-Aldeco, *Modern Electrochemistry 2 A*, 2nd edition, Kluwer/Plenum, New York (2000) 1107.
[26]K. I. Popov, S. S. Djokić, and B.N. Grgur, *Fundamental Aspects of Electrometallurgy*, Kluwer/Plenum, New York (2002) Chapter 3, 87, 88.
[27]P. B. Price and D. A. Vermilyea, *J. Chem. Phys*. **28** (1958) 720.
[28]W. Lorenz, *Z. Electrochem*. **58** (1954) 912.
[29]B. E. Mattsson and J. O'M. Bockris, *Trans. Faraday Soc*. **55** (1959) 1586.
[30]K. I. Popov, S. S. Djokić, and B.N. Grgur, *Fundamental Aspects of Electrometallurgy*, Kluwer/Plenum, New York (2002) Chapter 3, 56.
[31]K. I. Popov, V. Radmilović, B. N. Grgur, and M. G. Pavlović, *J. Serb. Chem. Soc*. **59** (1994) 47.
[32]K. I. Popov, N. V. Krstajić, S. R. Popov, and M. I. Čekerevac, *J. Appl. Electrochem*. **16** (1986) 771.
[33]K. I. Popov and N. V. Krstajić, *J. Appl. Electrochem*. **13** (1983) 775.
[34]K. I. Popov, N. V. Krstajić, and S. R. Popov, *J. Appl. Electrochem*. **15** (1985) 151.
[35]I. Markov, A. Boynov, and S. Toshev, *Electrochim. Acta* **18** (1973) 377.
[36]S. Štrbac, Z. Rakočević, K. I. Popov, M. G. Pavlović, and R. Petrović, *J. Serb. Chem. Soc*. **64** (1999) 483.
[37]A. Dimitrov, S. Hadži-Jordanov, K. I. Popov, and M. G. Pavlović, *J. Appl. Electrochem*. **28** (1998) 791.
[38]V. Radmilović, K. I. Popov, M. G. Pavlović, A. Dimitrov, and S. Hadži-Jordanov, *J. Solid State Electrochem*. **2** (1998) 162.
[39]K. I. Popov, B. N. Grgur, E. R. Stoiljković, M. G. Pavlović, and N. D. Nikolić, *J. Serb. Chem. Soc*. **62** (1997) 433.
[40]G. D. Adžić, A. R. Despić, and D. M. Dražić, *J. Electroanal. Chem*. **220** (1988) 169.
[41]G. D. Adžić, A. R. Despić, and D. M. Dražić, *J. Electroanal. Chem*. **241** (1988) 353.

[42]N. Ya. Kovarskii and T. A. Arzhanova, *Elektrokhimiya* **22** (1986) 452.
[43]M. L. Avramov Ivić, S. D. Petrović, P. M. Živković, N. D. Nikolić, and K. I. Popov, *J. Electroanal. Chem*. **549** (2003) 129.
[44]K. I. Popov, M. G. Pavlović, Lj. J. Pavlović, M. I. Čekerevac, and G. Ž. Remović, *Surf. Coat. Technol*. **34** (1988) 355.
[45]K. I. Popov, N. V. Krstajić, Z. D. Jerotijević, and S. P. Marinković, *Surf. Technol*. **26** (1985) 185.
[46]K. J. Vetter, Electrochemical kinetics, Khimiya, Moskva, 1967, p. 699, Section 162 C, and references therein (in Russian).
[47]K. I. Popov, N. V. Krstajić, and S. R. Popov, *Surf. Technol*. **20** (1983) 203.
[48]K. I. Popov, S. S. Djokić, and B.N. Grgur, *Fundamental Aspects of Electrometallurgy*, Kluwer/Plenum, New York (2002) Chapter 3, 78.
[49]G. Wranglen, *Electrochim. Acta* **2** (1960) 130.
[50]A. R. Despić and K. I. Popov, "*Transport controlled Deposition and Dissolution of Metals*", in Ed. by B. E. Conway and J. O'M. Bockris, *Modern Aspects of Electrochemistry*, Vol. 7, Plenum, New York (1972) Chapter 4, 241.
[51]I. N. Justinijanović and A. R. Despić, *Electrochim. Acta* **18** (1973) 709.
[52]K. I. Popov, M. I. Čekerevac, and Lj. M. Nikolić, *Surf. Coat. Technol*. **34** (1988) 219.
[53]K. I. Popov and M. I. Čekerevac, *Surf. Coat. Technol*. **37** (1989) 435.
[54]I. M. Epstein, *Elektrokhimiya* **2** (1966) 734.
[55]K. I. Popov, N. V. Krstajić, and M. I. Čekerevac, "*The Mechanism of Formation of Coarse and Disperse Electrodeposits*" in Ed. by R. E. White, B. E. Conway, and J. O'M. Bockris, *Modern Aspects of Electrochemistry*, Vol. 30, Plenum, New York (1996) Chapter 3, 294.
[56]K. I. Popov, N. V. Krstajić, and M. I. Čekerevac, "*The Mechanism of Formation of Coarse and Disperse Electrodeposits*" in Ed. by R. E. White, B. E. Conway, and J. O'M. Bockris, *Modern Aspects of Electrochemistry*, Vol. 30, Plenum, New York (1996) Chapter 3, 308.
[57]S. Meibhur, E. Yeager, A. Kozawa, and F. Hovorka, *J. Electrochem. Soc*. **110** (1963) 190.
[58]K. I. Popov, M. G. Pavlović, E. R. Stojilković, and Z. Ž. Stevanović, *Hydrometallurgy* **46** (1997) 321.
[59]N. Ibl and K. Schadegg, *J. Electrochem. Soc*. **114** (1967) 54.
[60]P. M. Živković, N. D. Nikolić, M. Gvozdenović, and K. I. Popov, *J. Serb. Chem. Soc*. **74** (2009) 291.
[61]J. O'M. Bockris, A. K. N. Reddy, and M. Gamboa-Aldeco, *Modern Electrochemistry 2 A*, 2nd edition, Kluwer/Plenum, New York (2000) 1095.
[62]A. R. Despić and K. I. Popov, "*Transport controlled Deposition and Dissolution of Metals*", in Ed. by B. E. Conway and J. O'M. Bockris, *Modern Aspects of Electrochemistry*, Vol. 7, Plenum, New York (1972) Chapter 4, 204.
[63]Yu. Chizmadzhev and Yu. G. Chirkov, "*Porous Electrodes*", in Ed. by E. Yeager, J. O'M. Bockris, B. E. Conway, and S. Sarangapani, *Comprehensive Treatise of Electrochemistry*, Vol. 6, Plenum, New York and London (1983) Chapter , 317.
[64]M. V. Ananth, V. V. Giridhar, and K. Renuga, *Int. J. Hydrogen Energ*. **34** (2009) 658.
[65]C. A. Marozzi and A. C. Chialvo, *Electrochim. Acta* **46** (2001) 861.
[66]L. Zhou, Y. F. Cheng, and M. Amrein, *J. Power Sources* **177** (2008) 50.
[67]M. Imamura, T. Haruyama, E. Kobatake, Y. Ikariyama, and M. Aizawa, *Sens. Actuators B* **24–25** (1995) 113.
[68]H. -K. Seo, D. -J. Park, and J. -Y. Park, *Thin Solid Films* **516** (2008) 5227.
[69]I. G. Casella, *Electrochim. Acta* **54** (2009) 3866.

[70]S. A. S. Machado, J. Tiengo, P. de Lima Neto, and L. A. Avaca, *Electrochim. Acta* **39** (1994) 1757.
[71]L. Li, F. Ye, L. Chen, T. Wang, J. Li, and Z. Wang, *J. Power Sources* **186** (2009) 320.
[72]V. Diaz, S. Real, E. Teliz, C. F. Zinola, and M. E. Martins, *Int. J. Hydrogen Energ*. **34** (2009) 3519.
[73]D. Pletcher, *J. Appl. Electrochem*. **14** (1984) 403.
[74]K. Lohrberg and P. Kohl, *Electrochim. Acta* **29** (1984) 1557.
[75]N. D. Nikolić, Lj. J. Pavlović, M. G. Pavlović, and K. I. Popov, *J. Serb. Chem. Soc*. **72** (2007) 1369.
[76]N. D. Nikolić, K. I. Popov, Lj. J. Pavlović, and M. G. Pavlović, *J. Electroanal. Chem*. **588** (2006) 88.
[77]N. D. Nikolić, Lj. J. Pavlović, M. G. Pavlović, and K. I. Popov, *Electrochim. Acta* **52** (2007) 8096.
[78]N. D. Nikolić, G. Branković, V. M. Maksimović, M. G. Pavlović, and K. I. Popov, *J. Solid State Electrochem*. **14** (2010) 331.
[79]N. D. Nikolić, G. Branković, V. M. Maksimović, M. G. Pavlović, and K. I. Popov, *J. Electroanal. Chem*. **635** (2009) 111.
[80]G. E. Dima, A. C. A. de Vooys, and M. T. M. Koper, *J. Electroanal. Chem*. **554–555** (2003) 15.
[81]W. -Y. Ko, W. -H. Chen, C. -Y. Cheng, and K. -J. Lin, *Sens. Actuators B* **137** (2009) 437.
[82]D. Pletcher and Z. Poorbedi, *Electrochim. Acta* **24** (1979) 1253.
[83]K. I. Popov, T. M. Kostić, N. D. Nikolić, E. R. Stojilković, and M. G. Pavlović, *J. Electroanal. Chem*. **464** (1999) 245.
[84]A. J. Arvia and R. C. Salvarezza, *Electrochim. Acta* **39** (1994) 1481.
[85]W. -Y. Ko, W. -H. Chen, S. -D. Tzeng, S. Gwo, and K. -J. Lin, *Chem. Mater*. **18** (2006) 6097.

5

Electrochemical Micromachining and Microstructuring of Aluminum and Anodic Alumina

Dmitri A. Brevnov[1] and Peter Mardilovich[2]

[1]*Applied Materials Inc., Santa Clara, CA 95052, USA*
[2]*Hewlett-Packard Company, Corvallis, OR 97330, USA*

I. INTRODUCTION

At a time when natural recourses are getting scarce and the impact of human civilization on the environment is increasing, the cost and abundance of raw materials have to be considered in every industry. Since the discovery of the electrolytic production of aluminum in the late nineteenth century, Al has been employed for manufacturing a variety of products ranging from household appliances to airplanes. The electrometallurgical production of Al consumes a large amount of electrical energy and is associated with hazardous emissions. Nevertheless, Al remains widely used in industry due to its abundance on our planet, durability, and useful electrical, gravimetric, thermal, and mechanical properties.

The durability of Al is due to the thin surface layer of aluminum oxide, which is formed when Al is exposed to air. Thick Al_2O_3 layers may be produced by anodization, which results in either porous

S.S. Djokić (ed.), *Electrodeposition: Theory and Practice*,
Modern Aspects of Electrochemistry 48, DOI 10.1007/978-1-4419-5589-0_5,

Al_2O_3 or a dense oxide layer, called barrier Al_2O_3.[1–4] The former oxide may be grown under conditions, which result in two unique features: regularly hexagonal and straight-through arrangement of pores.[1–4] The characteristic interpore distance can be varied from 10 to 500 nm, with the lower limit being smaller than the dimensions of features obtained from traditional photolithographic techniques. This peculiarity of the pore arrangement, combined with a possibility to control the pore diameter, has resulted in the employment of porous Al_2O_3 as a template for synthesis. All of these techniques could be considered as the bottom-up approach for the fabrication of nanostructures.

The emphasis in this chapter, however, is given exclusively to the top-down approach for the fabrication of microstructures by using a combination of photolithography and subsequent porous-type anodization of either Al films or Al substrates that could be a few hundred microns thick. In the top-down approach, the anodization mask is placed on the Al surface and Al is locally anodized by porous-type anodization. As a result, microstructures are fabricated with alternating regions of Al and porous Al_2O_3. Next, either porous Al_2O_3 or non-anodized Al can be selectively etched, which allows for the fabrication of either metallic or ceramic 3D features. This chapter will focus on electrochemical micromachining (EMM)[5] based on localized porous-type anodization and selective etching, technological issues associated with these processes, and applications of EMM of Al for the fabrication of 3D metallic and ceramic microstructures.

This chapter is not intended to be a comprehensive review of literature. For example, micromachining based on porous-type anodization of the entire Al substrate, subsequent lithography, and selective and anisotropic etching of unprotected regions of porous Al_2O_3 will not be covered in this chapter. This technique has been described in other publications.[6–11] This chapter represents our attempt to draw attention to the unique capability of localized porous-type anodization of Al for the fabrication of Al or Al_2O_3 microstructures and to demonstrate some examples of fabricated or feasible devices. In addition, this chapter is intended to summarize advances made in this area from the 1970s to the present time.

II. ELECTROCHEMICAL MICROMACHINING AND LOCALIZED ANODIZATION

1. Electrochemical Methods for 3D Microstructure Fabrication: Additive Plating and Wet Subtractive Etching

3D Metallic microstructures can be fabricated by subtractive etching and additive plating.[12–22] While subtractive etching is based upon metal removal from unmasked areas, additive plating results in the deposition of metals in the areas defined by photolithographic masks. Plating methods are used for the fabrication of fine features with a narrow line width and small pitch. In contrast, as a category of subtractive etching, wet (chemical and electrochemical) etching is typically employed for the fabrication of wide metallic features. The technological limitation of wet etching is imposed by the mostly isotropic nature of the metal removal, which results in undercutting. In this case, removal of metal in unprotected areas produces trapezoidal features, whose shape is dictated by the ratio of the vertical and lateral dissolution rates. Thus, this phenomenon reshapes metallic features and has to be taken into account during manufacturing. Undercutting is characterized by the etch factor (EF), which is defined as the ratio of the amount of straight-through etch and the amount of undercut.[13,17]

Aluminum and other valve metals are typically microstructured by subtractive etching techniques because their formal potentials are too negative to allow for electrodeposition from aqueous solutions.[12–22] Microstructuring of Al films can be performed by either wet chemical etching (as an example, in a mixture of H_3PO_4/HNO_3/H_2O)[23] or chlorine-based plasma etching.[24,25] While wet chemical etching of patterned Al films was used previously in industry, reactive ion etching (RIE) is now the preferred method for the etching of patterned Al substrates. This choice is due to a high EF, which is obtained with RIE. Wet (chemical and electrochemical) etching results in the narrowing of Al features due to metal removal under the etching mask. At the same time, wet etching still remains a cost-effective alternative to RIE for applications, in which economical benefits overcome technological limitations.

2. Fabrication of 3D Metallic and 3D Ceramic Microstructures Based on Electrochemical Micromachining of Al

In addition to wet chemical etching, EMM of Al films can be performed by using porous-type anodization.[7,26–32] Under conditions of anodic polarization in acidic electrolytes (e.g., sulfuric, phosphoric, and oxalic acid), this process results in the material known as porous Al_2O_3, which is characterized by the hexagonal and straight-through pore arrangement.[1–4] As shown in Fig. 1, EMM by porous-type anodization combines photolithography (Step 1), porous-type anodization (Step 2), and chemical etching of porous Al_2O_3 (Step 3a). The last step is selective toward porous Al_2O_3 over Al preserved under the anodization mask. This fabrication procedure results in the Al microstructures that comprise (as an example) metallic pillars, which are formed in the areas protected by the anodization mask. As an alternative to metallic microstructures, ceramic microstructures composed of porous Al_2O_3 can be fabricated by substituting the selective dissolution of porous Al_2O_3 with selective dissolution of Al, as illustrated in Fig. 1 (Step 3b). Consequently,

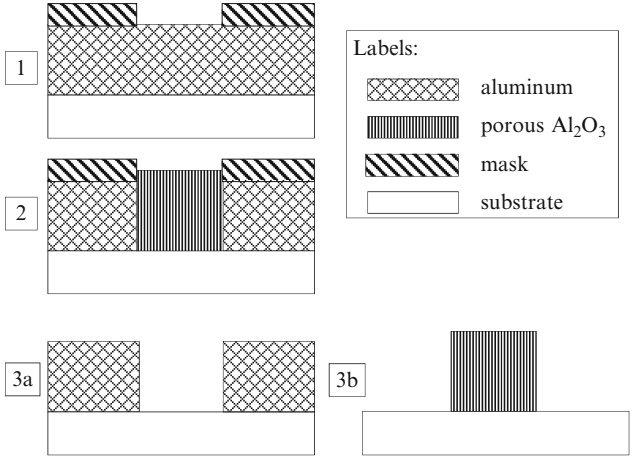

Figure 1. Process flow: (1) photolithography (may include an optional step of negative mask transfer by barrier-type anodization), (2) porous-type anodization, (3) chemical etching of either (3a) porous Al_2O_3 or (3b) Al.

porous-type anodization of patterned Al films can be used for the fabrication of either metallic or ceramic microstructures with their dimensions being defined by the design of anodization masks (pitch and width) and EF.

3. Undermask Anodization During Localized Anodization of Al and Fidelity of the Mask Transfer

Models have been developed to explain the conversion of Al to porous Al_2O_3, which takes place under conditions of anodic polarization of Al in acidic electrolytes.[33–36] The anodized films are structured with three distinct layers: the base Al film, an intermediate and scalloped layer of barrier Al_2O_3, and a relatively thick layer of porous Al_2O_3. While the thickness of barrier Al_2O_3 is linearly proportional to the anodization voltage, the thickness of porous Al_2O_3 is proportional to the anodization time. The steady-state current during porous-type anodization is established when the rate of field-enhanced dissolution of Al_2O_3 at the bottom of pores is equal to the rate of Al_2O_3 formation at the Al/barrier Al_2O_3 interface. These two processes are controlled by the electrical field (10^8–10^9 V/m) distributed at the scalloped layer of barrier Al_2O_3.[33–36] Due to the hemispherical nature of pore bases, the distribution of electrical field has been shown to be inhomogeneous in two directions: laterally along the sample surface and vertically along the thickness of barrier Al_2O_3.[34] During porous-type anodization of patterned Al films, the distribution of electrical field in the barrier Al_2O_3 has the direct effect on the vertical pore growth in the unmasked areas and tilted/lateral pore growth under the anodization mask.

The conversion of Al to porous Al_2O_3 proceeds in the direction normal to the equipotential surfaces.[34] Thus, at the vertical interface between Al preserved under the anodization mask and porous Al_2O_3, pores propagate under the anodization mask.[27,30–32] The fidelity of the mask transfer during porous-type anodization of patterned Al substrates (which is called localized anodization) is compromised by the pore curvature as schematically shown in Fig. 2.[32] The metallic pillars, which are revealed after chemical etching of porous Al_2O_3, are trapezoidal and narrower than the width of the anodization mask. Figure 2 represents two microstructures obtained after (a) localized anodization of Al and (b) chemical etching

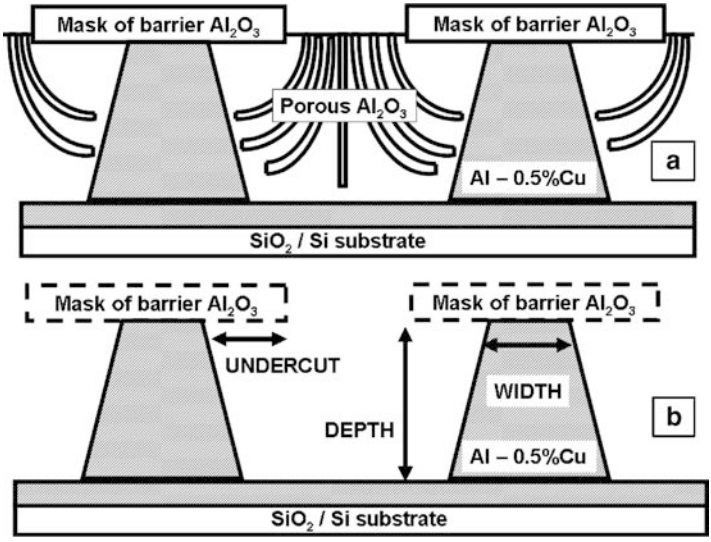

Figure 2. Cross-sectional schematics of microstructures: (**a**) features of Al and porous Al_2O_3 obtained after localized porous-type anodization, (**b**) trapezoidal features of Al obtained after chemical etching of porous Al_2O_3. Reproduced from Ref. [32] with permission from IOP Publishing Ltd.

of porous Al_2O_3. The undermask anodization (Fig. 2a) is analogous to undercutting, which is typically observed during wet chemical etching of patterned metallic substrates. Due to this similarity, EF is defined as the ratio of microgrooves' depth (D) to undercut (U) and calculated according to (1). U is equal to half of the difference between the width of the anodization mask (W_{mask}) and the width of metallic pillars (W_{pillar}).

$$\text{EF} = D/U = D/(0.5 \times (W_{\text{mask}} - W_{\text{pillar}})) \qquad (1)$$

Figure 3 shows trapezoidal metallic features embedded in the regions of porous Al_2O_3 (Fig. 3a), which are obtained after localized anodization, and metallic pillars, which are obtained after chemical etching of porous Al_2O_3 (Fig. 3b). Being qualitative, Figs. 2 and 3 provide a framework for the analysis of the technological issues associated with localized anodization of Al films.

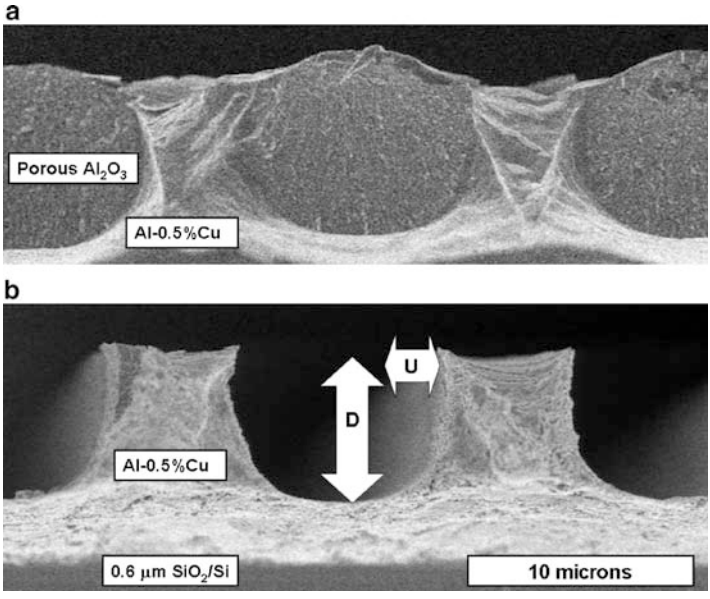

Figure 3. Cross-sectional micrographs: (**a**) microstructures with alternative regions of Al and porous Al_2O_3 obtained after localized porous-type anodization, (**b**) trapezoidal metallic features obtained after chemical etching of porous Al_2O_3. Two *white arrows* show the depth of microgrooves (*D*) and undercut (*U*).

4. Technological Limitations and Economical Benefits of Electrochemical Micromachining of Al

Si is micromachined for the fabrication of 3D structures and microelectromechanical systems (MEMS).[5,12–22] EMM of Cu and Ti is used in aerospace, medical, and microelectronic industries. In a similar way, EMM of patterned Al and Al-based alloys can be utilized in a wide number of applications, including energy storage devices, microanalytical systems, microfluidic, optical, and microelectronic devices. Regardless of the limitation imposed by a limited EF, this technique may constitute an economical and scalable to large geometric areas platform for microstructuring of Al substrates. Metallic or ceramic features can be fabricated with dimensions defined by the mask design and EF. The following sections will focus on technological issues associated with localized anodization of Al

films and past, current, and potential future applications of EMM of Al and Al alloys, including fabrication of 3D metallic and ceramic microstructures.

III. TECHNOLOGICAL ASPECTS OF LOCALIZED ANODIZATION OF ALUMINUM SUBSTRATES

1. Mask Reliability During Localized Anodization

As discussed in Sect. II, EMM of patterned Al substrates by porous-type anodization involves three processing steps: photolithography to define the anodization mask, porous-type anodization, and chemical etching of porous Al_2O_3, which is formed in the unmasked areas. To guarantee the fidelity of the mask transfer during localized anodization, it is critically important that the anodization mask remains adhesive to the Al surface during severely oxidative conditions in the anodization bath. In addition, the anodization mask has to accommodate the volumetric expansion, which typically takes place when Al is converted to porous Al_2O_3. Although the volumetric expansion can be minimized by choosing the electrolyte temperature and acidity, the strain is still generated at the anodization mask/Al interface, which may result in the anodization mask delamination. These two requirements limit the choice of the appropriate material, which can function as the anodization mask.

The adhesion of photoresist to the Al surface during anodization may be modified by the kind of photoresist, its thickness, and the baking conditions. However, it is still problematic that photoresist stays adhesive to the Al surface especially during localized anodization of thick Al substrates. Consequently, other anodization masks have been developed and implemented. They can be divided into three groups: (1) silica,[26] (2) barrier metals (e.g., Ti, Ta, Nb)[27–29] and their oxides, and (3) barrier Al_2O_3.[26,31,32] For the first and second groups, the fabrication process has to include additional processing steps: deposition of a blanket film on Al, photolithography, and either wet or dry etching of the blanket film. Then, the etched layer can be used as the anodization mask for localized anodization. Although additional deposition and etching steps have technological merits and ensure the mask reliability, this process flow is inherently costly and technologically complex. Consequently, barrier Al_2O_3 meets both technological and economical requirements.

Barrier Al_2O_3 is generated in neutral solutions (e.g., borates, phosphates) under conditions of anodic polarization.[3,4] Barrier-type anodization is a self-limited process and the thickness of barrier Al_2O_3 is linearly proportional to the anodization voltage with the coefficient of 1.2–1.4 nm/V. In order to use barrier Al_2O_3 as the mask for porous-type anodization, the fabrication procedure is extended to include three steps: barrier-type anodization of Al substrates patterned with photoresist, photoresist stripping, and porous-type anodization in the areas initially covered with photoresist. The negative pattern transfer was reported for EMM by porous-type anodization of patterned Ti[18,19] and Al[26,31,32] substrates. This procedure eliminates requirements for photoresist to be chemically stable and stay adhesive to the substrate for a long period of time under oxidative conditions during porous-type anodization. It is important to mention that barrier-type anodization may undercut photoresist and extend the masked areas. However, this process is short (60–120 s) and can be taken into account during manufacturing. Thus, barrier Al_2O_3 is likely to remain the most reliable and economical mask for localized anodization of Al substrates because of its properties (superb adhesion to Al and high corrosion resistance).

The utility of barrier Al_2O_3 as the anodization mask is demonstrated in Fig. 4, which shows two trapezoidal regions of the metallic phase alternating with regions of porous Al_2O_3.[32] These micrographs were obtained upon completion of porous-type anodization of 3-μm-thick Al–0.5%Cu films. Due to the volumetric expansion, cracks (inset, Fig. 4) are formed at the interface between the Al–0.5%Cu phase and porous Al_2O_3. However, pores do not initiate from the top of the substrate due to the protective character of the anodization mask, under which the metallic phase is preserved. The reliability of barrier Al_2O_3 as the anodization mask is further illustrated in Fig. 5. The mask of ∼120-nm-thick barrier Al_2O_3 effectively blocks the formation of porous Al_2O_3 in the protected areas and does not delaminate from the substrate regardless of the volumetric expansion, as observed on each side of the trapezoidal metallic feature. Both Figs. 4 and 5 confirm that the choice of the anodization mask is critical for the reliable mask transfer during localized anodization.

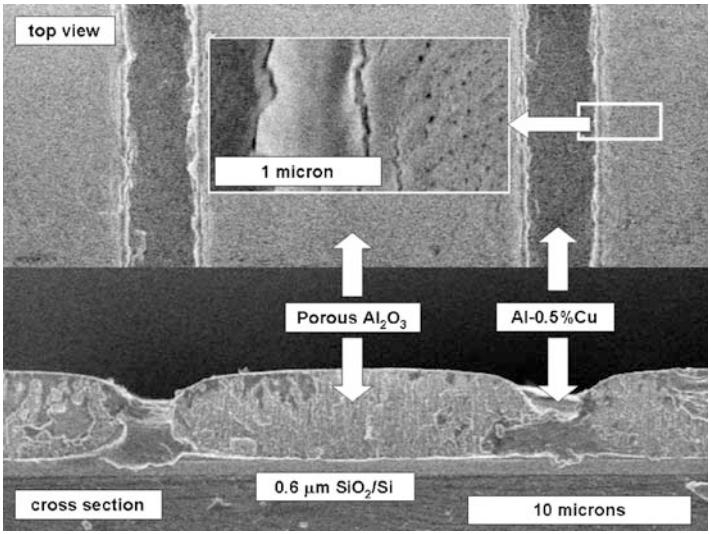

Figure 4. Regions of Al–0.5%Cu alternating with regions of porous Al_2O_3 obtained upon completion of localized porous-type anodization of ~3-μm-thick Al–0.5%Cu films. The *inset* is a magnified image of the interface between Al–0.5%Cu and porous Al_2O_3. Reproduced from Ref. [32] with permission from IOP Publishing Ltd.

2. Etch Factor as a Function of Process Conditions

A high EF is typically needed in manufacturing in order to obtain features with controlled dimensions and a high aspect ratio.[5,13,17] The quantitative analysis of metallic features obtained with EMM by localized anodization allows one to evaluate how EF defined by (1) depends on the process conditions. As discussed in Sect. II, at the vertical interface between the metallic phase and porous Al_2O_3, pores propagate under the anodization mask, which results in the trapezoidal shape of metallic features. The pore curvature may depend on the voltage of porous-type anodization, electrolyte composition and temperature, the depth of porous-type anodization, the presence of alloying elements in Al (e.g., Cu, Si), and the dimensions of features, which undergo porous-type anodization.

Under potentiostatic conditions, the applied voltage dictates the rate of porous Al_2O_3 formation. Thus, the ratio of the vertical and lateral anodization rates may vary with voltage. Figures 6 and 7

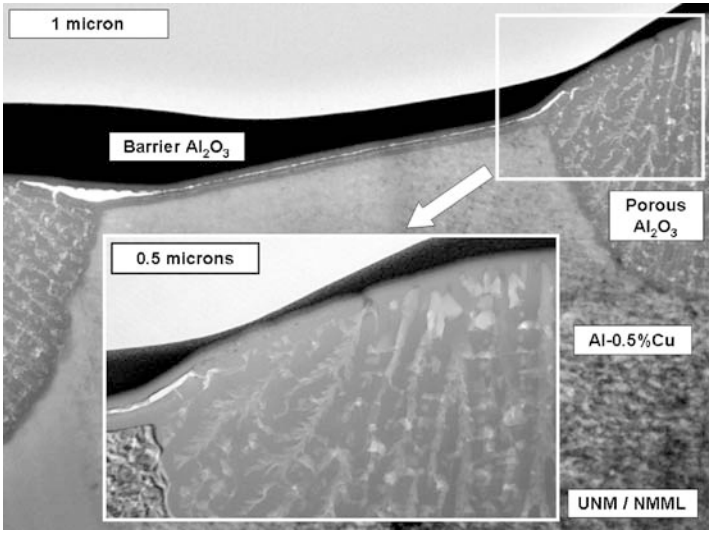

Figure 5. TEM micrograph showing the Al–Cu phase preserved under the anodization mask of barrier Al_2O_3. The magnified interface between Al–0.5%Cu and porous Al_2O_3 is shown as *inset*. Reproduced from Ref. [32] with permission from IOP Publishing Ltd.

show pillars of Al–0.5%Cu phase with concave slopes obtained by EMM of ~3-μm-thick Al–0.5%Cu films.[32] While Fig. 6 shows pillars fabricated with the porous-type anodization voltage of 20 V, Fig. 7 shows pillars fabricated with voltage of 60 V. Indicated with arrows on high magnification micrographs (the lower part of each figure) are two critical dimensions: D and U, which are developed on one side of anodization mask and calculated according to (1).

The analysis of Figs. 6 and 7 suggests that U decreases and, as a result, EF increases (from 2.6 to 4.3) as the voltage of porous-type anodization is increased. These observations imply that, in contrast to isotropic wet chemical etching,[5,13,17] localized anodization of Al–0.5%Cu films has some directionality. Similar observations were reported by Lazarouk et al. and were supplemented with modeling of the electrical field distribution during localized anodization.[27] As discussed in Sect. II, the theoretical model of porous Al_2O_3 growth suggests an inhomogeneous distribution of electrical field in the scalloped layer of barrier Al_2O_3, which is formed at the

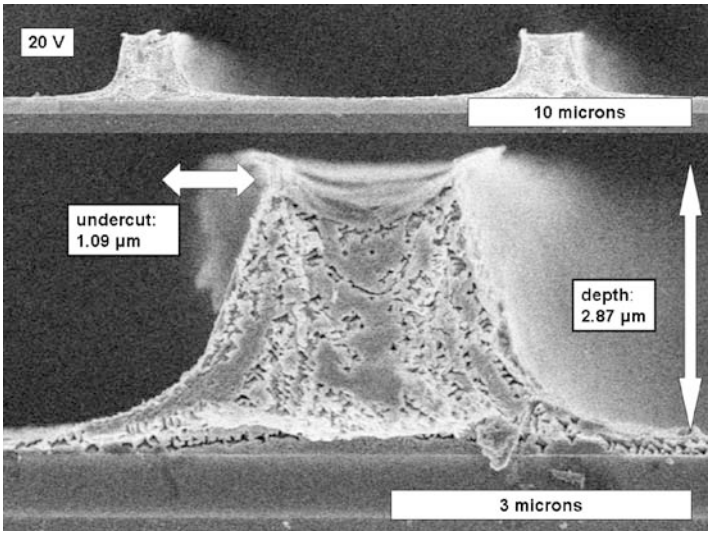

Figure 6. Cross-sectional SEM micrographs showing metallic pillars of ~3-μm-thick Al–0.5%Cu preserved under the anodization mask of barrier Al_2O_3. Porous–type anodization voltage is 20 V. Reproduced from Ref. [32] with permission from IOP Publishing Ltd.

interface between porous Al_2O_3 and the underlying Al substrate.[34] The voltage dependence of EF indicates that the inhomogeneous distribution of electrical field is amplified when the voltage of porous-type anodization is increased. Consequently, pores preferentially grow in the vertical direction, thus minimizing the undermask anodization. It is important to note that these results were obtained with Al–0.5%Cu films. Porous-type anodization of Al films with a few % Cu is known to result in the Cu enrichment underneath the scalloped layer of barrier Al_2O_3.[37–39] This enrichment may influence undercutting and EF. The effect of alloying element(s) on the anisotropy of localized anodization has not been extensively studied and may need additional investigation.

In addition to voltage, the rate of porous-type anodization depends on the electrolyte composition, acidity, and temperature. These variables affect the rate of Al_2O_3 dissolution at the pore bottoms in the isotropic way and are not expected to increase EF. Another variable to consider is the depth of porous-type anodization.

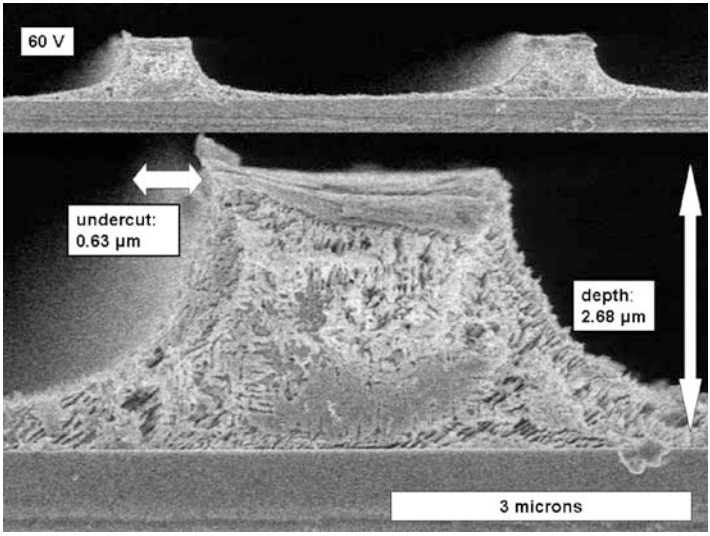

Figure 7. Cross-sectional SEM micrographs showing metallic pillars of ~3-µm-thick Al–0.5%Cu preserved under the anodization mask of barrier Al_2O_3. Porous–type anodization voltage is 60 V. Reproduced from Ref. [32] with permission from IOP Publishing Ltd.

Cosse et al. showed that EF decreases as the thickness of anodized Al–0.5%Cu films increases from 3 to 10 µm.[32] Kikuchi et al. reported that EMM of Al specimens resulted in the hemispherical 20-µm-deep microgrooves.[40] In this case, porous-type anodization of patterned Al substrates was isotropic. These results suggest that localized anodization becomes isotropic as the anodization process proceeds. These conclusions are consistent with those obtained with other EMM methods, which indicate that EF decreases as the depth of metal removal increases.[13,17]

In order to evaluate EF, one has to consider the dimensions of features undergoing porous-type anodization, which are typically 1–100 µm wide. Data reported in literature suggest that EF decreases when the width of unmasked areas decreases. For example, Renshaw showed the hemispherical cavities of porous Al_2O_3 formed by porous-type anodization through defects in the nonporous surface oxide films.[41] Brevnov et al. reported the radial propagation of pores initiated at the anodization mask defects, which results in

the hemispherical shape of the anodized features. In both cases, the defects were less than 1 μm wide.[31] Thus, localized anodization becomes isotropic as the width of unmasked areas undergoing porous-type anodization decreases.

In conclusion, the requirement to obtain a high aspect ratio features dictates a necessity to increase EF. As discussed in this section, the anisotropy of localized anodization depends on the process conditions, such as anodization voltage, electrolyte composition and temperature, the depth of porous-type anodization, the presence of alloying elements in Al, and the dimensions of features, which undergo porous-type anodization. As shown, voltage is the primary variable, which allows one to increase EF. At the same time, localized anodization of patterned Al substrates became isotropic as the depth of porous Al_2O_3 formation increases and the width of anodized features decreases. These trends have to be taken into account while utilizing porous-type anodization for EMM of Al substrates.

3. Current Density Distribution at the Pattern Scale During Localized Anodization

Porous-type anodization of patterned Al substrates may proceed with the nonuniform current density distribution along the surface. The current density distribution can be considered on three different scales: the work piece, pattern, and feature scales.[42–45] The pattern scale nonuniformity results from the uneven coverage of patterned features from one area of the substrate to another. The pattern scale nonuniformity was thoroughly investigated in the area of electrodeposition.[42] Areas with high and low photoresist coverage may attract uneven current densities and, consequently, develop uneven deposit thicknesses from one zone to another. In a similar way, the pattern scale nonuniformity was observed for localized anodization of Al films.[46,47] For example, the pattern scale nonuniformity was reported during anodic processing of Al films for the fabrication of Al interconnection patterns.[46] An uneven coverage of the anodization mask results in a variable thickness of porous Al_2O_3 between regions with high and low coverages. Upon etching of porous Al_2O_3, this variability is duplicated in the depths of microgrooves and affects the shape of metallic pillars. In a manufacturing environment, EMM is most often applied to substrates, which have an uneven coverage of patterned features. Consequently, it is important to understand how the anodization mask coverage controls the uniformity of current

density distribution at the pattern scale and to establish a relationship between the anodization mask coverage and dimensions of etched features. In this section, the current density distribution at the pattern scale will be discussed in some detail.

The pattern scale nonuniformity during anodic processing of Al substrates may be treated in the same theoretical framework as electrodeposition.[42] Taking into account the rate-limiting process, electrodeposition typically proceeds under either ohmic or kinetic control. Similarly, the rate of porous-type anodization may be limited by either the ohmic resistance or the resistance of ion migration in the scalloped layer of barrier Al_2O_3 (kinetic control). It is helpful to use the Wagner number, W_a, defined as the ratio of anodic polarization resistance to the ohmic resistance of electrolyte.[42,48] When the former dominates ($W_a > 10$), the current density in the anodization bath is secondary. Thus, for high W_a, the distribution of secondary current density has to be rationalized in order to explain the nonuniformity observed at the pattern scale.

In order to illustrate how the anodization mask coverage affects the distribution of secondary current density and the shape of metallic features, as an example, one may consider the mask design including areas with variable anodization mask coverage (features with the same width and different pitches).[47] Figures 8 and 9 demonstrate regions of Al–0.5%Cu phase, which alternate with regions of porous Al_2O_3 and are separated by 15 and 60 μm pitches, respectively. While the upper part of each figure is a low magnification image, the lower part is a magnified image showing either two (Fig. 8) or one (Fig. 9) region of Al–0.5%Cu phase. The trapezoidal metallic pillars revealed after chemical etching of porous Al_2O_3 are shown in Fig. 10. Under chosen process conditions for porous-type anodization (3% w/v oxalic acid, 30°C, and 35 V), W_a was larger than 100. The areas with a high coverage of anodization mask of barrier Al_2O_3 attract a low current density and, consequently, develop thin layers of porous Al_2O_3. Chemical etching of porous Al_2O_3 reveals that microgrooves formed in the areas with the high coverage of anodization mask of barrier Al_2O_3 (pitch of 15 μm) are shallower than the ones formed in the areas with the low coverage of anodization mask (pitch of 60 μm). Consequently, the distribution of secondary current density is nonuniform and the current is converged to the areas with a low coverage and partially excluded from areas with a high coverage. Similar to electrodeposition on patterned substrates

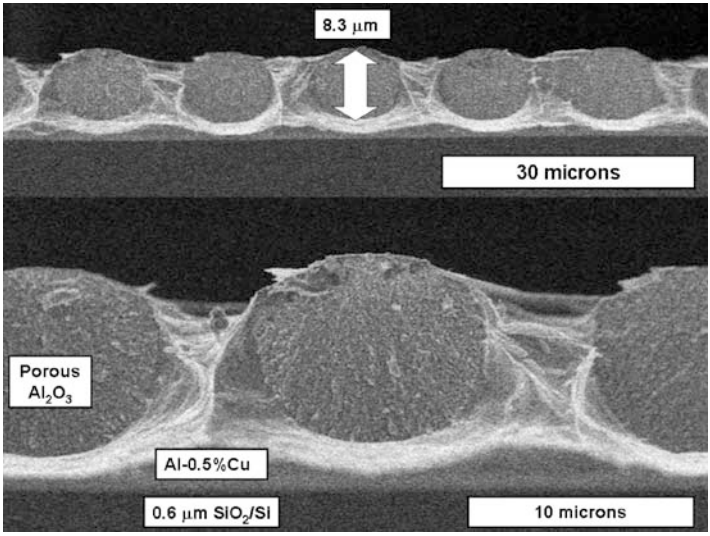

Figure 8. Regions of ~9.5-μm-thick Al–0.5%Cu phase alternating with regions of porous Al_2O_3 obtained upon completion of porous-type anodization. Pitch is 15 μm. Porous-type anodization time is 80 min. Reproduced from Ref. [47] with permission from ECS – The Electrochemical Society.

with variable mask coverage, the rate-limiting ionic current during porous-type anodization of patterned Al films follows the pathway of least resistance, as defined the anodization mask coverage.

The nonuniform distribution of secondary current density during localized anodization of Al with variable mask coverage may result in a loss of electrical connection and prevent some areas from complete conversion of Al to porous Al_2O_3. For example, areas with a low coverage of the anodization mask (Fig. 10c) are anodized faster than areas with a high coverage of the anodization mask (Fig. 10a). Thus, if the former areas are surrounded by the latter areas, the electrical connection is lost before the complete anodization of the former areas. In contrast, when the design of anodization mask has a single pitch and width, deep trenches are formed in the unmasked areas as demonstrated in Fig. 11. The problem with a loss of the electrical connection was solved by using a conductive underlayer between the Al film and Si substrate.[46] A possibility of wet chemical etching may also be considered. In summary, the distribution of

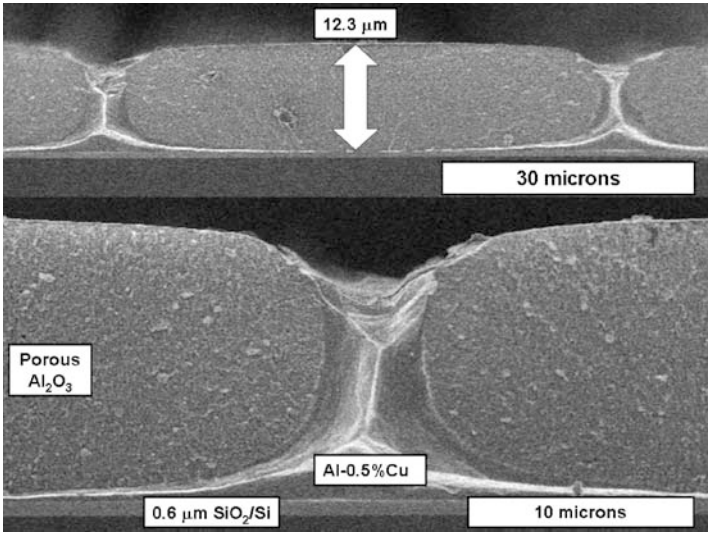

Figure 9. Regions of ~9.5-μm-thick Al–0.5%Cu phase alternating with regions of porous Al_2O_3 obtained upon completion of porous-type anodization. Pitch is 60 μm. Porous-type anodization time is 80 min. Reproduced from Ref. [47] with permission from ECS – The Electrochemical Society.

current density during localized anodization of substrates with variable mask coverage has to be considered in order to rationalize the rate of porous-type anodization and the shape of metallic features. The distribution of current density is primarily effected by mask dimensions and the rate-limiting step (e.g., W_a).

IV. LOCALIZED ANODIZATION AND ELECTROCHEMICAL MICROMACHINING: APPLICATIONS AND DEVICES

This section will review selected applications and devices produced by using localized porous-type anodization and, optionally, selective etching of either porous Al_2O_3 or Al. The fabrication of these devices shares the common technological issues and challenges discussed in Sect. III: the choice of a reliable mask material, the fidelity of the mask transfer, the trapezoidal profile of metallic features, the

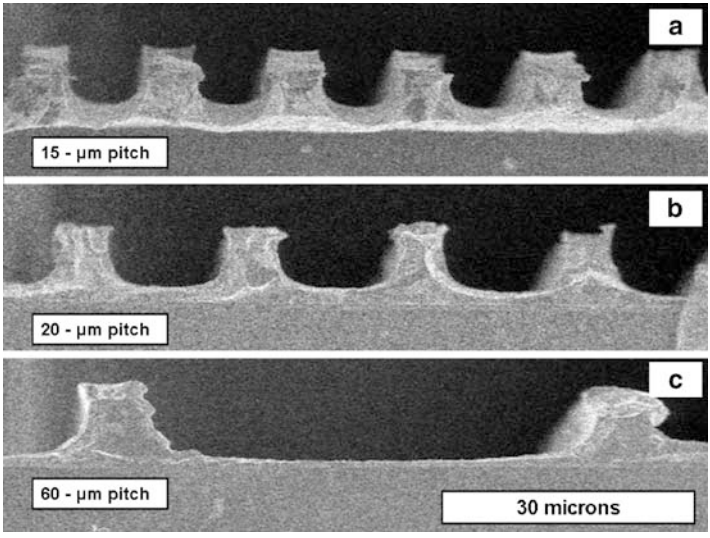

Figure 10. Cross-sectional SEM micrographs showing multiple pillars of the ~9.5-μm-thick Al–0.5%Cu. Porous-type anodization time is 80 min. Pitch is 15 μm (**a**), 20 μm (**b**), and 60 μm (**c**). Reproduced from Ref. [47] with permission from ECS – The Electrochemical Society.

effect of the mask design on the rate of porous-type anodization and on the completion of anodization of the entire thickness of Al without traces of Al islands (which could be responsible for the lateral conduction between individual electrodes/interconnects), and volumetric expansion of porous Al_2O_3 during anodization.

1. Metallization Applications in the Microelectronics and Solar Cells Industry, and Fabrication of Passive Components

Prior to the introduction of Cu electroplating, the primary method used to form a multilevel structure of interconnections in integrated circuit applications was Al and Al-alloy metallization.[49] Localized porous-type anodization was developed in the 1970s to obtain planar interconnection metallization for multilevel large-scale integration (LSI).[26,46,50] For example, Schwartz and Platter showed that the subtractive etching for Al interconnects could be substituted

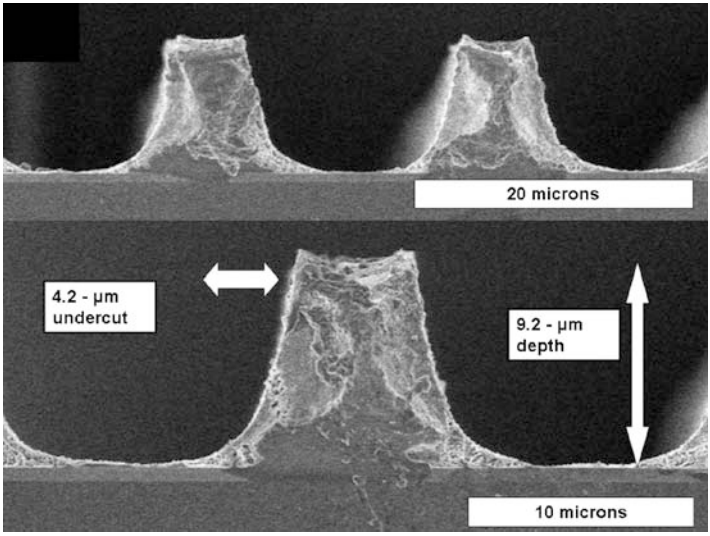

Figure 11. Cross-sectional SEM micrographs showing pillars of ~9.5-μm-thick Al–0.5%Cu obtained after localized porous-type anodization and chemical etching of porous Al_2O_3.

by the anodic conversion of unwanted Al to an insulating film of Al_2O_3.[26] Figure 12 schematically shows the two-level metallization structure with the anodic oxide formed by localized porous-type anodization. For integrated circuit applications, Al is often doped with small amounts of Si and/or Cu to control Al spiking, electromigration, and to improve resistance to hillock formation.[49] Consequently, Schwartz and Platter reported anodic processing of Al alloys.[26] In parallel to the development of anodic processing at IBM,[26,46] similar approaches were developed and reported in other publications.[28,29,51–53] For example, Labunov et al. disclosed a process for making multilevel interconnects by using localized porous anodization.[51] The reliability of multilevel Al metallization was investigated with porous Al_2O_3 as an interlayer insulator.[28,29] The dielectric constant of porous Al_2O_3 was lowered by using the pore widening procedure.[28,29] Localized porous-type anodization was utilized to fabricate multilevel interconnects from 1- to 3-μm-thick Al films with a Ta underlayer deposited on some substrates.[53]

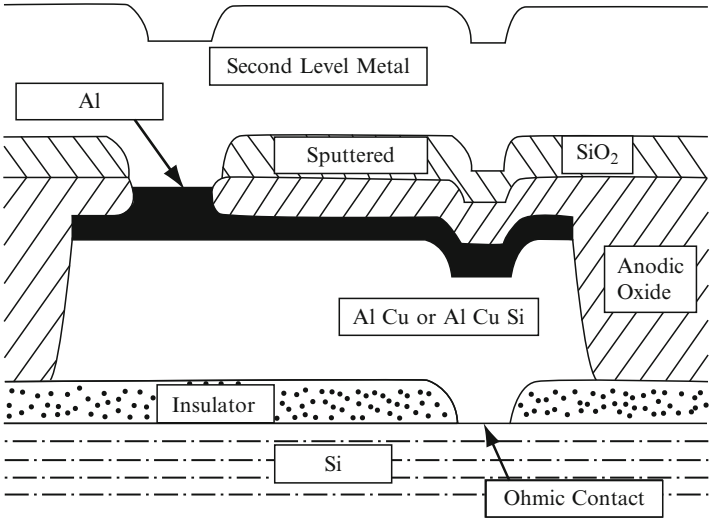

Figure 12. Schematic of two-level interconnection metallization formed by anodic processing. Reproduced from Ref. [26] with permission from ECS – The Electrochemical Society.

Experimental conditions for porous-type anodization were identified, which favor the formation of almost rectangular features with the pattern transfer accuracy of 15%.[53]

Back-side point contact monocrystalline Si solar cells demonstrate high energy conversion efficiencies. In order to achieve these efficiencies for large area solar cells, metallization approaches that minimize the series resistance are required. Two-level metallization schemes were shown to be superior to the use of interdigitated metallic fingers.[54,55] Al deposition, SiO_2 deposition, photolithography, and double-localized anodization were reported for the fabrication of the two-level metallization for high-efficiency Si solar cells.[54,55] Currently, Cu electroplating is used for the metallization of high-efficiency back-side point contact Si solar cells.

In addition to the multilevel metallization and formation of interconnects, anodic processing of Al was employed for the fabrication of integrated passive components: thin film capacitors and inductors.[56,57] For example, localized porous-type anodization of Al films was used to convert 20-μm-thick Al to the dielectric layer of porous Al_2O_3 and to define metal–dielectric–metal structures.[56] The

employment of porous Al_2O_3 as a dielectric layer reduced the process complexity in comparison to the use of chemical vapor deposition methods for the fabrication of dielectric layers. Fabrication of passive components was shown to be compatible with the multilevel Al metallization, thus allowing for further integration.[56,57]

2. Surface Microstructuring

In addition to the anodic processing of Al films, localized porous-type anodization, combined with selective etching of either Al or porous Al_2O_3, can be used for the surface microstructuring of thick Al substrates.[7,30,58] As an example, Fig. 13 demonstrates a schematic presentation of processing steps. Photolithography (Step 1) was used to define 25-μm-diameter circular features separated by 37.5 μm pitch. Time and conditions of localized porous-type anodization (Step 2) were chosen such that U exceeded half of the pitch. Consequently, under chosen process conditions and feature dimensions, any three adjacent anodized areas overlapped. Finally,

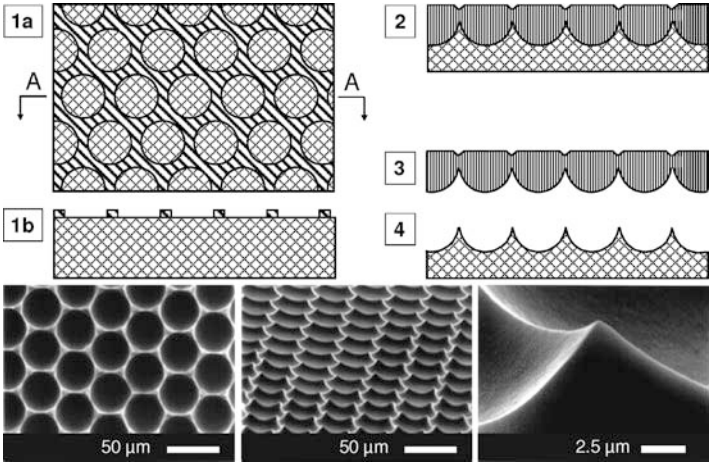

Figure 13. Process flow for surface microstructuring with undercut exceeding half of the pitch. (1) photolithography, (1a) top view and (1b) cross-section view; (2) porous-type anodization; (3) selective etching of Al; and (4) selective etching of porous Al_2O_3. *Lower panel*: SEM images of the microstructured Al surface: top view (*left*), tilted view (*middle*), and a single Al tip at high magnification (*right*). Images reproduced from Ref. [30] with permission from ASME.

the microstructured surface was obtained by selective etching of Al (Step 3) or porous Al_2O_3 (Step 4).[7,30]

When all photolithographic features have the same dimensions (width and pitch) and the mask reliability is not compromised, the microstructured Al surface is uniform, as illustrated in the lower part of Fig. 13. The trigonal tips were generated at intersections of three boundaries between adjacent anodized areas (Fig. 13, the right image). The apex of these tips could be as sharp as 60°,[7,30] which indicates an EF of 1.7. By using patterns with different symmetry, shape, dimensions, and periodicity, the final surface may have a wide range of structures. For example, by employing a mask with parallel lines, Zhao et al. demonstrated a ridge-like Al strip pattern after removing the porous Al_2O_3 layer.[58]

When photolithographic features have different dimensions, one has to consider the effect of the mask design on the distribution of the current density during localized porous-type anodization, as described in Sect. III. When the current density distribution is secondary, heavily masked areas develop thinner layers of porous Al_2O_3 than lighter masked areas. The same conclusions were obtained for localized porous-type anodization of thick Al substrates, with empirical dependencies developed between the feature dimension and porous Al_2O_3 thickness.[7,30] Moreover, it was shown that the variability of porous Al_2O_3 thickness could be advantageous because it might allow for multilevel microstructuring in the Z-direction.[30]

Bulk Al or Al foil can be anodized to a significant depth. Therefore, selective etching of non-anodized Al becomes possible, revealing the freestanding porous Al_2O_3 film. The bottom topography of this film is opposite to that created in the Al substrate (Fig. 13, Step 4). Mechanical robustness of the Al_2O_3 film can be enhanced, if necessary, by applying a protective layer on the top after porous-type anodization. For example, porous Al_2O_3 can be covered with an epoxy or a similar polymer film. Figure 14 shows an example of the microstructured Al_2O_3 surface. This patterned structure with the pitch of 37.5 μm is an exact 3D negative replica of the Al surface presented in the lower part of Fig. 13. The top view micrographs (Fig. 14) show the symmetry, the hexagonal shape (defined by the photolithographic mask), and the high quality of boundaries between adjacent anodized areas. These observations confirm that, if localized porous-type anodization is carried out for a sufficient

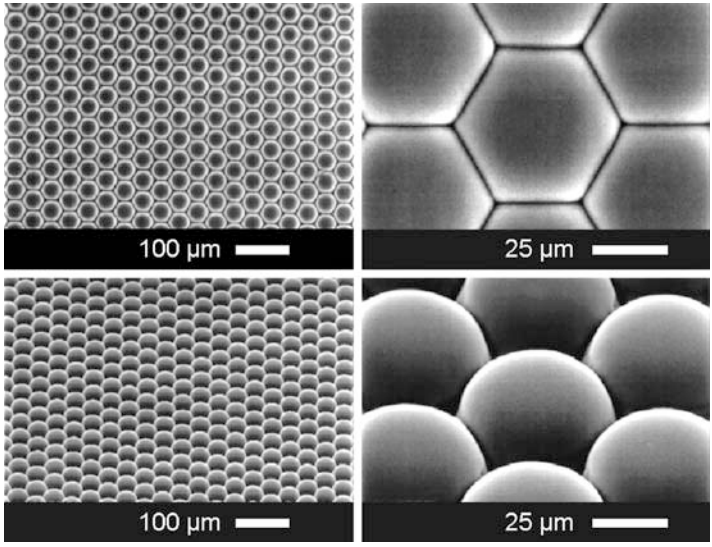

Figure 14. SEM images of microstructured surface of freestanding porous Al_2O_3 after Al etching (Fig. 13, Step 3) at different magnifications. Top (*top*) and tilted (*bottom*) views. Images reproduced from Ref. [30] with permission from ASME.

time, the complete overlap of boundaries between adjacent anodized areas may take place. The necessary time is determined by the mask design, feature dimensions, the rate of porous-type anodization, and EF.

The unique property of the microstructured porous Al_2O_3 substrate derives from the nature of a layer of barrier Al_2O_3 located at the pore bottoms. This layer consists of dense, amorphous Al_2O_3 without any porosity or grain boundaries and, as such, exhibits a high degree of impermeability to hydrogen, nitrogen, and salt solutions.[59,60] Thus, despite the overall porosity, the microstructured porous Al_2O_3 substrate may be impermeable – even for gases – if the boundaries between features are completely closed. This property is important for the incorporation of the microstructured porous Al_2O_3 substrate into functional devices as described in the following sections.

Figure 15 illustrates another example of surface microstructuring. In this case, the process conditions and porous-type anodiza-

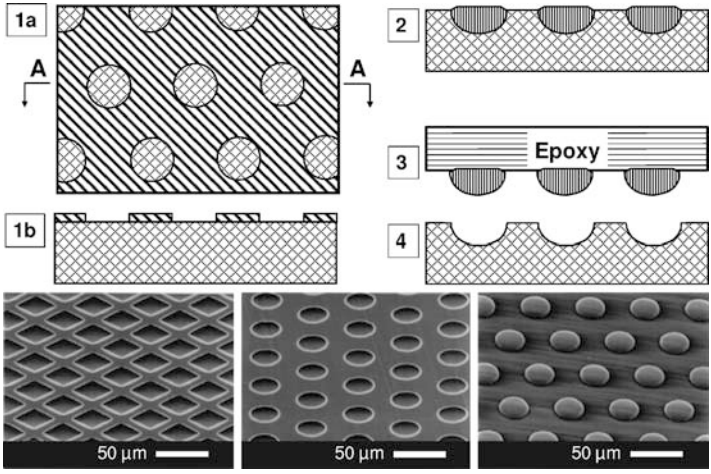

Figure 15. Process flow for surface microstructuring with undercut being less than half of the pitch. (1) photolithography, (1a) top view and (1b) cross-section view; (2) porous-type anodization; (3) application of an epoxy on the top and selective etching of Al from the back; and (4) selective etching of porous Al_2O_3. SEM images of microstructured Al surface after Step 4, tilted samples with different shapes of anodized/etched features (*left* and *middle*) and separated features of porous Al_2O_3 on the epoxy film, after Step 3 (*right*). Images reproduced from Ref. [30] with permission from ASME.

tion time were chosen such that U did not exceed half of the pitch. Anodization was stopped before adjacent anodized areas overlapped due to the lateral pore propagation (Step 2). After porous Al_2O_3 etching (Step 4), the Al surface maintained its initial flatness on the top and contained an array of identical cavities, as defined by the photolithographic mask.[30] Their depths are controlled by the conditions of anodization and the mask design, as discussed above. Tilted SEM micrographs show square (25 × 25 µm) and circular (25 µm diameter) cavities arranged in square and triangular lattices, respectively. Both types of cavities were anodized to a depth of approximately 6 µm. In this case, selective etching of Al was possible only if a protective and supporting layer of epoxy was deposited on porous Al_2O_3 (Step 3). The bottom-right SEM micrograph shows the porous Al_2O_3 features on the epoxy surface, which confirm their uniformity and smoothness. In conclusion, Figs. 13–15 show

selected examples of microstructured surfaces composed from either Al or porous Al_2O_3.

3. Freestanding Porous Al_2O_3 Substrates and Devices

As shown in the previous section, localized porous-type anodization and selective etching of Al can be used for the fabrication of complex microstructures composed from freestanding porous Al_2O_3. As an example, Fig. 16a and b demonstrates SEM and optical images of microstructured porous Al_2O_3 substrates, which are utilized for sensor applications (Fig. 16c, d). The lateral dimensions of freestanding ceramic substrates were controlled by the mask design and process conditions. The thickness was controlled by the current density and duration of anodization (2 min anodization

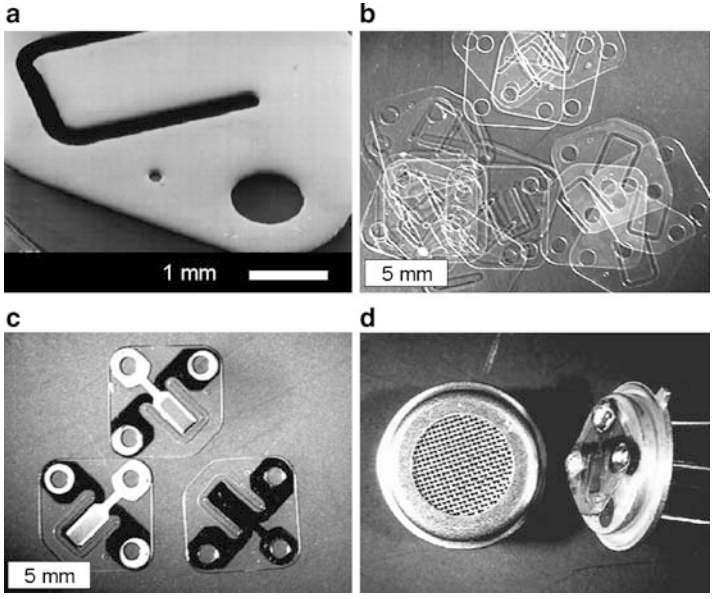

Figure 16. (**a**) SEM of gas microsensor substrate prepared by localized porous–type anodization of Al. (**b**, **c**) Optical images of gas microsensor substrate without and with electrodes. (**d**) Packaged humidity sensor with microheater. Images reproduced from Ref. [7] with permission from ECS – The Electrochemical Society and from Ref. [69] with permission from ASME.

at 15 mA/cm^2, or 1.8 C/cm^2, yields 1-μm-thick porous Al_2O_3). The thickness of workable freestanding porous Al_2O_3 substrates may vary from ~30 to ~300 μm.[4,8] Thicker than ~300 μm substrates may be obtained while using double-sided anodization.[61] Porous Al_2O_3 substrates prepared under certain conditions are optically transparent (Fig. 16b), which may expand their potential applications.

In addition to the most straightforward technique (Al selective etching), the freestanding porous Al_2O_3 substrates may be obtained by the electrochemical detachment of porous Al_2O_3 without Al etching.[62,63] This approach includes an additional electrochemical step, in which one or several short voltage pulses, slightly exceeding the anodization voltage, are applied. The electrolyte (a mixture of perchloric acid, $HClO_4$ with acetic anhydride, $(CH_3CO)_2O$, and hydrochloric acid, HCl) is chosen in such a way that the electric field-assisted Al_2O_3 dissolution rate exceeds its formation rate. A number of other electrolytes have been studied and their efficiencies for the Al_2O_3 detachment have been investigated (including the voltage excess and pulse duration).[64,65] Electrochemical detachment of freestanding Al_2O_3 is accompanied by the pore opening from the barrier layer side.[62–65] Thus, the detachment introduces the throughout porosity and transforms the impermeable alumina into a ceramic membrane with a controllable pore diameter.

In addition to the throughout porosity and to be utilized in a number of applications, micromachined anodic alumina ceramic is required to have the following properties: high thermal stability (at least up to 1,000°C), a high surface area, and flatness. However, as-prepared anodic alumina is amorphous, has the surface area of a few m^2/g, and cannot be used at temperatures higher than 600°C. Furthermore, if heated above 700°C, severe buckling and cracking occurs for the oxide prepared in any electrolyte. The thermal instability, which is due to phase transitions, limits the applicability of as-prepared anodic alumina. These crystalline phase transitions in amorphous anodic alumina prepared in phosphoric acid,[66] oxalic acid,[59] or sulfuric acid[67,68] and annealed at temperatures up to 1,200°C were characterized by XRD, TGA, BET, IR, and other techniques. Between 800 and 900°C, all these oxides undergo rapid and significant changes in the composition and concentration of impurities, specific surface area, mechanical properties, coordination number of Al^{3+}, and chemical stability. The temperature, at which

this transition takes place, depends on the nature of the electrolyte and anodization conditions. Significant transformation of the oxygen sublattice occurs during the amorphous oxide to polycrystalline oxide phase transition. This phase transition is accompanied by a dramatic increase in the alumina surface area, from a few m^2/g to almost $100\,m^2/g$, due to the appearance of new nanopores in the initially dense portion of anodic alumina.[59] Less significant changes take place at temperatures around 1,150°C, during the formation of alpha-alumina when the cubic lattice transforms into the hexagonal close-packed lattice.

To overcome the thermal instability of as-prepared anodic alumina during the crystallization process (buckling and cracking), a method was proposed to anneal the amorphous anodic alumina at temperatures up to 1,200°C without the aforementioned destruction.[62] The freestanding amorphous alumina is placed between two ceramic plates held together with sufficient pressure, and gradually heated up to and beyond the temperature of the amorphous to crystalline phase transition. The heating rate at temperatures, which results in oxide crystallization, should be around 2°C/min. This method enables the fabrication of high temperature stable, flat anodic alumina substrates with the surface area as high as $100\,m^2/g$. Because of its robustness at very high temperatures, excellent microheaters can be made from such micromachined ceramics. By using a Pt thin film as the resistive element, a microheater was fabricated with the following specifications: temperatures up to 1,200°C, power consumption as low as $50\,\mu W/°C$, fast response, and stability after 100,000 cycles from room temperature to 500°C in air.[8,69,70] Microheaters with these specifications are attractive for a variety of applications, especially for gas microsensors and sensors arrays. A combination of the microheater and a sensing element, formed by the deposition of different materials inside the porous ceramics, creates a platform for resistive, capacitive, and catalytic microsensors.[69,71–73]

Figure 16c and d shows a low temperature humidity microsensor with a three-electrode design. This sensor operates over a wide range of humidity if anodic alumina porosity and pore size are properly tuned. By using the integrated microheater, the operating temperature of such sensors is lowered to −60°C.[69,74] Periodic temperature pulsations of the sensing element to the level of complete H_2O desorption and even some OH-groups desorption

(~600°C) completely refresh and reactivate the alumina surface. As a result, the sensor has the maximum sensitivity to a low humidity level every time humidity is measured. With the integrated microheater, the sensitivity limit was shown to be less than 1 ppm.[69,74]

The micromachined ceramics platform was also used for the fabrication of oxygen and combustible catalytic sensors.[69] Similar to the design of the humidity sensor, the three-electrode configuration, microheater, and sensing electrode were used in both cases. Titanium oxide was employed as a sensing material for oxygen. These microsensors demonstrated excellent sensitivity to oxygen at temperatures as low as 650°C. The response time was in the low tens of millisecond range. The main performance advantages were the low power consumption of the microheater, high sensitivity, and negligible cross-sensitivity to CO and NO_x. The catalytic combustible gas microsensor was fabricated by depositing a Pd-based catalyst (wet impregnation and sintering) on the sensing surface. This area was maintained at operational temperatures of 450–550°C. In the presence of a gas combustible on the catalyst surface, additional heat was generated. The heat increased the temperature of the sensing element, which increased the microheater resistance, thus providing a measurable signal.

The presented examples show that the electrochemically micromachined anodic alumina is advantageous for the fabrication of sensors and sensor arrays because of its thermal stability, controllable porosity, and a variety of options for the deposition of sensing materials. The fabricated and tested sensors have demonstrated high sensitivity and selectivity, long-term stability, low power consumption, as well as the reactivation function in the pulse mode.

4. Multilevel Alumina Ceramics and Its Applications

This section will describe applications of freestanding anodic alumina ceramics, developed by Grigorishin and co-workers for vacuum microelectronics.[70,75–82] Electrostatic[75,81] and thermoactivated switching devices,[82] LC high-frequency oscillators,[76,77,79] AC amplifiers,[75,80] triggers, and other logic vacuum integrated circuits (VICs)[75,77] were fabricated and characterized. Passive and active elements, interconnects, and packaging solutions were developed to fabricate these devices. Passive elements and interconnects were prepared by conventional physical vapor deposition and reactive sputtering of materials on the thermally stabilized alumina

ceramics. The dimensions of these elements were specified to obtain the required performance specifications.

Active elements, such as microtriodes, which consist of thermal cathode, anode, and control grid, were fabricated by using two separate alumina films or components. The cathode component was prepared by localized anodization with selective etching of non-anodized Al. Figure 17a shows an optical image of a portion of the substrate for this part. Due to extensive localized heating, a special design was required to compensate for related stresses (Fig. 17a-2). The most challenging problem was to develop the anode–grid component with a fine grid, which was separated from the anode base with high tolerance. Figure 17b and c demonstrates optical and SEM

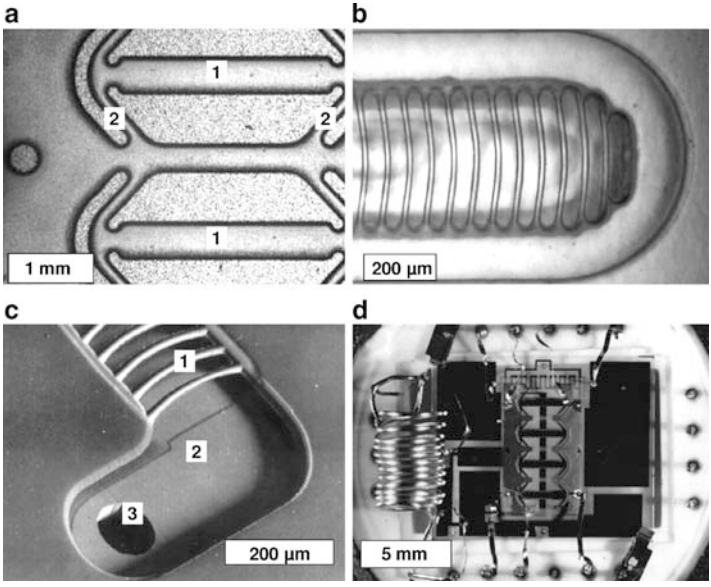

Figure 17. (**a**, **b**) Optical and (**c**) SEM images of 3D anodic alumina ceramics with multilevel microrelief, substrates for cathode components (**a**: 1 – heating zone and 2 – thermomechanical stress compensator) and anode–grid components (**b** and **c**: 1 – fine grid, 2 – recess in the substrate for film anode, and 3 – interconnect via). (**d**) Example of a device, thermionic ultra-high-frequency oscillator, based on anode–grid and cathode components assembled in metalloceramic package. Images reprinted from Ref. [75] with permission from Elsevier Ltd. Image (**d**) reproduced from Ref. [76] with permission from IEEE (© 1999 IEEE).

images of part of a substrate for the one anode–grid design. Shown is a single piece of alumina ceramic, which has a very complex 3D multilevel topography: a fine grid from alumina (1), a recess in the substrate, in which the thin film anode would be deposited (2), and via for electrical connections and assembling (3). Fabricated VICs performed impressively in harsh thermal and radioactive environments. They operated at temperatures of above 600°C, radiation level of 10^{17} N/cm^2, γ-radiation dose of 10^6 R, pressures from 10^{-6} mmHg (or Torr) to 100 atm., including the simultaneous effect of all these impacts.[75–77] Figure 17d shows a developed and tested thermionic VIC: an ultra-high-frequency oscillator in a metalloceramic package.

The devices based on anodic alumina ceramics and their specifications have been discussed at a number of specialized conferences, related to vacuum microelectronics.[70,75–82] Based on the published information, one can conclude that at least the following technological challenges were addressed during the fabrication of these devices: planarization of the initial Al foil, optimization of the mask material, multistep photolithography and carefully controlled anodization steps, precise Al etching to a specific depth between anodizations, and high temperature annealing of alumina ceramics with a multilevel topography. To illustrate the potential of this technology, a few examples of devices based on alumina ceramics with the 3D multilevel topography have been presented here. The details or specifications of the fabricated devices can be found in the aforementioned publications.

Microstructured surfaces, as well as micromachined substrates and devices discussed in Sects. II, III, and IV, are suitable for a number of applications. They include reflective and absorbing surfaces, wavelength-sensitive filters, multiaperture lens arrays and Fresnel microoptics, field emitter arrays, precision apertures, or molds for microstructured surfaces of other materials. Microstructured alumina ceramics can also be used for tuned broadband infrared emitters. In addition, due to the robustness at high temperatures and well-developed and controlled porosity, the freestanding, heat-treated micromachined anodic alumina substrates can be used for the fabrication of sensors that incorporate a high temperature microheater with low power consumption.

V. CONCLUSIONS

This chapter has reviewed the top-down approach for the microstructuring of Al: localized porous-type anodization and EMM based on selective wet etching of either porous Al_2O_3 or Al. The technological limitation of localized porous-type anodization is imposed by the lateral pore propagation, which results in undercutting and, consequently, trapezoidal metallic features. However, in contrast to mostly isotropic wet chemical etching, localized porous-type anodization has some directionality. Thus, this technique can be used as an alternative to plasma-based etching of Al for applications, in which economical benefits overcome technological limitations.

EMM can be applied to either Al films, typically deposited on SiO_2/Si substrates, or Al foils. The dimensions of metallic features are determined by the same rules: the etch factor, the depth of porous-type anodization, the mask design, and process conditions. In addition to the fabrication of metallic microstructures, EMM can be used to produce microstructured ceramic substrates composed of porous Al_2O_3. For the fabrication of both types of 3D microstructures by localized porous-type anodization, the following technological problems have to be addressed: the reliability of a mask material, the fidelity of the mask transfer, volumetric expansion of porous Al_2O_3 during anodization, and the effect of the mask design on the rate of porous-type anodization and on the completion of anodization of the entire thickness of Al without traces of Al islands.

This chapter has also reviewed selected applications and devices incorporating metallic and/or ceramic microstructures. Localized porous-type anodization and selective etching were applied for metallization, fabrication of integrated passive components, and surface microstructuring. Microstructured ceramics based on anodic alumina was shown to be advantageous due to its high thermal stability and compatibility with 3D multilevel microstructuring. Micromachined metallic and/or ceramic substrates may be suitable for additional applications, which result from the abundance of Al, cost-effective methods for its microstructuring, and a possibility for the deposition of a variety of materials in porous Al_2O_3. Moreover, the unique features of porous Al_2O_3 (the controlled pore diameter and regularly hexagonal and straight-through arrangement of pores) allow one to fabricate structures with dimensions below the limit of traditional photolithography. Thus, a combination of the bottom-up

and top-down approaches may result in new micro- and nanostructures with functionalities not expected from the application of only one of these approaches.

ACKNOWLEDGMENTS

Dmitri A. Brevnov is thankful to Prof. Harry O. Finklea (West Virginia University, Morgantown, WV, USA) and Prof. Plamen Atanassov (University of New Mexico (UNM), Albuquerque, NM, USA) for their mentoring. The financial support for Dr. Brevnov's research at UNM was provided in part by Intel Corp. (Santa Clara, CA, USA), funded through Center for Micro-Engineered Materials (UNM). Peter Mardilovich thanks Dr. Alexander Govyadinov (Hewlett-Packard Company, Corvallis, OR, USA) for helpful discussions on the history of development of multilevel alumina ceramics in the National Academy of Sciences of Belarus in 1970s–1980s.

REFERENCES

[1]F. Keller, M. S. Hunter, and D. L. Robinson, *J. Electrochem. Soc*. **100** (1953) 411.
[2]J. W. Diggle, T. G. Downie, and C. W. Goulding, *Chem. Rev.* **69** (1969) 365.
[3]A. Despic and V. Parkhutik, in *Modern Aspects of Electrochemistry*, Vol. 20, Ed. by J. O'M. Bockris, R. E. White, and B. E. Conway, Plenum Press, New York (1989) 401.
[4]H. Takahashi, M. Sakairi, and T. Kikuchi, in *Modern Aspects of Electrochemistry*, Vol. 46, Ed. by S.-I. Pyun and J.-W. Lee, Springer, New York (2009) 59.
[5]S. Krongelb, L. T. Romankiw, E. D. Perfecto, and K. H. Wong, in *Microelectronic Packaging*, Ed. by M. Datta, T. Osaka, and J. M. Schultze, CRC Press, Boca Raton (2005) 337.
[6]P. P. Mardilovich, A. N. Govyadinov, V. V. Kozharinov, and R. Paterson, in *Advances in Science and Technology. Ceramics: Charting the Future*, Ed. by P. Vincenzini, Techna, Florence, Italy (1995) 2763.
[7]P. Mardilovich, D. Routkevitch, and A. Govyadinov, in *Microfabricated Systems and MEMS V, Proceedings by Electrochemical Society, 2000–19*, Ed. P. J. Hesketh et al. (2000) 33.
[8]D. Routkevitch, A. Govyadinov, and P. Mardilovich, in *Proceedings of the ASME International Mechanical Engineering Congress and Exposition, Nov. 5–10, 2000, Orlando, Florida*, Vol. 2, ASME, New York (2000) 39.
[9]S. Tan, M. Reed, H. Han, and R. Boudreau, in *Proceedings of IEEE MEMS'95* (1995) 267.
[10]A.-P. Li, F. Müller, A. Birner, K. Nelsh, and U. Gösele, *Adv. Mater.* **11** (1999) 483.
[11]M. J. Madou, *Fundamentals of Micromachining: The Science of Miniaturization*, 2nd edition, CRC Press, Boca Raton (2002) 519.
[12]R. Alkire and H. Deligianni, *J. Electrochem. Soc*. **135** (1988) 1093.

[13]M. Datta and L. T. Romankiw, *J. Electrochem. Soc*. **136** (1989) 285C.
[14]A. C. West, C. Madore, M. Matlosz, and D. Landolt, *J. Electrochem. Soc*. **139** (1992) 499.
[15]M. Datta, R. V. Shenoy, and L. T. Romankiw, *J. Eng. Ind*. **118** (1996) 29.
[16]R. V. Shenoy, M. Datta, and L. T. Romankiw, *J. Electrochem. Soc*. **143** (1996) 2305.
[17]M. Datta, *IBM J. Res. Dev*. **42** (1998) 655.
[18]C. Madore, O. Piotrowski, and D. Landolt, *J. Electrochem. Soc*. **146** (1999) 2526.
[19]Y. Ferri, O. Piotrowski, P.-F. Chauvy, C. Madore, and D. Landolt, *J. Micromech. Microeng*. **11** (2001) 522.
[20]O. Zinger, P.-F. Chauvy, and D. Landolt, *J. Electrochem. Soc*. **150** (2003) B495.
[21]D. Landolt, P.-F. Chauvy, and O. Zinger, *Electrochim. Acta* **48** (2003) 3185.
[22]P.-F. Chauvy and D. Landolt, *J. Appl. Electrochem*. **33** (2003) 135.
[23]J. J. Kelly and C. H. de Minjer, *J. Electrochem. Soc*. **122** (1975) 931.
[24]P. E. Riley, *J. Electrochem. Soc*. **140** (1993) 1518.
[25]W. E. Frank, *Microelectron. Eng*. **33** (1997) 85.
[26]G. C. Schwartz and V. J. Platter, *J. Electrochem. Soc*. **122** (1975) 1508.
[27]S. Lazarouk, I. Baranov, G. Maiello, E. Proverbio, G. Decesare, and A. Ferrari, *Electrochem. Soc*. **141** (1994) 2556.
[28]S. Lazarouk, S. Katsouba, A. Demainaovich, V. Stanovski, S. Viotech, V. Vysotski, and V. Ponomar, *Solid-State Electron*. **44** (2000) 815.
[29]S. Lazarouk, S. Katsouba, A. Leshok, A. Demainaovich, V. Stanovski, S. Viotech, V. Vysotski, and V. Ponomar, *Microelectron. Eng*. **50** (2000) 321.
[30]P. Mardilovich, A. Govyadinov, and D. Routkevitch, in *Proceedings of the ASME International Mechanical Engineering Congress and Exposition, Nov. 5–10, 2000, Orlando, Florida*, Vol. 2, ASME, New York (2000) 45.
[31]D. A. Brevnov, T. C. Gamble, P. Atanassov, G. P. López, T. M. Bauer, Z. A. Chaudhury, C. D. Schwappach, and L. E. Mosley, *Electrochem. Solid-State Lett*. **9** (2006) B35.
[32]J. T. Cosse, G. P. López, P. Atanassov, T. M. Bauer, Z. A. Chaudhury, C. D. Schwappach, L. E. Mosley, and D. A. Brevnov, *J. Micromech. Microeng*. **17** (2007) 89.
[33]J. P. O'Sullivan and G. C. Wood, *Proc. R. Soc. Lond. A*. **317** (1970) 511.
[34]V. P. Parkhutik and V. I. Shershulsky, *J. Phys. D: Appl. Phys*. **25** (1992) 1258.
[35]F. Li, L. Zhang and R. M. Metzger, *Chem. Mater*. **10** (1998) 2470.
[36]J. E. Houser and K. R. Hebert, *J. Electrochem. Soc*. **153** (2006) B566.
[37]H.-H. Strehblow, C. M. Melliar-Smith, and W. M. Augustyniak, *J. Electrochem. Soc*. **125** (1978) 915.
[38]R. L. Chiu, P. H. Chang, and C. H. Tung, *J. Electrochem. Soc*. **142** (1995) 525.
[39]H. Habazaki, K. Shimizu, P. Skeldon, G. E. Thompson, G. C. Wood, and X. Zhou, *Trans. Ins. Met. Finish*. **75** (1997) 18.
[40]T. Kikuchi, M. Sakairi, H. Takahashi, Y. Abe, and N. Katayama, *J. Electrochem. Soc*. **148** (2001) C740.
[41]T. A. Renshaw, *J. Electrochem. Soc*. **108** (1961) 185.
[42]J. O. Dukovic, in *Advances in Electrochemical Science and Engineering*, Vol. 3, Ed. by H. Gerischer and C. W. Tobias, VCH Publishers Inc., New York, NY (1994) 117.
[43]A. C. West, M. Matlosz, and D. Landolt, *J. Electrochem. Soc*. **138** (1991) 728.
[44]S. Mehdizadeh, J. O. Dukovic, P. C. Andricacos, L. T. Romankiw, and H. Y. Cheh, *J. Electrochem. Soc*. **139** (1992) 78.
[45]C. Madore and D. Landolt, *J. Micromech. Microeng*. **7** (1997) 270.
[46]G. C. Schwartz and V. J. Platter, *J. Electrochem. Soc*. **123** (1976) 34.

[47]D. A. Brevnov, T. C. Gamble, P. Atanassov, and L. E. Mosley, *J. Electrochem. Soc*. **153** (2006) C801.
[48]R. Akolkar, U. Landau, H. Kuo, and Y.-M. Wang *J. Appl. Electrochem*. **34** (2004) 807.
[49]A. J. Learn, *J. Electrochem. Soc*. **123** (1976) 894.
[50]D. R. Collins, S. R. Shortes, W. R. McMahon, R. C. Bracken, and T. C. Penn, *J. Electrochem. Soc*. **120** (1973) 521.
[51]V. Labunov, V. Sokol, V. Parkun, and A. Vorob'yova, *Process for Making Multilevel Interconnectors of Electronic Components*, U.S. Patent 5,580,825 (1996).
[52]V. Surganov, A. Mozalev, and V. Boksha, *Microelectron. Eng*. **37–38** (1997) 335.
[53]A. I. Vorob'eva, V. A. Sokol, and V. M. Parkun, *Russ. Microelectron*. **3** (2003) 136 translated from *Mikroelectronika* **32** (2003) 177.
[54]R. M. Swanson, S. K. Beckwith, R. A. Crane, W. D. Eaides, Y. H. Kwark, R. A. Sinton, and S. E. Swirhun, *IEEE Trans. Electron Devices* **31** (1984) 661.
[55]P. Verlinden, R. M. Swanson, R. A. Sinton, and D. E. Kane, in *IEEE Photovoltaic Specialists Conference*, Vol. 1, IEEE, Las Vegas, NV (1988) 532.
[56]V. Surganov, *IEEE Trans. Compon. Packag. Manuf. Technol. – Part B Adv. Packag*. **17** (1994) 197.
[57]S. D. Wijeyesekera, J. Jing, D. C. Benson, and T. Sasagawa, *Thin Film Capacitors*, U.S. Patent 6,404,615 B1 (2002).
[58]X. Zhao, P. Jiang, S. Xie, L. Liu, W. Zhou, Y. Gao, L. Song, J. Wang, D. Liu, X. Dou, S. Luo, Z. Zhang, Y. Xiang, and G. Wanga, *J. Electrochem. Soc*. **152** (2005) B411.
[59]P. P. Mardilovich, A. N. Govyadinov, N. I. Mukhurov, A. M. Rzhevskii, and R. Paterson, *J. Memb. Sci*. **98** (1995) 131.
[60]K. Itaya, S. Sugavara, K. Arai, and S. Saito, *J. Chem. Eng. Jpn*. **17** (1984) 514.
[61]M. Mehmood, A. Rauf, M. A. Rasheed, S. Saeed, J. I. Akhter, J. Ahmad, and M. Aslam, *Mater. Chem. Phys*. **104** (2007) 306.
[62]R. Paterson et al. *Permeable Anodic Alumina Film*. PCT, GB 95/01646, WO 96/01684 (1996).
[63]H. L. Lira and R. Paterson, *J. Memb. Sci*. **206** (2002) 375.
[64]J. H. Yuan, W. Chen, R. J. Hui, Y. L. Hu, and X. H. Xia, *Electrochim. Acta* **51** (2006) 4589.
[65]W. Chen, J. S. Wu, J. H. Yuan, X. H. Xia, and X. H. Lin, *J. Electroanal. Chem*. **600** (2007) 257.
[66]I. W. M. Brown, M. E. Bowden, T. Kemmitt, and K. J. D. MacKenzie, *Curr. Appl. Phys*. **6** (2006) 557.
[67]A. Kiechner, K. J. D. MacKenzie, I. W. M. Brown, T. Kemmitt, and M. E. Bowden, *J. Memb. Sci*. **287** (2007) 264.
[68]R. Ozao, M. Ochiai, H. Yoshida, Y. Ichimura, and T. Inada, *J. Therm. Anal. Calorim*. **64** (2001) 923.
[69]A. Govyadinov, P. Mardilovich, and D. Routkevitch, in *Proceedings of the ASME International Mechanical Engineering Congress and Exposition, Nov. 5–10, 2000, Orlando, Florida*, Vol. 2, ASME, New York (2000) 313.
[70]A. N. Govyadinov, I. L. Grigorishin, and P. P. Mardilovich, in *Proceedings of the 7th Conference of ITG Committee 5.7 "Vacuum Electronics and Displays", 2–3 May 1995*, Garmisch-Partenkirchen, Germany, ITG-Fachbericht, VDE, Verlag, **132** (1995) 161.
[71]D. Routkevitch, A. Govyadinov, P. Mardilovich, S. Hooker, and K. Novogradecz, in *Proceedings of the 198th Meeting of the Electrochemical Society, 22–27 October 2000*, Phoenix, AZ, Abstract 1115 (2000).

[72]D. Routkevitch et al., *Nanostructured Ceramic Platform for Micromachined Devices and Device Arrays*, U.S. Patent 6,705,152 (2004).
[73]T. Yadav et al., *Semiconductor and Device Nanotechnology and Methods for their Manufacture*, U.S. Patent 6,946,197 (2004).
[74]P. Mardilovich, A. Govyadinov, and D. Routkevitch, in *Proceedings of the 198th Meeting of the Electrochemical Society, 22–27 October 2000*, Phoenix, AZ, Abstract 1116 (2000).
[75]I. L. Grigorishin, I. F. Kotova, and N. I. Mukhurov, *Appl. Surf. Sci*. **111** (1997) 101.
[76]N. I. Mukhurov, in *Proceedings of Electronics and Radiophysics of Ultra-High Frequencies, 24–28 May 1999*, IEEE, St. Petersburg, Russia (1999) 323.
[77]I. L. Grigorishin, N. I. Mukhurov, O. M. Surmach, and I. F. Kotova, in *Proceedings of the 7th International Vacuum Microelectronics Conference (IVMC'94), 4–7 July 1994, Revue "Le Vide, les Couches Minces"*, Grenoble, France, Suppl. No. 271 (1994) 304.
[78]I. L. Grigorishin, G. I. Efremov, N. I. Mukhurov, and P. E. Protas, in *Proceedings of the 7th International Vacuum Microelectronics Conference (IVMC'94), 4–7 July 1994, Revue "Le Vide, les Couches Minces"*, Grenoble, France, Suppl. No. 271 (1994) 308.
[79]I. L. Grigorishin, N. I. Mukhurov, and I. F. Kotova, in *Proceedings of the 7th Conference of ITG Committee 5.7 "Vacuum Electronics and Displays", 2–3 May 1995*, Garmisch-Partenkirchen, Germany, ITG-Fachbericht, VDE, Verlag **132** (1995) 167.
[80]I. L. Grigorishin, N. I. Mukhurov, and I. F. Kotova, in *Technical Digest of the 9th International Vacuum Microelectronics Conference, 7–12 July 1996*, St. Petersburg, Russia (1996) 589.
[81]I. L. Grigorishin, N. I. Mukhurov, and G. I. Efremov, in *Technical Digest of the 9th International Vacuum Microelectronics Conference, 7–12 July 1996*, St. Petersburg, Russia (1995) 593.
[82]G. I. Efremov and N. I. Mukhurov, in *Electronics, Circuits and Systems, Proceedings of ICECS'99, The 6th IEEE International Conference* **2** (1999) 1047.

6

Electroless Deposition: Theory and Applications

Stojan S. Djokić[1] and Pietro L. Cavallotti[2]

[1] *Elchem Consulting Ltd., Edmonton, AB, Canada T5X 6B3*
[2] *CMIC, Dept. Politecnico, Via Mancinelli, 7, 20131 Milano, Italy*

I. INTRODUCTION

Electroless deposition is a process that has been used in practice for centuries. Although not recognized as such, electroless deposition of noble metals, e.g., silver or gold was known to the ancient civilizations. In spite of very slow developments throughout the centuries, significant scientific results have been achieved in the second part of the twentieth century.[1–3] The research achievements in the area of electroless deposition have contributed to tremendous applications and developments in various industries.

In general terms, for the electroless deposition no external current is required. Coatings produced by electroless deposition are uniform and continuous, which makes this process very attractive for different applications. Applications of electroless deposition are related to electronics, energy conversion, aerospace, and biomedical and automotive industries. In addition, new applications in the area of metallization of polymers, ceramics, and fabrics, production of

S.S. Djokić (ed.), *Electrodeposition: Theory and Practice*,
Modern Aspects of Electrochemistry 48, DOI 10.1007/978-1-4419-5589-0_6,

various powders, corrosion and wear-resistant coatings, decorative and catalytic surfaces, etc. are being developed.

The aim of this chapter is to discuss the recent research, developments, and applications of electroless deposition.

II. GENERAL CONSIDERATIONS OF ELECTROLESS DEPOSITION

Studies and practices of plating of different types of coatings from aqueous solutions without an external current source were described in the literature as *electroless* deposition. The research was predominantly related to the deposition of metals and/or alloys. However, it seems that the deposition of compounds without an external current source was in a way neglected. It is to be noted that electroless deposition of oxides, salts, polymers, etc. is also possible.

Metal electrodeposition, where the reduction of metal ions takes place, is always a cathodic reaction. In most of the cases electrodeposition of oxides is the anodic process resulting from the oxidation of metals.

In the analogy, for the electroless deposition of metals, the presence of reducing agents is needed, while for the electroless deposition of compounds, oxidizing agents are usually required.

In terms of kinetics and mechanisms, electroless deposition processes have many similarities. In an attempt to analyze the electroless deposition, several mechanisms such as atomic hydrogen, hydride ion, metal hydroxide, electrochemical, and universal have been proposed.[1–3] It is important to note that these mechanisms were developed for cases of nickel and copper electroless deposition, which were the most widely studied metals in this respect. Based on the proposed mechanisms, most of the features of electroless deposition can be explained. However, there are some characteristics of electroless deposition, which cannot be explained using these mechanisms. The major problems arise when attempting to generalize the proposed models explaining the mechanistic aspects.

Electroless deposition can be defined as a deposition of solid phase of continuous coatings (films) or powders of metals, alloys, or compounds from aqueous or nonaqueous solutions or melts without an external current source. Based on this definition, electroless deposition is a purely chemical process, which involves oxido-reduction

reactions. From a thermodynamic point of view, the electroless deposition can be considered as spontaneous, since

$$\Delta G^\circ < 0 \tag{1}$$

where ΔG° is the standard Gibbs energy given as:

$$\Delta G^\circ = -zFE^\circ \tag{2}$$

or

$$\Delta G^\circ = -RT \ln K \tag{3}$$

where K is the equilibrium constant for a generic reaction:

$$\mathrm{A} + \mathrm{B} \rightarrow \mathrm{AB} \tag{4}$$

$$K = \frac{[\mathrm{AB}]}{[\mathrm{A}][\mathrm{B}]} \tag{5}$$

where R is the universal gas constant, T is the temperature, z is the number of exchanged electrons, F is the Faraday's constant, E° is the standard electrode potential, A and B are reactants, and AB is the product.

Equation (2) suggests that an electroless process takes place only if $E^\circ > 0$. On the other hand, this further means that from any electroless process energy can be produced.

There are two main types of electroless deposition of metals:

1. Displacement deposition
2. Autocatalytic deposition

Further discussion explains both displacement and autocatalytic types of electroless deposition.

1. Displacement Deposition

The displacement deposition is also known as galvanic or immersion plating. In this process, when a less noble metal (M_1) is immersed into a solution containing metallic ions (M_2^{z2+}) of a more noble metal (M_2), reduction of these ions takes place according to the following reaction:

$$M_2^{z2+} + z_2 e^- \rightarrow M_2^\circ \tag{6}$$

and consequently, deposition of metal M_2 in the form of a powder or a continuous film at the surface of less noble metal, M_1 occurs.

The other half reaction is related to the dissolution of less noble metal, M_1°, i.e.,

$$M_1^\circ \rightarrow M_1^{z_1^+} + z_1 e^- \tag{7}$$

In this way, by combining (6) and (7), the displacement or galvanic deposition can be described as:

$$M_2^{z_1^+} + \frac{z_2}{z_1} M_1^\circ \rightarrow M_2^\circ + \frac{z_2}{z_1} M_1^{z_1^+} \tag{8}$$

Note that the less noble metal M_1 acts as a reducing agent of metallic ions of a more noble metal, M_2, which consequently plays the role of an oxidizing agent.

It is obvious that the galvanic displacement deposition occurs only at the surface of less noble metal (powders or various shape substrates).

Theoretically, there are many examples of this type of reaction, taking into the consideration the fact that, as soon as the less noble metal is immersed into a solution containing ions of more noble metal, the deposition of this "more noble" metal will start. However, practical importance of this type of deposition is related to the following systems: Ag/Zn, Au/Ni, Au/Ag, Cu/Zn, Cu/Fe, Cu/Al, Pd/Ni, Pt/Fe, Pt/Co, and similar.

According to the basic thermodynamic principles, as soon as the surface of the less noble metal is covered with the more noble metal, the deposition stops. This is schematically represented in Fig. 1, for a flat (a) and powder (b) substrates.

From a theoretical point of view, if a monolayer of the noble metal is deposited onto the surface of less noble metal, then thicker deposits under the conditions of galvanic displacement cannot be deposited. However, as experimentally observed, this is not true. Deposits thicker than one monolayer have frequently been observed using the galvanic displacement deposition.

This behavior can be attributed to the porosity of noble metal deposited onto less noble metal and as well as to differences between the rates of crystal growth (more noble metal) and dissolution (less noble metal). Due to the porosity of the deposited metal, the ions of the more noble metal will penetrate and get in contact with the

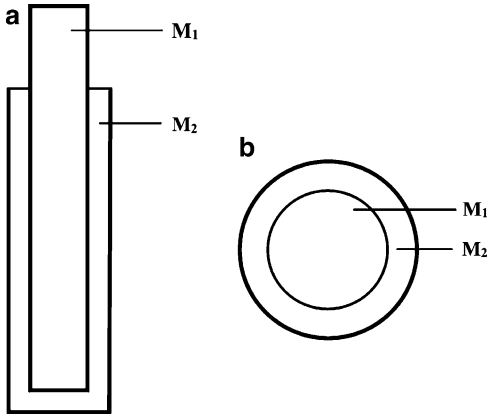

Figure 1. Galvanic displacement deposition of a more noble metal (M_2) on a less noble metal (M_1) on a flat (**a**) and powder (**b**) substrates.

less noble metal. Under these conditions, the further deposition takes place and in this way the growth of film occurs.

This is illustrated by the SEM micrographs of Cu deposited onto flat (Fig. 2) or powdery (Fig. 3) aluminum substrates immersed into alkaline solutions containing Cu(II) ions.[4]

As can be seen from the micrographs presented in Fig. 2, on the flat Al samples a growth of Cu films occurs, or simply speaking, a deposit significantly thicker than one monolayer with a rough surface morphology was obtained.

Similarly, when powdery aluminum substrates are used, due to the porosity of deposited Cu and dissolution of Al, hollow copper particles can be obtained, as illustrated in Fig. 3. These results strongly suggest that there is a difference between the rates of dissolution (oxidation of less noble metal) and deposition (reduction of more noble metal).

Although the galvanic displacement can quite successfully be used for the production of catalytic surfaces, electrolyte and water purification as well as for heavy or noble metal removal in hydrometallurgical plants, it seems that the use of this type of deposition is limited in the sophisticated electronics or biomedical applications due to poor adherence and porosity of the deposited film. It is obvious that further studies are required if this process is aimed for the use in electronics, biomedical, or hi-tech industries.

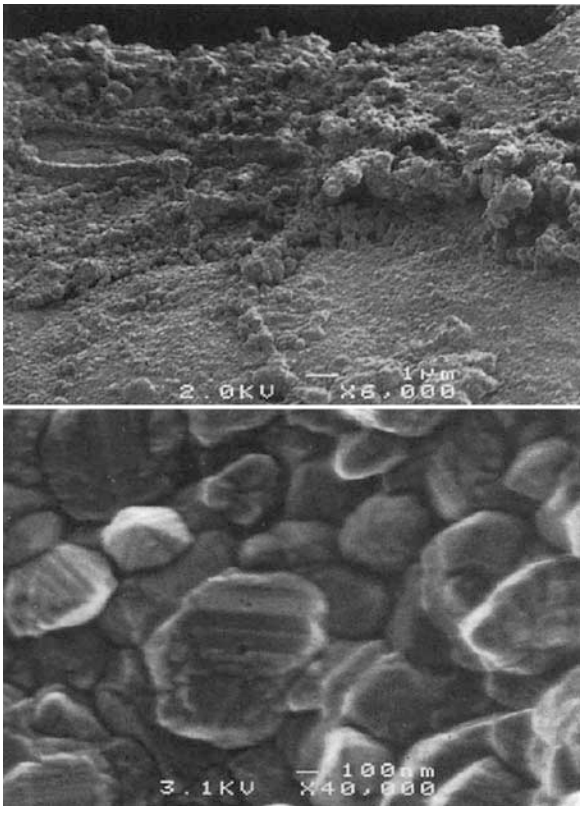

Figure 2. SEM micrographs of the copper deposits cemented on flat aluminum substrate in alkaline conditions.[4] Reprinted with permission from ECS – The Electrochemical Society.

For the electronics and biomedical applications, the galvanic displacement deposition can be successful when very thin films are required and when an appropriate surface pretreatment is carried out to achieve a good adhesion of the deposited metallic film.

2. Autocatalytic Deposition

The galvanic displacement deposition proceeds exclusively at the surface of a less noble metal, which acts as the reducing agent.

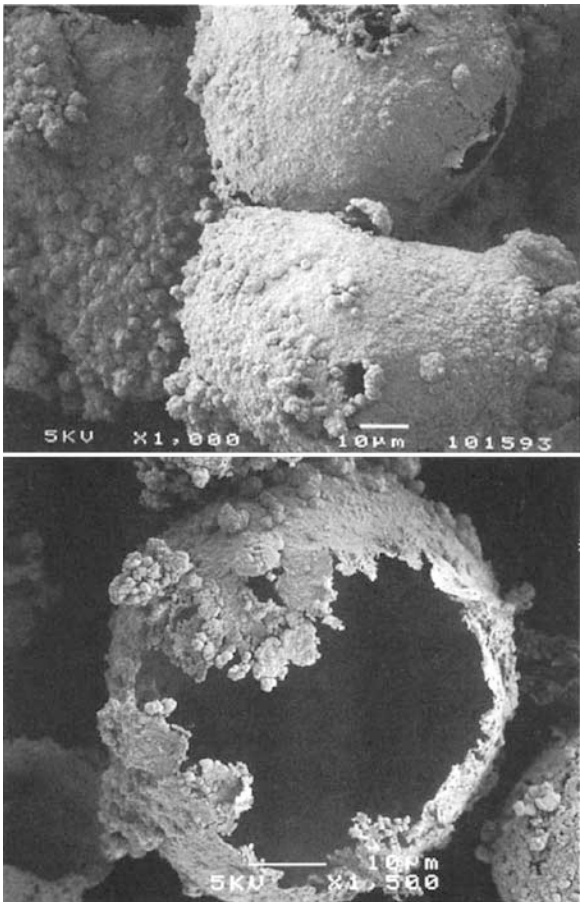

Figure 3. SEM micrographs of the hollow Cu particles produced by the galvanic deposition of Cu onto Al particles in alkaline solutions.[4] Reprinted with permission from ECS – The Electrochemical Society.

In the *autocatalytic* deposition there are various reducing agents (e.g., formaldehyde, hydrazine, hypophosphite, ascorbic acid, polyhydroxy alcohols, and hydrogen) that have been reported in the literature. The nature of the reducing agent can significantly influence the kinetics of electroless deposition as well as surface morphology and physicochemical properties of deposits. Once when initiated,

this reaction may occur not only at the surface of an object, but in bulk solution as well, producing powders of various shapes and sizes. In this case the reaction is catalyzed by the metal being deposited.

In consideration of the so-called autocatalytic deposition processes, the following facts must be taken into consideration.

1. This type of metallic ion reduction can take place in the bulk solution or only at the catalytically active surfaces.
2. When the deposition is carried out at the solid surfaces, they (surfaces) must properly be activated to initiate the electroless deposition.
3. The concentrations of both oxidizing agent and reducing agent have to be properly chosen to avoid or at least to minimize the reduction into the bulk solution and a consequent precipitation of metallic powders.
4. All the parameters influencing the rate of oxido-reduction reactions (e.g., temperature, pressure, concentrations of additives, and complexing agents) have to be very carefully controlled to achieve the desirable thickness and/or properties of the deposit.
5. The growth of film or increase in thickness of the deposit is influenced by the autocatalytic activity of the surface on which a metal is deposited.

The electroless deposition of a metal M, using a reducing agent R^{n-}, can be described with the following generic reaction:

$$M^{z+} + R^{n-} \rightarrow M + R^{z-n} \tag{9}$$

As shown by this reaction, the metallic ions M^{z+} will be reduced to metal M, while the reducing agent ions R^{n-} will be oxidized to R^{z-n}. In this way, the reduction of metal ions occurs both at the surface of an object at which the deposition can proceed (an appropriate metallic surface or properly activated nonconductive materials, e.g., ceramics, polymers, and textiles) or in bulk solution.

The deposition at the surface usually occurs as a continuous film with a uniform surface morphology. On the other hand with an increase in the concentration of the reducing agent or temperature, the deposition of powders occurs, a phenomenon which is usually described as "bath instability."[1]

In the electroless deposition, the hydrolysis phenomena, as has already been published before,[3,5,6] plays a very significant role in the reduction of metallic ions from aqueous solutions.

Due to hydrolysis of a metallic ion, the following reaction may occur:

$$M^{z+} + xOH^- \rightarrow M(OH)_x^{(z-x)+} \tag{10}$$

The hydrolyzed metallic species ($M(OH)_x^{(z-x)+}$) are further reduced in the presence of an appropriate reducing agent (R^{n-}) to metal according to the reaction:

$$M(OH)_x^{(z-x)+} + R^{n-} \rightarrow M + R(OH)_x^{(z-x-n)+} + H_2O \tag{11}$$

The validity of the reaction (11) can be illustrated in the following real systems, where examples are chosen to describe the electroless deposition of different metals from hydrolyzed species using various reducing agents.

1. Electroless deposition of copper using formaldehyde as a reducing agent:

$$Cu(OH)_2 + HCOH \rightarrow Cu + HCOOH + H_2O \tag{12}$$

2. Electroless deposition of silver using formaldehyde as a reducing agent:

$$2AgOH + HCOH \rightarrow 2Ag + HCOOH + H_2O \tag{13}$$

3. Electroless deposition of Ni–P alloys using hypophosphite as a reducing agent:

$$\begin{aligned} Ni(OH)_2 + 2H_2PO_2^- &\rightarrow Ni + 2H_2PO_2^- \\ + 2H_2O &\rightarrow Ni + 2H_2PO_3^- + H_2 \end{aligned} \tag{14}$$

$$Ni + 2H_2PO_2^- \rightarrow 2P + Ni(OH)_2 + 2OH^- \tag{15}$$

4. Electroless deposition of Co or Ag using hydrazine as a reducing agent, respectively:

$$Co(OH)_2 + N_2H_4 \rightarrow Co + H_2 + N_2 + 2H_2O \tag{16}$$

$$2AgOH + N_2H_4 \rightarrow 2Ag + H_2 + N_2 + 2H_2O \tag{17}$$

5. Electroless deposition of Au or Cu with ascorbic acid, respectively:

$$2AuOH + C_6H_8O_6 \rightarrow 2Au + C_6H_6O_6 + 2H_2O \quad (18)$$

$$Cu(OH)_2 + C_6H_8O_6 \rightarrow 2Cu + C_6H_6O_6 + 2H_2O \quad (19)$$

where $C_6H_8O_6$ is ascorbic acid and $C_6H_6O_6$ is dehydroascorbic acid.

Similar reactions are applicable to other reducing agents (e.g., polyhydroxy alcohols) which can reduce hydrolyzed silver species to the metallic state.[7]

At the metallic surface, due to codeposition of other elements (e.g., P, B, or similar) as seen on the examples of Ni–P or Ni–B alloys, formation of hydrolyzed species may occur. This is illustrated by the equation (15) for the example of codeposition of Ni–P alloys. The hydroxides or other hydrolyzed species which are formed as intermediates can further be reduced to the metallic state in the presence of the reducing agent.

When dealing with aqueous solutions, an important question arises: why hydrolysis phenomena play such an important role in the electroless deposition of metals? It is generally believed that the metallic surfaces upon immersion in an aqueous solution can attract the OH^- ions. If this were true, then at the metallic surface a pH rise should be observed due to the adsorption of OH^- ions by the metal itself.

Consequently, due to an increase in pH, formation of hydrolyzed species may occur. The hydrolyzed species are further reduced to the metallic state in the presence of a reducing agent. This can be seen for any metal which is possible to deposit from aqueous solutions.

On the other hand, the hydrolysis of reducing agent can be represented with the following reaction:

$$R^- + H_2O \rightarrow RH + OH^- \quad (20)$$

with the equilibrium constant

$$K = \frac{[RH] \times [OH^-]}{[R^-]} \quad (21)$$

It is obvious that an increase in the concentration of the reducing agent leads to an increase in the concentration of OH^- ions, as shown by the reaction (20). This increase in the concentration of OH^- ions will lead to the formation of hydroxy complexes in bulk solution and the reduction of these complexes or hydroxides may take place into the bulk solution. This scenario could consequently lead to the precipitation of metallic powders in the bulk solution.[8]

3. Electroless Oxidation of Metals

While the metal or alloy electroless deposition reactions can be considered as cathodic processes, formation of oxides at the metallic surfaces without an external current source can be analyzed as anodic processes. This type of deposition can be illustrated in the example of chemical oxidation of aluminum in chromic acid solutions.[9]

In this oxido-reduction process, aluminum metal is oxidized and the anodic reactions can be represented as:

$$2Al + 3H_2O \rightarrow Al_2O_3 + 6H^+ + 6e^- \tag{22}$$

with $\Delta G^\circ = -870.766\,\text{kJ/mol}$ and $E^\circ = 1.5039\,\text{V}$ or

$$Al \rightarrow Al^{3+} + 3e^- \tag{23}$$

with $\Delta G^\circ = -485\,\text{kJ/mol}$ and $E^\circ = 1.6753\,\text{V}$.

The standard Gibbs energies and the standard electrode potentials for the reactions (22) and (23) were calculated according to the thermodynamic data available in the literature.[10] The cathodic reactions include the reduction of chromium Cr(VI) to Cr(III) and hydrogen evolution, as presented in the following equations:

$$Cr_2O_7^{2-} + 8H^+ + 6e^- \rightarrow Cr_2O_3 + 4H_2O \tag{24}$$

with $\Delta G^\circ = -705.612\,\text{kJ/mol}$ and $E^\circ = 1.6753\,\text{V}$ and

$$2H^+ + 2e^- \rightarrow H_2 \tag{25}$$

with $\Delta G^\circ = 0\,\text{kJ/mol}$ and $E^\circ = 0\,\text{V}$.

Based on the reactions (24) and (25), the overall process of oxidation of aluminum with chromic acid solutions can be written as:

$$4Al + 8H^+ + Cr_2O_7^{2-} \rightarrow Al_2O_3 + 2Al^{3+} + Cr_2O_3 + 3H_2 + H_2O \tag{26}$$

with $\Delta G^\circ = -2{,}546.378\,\text{kJ/mol}$.

In this way, the electroless oxidation of aluminum and production of a thin film composed of a mixture of Al_2O_3 and Cr_2O_3 can successfully be achieved.

III. MECHANISTIC ASPECTS OF ELECTROLESS DEPOSITION

The mechanisms explaining the features of autocatalytic deposition which were proposed so far are thoroughly presented in the published literature.[1–3] In general terms, these mechanisms can be distinguished into two main categories. The first category involves the mechanisms in which intermediate species, e.g., hydroxides, hydroxyl complexes, hydride ions, or hydrogen atom react with the reducing agent. The second category deals with mechanisms in which the autocatalytic deposition is explained using the mixed potential theory, with independent anodic and cathodic processes.

As it is already established in the published literature, both of the above categories have their advantages and disadvantages.[1,3] Furthermore, as it was suggested by Djokić[6] in the example of electroless deposition of cobalt with hydrazine, the contribution from both electrochemical and metal hydroxide mechanisms is quite possible.

The autocatalytic deposition of Ni and Co was intensively studied, although the most realistic mechanism has not yet been proposed. In the explanation of the mechanisms of autocatalytic deposition, the authors use the principles of the electrodeposition, although there are significant differences among the two processes.

When compared with electrodeposition, in the example of iron group of metals or their alloys, the proposed mechanism explaining the autocatalytic deposition must take into consideration the following aspects.

1. In the autocatalytic deposition of Ni, Co, and Fe, different kinetic behavior is observed. For example, Ni is the most easily deposited by autocatalytic deposition with the common reducing agents in the acidic and alkaline conditions. Cobalt is usually deposited in alkaline solutions and with great difficulty in acidic solutions. Fe is deposited with a great difficulty, frequently with the help of small currents, resulting from displacement reactions of more electronegative metals.

2. There is an obvious difference in the kinetic behavior between the electrodeposition and autocatalytic deposition of metals such as Pb, Cd, and Zn. These metals are easily electrodeposited at low overvoltages and high exchange currents. However, they act as inhibitors or stabilizers when added in very small amounts to solutions from which an autocatalytic deposition of iron group of metals or alloys is carried out.
3. In the electrodeposition of alloys from the iron group of metals, anomalous deposition is observed, i.e., the more electronegative metal tends to be deposited preferentially. In the autocatalytic deposition this behavior is not observed.
4. During the electrodeposition of iron group of metals, hydrogen is evolved either at low or at very high currents approaching the limiting current density for metal deposition. In the autocatalytic deposition, hydrogen evolution is predominantly a consequence of the oxidation of the reducing agent.
5. The products of the oxidation of reducing agent (phosphite in the case of hypophosphite or borate in the case of boron-containing agents) do not directly influence the kinetics of deposition.
6. Autocatalytic deposition can easily be utilized to completely coat a nonconductive surface starting from few catalytic nuclei usually consisting of palladium or similar. It can also start on a glass surface by simple adsorption of hydrolyzed nickel ions on the surface.
7. The different morphology of the Ni–P deposits produced during the autocatalytic deposition (homogenous with pores) and electrodeposition (lamellar), when process is carried out at low temperature and containing phosphite or hypophosphite.[11]

Autocatalytic deposition of nickel and other metals was investigated by means of the electrochemical techniques.[1–3] For this purpose, both steady-state and transient methods were applied. The results of these studies give important information about the reactions occurring during the autocatalytic deposition and about the surface where the intermediate species of reaction are stabilized by adsorption.

The surface potential is determined by the anodic reaction, i.e., reducing agent oxidation, where hydrogen is replaced with a depolarized hydroxyl ion. In this scenario, the stabilizer action can

be well understood. In fact, stabilizers such as Pb^{2+} or Cd^{2+} and thio-compounds were identified by Gutzeit[12] as the species which act as poison in hydrogen exchange catalyzed reactions. Their action is related to a defined critical concentration. If the concentration is less than the critical, the stabilizers are not influencing the rate of deposition, while they decrease this rate at concentrations higher than the critical.[13,14] This behavior depends on the critical concentration which does not alter the surface potential and it is correlated to a diffusion-limited reaction.

Some authors[15–21] examined the voltammetric behavior of autocatalytic processes under different conditions. Measurements were performed in a complete deposition solution or in solutions which did not contain the reducing agent or the metal ions of interest (e.g., Cu^{2+}, Ni^{2+}, or similar). The results showed that the values of rates of deposition obtained gravimetrically can be comparable to those obtained by mixed potential theory only in particular cases, e.g., autocatalytic deposition of Cu and NiB.

In many other cases, however, there is a direct influence of the reducing agent on the metal deposition reaction. This is observed for NiP autocatalytic deposition. de Minjer[22] showed that it is possible to deposit nickel cathodically when the electrode is connected through a liquid junction to another nickel electrode, at which the reducing agent oxidation proceeds independently. However, the rate of deposition under these conditions, based on de Minjer's observations, is much lower when the two reactions are separated than when they occur simultaneously at the same surface.

Cavallotti's group has made similar experiments with two separated solutions. The first solution contained 0.27 M NaH_2PO_2 and the second 0.11 M $NiSO_4$, 0.5 M Na_2HPO_3, and 0.5 M lactic acid at pH 4.6. The solutions were placed in two different vessels connected with a liquid junction through a glass frit. In the solution containing $H_2PO_2^-$, a copper sheet previously coated with NiP in the complete standard autocatalytic deposition solution was immersed. In the solution containing nickel salt, a copper sheet was immersed. The two electrodes immersed in different solutions were externally connected with a copper wire. At 85°C a very small H_2 evolution was observed on the NiP electrode in the solution with $H_2PO_2^-$ and no deposition was observed on the copper electrode. When pH of the solution containing $H_2PO_2^-$ was significantly increased by the addition of ammonia, H_2 evolution increased. At the same time, deposition of NiP was observed on the copper sheet with a very small

H_2 evolution. The phosphorous content in the NiP deposit was about 16% by mass, which is a result of the phosphite reduction. At the glass frit, NiP deposition also started, showing that there is no need of a metallic surface to initiate the autocatalytic deposition process. This observation can be attributed to the nickel hydroxide species adsorbed at the glass surface, which is obviously a suitable catalyst for the initiation of the deposition process.

The codeposition of elements, such as phosphorus or boron, by direct interaction of the reducing agent with the catalytic surface was examined by some authors; however, the interpretations are not completely satisfying. An indirect mechanism for hypophosphite reduction was proposed by Zeller and Landau.[23] In this approach formation of phosphine as an intermediate and a direct interaction with radicals such as hydrogen atom H, hydride H^-, or NiOH was suggested.[5,12,24–26] However, the possible direct reduction of phosphite to phosphorous must also be considered. In favor of this hypothesis, there is the electrodeposition of NiP alloys from solutions containing Ni^{2+} and phosphite. The interaction of Ni^{2+} with the phosphite ions produces, at high pH, nickel phosphate precipitate when nickel ions are not adequately complexed.

An adequate mechanism, however, must describe all the steps occurring during the deposition process, as listed below for the example of electroless deposition of nickel or cobalt with appropriate reducing agents, i.e.:

1. Reduction of metal ions (Ni^{2+} or Co^{2+}) and hydrogen evolution reaction
2. Oxidation of the reducing agent (e.g., hypophosphite, DMAB, and hydrazine)
3. Codeposition of P or B as seen in the autocatalytic deposition of Ni or Co with hypophosphite or boron-containing reducing agents

A careful consideration of all the above points suggests that the mechanism based on intermediate hydrolyzed species is clearly more heuristic.[1,5,6,15] This approach explains the importance of the adsorption of colloids at the surface at which the autocatalytic deposition takes place.

Using the mechanisms of intermediate hydrolyzed species is very beneficial in understanding and the explanation of autocatalytic deposition of other metals, e.g., Cu, Ag, Au, or similar, as shown in Sect. II.2.

IV. RECENT DEVELOPMENTS AND APPLICATIONS OF ELECTROLESS DEPOSITION

Since the appearance of the Brenner's paper[27] in 1947, electroless deposition was extensively studied for many industrial applications. The most investigated systems by far include nickel, copper, silver, gold, and related alloys.

It is to be noted that almost all the metals and/or alloys that can be electrodeposited from aqueous solutions can also be electrolessly deposited under proper conditions. Due to simplicity, excellent throwing power, uniform deposits, and ability to coat various complex shapes, electroless deposition was intensively investigated for many industrial applications. In this section, recent developments in the field of electroless deposition are discussed. Considering very different applications of electroless deposition, the discussion is presented as follows:

1. Electronics applications
2. Electromagnetic shielding applications
3. Magnetic materials
4. Energy device applications
5. Biomedical applications
6. Anticorrosion applications
7. Electroless deposition and nanotechnology

1. Electroless Deposition in Electronics Applications

Many electroless deposition processes are very useful for the fabrication of various devices in the electronics industry. Significant importance for the electronics applications have metals such as silver, gold, nickel, copper, cobalt, palladium, and related alloys. All of these mentioned metals can quite simply and successfully be deposited via electroless deposition.

Gold electroless deposition processes are used for producing highly conductive surfaces such as in the fabrication of electrical contacts in the electronic industry. The materials consisting of deposited gold are usually classified as soft gold and hard gold. The soft gold is used for metallizing bonding pads and fabricating microbumps on silicon integrated circuit (IC) chips and ceramic packaging boards.[28]

The hard gold is used in electrical connectors, printed circuits boards, and mechanical arrays and it is produced by electrodeposition. The electrolytic methods (electrodeposition) are not discussed in this chapter.

At present, electroless deposition of gold usually produces the so-called soft gold. An investigation of electroless deposition of gold on Ni–P or Ni–B surfaces from cyanide or noncyanide solutions using hydrazine, hydrazine sulfate, sodium borohydride, and ascorbic acid as reducing agents was done by Djokić.[29] The results of this work showed that the surface morphology, structure, and properties of electrolessly deposited gold strongly depend on the nature of reducing agent. The borohydride solution used in this work was unstable. Using hydrazine or hydrazine sulfate, gold was plated only onto Ni–B, but not onto Ni–P surfaces. These deposits exhibited very good appearance, but a poor adhesion. With ascorbic acid, gold was deposited on both Ni–B and Ni–P surfaces. These deposits had a very good appearance, acceptable adhesion, and solderability.

Later, Osaka et al.[28] investigated the electroless deposition of gold onto Ni–B and Ni–P substrates from cyanide or noncyanide solutions using hydrazine or ascorbic acid as reducing agents of gold ions from the mentioned solutions, respectively. Using the cyanide-based solutions, which were originally proposed by Iacovangelo[30] (see Table 1) and hydrazine as a reducing agent, Osaka[28] reported that the electroless gold on electroless Ni–B substrates was adherent and uniform, while the same deposit on electroless Ni–P was nonadherent and nonuniform. This result is similar to the observations described previously by Djokić.[29]

Table 1.
Composition and operating conditions of cyanide-based electroless gold deposition.[30]

Reagent	Concentration (mol/dm^3)
K_2CO_3	0.75
KOH	0.87
KCN	0.01
$KAu(CN)_2$	0.017
$N_2H_4 \cdot H_2O$	0.50
Agitation	Magnetic stirrer
Temperature	80°C

Reproduced with permission from ECS – The Electrochemical Society

On the Ni–B substrate, Osaka[28] noticed numerous crystals of uniform size after the initial plating period of 5 s. Contrarily, on the Ni–P surfaces only a small number of gold crystals were observed. The good adhesion and uniform deposition at the Ni–B surfaces were attributed to the density of nuclei produced at the initial stages of gold deposition.

To find the conditions in which the electroless deposition of gold at Ni–P surfaces with an acceptable appearance and adhesion would be possible, the activation of Ni–P substrates with 10% HCl solution or a mixture of 0.1 M NH_4F and sodium sulfamate was investigated. The results showed that only "low phosphorus" alloys (P content less than 5 wt%) pretreated with ammonium fluoride/sodium sulfamate mixture can be used for a successful electroless gold plating from cyanide solution and hydrazine as a reducing agent.[31]

In the electroless deposition of gold from noncyanide solutions onto Ni–B and Ni–P surfaces, solutions containing thiosulfate and sulfite were used. The composition of a noncyanide solution for electroless deposition of gold used by Kato et al.[32] is presented in Table 2.

Based on the electrochemical polarization measurements, Kato et al.[32] concluded that sulfite ions in the solution presented in Table 2 serve as the reducing agent of Au(III) ions. Since the deposition of gold was observed only on Ni–B substrate but not onto Au, the authors concluded that the reaction is not autocatalytic. The authors attributed an increase in thickness of the deposited gold to the so-called substrate catalyzed reaction and further considered that the reaction does not proceed via galvanic displacement.

Table 2.
Composition of noncyanide solution for electroless deposition of gold used by Kato et al.[32]

Reagent	Concentration (mol/dm^3)
$NaAuCl_4 \cdot 2H_2O$	0.01
Na_2SO_3	0.32
$Na_2S_2O_3 \cdot 5H_2O$	0.08
Na_2HPO_4	0.32
pH (adjusted with NaOH)	9.0
Agitation	Mechanical stirrer
Temperature	60°C

Reproduced with permission from ECS – The Electrochemical Society

On the basis of results for gold plating from noncyanide solution presented in Table 2, Sato et al. have concluded the following:[33]

1. Acceptable gold films with good adhesion and low porosity can be obtained when plating is carried out onto Ni–B substrates from solutions containing 0.01 M sodium thiosulfate.
2. Only at the low phosphorus content in Ni–P substrates (<5 wt%), electroless plating from solutions with "low" thiosulfate concentration (0.01 M) can produce thin gold films which are uniform and with insignificant porosity.

In this way, they showed that the adherent gold films can be obtained on both Ni–B and low phosphorus content Ni–P surfaces.

It seems that the solution for electroless deposition of gold with ascorbic acid as a reducing agent developed by Sullivan and Kohl[34] and presented in Table 3 produces very uniform coating with excellent adhesion, low porosity, good solderability, and very small crystallite size (about 25 nm).[29]

Electroless copper plating has extensively been used in many electronics applications, e.g., printed circuits industry, such as plating of bare laminate and plating through hole. Different reducing agents such as formaldehyde, glyoxylic acid, borohydride, and ascorbic acid, have been used so far. A comparison between formaldehyde and glyoxylic acid as reducing agent shows that the glyoxylic acid is a promising agent for the electroless Cu plating.[35]

Increasing demand for high-performance electronics devices has led to the rapid advances in the Ultra-Large-Scale Integration (ULSI) fabrication technology. Conventional ICs are produced using the Complementary-Metal-Oxide-Semiconductor (CMOS) technology with aluminum interconnects.[36] However, due to its higher electrical conductivity and superior resistance against electromigration in comparison to the conventionally used aluminum wiring, copper offers significant improvements in performance and reliability.

Table 3.

Noncyanide solution for electroless deposition of gold.[34]

Solution A		Solution B	
Reagent	Concentration (g/L)	Reagent	Concentration (g/L)
$K_3Au(S_2O_3)_2$	2	$H_3C_6H_5O_7$	84
Ascorbic Acid	8.8	KOH	65

Solution B is used to adjust pH of solution A to 6.4; temperature 20–50°C

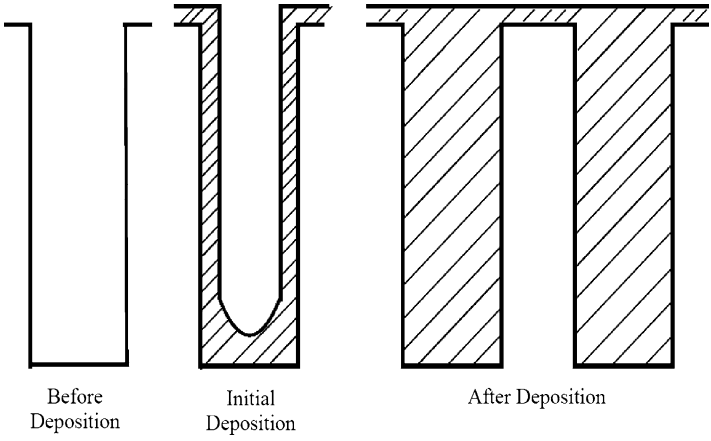

Figure 4. Schematic presentation of holes in which copper was electrolessly deposited.

The damascene copper interconnects are produced by electrodeposition of copper onto PVD Cu seed layer. The electrodeposition of copper layer is carried out to fill in vias and trenches and consequently to form the metal interconnects. The bottom-up fill of copper in fine via holes as schematically presented in Fig. 4 has successfully been demonstrated by Wang et al.[37] using the electroless deposition process.

Wang et al.[37] used $TaN/SiO_2/Si$ substrates with hole pattern, as schematically presented in Fig. 4, for investigating filling via hole by electroless deposition. For this purpose, the ionized cluster beam (ICB) Pd layers with a thickness of 1–2 nm were deposited. The diameter of holes was in the range 0.31–1.0 μm with depth 1.5 μm. The solution for electroless deposition of copper and operating conditions, used in Wang's work, is presented in Table 4.

Importantly, when the solution presented in Table 4 contains bi(3-sulfopropyl) disulfide (SPS) within the range of 0.05–0.5 mg/L, electroless deposition of copper is successful for bottom-up fill via holes.[37]

To achieve successful Cu interconnects, it is essential to deposit effective barrier layers to avoid the oxidation and diffusion of Cu into interlevel dielectrics such as SiO_2. Both oxidation and diffusion of

Table 4.
Composition of the solution and operating conditions for electroless deposition of copper.[37]

Reagent	Concentration (g/L)	Role
$CuSO_4 \cdot 5H_2O$	6.6	Cu^{2+} ions
EDTA	70	Complexing agent
Glyoxylic acid	18	Reducing agent
2, 2′-Dipyridine	0.04	Stabilizer
Polyethylene glycol ($M_w = 4{,}000$)	0.5	Surface activator
TMAH		Adjusting pH to 12.5
Temperature	70°C	

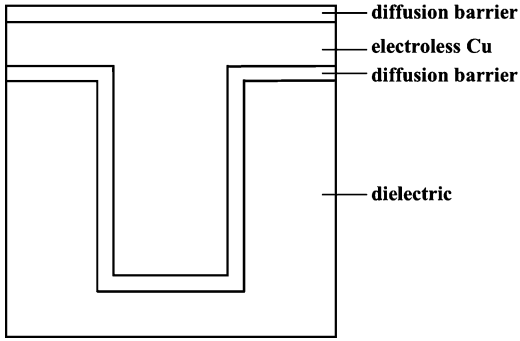

Figure 5. Schematic presentation of a hole with barrier layers and electroless copper.

copper can significantly influence the performance of the electronics device. A schematic presentation of a hole with barrier layers and electroless copper is given in Fig. 5.

One way of the electroless deposition of barrier coating on copper interconnects was suggested by Shacham-Diamand.[36] In this approach, CoWP barrier layers were electrolessly deposited from a solution containing tungstate ions (as Na_2WO_4), cobalt ions (as $CoSO_4$), citrate ions, additives, and hypophoshite as a reducing agent. Copper can electrolessly be deposited onto CoWP surfaces; however, the substrate should be activated prior to electroless deposition. This can be achieved either by the activation with Pd(II) ions or by the so-called contact deposition.[3]

Other deposited barrier layers may include Ni–P, Ni–B, Ni–Mo–P, Co–P, or similar combinations. All of the mentioned alloys can quite easily be deposited by means of electroless deposition.

Electroless copper seed layer on TaN surfaces for Cu metallization in the back-end-of-line semiconductor fabrication was also investigated.[38] After etching in diluted HF solution and activation with $PdCl_2$, the electroless deposition of copper (to be used as a seed layer) was carried out from $CuSO_4$/EDTA solution containing Triton X-100, tetramethyl ammonium hydroxide (TMAH), and formaldehyde as a reducing agent of Cu(II) ions.

Improving electroless Cu via filling with optimized Pd activation was reported by Lau et al.[39] In this work a proper cleaning of the TiN surfaces involving HF and then further activation with $PdCl_2$ was recommended. Other reports on electroless deposition of copper on silicon[40] or on TiSiN[41] are available in the literature.

An electroless deposition method for the preparation of thin Cu_3Se_2 films on silicon substrate which can be used as II–VI semiconductor was proposed by Yang and He.[42] The process is carried out at room temperature using silicone immersed into a solution containing SeO_2, $CuSO_4$, and HF. The deposition was described as a simple galvanic process.

Electroless deposition can successfully be used in the production of various composite materials useful for the electronics applications. The examples include silver-coated copper or nickel particles, used in screen printing,[43] gold-coated nickel powders, silver and/or palladium-coated polymers or glass powders used in ball grid array, etc.

It is to be noted that among other materials, electroless-deposited silver–tungsten thin films were recommended for microelectronics and microelectromechanical systems (MEMS).[44,45]

2. Electroless Deposition for Electromagnetic Shielding

Another important application of electroless deposition of metals such as Ni or Co on fibers or nonconductive particulates is important for the electromagnetic shields.[46,47] Many polymer films, fibers, and plastics are metallized for microelectronics, computers, and automotive industries to provide the electromagnetic shielding.

Ability of a material to absorb or reflect the electromagnetic radiation (EMR) in a given frequency range determines the particular

application. Electromagnetic shields and electromagnetic wave absorbers use materials such as metals, complex composite structures, or conductive polymers.[48] Composite materials with a dielectric matrix (e.g., polymers or ceramics) and conductive or magnetic fillers of different shape and size have a significant importance for the electromagnetic shielding.

Electroless deposition offers an attractive way of producing various fillers with a conductive surface or desirable magnetic properties, which can further be used in the production of composite materials with dielectric matrices for electromagnetic shielding.

Electroless deposition of Ni and Co onto polyacrylonitrile (PAN) fibers for applications in the electromagnetic shielding was investigated.[47] PAN fibers electrolessly coated with Ni or Co were employed for the fabrication of knitted linen used in multilayer flexible electromagnetic wave absorbers. Although the composition of the electroless plating solution was not reported, this process (production of metal-coated nonconductive fibers) is fairly feasible, and it can be quite successful using various Ni- or Co-electroless plating compositions with a number of reducing agents. Based on the electrical and magnetic properties, it was demonstrated that the electrolessly coated PAN fibers with Ni and Co can successfully be applied for the electromagnetic shielding.

To obtain high quality of electromagnetic interference shielding materials, polyethylene terephthalate (PET) films were coated with copper from an alkaline Cu(II) solution and using formaldehyde as a reducing agent.[46] Prior to electroless Cu plating, PET samples were pretreated through plasma etching and then with $SnCl_2/PdCl_2$ catalysts. The most effective way of etching of PET polymer was the application of plasma etching. In this case, the adhesion of copper was improved and the high electromagnetic interference shielding effectiveness over a wide range of frequency levels was obtained.

3. Electroless Deposition of Magnetic Materials

Electroless-deposited magnetic materials based on Co, Ni, and Fe have important applications in the electronics and computer industries. These materials are used in recording media. Two types of the recording media have been intensively investigated: longitudinal recording system, where the magnetization in the recorded bits are parallel to the media surface and perpendicular recording system,

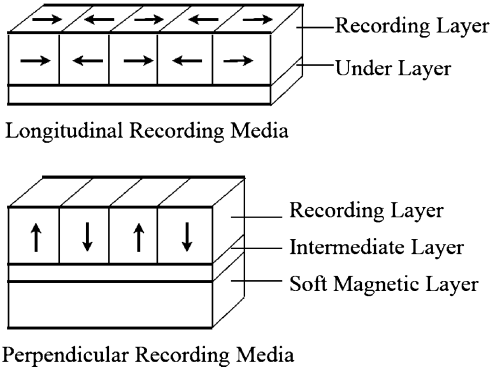

Figure 6. Schematic presentation of longitudinal and perpendicular recording media.

with the magnetization in the direction perpendicular to the media surface. This is schematically presented in Fig. 6.

One of the problems of longitudinal recording media is the formation of zigzag bit transitions.

In the case of perpendicular recording media the device consists of recording layer with a perpendicular anisotropy, a soft magnetic underlayer (SUL), and an intermediate layer. The SUL is essential for improving the performance of perpendicular recording media. Electroless deposition is very suitable for the production of SUL.

Recording performance of the perpendicular recording media with an electroless-deposited Ni–P soft magnetic underlayer (Ni–P SUL) was investigated by Uwazumi et al.[49] Ni–P SUL with a thickness range 1.5–3.0 μm and a low phosphorus content was electroless plated on a polished nonmagnetic Ni–P layer (phosphorus content of about 20 wt%). After plating the surface of Ni–P SUL was polished.

For the media preparation, 25-nm-thick CoZrNb soft magnetic film was sputtered onto Ni–P SUL and then a thick CoPtCr–SiO_2 granular recording layer. For comparison, a media with 200-nm-thick sputtered CoZrNb SUL was used. The results showed that an electroless-deposited ferromagnetic Ni–P layer (low phosphorus content), which is suitable for mass production as a SUL for a double-layered perpendicular recording media, exhibits almost the same magnetic properties and recording performances as a 200-nm-thick sputtered SUL. In addition, the spike noise which is commonly observed from SUL was not found for the media with Ni–P SUL.

This result indicates great potential for electroless-deposited ferromagnetic Ni–P layer for the perpendicular recording media. Similar results were obtained by Asahi et al.,[50] where electroless deposition of CoNiFeP alloys under the influence of an external magnetic field was investigated. The electroless-deposited CoNiFeP SUL exhibited a sufficient overwrite performance and high signal-to-noise ratio in comparison with typical SUL fabricated by sputtering.

4. Electroless Deposition for Energy Conversion and Catalytic Purposes

The demand for the electrical energy sources, i.e., batteries and fuel cells, is continuously increasing. Very important developments have been made in the recent years in products related to electronics, leisure, military, or telecommunication equipment.

Miniature batteries and fuel cells have been attracting many research groups. The prospective potential for miniaturization such as in MEMS technology requires development of microfuel cells.

The combination of anode/electrolyte/cathode in proton exchange membrane fuel cell is usually referred to as the membrane electrode assembly (MEA).[51] Usually the MEA was produced by attaching a catalyst layer (frequently Pt, Pt alloys, or other noble metals) on one side of porous gas diffusion electrodes. The catalysts layers consisting of noble metals are usually deposited by sputtering.[52]

Electroless deposition of the catalytic Pt or Pt–Ru layer was proposed for the preparation of electrodes in microdirect methanol fuel cells.[53] A porous silicone substrate is prepared by the anodic etching in HF–ethanol–water (1:1:1) solution. After the etching, at the surface of porous silicon substrate, a thin film of titanium is sputtered and then a film of Pt or Pt–Ru alloy with thickness of about 150–200 nm was electroless deposited. The electrodes prepared in this way helped in minimization of the fuel cell size and increased the reactive area of the catalyst over the silicon electrode surface.

In another approach, silicon wafers were treated with HCl–CH_3OH (1:1) solution, then with concentrated H_2SO_4, and finally washed with acetone.[54] The wafers were afterwards coated with nanostructured poly-(chloro-*p*-xyrylene) (PPX-Cl) polymer by

vapor deposition.[55] Onto the surface of PPX-Cl polymer copper was electroless deposited via Pd activation to produce a catalyst for the energy conversion applications.

In the solid oxide fuel cells one of the very promising anode materials is the so-called nickel yttria stabilized zirconia (Ni-YSZ) cermet. This anode material must have sufficient electrical conductivity, high catalytic activity, and also be stable in a reducing environment. A preparation of nickel-coated YSZ powder for application as an anode for solid oxide fuel cell was reported.[56] The YSZ powders were activated with $SnCl_2/PdCl_2$ catalyst and then nickel was electroless deposited. Although the authors did not describe the procedure for electroless nickel deposition, they reported that the coating, i.e., nickel, did not contain any impurities such as phosphorus or boron. The amount of nickel in Ni-YSZ powder was in the range 5–60 vol%. The electrodes were prepared by sintering at 1,200–1,350°C for 2 h. The conductivity of Ni-YSZ cermets containing 20 vol% Ni was estimated at about 450 s/cm at 1,000°C, therefore suggesting that they should be better suited for solid oxide fuel cells anode applications than conventionally prepared materials.

Electroless deposition of noble metals, e.g., palladium, platinum, or similar, onto ceramic or polymeric substrates has also been intensively investigated in the recent years. Platinum/carbon nanotubes electrocatalysts were prepared via immersion of multiwalled carbon nanotubes into 0.0075 M H_2PtCl_6 solution for 12 h. The reduction was then performed using a mixture of 0.1 M $NaBH_4$ in 1 M NaOH.[57] In another experiment, the authors prepared the electrocatalyst by the immersion of carbon nanotubes in K_2PtCl_6 solution and a subsequent reduction of Pt ions with ethylene glycol. After washing and drying the recovered carbon nanotubes loaded with platinum were used for the oxygen reduction reaction in polymer electrolyte membrane fuel cells (PEMFC) and the performance of PEMFC was analyzed with respect to catalyst synthesis and Pt loading.

It was found that the electrodes prepared by $NaBH_4$ route had Pt loading of 19.6%, fine Pt particle size, and improved performance for the fuel cell applications. On the other hand, the catalysts prepared by ethylene glycol route had Pt loading of 32% and not as good fuel cell performance, which was attributed to the larger Pt particle size and agglomeration. In this way for a better performance in fuel cell applications, a uniform dispersion with a narrow Pt particle range and low Pt loading is more desirable.

Nafion 117 membranes were electroless coated with Pt from a solution of H_2PtCl_6 and hydrazine (N_2H_4) as reducing agent.[58] The coated membrane was used to make an MEA of proton exchange membrane fuel cell which was tested at 60°C in a saturated H_2/O_2 system. The maximum current density of about 80 mA/cm^2 at 0.3 V was obtained in this system.

Palladium electroless deposition was used for coating of Nafion 117 for the application as a membrane in direct methanol fuel cell.[59] After the activation of the polymer membrane (Nafion 117) with Pd(II) complexes, reduction was carried out with sodium borohydride, $NaBH_4$. Further, autocatalytic deposition of palladium was performed using a commercially available solution. Compared to bare Nafion, the Nafion/Pd composites considerably reduced methanol crossover. This resulted in enhanced cell performance, which was attributed to the existence of the Pd layer at the surface of polymer.

Palladium membranes have been prepared by electroless deposition on porous stainless steel substrates.[60] The performance of these membranes as hydrogen diffusion electrodes was evaluated using a three-electrode cell in alkaline solution. The technical feasibility of these membranes as gas diffusion electrodes has been proven; however, the activity of hydrogen oxidation was high at the beginning and significantly decreased with time. This behavior was attributed to the slow entry of hydrogen at the H_2/Pd interface.

Electroless deposition of nickel onto polytetrafluoroethylene (PTFE) particles was carried out and then the electrode plate (Ni-PTFE) was made by pressing and subsequent sintering at 350°C.[61] Ni served as a catalyst in both the anode and the cathode in alkaline fuel cells. However, Pt, Pd, and Ag were used as catalysts additionally. In this work, Pt or Pd was additionally deposited on Ni-PTFE surfaces via displacement (galvanic) deposition using K_2PtCl_6 or $PdCl_2$ solutions, respectively. The results showed that the catalytic performance of Ni-PTFE, which was insufficient to use in practical cell, can be improved by the deposition of Pd or Pt. In terms of current density, alkaline fuel cells with Ni-PTFE electrodes on which Pt or Pd was electroless deposited showed improved performance. Furthermore, the Pd-plated Ni-PTFE electrodes can be used as a high-performance anode with small charge-transfer resistance, which is very beneficial in alkaline fuel cells applications.

These Pd-plated Ni-PTFE electrodes may have an advantage when the electrode is very thin or when a very small cell volume is required.

Nickel/metal hydride (Ni/MH) batteries have been widely used as power sources for many applications such as digital cameras, power tools, and portable electronic devices. In addition, the usage of Ni/MH batteries as power sources in hybrid electric vehicle (HEV) is notable.[62] The positive electrode was prepared by plating of nickel onto nonwoven polyolefin fabric having three-dimensional micronetwork. The fabric was first treated with Pd–Sn catalyst. Secondly, electroless nickel was applied onto the activated surface, and finally, nickel was electrodeposited. The cylindrical sealed cell using the prepared substrate as the electrode material exhibited superior high rate discharging capability to the similar commercially available cells.[63]

Among other approaches in the field of catalysis and energy devices applications, it is important to note that electroless deposition of CoO thin films useful in photonic, chromogenic, or energy conversion coatings was investigated as well.[64]

Synthesis of tungsten oxide on Cu surfaces by electroless deposition for electrochromic and photocatalytic applications[65] and amorphous cobalt–boron/nickel foam as an effective catalyst for hydrogen generation from alkaline sodium borohydride solution[66] have also been investigated. In addition, reports on electroless silver deposition on $Ba_{0.5}Sr_{0.5}Co_{0.8}Fe_{0.2}O_{3-\delta}$ for low-temperature solid oxide fuel cell[67] and Cu/Al_2O_3 catalyst,[68] prepared via electroless deposition of Cu onto Al_2O_3, are available in the literature.

It is obvious that in the field of energy devices and/or catalysis further research of the electroless deposition itself would lead to remarkable practical achievements.

5. Electroless Deposition for the Biomedical Applications

The biomedical field has received significant attention from research professionals in many different areas including chemistry, physics, engineering, biology, and medicine. Many new materials for use as drug delivery systems, implants, artificial organs, hearing aids, pacemakers, etc. are being developed nowadays.

Owing to the simplicity of electroless deposition of metals, alloys, and compounds, this method offers huge advantages for the

development of new biomedical devices, of course, if a proper and an in-depth understanding of this approach is applied in the production of such devices.

It was suggested that metal matrices can be attractive materials for drug delivery systems[69] due to the following reasons:

1. The ability to deliver both hydrophilic and hydrophobic molecules over a long period of time
2. Denser pharmaceutical content in the coating
3. Longer term and controllable release kinetics
4. The ability to protect drugs from water and oxygen while being stored in potentially inert film
5. The ability to apply different compounds to different nanolayers of the coating and to release different drugs at different times

Gertner and Schlesinger investigated the drug delivery from electroless-deposited Ni–P thin films.[69] For this purpose, Ni–P thin films were deposited on stainless steel using sodium hypophosphite as a reducing agent. During the electroless deposition, drugs such as fluorouracil, tetracycline, albumin, and rapamycin were added to the plating solution. The amount of medications codeposited with Ni–P was in the range from 1/200 to 1/30 of the total weight of coating.

The release of medications from electroless Ni–P films was investigated by the measurement of the amount of the active component in physiological saline solution in which coatings were immersed. The results showed a continuous release of the active medications from the films within the time frame of about 40 days.

The model proposed by Gertner and Schlesinger opens excellent opportunities for future investigations of electroless-deposited metals for use as matrices in the continuous drug release devices. It is quite unlikely that the Ni–P matrices will find a realistic application for the drug release devices, since they may release Ni(II) ions while implemented in vivo. However, other biocompatible matrices including polymers or oxides which can be produced electrolessly may have great potential in this area. These aspects deserve in-depth future investigations.

Alumina is a well-known bioinert ceramic material which can be used in total hip prosthesis and dental implants since it exhibits good biocompatibility, strength, and excellent corrosion resistance.[70,71] The application of alumina has some limitations due to poor fracture toughness. The incorporation of ductile phase may lead to the

improvement of mechanical properties. However, the ductile phase must also be compatible. Electroless deposition of silver on Al_2O_3 powder was recommended for this purpose. It was demonstrated that, if Al_2O_3 powder is pretreated with silver acetate prior to electroless deposition, a thin uniform layer of silver (about 5 nm thick) can be obtained. Contrarily, if no pretreatment of Al_2O_3 powders is carried out, larger Ag particles (about 100 nm in diameter) are obtained. The electroless deposition of silver was carried out from a silver ammonia-based solution and formaldehyde as a reducing agent.

Antimicrobial properties of silver have been known and utilized for centuries. It is well established that only silver ions are antimicrobially active, while elemental silver is not. Many biomedical devices have been coated with silver and/or silver compounds for antimicrobial purposes. The applications of surfaces treated with silver or its compounds include devices such as topical wound dressings, urinary catheters, endotracheal tubes, cardiac valves, etc.[72] Electroless deposition of silver or its compounds can quite successfully be used for coating of biomedical devices.

Biological activity of electroless-deposited silver on plasma-activated polyurethane was investigated by Gray et al.[73] Silver was deposited onto polyurethane samples using commercially available solutions. Some antimicrobial activity of these samples was observed.

Silver-coated dressings used to enhance healing in burns and skin grafts are commercially available nowadays. Silver nylon dressing was reported as an effective material to reduce the radiation dermatitis in patients undergoing chemotherapy.[74] Silver-coated dressings (in which silver was electrolessly deposited onto nylon fabric) were used to examine the reduction in the rate of mediastinal infections in cardiac surgery patients.[75] The results showed that silver-coated nylon dressings exhibited the reduction in mediastinal infections. It was found that the electroless-deposited silver compounds onto various textile materials are antimicrobially active, while pure metallic silver exhibits a very low or no antimicrobial activity.[76,77]

The tissue engineering concept offers development of useful substrates for repair replacement or regeneration of organs and tissues. Hydroxyapatite ($C_{10}(PO_4)_6(OH)_2$, HA) is the major constituent of the bone and teeth. Deposition of calcium phosphate

coatings from an autocatalytic electroless solution on a high-molecular-weight polyethylene starch/ethylene vinyl alcohol blend and starch/cellulose acetate mixture was investigated.[78] The results indicated that calcium phosphate films can successfully be deposited onto investigated materials. The coatings exhibited a clear bioactive nature after the immersion in a simulated body fluid. These materials were recommended for bone bonding, bioabsorbable implantations, and fixation devices.

Using a similar procedure, a composite material for tissue engineering applications composed of HA and carboxymethylchitosan was obtained by a coprecipitation method. In vitro tests exhibited a great potential of this class of materials for bone tissue-engineering applications.[79]

Based on the current trends, it is believed that electroless deposition of metals, alloys, and compounds for various biomedical applications will significantly grow in the future.

6. Electroless Deposition and Anticorrosion Applications

Conventionally used coatings are expected to exhibit a reasonable performance in respective applications. Corrosion behavior of the applied materials must seriously be taken into considerations to avoid the deterioration in the performance. Depending on the application, corrosion behavior of electrolessly obtained materials must be investigated under proper conditions for the particular purpose.

In this section, the corrosion aspects of different electroless-deposited metals and/or alloys are discussed.

Electroless deposition of thin films of Ni–P alloys has found numerous applications in many fields due to their excellent corrosion resistance, high wear resistance, high hardness, and acceptable ductility.

Electroless deposition of Ni–P was used for the protection of magnesium alloys from corrosion.[80,81] AZ91D magnesium alloy was plated with an electroless Ni–P coating to improve the corrosion resistance.[82] This magnesium alloy was first phosphatized in a zinc phosphating solution containing sodium molybdate (Na_2MoO_4) and then Ni–P was electroless deposited. The Ni–P coating exhibited a very good corrosion resistance.

Corrosion properties of electroless nickel coatings with codeposited PTFE or silicon carbide (SiC) particles in H_2SO_4 and NaCl

solutions were also investigated.[83] It was found that both coatings, electroless Ni–P alone or electroless Ni–P with codeposited PTFE or SiC particles, exhibited a very good corrosion resistance in H_2SO_4 and NaCl solutions.

Ni–B coatings have superior wear resistance and a very high hardness. However, compared to electroless Ni–P alloys, they exhibit a relatively low corrosion resistance. To improve the corrosion resistance, electroless Ni–P/Ni–B duplex coatings were prepared using dual solutions (acidic hypophosphite and alkaline borohydride).[84] The measurements showed that microhardness, wear, and corrosion resistance of the duplex coating were higher than individual Ni–P or Ni–B coatings of similar thickness. The Ni–P/Ni–B duplex coatings having Ni–P as the outer layer have exhibited better corrosion resistance.

The electroless CoFeB films which are used as a soft magnetic material in computers industry have acceptable magnetic behavior, but poor corrosion resistance compared with the electrodeposited Ni–Fe (permalloy) coatings.[85] However, the addition of Ni to the CoFeB film improves corrosion resistance without affecting its soft magnetic properties. The best magnetic and electronic properties had a film with the composition $Co_{77}Ni_{13}Fe_9B_1$.

The incorporation of copper in electroless Ni–P–PTFE coatings leads to the improvement of corrosion resistance.[86] When the copper content in Ni–P–Cu–PTFE coatings was about 6.5%, the anticorrosion performance was the best. The anticorrosion performance of the Ni–P–Cu–PTFE coatings in 1 M HCl and 20% NaCl solutions was better than that of Ni–P–PTFE coatings or pure Cu.

Electroless Ag-PTFE composite coatings were prepared on stainless steel substrates for the prevention of biofilm growth.[87] The anticorrosion properties of Ag-PTFE composite coatings were investigated in 0.9% NaCl solution. The results showed that the corrosion resistance of the Ag-PTFE composite coating was superior to that of stainless steel.

Magnesium is a very important metal that may have great applications in portable microelectronics, telecommunications, and aerospace industries, due to its low density. However, a poor corrosion resistance of magnesium limits its applications. On the other hand, coating of magnesium surfaces with other metals via electroless deposition can be quite difficult due to its reactivity with the most of the plating solutions.

Prior to electroless deposition of silver onto Mg alloys, organosilicon heat-resistant coating was applied at the surface.[88] Further activation of this intermediate layer and electroless deposition of silver using glucose as a reducing agent were performed in the usual way. Importantly, the corrosion resistance of silver-coated magnesium alloys with an intermediate organo-silicon layer was significantly improved in 3.5% NaCl solution when compared to uncoated magnesium alloys. On the other hand, an introduction of the organosilicon layer onto the surface of magnesium alloys provides a new concept for plating on reactive metals, which are considered difficult to plate under the normal conditions.

Electroless deposition of various coatings which are used as anticorrosion coatings will grow in the future for different applications in the electronics, energy devices, aerospace, and biomedical fields.

7. Electroless Deposition and Nanotechnology

At the end of the last century, the field of *nanotechnology* was introduced. Due to significant investments worldwide, nanotechnology was intensively growing in the last two decades.

The realistic applications of the nanotechnology itself are not very clear at present; however, many research projects were related to the miniaturization for the electronics, sensors, immunodiagnostics, and other biomedical applications. Another approach of nanotechnology is development of metal nanostructure which can be useful as catalysts for various industrial processes, energy conversion devices, or environmental applications.

Electroless deposition is a very useful approach in the production of various metallic and ceramic nanostructures. In this section, a brief review of electroless deposition processes used in nanotechnology field is presented.

As in other electroless processes, chemical reduction of ions such as Fe^{2+}, Cu^{2+}, Ag^{+}, Au^{+}, Pd^{2+}, and Pt^{4+} from their aqueous solutions is carried out using various reducing agents to produce different shapes of nanoparticles. Depending on metal, typical reducing agents involve borohydride, dimethyl amino borane, ascorbic acid, hydrazine, formaldehyde, etc.

A review on the production of multifunctional nanorods for biomedical applications has been published recently.[89]

Gold nanoparticles were electrolessly deposited on the surface of carbon nanotubes from cyanide solution using borohydride as a

reducing agent.[90] The carbon nanotubes coated with spherical gold particles having diameter of about 3–4 nm were recommended for use as catalysts in industrial applications.

Nanostructured gold was produced from $AuCl_4^-$ solution in which nanoparticles of conductive polymer, polypyrrole, were suspended.[91] Upon the exposure of polypyrrole nanoparticles to the $AuCl_4^-$ solution, a rapid change in purple color of the solution was observed, which was attributed to the presence of gold nanoparticles. The formation of gold nanoparticles was observed in the solution and at the surface of polypyrrole. The particle size, based on the TEM images, was estimated at about 100–200 nm. These particles can easily be dispersed into solution by the ultrasonic treatment. The results of this work show that the polypyrrole acts as a reducing agent of Au(III) ions to Au°, which consequently leads to the oxidation of polypyrrole.

The formation of elemental gold layer at the surface of conductive polymers has been reported in the literature.[92,93] Synthesis of nanostructures and self-assembled palladium nanowires from Pd(II) complexed solutions using hydrazine as a reducing agent were reported by Shi et al.[94,95] The process was carried out for 120 s at 60°C. Electroless deposition of nanowires of other metals is also possible and quite realistic. However, no particular engineering applications are yet known.

Selective electroless nickel plating of particle arrays on polyelectrolyte multilayer was investigated for the potential applications in sensors, optoelectronics, and biochips.[96] This process is based on the preparation of functional colloidal arrays on surfaces. In the next step metal deposition is carried out on the surfaces of the patterned particles secured on the substrate. Samples of colloidal arrays on patterned polyelectrolyte templates are first pretreated with a Pd(II)-based catalyst. After rinsing with deionized water and drying, samples were plated with nickel using dimethylamine borane (DMAB) as a reducing agent. Based on the results of this work,[96] it was shown that the selective electroless nickel deposition on 3D patterned surfaces can be successful.

Copper was electrolessly deposited on suspended Al_2O_3 nanoparticles by the addition of Cu(II)–EDTA alkaline solution and formaldehyde as a reducing agent.[97] This approach can be used for various ceramic or polymeric nanoparticles and different metals.

Incorporation of nanoparticles of zinc oxide during electroless deposition of nickel for the improvement of metallurgical or corrosion resistance properties was also investigated.[98] Zinc oxide nanoparticles (<25 nm) were produced by anodic dissolution of zinc metal against platinum cathode immersed in electrolyte consisting of tetra-ammonium bromide and 0.1 M acetonitrile mixture in 4:1 ratio at current density of 5 mA/cm.^{2} Nickel was then deposited on mild steel substrates from an alkaline solution in which ZnO nanoparticles were suspended and using sodium hypophosphite as a reducing agent. The incorporation of ZnO nanoparticles resulted in surface uniformity and homogenicity and also improved the corrosion resistance of Ni–P–ZnO coating.

Carbon substrate serves as a sacrificial reductant and converts aqueous MnO_4^- to insoluble MnO_2, which in turn can be useful for batteries and capacitors.[99] In this aspect, the incorporation of homogenous nanoscale MnO_2 within ultraporous carbon structures via self-limiting electroless deposition was reported.[99] The deposited nanoscopic MnO_2 on carbon exhibited exceptionally high capacitance.

Among other reports, the DNA-templated Cu nanowire fabrication by electroless metallization[100] or biotemplate synthesis of 3-nm nickel and cobalt nanowires, which may find reality in biomedical applications,[101] should be mentioned.

The research of electroless deposition in relation with nanotechnology will definitely be expanded in the future. This process (electroless deposition) can quite successfully produce a variety of nanostructures, which have been known and understood far before the appearance of nanotechnology. Nanostructures produced via electroless deposition may have great potential for various engineering applications in the future.

However, how the real applications would work, the future will tell.

V. CONCLUSIONS

Electroless deposition has attracted researchers in the recent years due to significant developments in electronic, energy devices, automotive, aerospace, and biomedical industries. If properly carried out, this quite simple process produces on complex shapes very

uniform and continuous coatings, which are difficult to obtain with other competitive technologies. Additionally, when needed, electroless deposition offers a very efficient way of production of powders of various shapes and sizes, of course under the specific conditions, as referenced herewith.

Almost all metals and/or alloys that can be electrodeposited from aqueous solutions can also be produced via electroless deposition, if proper reducing agents and conditions are applied. The advantage of electroless deposition is that an external current is not required. Furthermore, films of metals, alloys, and compounds such as ceramics or polymers are very attractive for the field of nanotechnology. It is important to note that the deposits (coatings or particulates) produced by electroless deposition are predominantly "nano"-crystalline.

Electroless deposition, as a very important area of the modern technology, needs further developmental studies to ensure the successful operation of the process and desirable properties of the finally obtained material. Significant further work is definitely required to learn more about the kinetics and mechanisms of the reactions involved in these sophisticated processes.

ACKNOWLEDGMENTS

Sections I, II, and IV were written by Djokić and the Sect. III was jointly written by Cavallotti and Djokić. For an intensive literature search and manuscript preparation, Djokić is thankful to Miss. Nada Djokić.

REFERENCES

[1]O. Mallory and J.B. Hajdu, *Electroless Plating: Fundamentals and Applications*, AESFS, Orlando, FL, 1990.
[2]Y. Okinaka and T. Osaka, "*Electroless Deposition Processes: Fundamentals and Applications*", in *Advances in Electrochemical Science and Engineering*, Ed. by H. Gerischer and C. Tobias, VCH Publishers, New York, 1994, p.55.
[3]S. S. Djokić, "*Electroless Deposition of Metals and Alloys*", in *Modern Aspects of Electrochemistry*, Ed. by B. E. Conway and R.E. White, Kluwer Academic/Plenum Publishers, New York, 2002, p.51.
[4]S. S. Djokić, *J. Electrochem. Soc*. **143** (1996) 1300.
[5]G. Salvago and P.L. Cavallotti, *Plat. Surf. Finish*. **59**(7) (1972) 665.
[6]S. S. Djokić, *J. Electrochem. Soc*. **144** (1997) 2358.

[7]S.S. Djokić, *Plat. Surf. Finish*. **91**(6) (2004) 43.
[8]S. Djokić and N. Djokić, in *Abstract 2764, 214th Meeting of the Electrochemical Society*, Honolulu, Hawaii, October 12–17, 2008.
[9]S. Djokić, *Plat. and Surf. Finish*. **92**(5) (2005) 45.
[10]A. J. Bard, R. Parsons, and J. Jordan, Editors, *Standard Potentials in Aqueous Solutions*, Marcel Dekker, New York, 1985.
[11]P. Peeters, G. V. D. Hoorn, T. Daenen, A. Kurowski, and G. Staikov, *Electrochim. Acta* **47** (2001) 161.
[12]G. Gutzeit, *Plating*, **47** (1960) 63.
[13]X. Yin, L. Hong, B. -H. Chen, and T. -M. Ko, *J. Colloid. Interface Sci*. **262** (2003) 89.
[14]Z. Xiao, W. Wang, L. Ye, Y. Sha, and S. Tu, *Surf. Coat. Technol*. **202** (2008) 5008.
[15]P. Cavallotti and G. Salvago, in *Electrodeposition Technology: Theory and Practice* Vol. 87–17, Ed. By L. Romankiw, D. Turner, The Electrochem. Soc, Pennington, NJ, 1987, p. 327.
[16]M. Paunovic, *Plating* **55** (1968) 1161.
[17]M. Paunovic, *Plat. Surf. Finish*. **70**(2) (1983) 62.
[18]J. Flis and D. J. Duquette, *J. Electrochem. Soc*. **131** (1984) 51.
[19]C. K. Mital, P. B. Shrivastava, and R. G. Daneshwar, *Met. Finish*. **85** (6) (1987) 87.
[20]I. Ohno, O. Wakabayashi, and S. Haruyama, *J. Electrochem. Soc*. **132** (1985) 2323.
[21]L. M. Abrantes and J. P. Correia, *J. Electrochem. Soc*. **141** (1994) 2356.
[22]C. H. de Minjer, *Electrodep. Surf. Treatment* **3** (1975) 261.
[23]R. L. Zeller III and U. Landau, *J. Electrochem. Soc*. **139** (1992) 464.
[24]R. M. Lukes, *Plating* **51** (1964) 969.
[25]P. Cavallotti and G. Salvago, *Electrochimica Metallorum* **III** (1968) 239.
[26]G. Cui, N. Li, D. Li, and M. Chi, *J. Electrochem. Soc*. **152** (2005) C669.
[27]A. Brenner and G. Riddell, *J. Res. Natl. Bur. Std*. **39** (1947) 385.
[28]T. Osaka, Y. Okinaka, J. Sasano, and M. Kato, *Sci. Technol. Advanced Mater*. **7** (2006) 425.
[29]S. S. Djokić, in *Fundamental Aspects of Electrochemical Deposition and Dissolution, Proceedings*, Vol. 99–33, Ed. by M. Matlosz et al., The Electrochemical Soc. Inc., Pennington, NJ, 2000, p.381.
[30]C. D. Iacovangelo and K. P. Zarnoch, *J. Electrochem. Soc*. **138** (1991) 983.
[31]T. Osaka, T. Misato, H. Sato, H. Akiya, T. Homma, M. Kao, Y. Okinaka, and O. Yoshioka, *J. Electrochem. Soc*. **147** (2000) 1059.
[32]M. Kato, J. Sato, H. Otani, T. Homma, Y. Okinaka, T. Osaka, and O. Yoshioka, *J. Electrochem. Soc*. **149** (2002) C164–C167.
[33]J. Sato, M. Kato, H. Otani, T. Homma, Y. Okinaka, T. Osaka, and O. Yoshioka, *J. Electrochem. Soc*. **149** (2002) C168–C172.
[34]E. A. M. Sullivan and P. A. Kohl, *J. Electrochem. Soc*. **142** (1995) 2250.
[35]X. Wu and W. Shu, *Synthesis and Reactivity in Inorganic, Metal-Organic and Nano-Metal Chemistry* **38** (2008) 292.
[36]Y. Shacham-Diamand and S. Lopatin, *Electrochim. Acta* **44** (1999) 3639.
[37]Z. Wang, O. Yaegashi, H. Sakaue, T. T. Takahagi, and S. Shingubara, *J. Electrochem. Soc*. **151** (2004) C781.
[38]S. P. Chong, Y. C. Ee, Z. Chen, and S. B. Law, *Surf. Coat. Technol*. **198** (2005) 287.
[39]P. P. Lau, C. C. Wong, and L. Chan, *Appl. Surf. Sci*. **253** (2006) 2357.
[40]G. K. Muralidhar, S. Bhansali, A. Pogany, and D. K. Sood, *J. Appl. Phys*. **83** (1998) 5709.
[41]Y. C. Ee, Z. Chen, S. Xu, L. Chan, K. H. See, and S. B. Law, *J. Vac. Sci. Technol*. A **22** (2004) 1852.

[42]Y. J. Yang and L. Y. He, *Russ. J. of Electrochem*. **41** (2005) 1241.
[43]S. Djokić, et al., Process for the production of silver coated particles, US Patent 5,945,158 (1999).
[44]A. Inberg, Y. Schacham-Diamand, E. Rabinovich, G. Golan, and N. Croitoru, *J. Electron. Mater*. **30** (2001) 355.
[45]A. Inberg, E. Ginsburg, Y. Schacham-Diamand, N. Croitoru, and A. Seidman, *Microelctr. Eng*. **65** (2003) 197.
[46]K. W. Oh, D. J. Kim, and S. H. Kim, *J. Appl. Polym. Sci*. **84** (2002) 1369.
[47]V. Bogush, *J. Optoelectron. Adv. Mater*. **7** (2005) 1635.
[48]J. Joo and A. J. Epstein, *Appl. Phys. Lett*. **65** (1994) 2278.
[49]H. Uwazumi, et al., *IEEE Trans. Magn*. **40** (2004) 2392.
[50]T. Asahi, T. Yokshima, J. Kawaji et al., *IEEE Trans. Magn*. **40** (2004) 2356.
[51]*Fuel Cell Handbook, 5th Edition*, Report prepared by EG&G Services for US Department of Energy, National Energy Laboratory, October 2000.
[52]K. Shah, W. C. Shin, and R. S. Besser, *J. Power Sources* **123** (2003) 172.
[53]X. Liu, C. Suo, Y. Zhang, W. Chen, and X. Lu, *DTIP of MEMS & MOEMS*, Tima Editions/DTIP Stresa, Italy 26–28 April 2006.
[54]J. Lowman, *NIN REU Research Accomplishments*, 2008, p. 82.
[55]M. C. Demirel, M. Cetinkaya, A. Singh, and W. J. Dressik, *Adv. Mater*. **19** (2007) 4435.
[56]S. K. Prathiar, A. D. Sharma, R. N. Basu, and H. S. Maiti, *J. Power Sources* **129** (2004) 138.
[57]N. Rajalakshmi, H. Ryn, M. M. Shaijumon, and S. Ramaprabhu, *J. Power Sources* **140** (2005) 250.
[58]W. Hawt, M. Hunsom, and K. Pruksathorn, *Korean J. Chem. Eng*. **23** (4) (2006) 555.
[59]T. J. Hejze, B. R. Gollas, R. K. Sourbrey, M. Schmied, F. Hofer, and *J. O. Besenghard, J. Power Sources* **140** (2005) 21.
[60]R. Rego, M. C. F. Oliveira, I. Esparbe, and P. L. Cabot, *J. Power Sources* **189** (2009) 1120.
[61]H. Kinoshita, S. Yonezawa, J. -Ho. Kim, M. Kawai, M. Takashima, and T. Tsukatami, *J. Power Sources* **183** (2008) 464.
[62]M. Yao, K. Okuno, T. Iwaki, M. Kato, K. Harada, J. Park, S. Tanas, and T. Sakai, *Electrochem. Soild State Lett*. **10** (2007) A56.
[63]M. Yao, K. Okuno, T. Iwaki, S. Tanase, K. Harada, M. Kato, K. Emura, and T. Sakai, *J. Power Sources* **171** (2007) 1033.
[64]F. C. Eze, *J. Phys. D: Appl. Phys*. **32** (1999) 533.
[65]S. H. Baeck, T. F. Jaramillo, G. D. Stucky, and E. W. McFarland, *Chem. Mater*. **15** (2003) 3411.
[66]H. B. Dai, Y. Liang, P. Wang, and H. M. Cheng, *J. Power Sources* **177** (2008) 17.
[67]W. Zhou, R. Ran, R. Cai, Z. Chao, W. Jin, and N. Xu, *J. Power Sources* **186** (2009) 244.
[68]H. Chang and C. Yang, *Ind. Eng. Chem. Res*. **36** (1997) 2080.
[69]M. E. Gertner and M. Schlesinger, *Electrochem. Solid-State Lett*. **6** (2003) J4.
[70]G. Willmann, H. J. Fruh, and H. G. Pfaf, *Biomaterials* **18** (1997) 873.
[71]G. M. Shi, J. K. Han, Z. D. Zhang, H. Y. Song, and B. T. Lee, *Surf. Coat. Technol*. **195** (2005) 333.
[72]S. Djokić, *ECS Transactions*, **11** (2008) 1.
[73]J. E. Gray, P. R. Norton, R. Alnouno, C. L. Marolda, M. A. Valvano, and K. Griffiths, *Biomaterials* **24** (2003) 2739.
[74]T. Voung, E. Franco, et al., *Int. J. Radiat. Oncol. Biol. Phys*. **59** (2004) 809.

[75]R. Huckfeldt, C. Redmond, et al., *Ostonomy Wound Manage.* **54** (10) (2008).
[76]S. Djokić, *J. Electrochem. Soc*. **151** (2004) C359.
[77]S. Djokić, Deposition products, composite materials and processes for the production thereof, US Patent 7,300,673 (2007).
[78]I. B. Leonor and R. L. Reis, *J. Mater. Sci. Mater. Med*. **14** (2003) 435.
[79]J. M. Oliveira, S. A. Coata, I. B. Leonor, P. B. Malafaya, J. F. Mano, and R. L. Reis, *J. Biomed. Mater. Res. A* **88** (2008) 470.
[80]R. Ambat and W. Zhou, *Surf. Coat. Technol*. **179** (2004) 124.
[81]H. W. Huo, Y. Li, and F. H. Wang, *Corros. Sci*. **46** (2004) 1467.
[82]J. S. Lian, G. Y. Li, L. Y. Niu, C. D. Gu, Z. H. Jiang, and Q. Jiang, *Surf. Coat. Technol*. **200** (2006) 5956.
[83]Y. S. Huang, X. T. Zeng, X. F. Hu, and F. M. Liu, *Electrochim. Acta* **49** (2004) 4313.
[84]T. S. N. Sankara Narayanan, K. Krishnaveni, and S. K. Seshadri, *Mater. Chem. Phys*. **82** (2003) 771.
[85]T. Yokoshima, D. Kaneko, M. Akahori, H. S. Nam, and T. Osaka, *J. Electroanal. Chem*. **491** (2000) 197.
[86]Q. Zhao, Y. Liu, and E. WAbel, *Mater. Chem. Phys*. **87** (2004) 332.
[87]Q. Zhao, Y. Liu, and C. Wang, *Appl. Surf. Sci*. **252** (2005) 1620.
[88]H. Zhao and J. Cui, *Surf. Coat. Technol*. **201** (2007) 4512.
[89]M. E. Pearce, J. B. Melanko, and A. K. Salem, *Pharmac. Res.* **24** (2007) 2335.
[90]X. Ma, X. Li, N. Lun, and S. Wen, *Mater. Chem. Phys*. **97** (2006) 351.
[91]J. Ding, H. Wang, T. Lin, and B. Lee, *Synth. Met*. **158** (2008) 585.
[92]K. G. Neoh, K. K. Tan, P. I. Goh, S. W. Huang, E. T. Kang, and K. L. Tan, *Polymer* **40** (1999) 887.
[93]J. Ding, W. E. Price, S. F. Ralph, and G. G. Wallace, *Polym. Int*. **53** (2004) 681.
[94]Z. Shi, S. Wu, and J. A. Szpunar, *Chem. Phys. Lett*. **422** (2006) 147.
[95]Z. Shi, S. Wu, and J. A. Szpunar, *Nanotechnology* **17** (2006) 2161.
[96]I. Lee, P. T. Hamond, and M. F. Rubner, *Chem. Mater*. **15** (2003) 4583.
[97]G. P. Ling and Y. Li, *Mater. Lett*. **59** (2005) 1610.
[98]S. M. A. Shibli, B. Jabeera, and R. I. Anupama, *Appl. Surf. Sci*. **253** (2006) 1644.
[99]A. E. Fischer, K. A. Pettigrew, D. R. Rolison, R. M. Strond, and J. W. Long, *Nano Lett*. **7** (2007) 281.
[100]H. Kudo and M. Fujihira, *IEEE Trans. Nanomater*. **5** (2005) 90.
[101]M. Knez, A. M. Bittner, F. Boes, C. Wege, H. Jeske, E. Maiβ, and K. Kern, *Nano Lett*. **3** (2003) 1079.

Index